

Journal of *Donghua University* (English Edition)

Former *Journal of China Textile University*

Vol. 42 No. 5

October 31, 2025

Journal of Donghua University (English Edition) (ISSN 1672-5220, CN 31-1920/TS) is published bimonthly and started in 1984.

Aims and Scope *Journal of Donghua University (English Edition)* draws together many aspects of science and technology of textiles and other related disciplines, from fundamental research and development to industrial application. Subject areas covered include: textiles, materials, clothing, chemistry, biomedical engineering, mechanical engineering, computer science, applied physics, management engineering, etc.

Subscription Information *Journal of Donghua University (English Edition)* is published 6 times a year. Volume 42 (6 issues) will be published in 2025. For information on subscription rates please contact Journal Center of Donghua University, 1882 West Yan'an Road, Shanghai 200051, China.

Director of Journal Center

WANG Kebin

Executive Editors

GAO Yu YANG Jianxia WU Yarong

Director of Editorial Board

LIU Shuhui

Vice Director of Editorial Board

ZHU Meifang

Editor-in-Chief

ZHU Meifang

Associate Executive Editor-in-Chief

CHEN Zhigang

Editorial Board Members

CHEN Biqiong	CHEN Nanliang	CHEN Zhigang	CUI Wenguo
DING Bin	DONG Kai	FANG Jian	FU Jiajia
GONG Jixian	GU Bohong	JIANG Jinhua	JIN Jianyong
KANG Yanming	LI Diansen	LI Fang	LI Jingchao
LIAO Guangfu	LIAO Yaozu	LIU Shuhui	LIU Wanjun
LIU Xuqing	LIU Yanan	LIU Yanbo	LIU Zunfeng
LUO Yan	MAO Jifu	MENG Weidong	PAN Ruru
PENG Yitian	QIN Xiaohong	REN Yuanlin	SHEN Bo
SI Yang	SONG Hui	SUN Gang	SUN Zhihong
TIAN Mingwei	WANG Chunrui	WANG Hongzhi	WANG Huaping
WANG Run	WANG Xianfeng	WANG Yunyi	WU Tong
XI Peng	XIN Binjie	XING Yanjun	XU Fujun
XU Yang	YAN Jianhua	YANG Jian	YI Tao
YOU Zhengwei	ZHANG Guanglin	ZHANG Kun	ZHANG Qinghua
ZHANG Qingsong	ZHANG Ruiyun	ZHAO Huijing	ZHU Meifang
ZHUANG Xupin			

Youth Editorial Committee Members

CAO Xinwang	FANG Yinchun	GUAN Fuwang	HUANG Xin
LIN Huiting	LIU Baojiang	NIU Yaolan	TANG Chunxia
YAN Jing	ZHANG Changhuan	ZHENG Xianhong	

Contents

Advanced Functional Materials

- 449 Poly(Octamethylene Citrate)-Based Elastomer Microspheres via Spray-Drying of Chitin Nanocrystal Constructed Pickering Emulsion GUAN Yu, GUO Furong, LIANG Kai, JI Yali
- 457 F-B Co-Doped TiO₂ Nanosheets Bounded with Highly Active Anatase (001) Facets for Improved Photocatalytic Hydrogen Evolution ZHANG Mengyao, WEI Li, LIU Lei
- 466 Analysis of Three Reactive Dyes and Their Six Derivatives by Capillary Electrophoresis HUANG Shuqing, SHEN Li, XU Zhongqai
- 476 Preparation and Power Frequency Shielding Effectiveness of Stainless Steel Conductive Fabric YANG Yang, ZHANG Yan, ZHANG Ruiyun, JI Feng, LI Wenjun, XU Xiaoyuan
- 485 Hydrogen Sensing Characteristics of Gas Sensor Based on Pt/Graphene Composite HOU Tianhao, PENG Yitian, DING Shuyang

Information Technology and Artificial Intelligence

- 494 MLGIA: Recognition of Traffic Panel Information Based on PaddlePaddle JI Yukai, GE Huayong, MENG Yaqun, LI Sisi
- 503 Security Defenses for Cross-Technology Communication in IoT Control System LI Tianyun, ZHANG Anqi, ZHANG Guanglin
- 513 Select-and-Answer Prompting: Facilitating LLMs for Improving Zero-Shot Reasoning WANG Yufang, TANG Xuesong, HAO Kuangrong
- 523 Subgraph Matching on Multi-Attributed Graphs Based on Contrastive Learning LIU Bozhi, FANG Xiu, SUN Guohao, LU Jinhu
- 534 Graph-Based Transform and Dual Graph Laplacian Regularization for Depth Map Denoising MENG Yaqun, GE Huayong, HOU Xinxin, JI Yukai, LI Sisi

Intelligent Detection and Control

- 543 Static Characteristic Analysis of Aerostatic Porous Bearing with a Restricted Layer YU Zhe, YAN Ruzhong, MA Xiaojian, ZHANG Haojie
- 550 Automated Bionic Wig Weaving Process Design and Weaving Path Planning LYU Hongzhan, YOU Jia, LI Junjie, LU Licheng, SUN Zhihong
- 558 Impact of Locally Resonant Phononic Crystal Plates on Noise Reduction in Automotive Mufflers ZHANG Mengyang, ZHU Congyun, DING Guofang, HUANG Qibai

DOI: 10.19884/j.1672-5220.202405003

Poly(Octamethylene Citrate)-Based Elastomer Microspheres via Spray-Drying of Chitin Nanocrystal Constructed Pickering Emulsion

GUAN Yu¹, GUO Furong², LIANG Kai^{1*}, JI Yali²

1. College of Chemistry and Chemical Engineering, Donghua University, Shanghai 201620, China

2. State Key Laboratory of Advanced Fiber Materials, College of Materials Science and Engineering, Donghua University, Shanghai 201620, China

Abstract: Poly(octamethylene citrate) (POC) is a promising bioelastomer material in the biomedical field. However, its thermosetting nature poses a significant challenge to processing and molding, especially manufacturing the POC-based elastomer particles as potential, degradable and toughened fillers. Firstly, a Pickering emulsion with a pre-polymer (pre-POC) solution in dimethyl carbonate as a dispersed oil phase, a Pullulan (PUL) aqueous solution as a continuous water phase, and chitin nanocrystal (ChiNC) as a particle-type emulsifier was constructed. Secondly, the POC-based core/shell structured microspheres were prepared by spray-drying of the emulsions, and characterized by a scanning electron microscope and a transmission electron microscope. Finally, the POC-based core/shell structured microspheres were used as elastomer fillers to strengthen and toughen a chitosan film, resulting in 26% increase in the tensile strength and 45% increase in the strain at break; the POC-based core/shell structured microsphere as a double-layer drug release system was built in which the hydrophilic drug of tetracycline hydrochloride (TCH) was released from the outer layer and the hydrophobic drug of curcumin was released from the inner layer, roughly following the Ritger-Peppas model.

Keywords: poly(octamethylene citrate); elastomer; spray-drying; microsphere; Pickering emulsion

CLC number: TQ323.4

Document code: A

Article ID: 1672-5220(2025)05-0449-08

Open Science Identity
(OSID)



0 Introduction

Poly(octamethylene citrate) (POC), a direct polycondensation product of citric acid and 1,8-octanediol, has attracted considerable attention since its first appearance due to its good biodegradability, biocompatibility, resilience and mechanical compliance with soft tissues^[1-3]. Especially, its related medical devices (such as CitrelockTM and CitresplinTM) have been approved or cleared by Food and Drug Administration of USA^[4], revealing that POC has great application

potentials as an implant material. POC is a typical thermosetting elastomer that is commonly processed into the required forms from its uncrosslinked pre-polymer (pre-POC)^[5-8]. Therefore, the hard-template is often designed for POC molding. For example, the particulate-leaching technique is used to prepare porous tissue engineering scaffolds, involving dissolving pre-POC in an organic solvent, blending it with a salt-template, crosslinking at an elevated temperature, and finally washing off salt^[9-10]. Similarly, the molds fabricated via three-dimensional (3D)-printing^[11] or soft-lithography^[12-13] have been explored as hard-templates to produce POC elastomer scaffolds of varied forms. Furthermore, by the aid of blending pre-POC with other machinable materials, POC could be directly processed or molded, such as electrospun nonwoven meshes as cell scaffolds involving dissolving pre-POC and other electrospinnable polymers in an organic solvent, electrospinning and then thermo-crosslinking^[8, 14]. By employing the pre-POC solution as a dispersed oil phase, the Pullulan (PUL) aqueous solution as a continuous water phase and the chitin nanocrystal (ChiNC) as a particle-type emulsifier, our team constructed a kind of oil-in-water (o/w) Pickering emulsions to produce POC/PUL core/shell fibers via electrospinning^[15]. It is a new processing strategy for POC. Different from classical emulsions stabilized by surfactants, Pickering emulsions are a class of solid particle-stabilized emulsions, and exhibit superior stability and low toxicity^[16]. Especially, the adoption of biologically sourced, nontoxic, biocompatible and biodegradable ChiNCs as emulsifiers instead of inorganic solids (e.g. silica^[17-18], clay^[19], graphene oxide^[20] and halloysite nanotubes^[21]) broadens the applications of such Pickering emulsions in food, cosmetics and biomedicine^[22-25]. PUL is an edible and naturally produced polysaccharide, possesses water-solubility, non-toxicity, non-carcinogenicity, non-mutagenicity and biodegradability, and is widely applied in food, cosmetics, pharmaceuticals and tissue engineering fields^[26-28]. The rubber/elastomer particles can be used as fillers to toughen the plastics matrix, and especially the core/shell structured

Received date: 2024-05-14

* Correspondence should be addressed to LIANG Kai, email: kliang@dhu.edu.cn

Citation: GUAN Y, GUO F R, LIANG K, et al. Poly(octamethylene citrate)-based elastomer microspheres via spray-drying of chitin nanocrystal constructed Pickering emulsion[J]. *Journal of Donghua University (English Edition)*, 2025, 42(5): 449-456.

particles can endow the matrix with different functions^[29]. However, there are few reports on biodegradable and implantable elastomer particles, though they have potentials to toughen the implantable bioplastics. Herein, we further study pre-POC/ChiNC/PUL o/w Pickering emulsions, explore the feasibility of preparation of POC-based core/shell structured microspheres via spray-drying, and discuss the application potentials of polymer reinforcement and core/shell structured microspheres in drug delivery.

1 Materials and Methods

1.1 Materials

PUL was supplied by Tokyo Chemical Industry Co., Japan. Chitin flakes from crab shells and chitosan (CS) were provided by Kehai Chitin Co., Ltd., China. Citric acid, 1, 8-octanediol, dimethyl carbonate (DMC), curcumin, hydrochloric acid and tetracycline hydrochloride (TCH) were purchased from Taitan Co., China. Phosphate buffered saline (PBS) was provided by Nanjing Yusheng Experimental Equipment Co., Ltd., China.

1.2 Preparation of pre-POC

Pre-POC was synthesized via one-pot melt polycondensation^[14]. Briefly, citric acid and 1, 8-octanediol at a molar ratio of 1:1 were mixed together, melt at 140–160 °C under stirring and nitrogen flow, and cooled to 140 °C to continue reacting for 1 h. The obtained viscous raw product was purified by dissolving in ethanol and precipitating in deionized (DI) water for three times to produce pre-POC (Fig. 1(a)).

1.3 Preparation of ChiNC

ChiNC was prepared via the hydrochloric acid hydrolysis of chitin^[30]. Briefly, chitin flakes (10 g) and 3 mol/L hydrochloric acid solution (300 mL) were mixed and stirred for 18 h at a refluxing temperature. The obtained residues were water-washed by centrifugation, dialyzed in DI water for 3 d, and finally lyophilized to

produce ChiNC powders (Fig. 1(b)). Before use, ChiNC was re-dispersed in DI water by ultrasonication.

1.4 Construction of o/w Pickering emulsion

DMC is a good solvent for pre-POC^[15]. It is harmfuless and water-immiscible, fulfilling the requirements as an oil-phase solvent. Herein, we used DMC as an oil-phase solvent to dissolve pre-POC and ChiNC as a particle-type emulsifier to construct the pre-POC/ChiNC o/w Pickering emulsion. The pre-POC was dissolved in DMC (a mass fraction of 50%), and then the pre-POC/DMC solution was added dropwise into the ChiNC aqueous suspension to form the pre-POC/ChiNC o/w Pickering emulsion under stirring. PUL (Fig. 1(c)) was dissolved in DI water (a mass fraction of 20%) followed by adding the ChiNC aqueous suspension to form the PUL/ChiNC water phase, and then the pre-POC/DMC solution was added dropwise to obtain the pre-POC/ChiNC/PUL o/w Pickering emulsion under stirring (Fig. 1(d)). The o/w volume ratios were 1:4, 2:3 and 1:1. Besides, curcumin, being as a hydrophobic-model drug, was dissolved in the pre-POC/DMC solution (a mass concentration of 3 g/L), and TCH, being as a hydrophilic-model drug, was dissolved in the PUL/ChiNC aqueous solution (a mass concentration of 0.025 g/L) to prepare drug-loaded emulsions.

1.5 Spray-drying

The pre-POC/ChiNC/PUL o/w Pickering emulsions were spray-dried in a B-290 spray drier (Buchi Co., Switzerland), as shown in Fig. 1(e). The inlet temperature was 110 °C, the aspiration ratio was 100%, the compressed air flow rate was 473 L/h, and the emulsion feed rate was 2 mL/min. The collected powders were further thermocured at 90 °C in vacuum for 7 d, resulting in the POC/ChiNC/PUL microspheres. Then the POC/ChiNC/PUL microspheres were water-washed repeatedly to remove PUL, resulting in the POC/ChiNC microspheres.

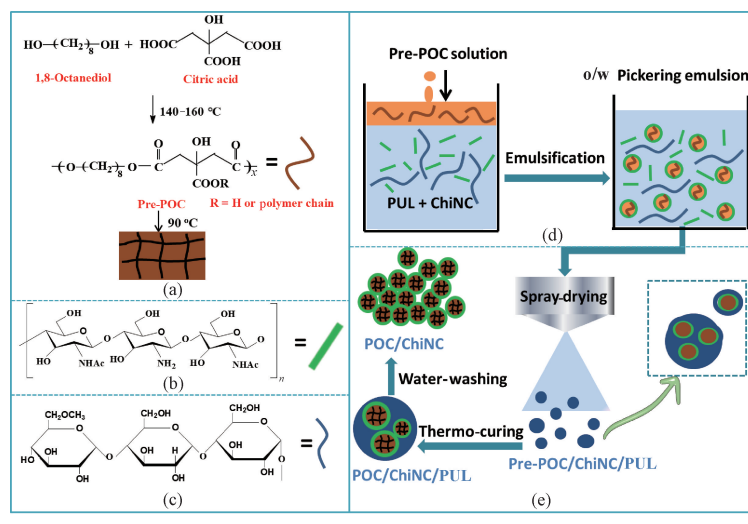


Fig. 1 Preparation of POC-based microspheres: (a) preparation of pre-POC; (b) structure of ChiNC; (c) structure of PUL; (d) preparation of pre-POC/ChiNC/PUL o/w Pickering emulsion; (e) spray-drying of emulsion

1.6 Preparation of POC-based microsphere toughened CS (CS/mPOC)

The POC/ChiNC/PUL microspheres (0.1 g) were suspended in the acetic acid solution (a mass fraction of 2%) via ultrasonication. In this process, the shell-forming PUL was dissolved in the acetic acid solution. Subsequently, 0.9 g CS being dissolved in the acetic acid solution was added with stirring, poured into a petri dish, and dried at 37 °C to form the CS/mPOC film. Meanwhile, the pure CS film was prepared as control.

1.7 Measurement and characterization

The emulsion was transferred to a slide glass by using a micropipette, and images of droplet morphology were captured by using a YPN-330E optical microscope (Yiyuan Optical Instrument Co, China). The average droplet size was determined by measuring at least 100 individual droplets by using the ImageJ software (NIH, USA). Additionally, the morphology of the emulsion was also observed on an SU8010 field emission scanning electron microscope (Hitachi Ltd., Japan). The emulsion was first dried at room temperature, then cryo-fractured in liquid nitrogen and finally sputter coated with gold.

The morphologies of spray-dried microspheres were examined by using the SU8010 field emission scanning electron microscope after being sputter coated with gold. In addition, the POC/ChiNC microspheres were dispersed in absolute alcohol by ultra sonication and observed on a JEM-2100 transmission electron microscope (JEOL Ltd., Japan).

Uniaxial tensile tests for films were performed on a HY-941 material testing machine (Hengyu Instrument Co., China) with a 100 N sensor at room temperature and a crosshead speed of 10 mm/min. The results of the elastic modulus, tensile strength and strain at break were the average of at least five measurements. Additionally, the CS/mPOC film was cryo-fractured in liquid nitrogen and sputter coated with gold for cross-section observation by using the SU8010 field emission scanning electron microscope.

1.8 In vitro drug release

The drug-loaded POC-based core/shell structured microspheres (1.5 g) as prepared in subsection 1.5 was suspended in 10 mL PBS (pH= 7.3), loaded into a dialysis bag with a molecular weight cut off of 10 000, and then immersed in a beaker containing 20 mL PBS, followed by low-speed stirring at room temperature. Every 6 h, 4 mL PBS was taken out from the beaker to measure the absorbance at 427 nm for curcumin and 269 nm for TCH on a UV-Vis spectrophotometer (Shanghai Mapada Instrument Co., Ltd., China), respectively, and then fresh PBS (4 mL) was replenished into the beaker. Beforehand, a serial dilution of curcumin or TCH in PBS was prepared within a range of 2–100 µg/mL. The linear fitting equations ($y_1 = 39.49x_1 + 0.011$ ($R^2 = 0.999$) for TCH and $y_2 = 4.79x_2 - 0.0024$ ($R^2 = 0.981$) for curcumin) were used to calculate the drug mass

concentration, respectively^[31], where y_1 and y_2 are the corresponding absorbance of the two drugs; x_1 and x_2 are the corresponding mass concentrations of the two drugs. The cumulative release rate Q of each drug was calculated according to^[32]

$$Q = (C_n V + V_1 \sum_{i=1}^n C_{n-i})/q, \quad (1)$$

where C_n is the solution mass concentration at the n th time, µg/mL, determined by the standard curve method; V is the solution volume, mL; V_1 is the sampling volume, mL; q is the total mass of each drug, g. TCH was dissolved out from the uncured microspheres by PBS and quantified via the UV-Vis spectrophotometer followed by curcumin dissolution using DMC and its quantification via the same method.

The release experiments of each sample were performed in triplicate and data were averaged. The release profiles of TCH and curcumin from microspheres were fitted by using the Ritger-Peppas model^[33]:

$$Q_t = K_0 \times t^n, \quad (2)$$

where Q_t is the cumulative release rate at time t ; K_0 is the release rate constant; n represents the release exponent, indicating the release mechanism.

Data are expressed as mean ± standard deviation. The one-way analysis of variance (ANOVA) was performed for comparing means between two or multiple groups, and a value of $p < 0.05$ was considered statistically significant.

2 Results and Discussion

2.1 Analysis of o/w Pickering emulsion

The effects of the oil-phase mass fraction and ChiNC contents on the stability of emulsions were studied by observing the sedimentation behavior of the emulsion droplets after 12 h. The results are shown in Fig. 2. The stability of the Pickering emulsion is enhanced as the mass fraction of pre-POC or the content of ChiNC increases. The diameters of emulsion droplets decrease with increasing the ChiNC content as shown in Fig. 3. The emulsion at a pre-POC mass fraction of 50% exhibits an optimal stability; when the ChiNC/pre-POC mass ratio is 7%, after 12 h, no sedimentation occurs, and the droplet diameter decreases to (2.5 ± 0.9) µm, and it is even smaller when more ChiNC is introduced.

Therefore, in the following study, we chose a pre-POC/DMC solution (a pre-POC mass fraction of 50%) and ChiNC at a ChiNC/pre-POC mass ratio of 7% to construct pre-POC/ChiNC/PUL o/w Pickering emulsions, in which PUL was used as protective and shell-layer material to prevent the core-layer material of pre-POC from adjoining together during subsequent thermo-curing. The results are shown in Fig. 4. The introduction of PUL into the continuous water phase of the emulsions at an o/w volume ratio of 1 : 4, 2 : 3 and

1:1 does not disrupt emulsion stability, and even possibly makes the emulsions more stable due to the viscous effect. To further confirm the emulsion morphology, the emulsions were fully air-dried in a fume hood, after which its cross-sectional morphology was examined by using scanning electron microscopy (SEM) as shown in Fig. 4(b). There are many cavities which are supposed to be generated by emulsion droplets being pulled out during brittle fracture in liquid nitrogen, and a small quantity of protrusions is identified as the remained droplets, further confirming this point. In brief, during the evaporation of the solvents (DMC and water), PUL forms a continuous matrix and the ChiNC that wraps pre-POC droplets is immobilized in the matrix, forming a sea-island structure, indirectly proving a good stability of pre-POC/ChiNC/PUL o/w Pickering emulsions.

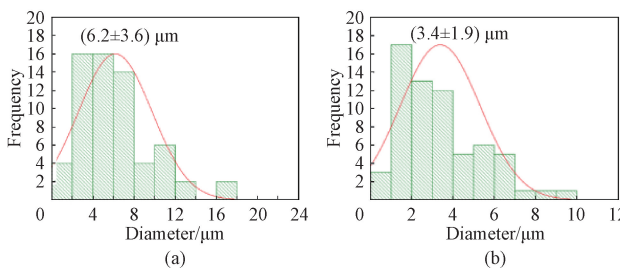
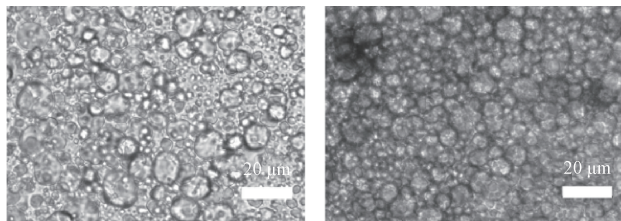


Fig. 3 Optical microscope images of emulsions for 12 h and corresponding droplet diameter distribution histograms at different ChiNC/pre-POC mass ratios: (a) 3%; (b) 5%; (c) 7%; (d) 10%

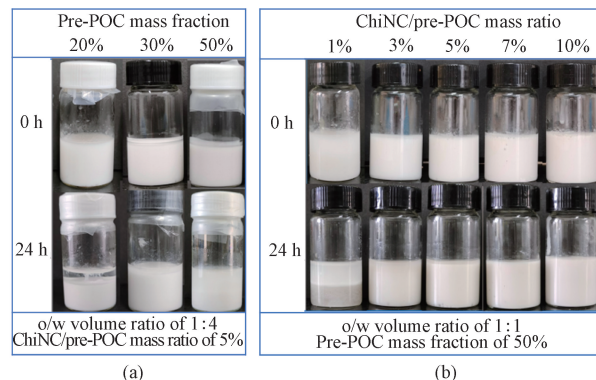


Fig. 2 Visual photos of pre-POC/ChiNC o/w Pickering emulsions: (a) at different pre-POC mass fractions; (b) at different ChiNC/pre-POC mass ratios

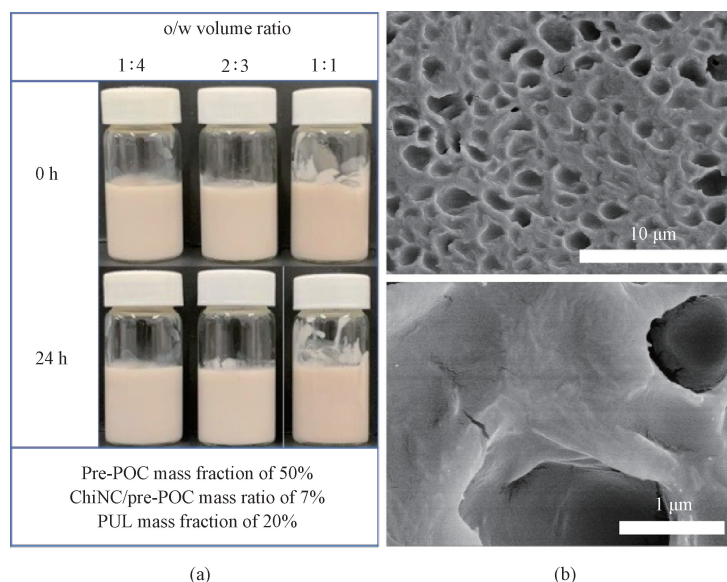
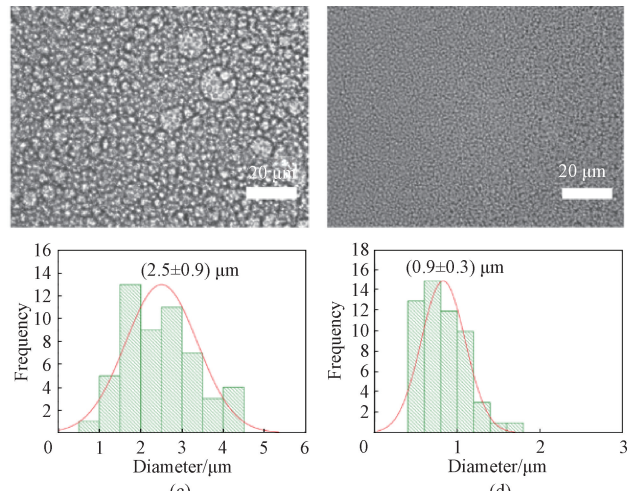


Fig. 4 Stability characterization of pre-POC/ChiNC/PUL o/w Pickering emulsions: (a) visual photos; (b) cross-sectional SEM images of air-dried emulsion at different magnifications

2.2 Analysis of POC-based microspheres

Spray-drying is a common industrial process to prepare polymer microspheres and microcapsules. Herein, the emulsion at an o/w volume ratio of 1:4 was subjected to spray-drying, followed by thermo-curing to produce POC/ChiNC/PUL microspheres. It is supposed that during spray-drying, the continuous phase of the PUL aqueous solution eventually turns into the shell layer of microspheres, the dispersed phase of the pre-POC solution eventually forms the core layer of microspheres, and ChiNCs are located between or within the two layers. It is worth noting that a dried and large microsphere might contain several smaller microspheres due to the limitation of atomization by a nozzle. During thermocuring, POC/ChiNC/PUL microspheres are formed with pre-POC translating into a crosslinked elastomer. Then, POC/ChiNC microspheres are formed by water washing to remove the shell-layer PUL. Figure 5 shows the morphologies and diameter distributions of the POC/ChiNC/PUL and POC/ChiNC microspheres. The diameter of POC/ChiNC microspheres was $(2.0 \pm 1.1) \mu\text{m}$ and lower than that of POC/ChiNC/PUL microspheres ($(3.8 \pm 1.8) \mu\text{m}$) due to the removal of shell-layer PUL. Transmission electron microscopy (TEM) was also used to further confirm the microstructure of the microspheres. Figure 6 (a) shows the morphologies of POC/ChiNC/PUL microspheres. There is a typical core-shell structure for the microsphere. For a larger spray-dried microsphere, there might be several smaller microspheres, i.e. forming multi-microsphere-aggregates (Fig. 6 (a)). After removing PUL, POC/ChiNC microspheres with a diameter of several hundred nanometers are formed as shown in Fig. 6(b). Thus, POC-based microspheres were successfully prepared by spray-drying the combined Pickering emulsion.

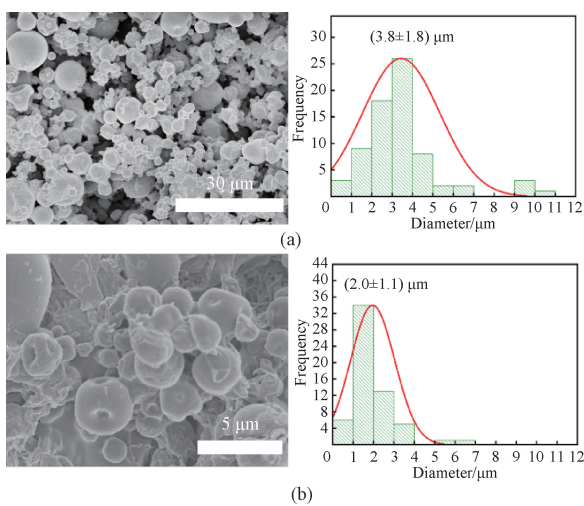


Fig. 5 SEM images and corresponding droplet diameter distribution histograms: (a) POC/ChiNC/PUL microspheres; (b) POC/ChiNC microspheres

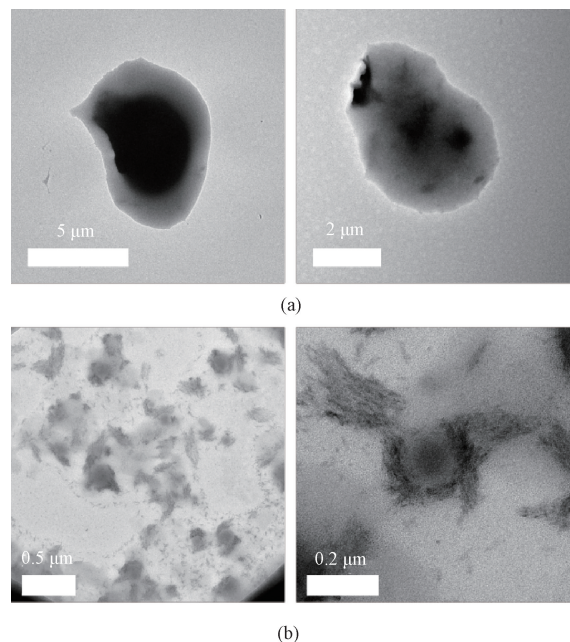


Fig. 6 TEM images: (a) POC/ChiNC/PUL microspheres; (b) POC/ChiNC microspheres

2.3 Analysis of CS/mPOC films

The POC-based microspheres could be used as a class of biodegradable fillers to toughen the biodegradable polymers. We chose brittle CS as the matrix and the POC/ChiNC/PUL microspheres as the fillers to preliminarily explore the feasibility of toughening CS by using the elastomer microspheres. The water solubility of PUL would cause the multi-microsphere-aggregates to be dissociated into individual microspheres for easy blending with CS in an aqueous system. The tensile properties are depicted in Figs. 7(a) and 7(b). In comparison to the CS film, the CS/mPOC film exhibits higher tensile properties: the tensile strength increases by 26%, the strain at break increases by 45% and the elastic modulus increases by 34%. Thus, the introduction of POC/ChiNC/PUL microspheres not only strengthens CS but also toughens CS. It has been reported that ChiNC is a good nanofiller for strengthening CS^[34]. Meanwhile, the coexist of ChiNC and POC could strengthen and toughen CS. The cross-sectional morphology of the CS/mPOC film is displayed in Fig. 7(c). Some light-colored protrusions, identified as the microspheres, are evenly distributed in the matrix, indicating a good compatibility of CS and POC/ChiNC/PUL. In brief, it is confirmed that the POC/ChiNC/PUL microspheres enhance the tensile properties of the CS film. The potential mechanism needs to be studied in our future work.

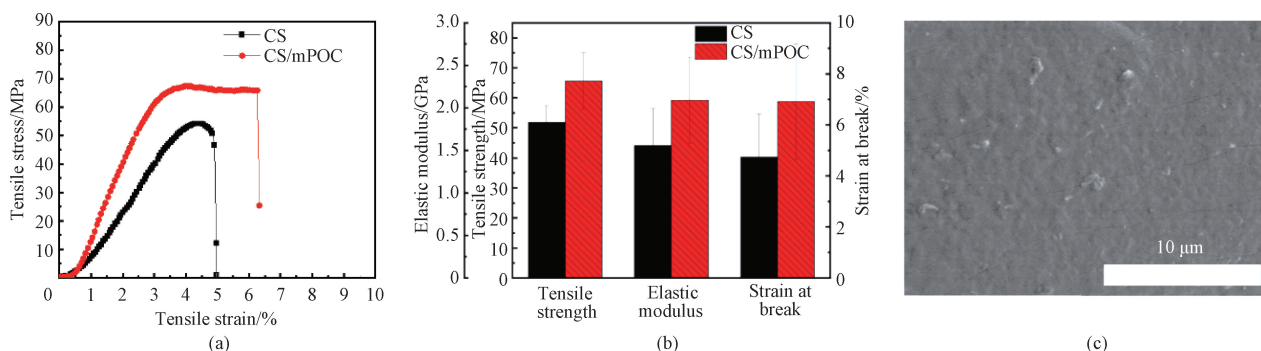


Fig. 7 Tensile properties and cross-sectional morphology: (a) tensile stress-strain curves of CS and CS/mPOC films; (b) tensile strength, elastic modulus and strain at break of CS and CS/mPOC films; (c) cross-sectional SEM image of CS/mPOC film

2.4 Drug release analysis of POC/ChiNC/PUL microspheres

Curcumin as a hydrophobic-model drug and TCH as a hydrophilic-model drug were dissolved in the oil phase and aqueous phase, respectively, to obtain drug-loaded core/shell structured microspheres via spray-drying. The cumulative release rate of each drug at time t is shown in Fig. 8. TCH in the PUL outer layer exhibits an obvious burst release in the first 48 h, up to an cumulative release rate of 48%, and then its release gradually increases to 99% until 480 h. Curcumin in the POC inner layer does not exhibit a significant burst release like TCH. The cumulative release rate of curcumin slowly increases at the first 192 h, up to 20%; then, it moderately increases at the second 192 h, up to about 70%; afterwards, the release is more slowly. The slow release of curcumin results from the low solubility of curcumin in the PBS solution, as well as low swelling and slow degradation of POC. Overall, the POC/ChiNC/PUL microspheres realize a double-layer drug release and dual therapeutic effects, in which the hydrophilic drug in the outer layer releases quickly and the hydrophobic drug in the inner layer releases slowly.

The diffusion mechanism of the drug release was confirmed by the Ritger-Peppas model. The fitted curves and corresponding parameters are displayed in Fig. 8.

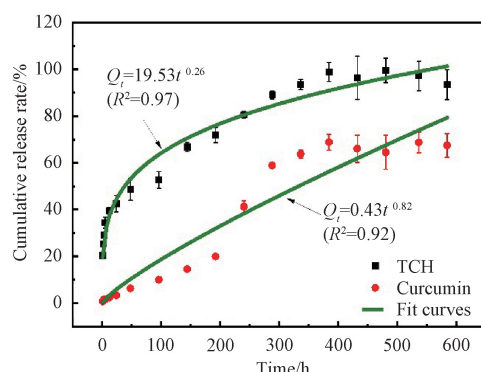


Fig. 8 Drug release curves for drug-loaded core/shell structured microspheres

In spherical matrices, the dominant drug release

mechanism can be assumed according to the n values. For $n \leq 0.43$, the release follows the Fickian diffusion; for $0.43 < n < 1.00$, the release behavior is the non-Fickian transport, with erosion and diffusion as the dominant mechanism^[33]. As the release exponent of TCH is 0.26 and lower than 0.43, the TCH release is mainly controlled by the Fickian diffusion; as the release exponent of curcumin is 0.82 and lower than 1.00, the curcumin release behavior is the non-Fickian transport, with erosion and diffusion as the dominant mechanism.

3 Conclusions

This study used the pre-POC solution in DMC as an oil phase, the PUL aqueous solution as a water phase and the ChiNC as an emulsifier to construct o/w Pickering emulsions. The stability of emulsions was enhanced with the increase of the pre-POC mass fraction and ChiNC content. With the increase of the ChiNC content, the diameters of emulsion droplets decreased. Moreover, the introduction of PUL into the continuous water phase did not disrupt the stability of emulsions. POC/ChiNC/PUL core/shell structured microspheres were successfully prepared via spray-drying. Such microspheres were used as biodegradable fillers to strengthen and toughen CS via simple aqueous mixing, i.e. 26% increase in the tensile strength and 45% increase in the strain at break. A double-layer drug release system was built to release the hydrophilic drug of TCH from the outer layer and the hydrophobic drug of curcumin from the inner layer, both roughly following the Ritger-Peppas model.

References

- [1] YANG J, WEBB A R, AMEER G A. Novel citric acid-based biodegradable elastomers for tissue engineering [J]. *Advanced Materials*, 2004, 16(6): 511-516.
- [2] WANG M, XU P, LEI B. Engineering multifunctional bioactive citrate-based biomaterials for tissue engineering [J]. *Bioactive Materials*, 2023, 19: 511-537.

- [3] WAN L, LU L L, LIANG X J, et al. Citrate-based polyester elastomer with artificially regulatable degradation rate on demand [J]. *Biomacromolecules*, 2023, 24(9) : 4123-4137.
- [4] WANG H F, HUDDLESTON S, YANG J, et al. Enabling proregenerative medical devices via citrate-based biomaterials: transitioning from inert to regenerative biomaterials [J]. *Advanced Materials*, 2024, 36(6) : 2306326.
- [5] CHUNG E J, SUGIMOTO M, KOH J L, et al. Low-pressure foaming: a novel method for the fabrication of porous scaffolds for tissue engineering [J]. *Tissue Engineering Part C: Methods*, 2012, 18(2) : 113-121.
- [6] BALER K, BALL J P, CANKOVA Z, et al. Advanced nanocomposites for bone regeneration [J]. *Biomaterials Science*, 2014, 2(10) : 1355-1366.
- [7] GUO J S, TIAN X G, XIE D H, et al. Citrate-based tannin-bridged bone composites for lumbar fusion [J]. *Advanced Functional Materials*, 2020, 30(27) : 2002438.
- [8] VOGT L, BOCCACCINI A R. Random and aligned electrospun poly(ϵ -caprolactone) (PCL)/poly(1, 8-octanediol-co-citrate) (POC) fiber mats for cardiac tissue engineering using benign solvents[J]. *European Polymer Journal*, 2021, 160: 110772.
- [9] JONES T, ZHANG B S, MAJOR S, et al. All-trans retinoic acid eluting poly (diol citrate) wafers for treatment of glioblastoma[J]. *Journal of Biomedical Materials Research Part B: Applied Biomaterials*, 2020, 108(3) : 619-628.
- [10] GUO Y, TRAN R T, XIE D H, et al. Citrate-based biphasic scaffolds for the repair of large segmental bone defects [J]. *Journal of Biomedical Materials Research Part A*, 2015, 103(2) : 772-781.
- [11] KIM K, JEONG C G, HOLLISTER S J. Non-invasive monitoring of tissue scaffold degradation using ultrasound elasticity imaging [J]. *Acta Biomaterialia*, 2008, 4(4) : 783-790.
- [12] ZHANG B Y, LAI B F L, XIE R X, et al. Microfabrication of AngioChip, a biodegradable polymer scaffold with microfluidic vasculature [J]. *Nature Protocols*, 2018, 13: 1793-1813.
- [13] MONTGOMERY M, AHADIAN S, DAVENPORT HUYER L, et al. Flexible shape-memory scaffold for minimally invasive delivery of functional tissues [J]. *Nature Materials*, 2017, 16: 1038-1046.
- [14] ZHU L, ZHANG Y Z, JI Y L. Fabricating poly (1, 8-octanediol citrate) elastomer based fibrous mats via electrospinning for soft tissue engineering scaffold [J]. *Journal of Materials Science: Materials in Medicine*, 2017, 28(6) : 93.
- [15] GUO F R, LIANG K, JI Y L. Electrospun poly (octamethylene citrate) thermoset fibrous mat from chitin nanocrystal constructed Pickering emulsion [J]. *Colloid and Polymer Science*, 2024, 302(6) : 891-900.
- [16] WU J, MA G H. Recent studies of Pickering emulsions: particles make the difference [J]. *Small*, 2016, 12(34) : 4633-4648.
- [17] STARVAGGI N C, BRADFORD B J, TAYLOR C D L, et al. Wettability-tuned silica particles for emulsion-templated microcapsules [J]. *Soft Matter*, 2023, 19(39) : 7635-7643.
- [18] TU S H, ZHAO Y L, TAN H T, et al. Ultralight silica foams with a hierarchical pore structure via a surfactant-free high internal phase emulsion process[J]. *Langmuir*, 2018, 34(35) : 10381-10388.
- [19] BON S A F, COLVER P J. Pickering miniemulsion polymerization using laponite clay as a stabilizer[J]. *Langmuir*, 2007, 23 (16) : 8316-8322.
- [20] FADIL Y, DINH L N M, YAP M O Y, et al. Ambient-temperature waterborne polymer/rGO nanocomposite films: effect of rGO distribution on electrical conductivity [J]. *ACS Applied Materials & Interfaces*, 2019, 11 (51) : 48450-48458.
- [21] LISUZZO L, CAVALLARO G, MILIOTI S, et al. Pickering emulsions stabilized by halloysite nanotubes: from general aspects to technological applications[J]. *Advanced Materials Interfaces*, 2022, 9(10) : 2102346.
- [22] SHARKAWY A, BARREIRO M F, RODRIGUES A E. Chitosan-based Pickering emulsions and their applications: a review [J]. *Carbohydrate Polymers*, 2020, 250: 116885.
- [23] RIGG A, CHAMPAGNE P, CUNNINGHAM M F. Polysaccharide-based nanoparticles as Pickering emulsifiers in emulsion formulations and heterogenous polymerization systems [J]. *Macromolecular Rapid Communications*, 2022, 43(3) : 2100493.
- [24] KONG L Q, YANG H F, QIAN Z H, et al. Diradical character and controllable magnetic properties in chitin through radical modification [J]. *Journal of Donghua University (English Edition)*, 2022, 39(1) : 15-21.
- [25] LIU X F, BU Y F, JI Y L. Preparation of chitin nanowhiskers via deep eutectic solvent [J]. *Journal of Donghua University (Natural Science)*, 2020, 46(4) : 584-588. (in Chinese)
- [26] SINGH R S, SAINI G K, KENNEDY J F. Pullulan: microbial sources, production and applications[J]. *Carbohydrate Polymers*, 2008, 73(4) : 515-531.
- [27] PRAJAPATI V D, JANI G K, KHANDA S M. Pullulan: an exopolysaccharide and its various applications[J]. *Carbohydrate Polymers*, 2013,

- 95(1) : 540-549.
- [28] GUERRINI L M, OLIVEIRA M P, STAPAIT C C, et al. Evaluation of different solvents and solubility parameters on the morphology and diameter of electrospun Pullulan nanofibers for curcumin entrapment [J]. *Carbohydrate Polymers*, 2021, 251: 117127.
- [29] LIU Y, WANG Y, ZHAO Y L, et al. Study on the properties of cyanate ester/epoxy adhesive toughened with core-shell rubber particle [J]. *Chemistry and Adhesion*, 2022, 44 (2) : 115-117, 146. (in Chinese)
- [30] GU S H, TIAN Y L, LIANG K, et al. Chitin nanocrystals assisted 3D printing of polycitrate thermoset bioelastomers [J]. *Carbohydrate Polymers*, 2021, 256: 117549.
- [31] MOHAMADY HUSSEIN M A, GULER E, RAYAMAN E, et al. Dual-drug delivery of Ag-chitosan nanoparticles and phenytoin via core-shell PVA/PCL electrospun nanofibers [J]. *Carbohydrate Polymers*, 2021, 270: 118373.
- [32] CAI J H, YANG Y Q, XIE S T, et al. Research on synthesis and drug release of rutin alginate/chitosan microspheres prepared by layer-by-layer self-assembly method [J]. *Polymer Bulletin*, 2018(5) : 58-66. (in Chinese)
- [33] LAKSHANI N, WIJERATHNE H S, SANDARUWAN C, et al. Release kinetic models and release mechanisms of controlled-release and slow-release fertilizers [J]. *ACS Agricultural Science & Technology*, 2023, 3(11) : 939-956.
- [34] YAN W X, SHEN L B, JI Y L, et al. Chitin nanocrystal reinforced wet-spun chitosan fibers [J]. *Journal of Applied Polymer Science*, 2014, 131(19) : 40852.

通过喷雾干燥甲壳素纳米晶构建的 Pickering 乳液 制备聚柠檬酸酯弹性体微球

管 裕¹, 郭芙蓉², 梁 凯^{1*}, 吉亚丽²

1. 东华大学 化学与化工学院, 上海 201620

2. 东华大学 先进纤维材料全国重点实验室 材料科学与工程学院, 上海 201620

摘要: 聚柠檬酸酯 (poly(octamethylene citrate), POC) 是一种在生物医学领域具有广阔应用前景的生物弹性体材料。然而, 其热固性本质使加工成型困难, 特别是制备 POC 基弹性体颗粒以作为潜在的可降解增强填料。首先, 该文以 POC 预聚物 (pre-POC) 的碳酸二甲酯溶液为分散油相, 普鲁兰水溶液为连续水相, 甲壳素纳米晶为颗粒型乳化剂, 成功构建了 Pickering 乳液。其次, 通过喷雾干燥乳液制备 POC 基核/壳结构微球, 并采用扫描电子显微镜和透射电子显微镜对其进行表征。最后, 将微球作为弹性体填料以提高壳聚糖膜的强度和韧性。结果表明, 复合膜的拉伸强度提高了 26%, 断裂伸长率增加了 45%; 将微球作为双层药物释放系统, 外层释放亲水性药物盐酸四环素, 内层释放疏水性药物姜黄素, 双层释放机理基本符合 Ritger-Peppas 模型。

关键词: 聚柠檬酸酯; 弹性体; 喷雾干燥; 微球; Pickering 乳液

DOI: 10.19884/j.1672-5220.202406004

F-B Co-Doped TiO₂ Nanosheets Bounded with Highly Active Anatase (001) Facets for Improved Photocatalytic Hydrogen Evolution

ZHANG Mengyao, WEI Li, LIU Lei*

Center for Advanced Low-dimension Materials, Donghua University, Shanghai 201620, China

Abstract: F-B co-doped TiO₂ nanosheets with exposed anatase (001) facets were synthesized via a one-pot solvothermal method, and their photocatalytic hydrogen evolution performance was investigated. Characterization results confirm that this method effectively promotes the growth of the highly active anatase (001) facets and enhances visible and infrared light absorption while inducing oxygen vacancies. Under optimal conditions, the hydrogen evolution reaches 20.57 μmol after 10 h of ultraviolet-visible (UV-Vis) light irradiation, exceeding the commercial TiO₂ nanoparticles Degussa P25 by more than 10 times. These findings highlight the potential of F-B co-doped TiO₂ nanosheets for efficient photocatalysis.

Keywords: F-B co-dope; TiO₂; photocatalysis; active facet; oxygen vacancy

CLC number: O614; O643

Article ID: 1672-5220(2025)05-0457-09

Document code: A

Open Science Identity
(OSID)



0 Introduction

In 1972, Fujishima et al.^[1] first reported the successful use of the photoelectrochemical method to harness solar energy for water splitting on TiO₂ electrodes. Since then, due to its advantages including high stability, high electron transferability, non-toxicity and low cost, TiO₂ has been widely applied as a robust photocatalyst in various fields such as energy and environment^[2-3]. However, its wide bandgap (anatase, 3.2 eV; rutile, 3.0 eV) limits its absorption to ultraviolet (UV) light, rendering it unable to utilize visible light in sunlight. Meanwhile, the photocatalytic activity of TiO₂ is further restricted by some other factors such as rapid recombination of photoinduced electron-hole pairs and the hydrogen-oxygen reverse reaction. Therefore, in order to improve the photocatalytic activity of TiO₂, it is crucial to enhance its visible light responsiveness, and inhibit the recombination of electron-hole pairs and the hydrogen-oxygen reverse reaction. Current methods for this purpose are mainly focused on

the following pathways, including morphology control, element doping, dye sensitization and compositing with other materials^[4-5].

Morphology control mainly involves restricting the growth of crystal facets with low catalytic activity while exposing those with high catalytic activity^[6]. Due to the high surface energy and the exposure of atoms with a low coordination number, as well as a wide Ti—O—Ti bond angle, anatase (001) facets exhibit higher catalytic activity over other facets, which has been indicated by both theoretical calculations^[7-8] and experimental results^[9-10]. By using hydrofluoric acid (HF) as a crystal growth modifier, Yang et al.^[11] first synthesized anatase single crystals with a 47% exposure ratio of anatase (001) facets via a hydrothermal method. Inspired by this pioneering work, researchers have continuously increased the exposure ratio of anatase (001) facets by selecting different crystal growth modifiers and optimizing reaction conditions. The exposure ratio of anatase (001) facets can reach 64% under the synergies of isopropanol and HF^[12], while by controlling the amount of HF and the hydrothermal reaction temperature, the exposure ratio can further increase to 89%^[13]. In a pure isopropanol system, using diethylenetriamine (DETA) as the crystal growth modifier, anatase ultrathin layers with nearly 100% exposed anatase (001) facets can be obtained^[14]. Recently, the influence of precursor resource^[15], reaction temperature^[16-17], ripening environment^[18] and synthesis strategy^[19-20] on the controlled exposure of anatase (001) facets has been extensively investigated. However, almost all the samples reported in the above studies only exhibit UV-responsive characteristics, which means that they can only perform the photocatalytic tasks under UV light irradiation.

Element doping can form new energy levels in the bandgap, thereby reducing the TiO₂ bandgap energy, expanding the light response range to the visible light region, and lowering the rate of recombination of photoinduced electron-hole pairs. It is a simple and effective method to improve the photocatalytic activity of TiO₂^[21-22]. Several metal elements, especially transition

Received date: 2024-06-13

Foundation item: National Natural Science Foundation of China (No. 81861138040)

* Correspondence should be addressed to LIU Lei, email: liulei@dh.edu.cn

Citation: ZHANG M Y, WEI L, LIU L. F-B co-doped TiO₂ nanosheets bounded with highly active anatase (001) facets for improved photocatalytic hydrogen evolution[J]. *Journal of Donghua University (English Edition)*, 2025, 42(5): 457-465.

metal elements, have been used for TiO_2 doping. However, the doping of metal elements reduces the thermal stability of TiO_2 and introduces additional active centers, resulting in an elevated recombination of photoinduced electron-hole pairs^[23]. Therefore, since Asahi et al.^[24] first reported in 2001 that N-doped TiO_2 exhibited enhanced visible light responsiveness and photocatalytic performance, non-metal element doping has gradually become a hot research topic. Non-metal element doping is difficult to affect the TiO_2 conduction band structure. Instead, it is usually achieved by reconstructing the TiO_2 valence band, shifting it upward to narrow the bandgap. This can significantly reduce the electronegativity of TiO_2 and greatly enhance its absorption of visible light. Commonly used non-metal elements for TiO_2 doping include carbon, nitrogen, sulfur and others with approximate atomic radius as oxygen^[25-26]. Sol-gel, hydrothermal and co-precipitation methods can all be applied to synthesize non-metal element-doped TiO_2 ^[27-28]. However, these doped TiO_2 materials generally exist in the morphological form of nanoparticles or nanoparticle assemblies. Non-metal element co-doped TiO_2 photocatalysts with a specific and uniform morphology are rarely reported.

Recent studies have found that oxygen vacancies play an important role in enhancing the catalytic activity of TiO_2 in heterogeneous catalytic reactions. Nakamura et al.^[29] demonstrated that plasma-treated TiO_2 containing oxygen vacancies exhibited significantly enhanced photocatalytic degradation of NO. A similar enhancement effect was also reported by Justicia et al.^[30]. In addition to modifying the electronic structure, oxygen vacancies can provide important reaction sites for reactant molecules^[31]. Although there are various methods to induce the formation of oxygen vacancies, such as heat treatment in vacuum, inert atmosphere or reducing atmosphere^[32], these methods display many obvious drawbacks, such as complex equipment, harsh synthesis conditions and high cost. Therefore, it is still a very important challenge to promote the formation of oxygen vacancies through a simple and direct method.

In this study, F-B co-doped TiO_2 (F-B- TiO_2) nanosheets with highly active anatase (001) facets, were synthesized through a simple one-pot solvothermal method. F-B co-doping significantly enhances the absorption of visible light by the as-synthesized TiO_2 and induces the formation of oxygen vacancies in the TiO_2 matrix. Compared to non-doped TiO_2 , F-B- TiO_2 nanosheets demonstrate significantly improved photocatalytic performance for hydrogen evolution from water under UV-visible (UV-Vis) light irradiation.

1 Materials and Methods

1.1 Chemical reagents

All chemical reagents are of analytical grade and

used without further purification. Hydrofluoboric acid (HBF_4), titanium trichloride (TiCl_3) and anhydrous ethanol were purchased from Shanghai Chemical Reagent Co., Ltd., China. Commercial TiO_2 nanoparticles Degussa P25 (P25 for short) were bought from Sigma-Aldrich (Shanghai) Trading Co., Ltd., China and used as a reference material for photocatalytic hydrogen evolution.

1.2 Synthesis of F-B- TiO_2 nanosheets

F-B- TiO_2 nanosheets were synthesized by using a simple one-pot solvothermal method. In a typical synthesis, a certain amount of TiCl_3 solution was added dropwise into 60 mL ethanol followed by stirring for 5 min. Subsequently, different amounts of HBF_4 were added, by which the volume of TiCl_3 was controlled to maintain a series of volume ratios with HBF_4 . After thorough mixing, the mixture was transferred into a 100 mL Teflon-lined stainless-steel autoclave and maintained for solvothermal treatment. The reaction was conducted at 200 °C for 12 h. After natural cooling, the samples were successively washed with deionized water and ethanol three times, respectively, and dried overnight at 60 °C in an oven. For simplicity, F-B- TiO_2 -X is used to denote different samples synthesized at various volume ratios of HBF_4 to TiCl_3 , where X represents the volume ratio of HBF_4 to TiCl_3 ($v(\text{HBF}_4) : v(\text{TiCl}_3)$). If X=0, it means there is no HBF_4 added during sample preparation.

1.3 Characterization

The obtained F-B- TiO_2 nanosheets were characterized by X-ray diffraction (XRD), UV-Vis-near Infrared (UV-Vis-NIR) absorption spectroscopy, X-ray photoelectron spectroscopy (XPS), scanning electron microscopy (SEM) and transmission electron microscopy (TEM). XRD data were obtained by using a Philips X' Pert PRO SUPER X-ray diffractometer (PANalytical, the Netherlands) ($\text{Cu K}\alpha$, $\lambda = 1.54056 \times 10^{-10}$ m) with an operating voltage and current of 40 kV and 40 mA, respectively. XPS spectra were acquired by using an ESCALAB 250Xi X-ray photoelectron spectrometer (Thermo Fisher Scientific, USA). UV-Vis-NIR absorption spectra were measured on a UV-2600 UV-Vis spectrophotometer (Shimadzu, Japan). SEM images were obtained with a SUPRATM 40 field emission scanning electron microscope (Carl Zeiss, Germany) and TEM images were obtained with a JSM-2010F transmission electron microscope (JEOL Ltd., Japan).

1.4 Photocatalytic activity testing

The photocatalytic activity of F-B- TiO_2 samples was evaluated through photocatalytic hydrogen evolution experiments. The experiments were conducted in a closed system (500 mL) connected to a gas chromatography, with a 150 W xenon lamp as the light source (irradiation from the top). F-B- TiO_2 (0.1 g) was dispersed in a 100 mL mixture of water and methanol (a volume ratio of 9:1). The amount of hydrogen evolution was directly detected online by gas chromatography.

2 Results and Discussion

2.1 Crystal structure analyses

Figure 1 shows the XRD patterns of some as-prepared F-B-TiO₂ samples in this experiment. Three samples were selected for XRD test: F-B-TiO₂-0 (a), F-B-TiO₂-0.50 (b) and F-B-TiO₂-0.75 (c). It can be seen that all the samples synthesized under different conditions exhibit pure anatase phase (JCPDS card No.21-1272), since all the identified peaks can be perfectly indexed to representative anatase crystal facets. The sharp and strong diffraction peaks indicate good crystallinity of the F-B-TiO₂ samples.

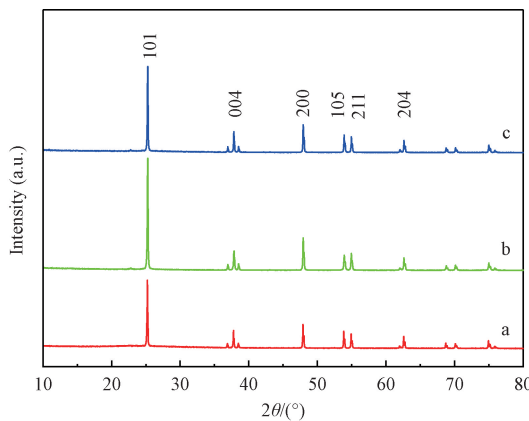


Fig. 1 XRD patterns of F-B-TiO₂ samples obtained at different volume ratios of HBF₄ to TiCl₃

2.2 Morphology characterization

The microscopic morphology, particle size and exposed crystal facets of F-B-TiO₂ samples were characterized by SEM and TEM. In the absence of HBF₄, the apparent color of the obtained sample is pure white as illustrated in the inset of Fig. 2(a). Its typical microscopic morphology is spherical aggregates composed with irregular building blocks, of which the exposed crystal facets are almost all anatase (101) facets with low

activity (red arrows in Fig. 2 (a)). When a small amount of HBF₄ was added (where the volume ratio of HBF₄ to TiCl₃ is 0.25), the apparent color of the final sample becomes slight grey. The microscopic structure changes from spherical to a flower-like structure composed of nanoplates with a thickness of about 150 nm (Fig. 2(b)). The exposure percentage of anatase (101) facets decreases significantly (red arrows in Fig. 2(b)), while some exposed anatase (001) facets can be identified (blue arrows in Fig. 2(b))^[11]. With an increased addition of HBF₄ to a volume ratio of HBF₄ to TiCl₃ of 0.50, the apparent color of the sample changes into blue-gray as shown in the inset of Fig. 2(c). The obtained flower-like structures separate from each other (Fig. 2(c)) instead of agglomerating together like the samples synthesized at a lower HBF₄ to TiCl₃ volume ratio (Fig. 2(b)). From the magnified SEM image, it can be found that the building blocks exhibit a more pronounced sheet-like structure (Fig. 2(d)). Although the diameters of the nanosheets vary slightly from each other, their thicknesses are quite uniform at around 70 nm. Compare with previous reports^[11-12], the edges of the nanosheets comprising the building blocks exhibit a relatively smooth and round surface, instead of displaying clear intersection lines of (101) and (001) facets or two (101) facets. Additionally, the exposed anatase (001) facets are not very smooth and intact but exhibit many recesses and pore structures as shown in Fig. 2(d). This phenomenon is further verified by the TEM image (Fig. 2(e)), in which the defects can be easily recognized by lower contrast in the sample sheet. Since the lengths of F-B-TiO₂ nanosheets are located between 0.5 and 1.5 μm, the exposure percentage of anatase (001) facets is estimated to be between 75% and 90%, which can be calculated by using ideal anatase single crystal as a model system. Further increasing HBF₄ to a volume ratio of HBF₄ to TiCl₃ of 0.75, it can be observed that the total amount of nanosheet-like structures decreases, and many nanometer-sized particles appear on the flower-like aggregates (Fig. 2(f)).

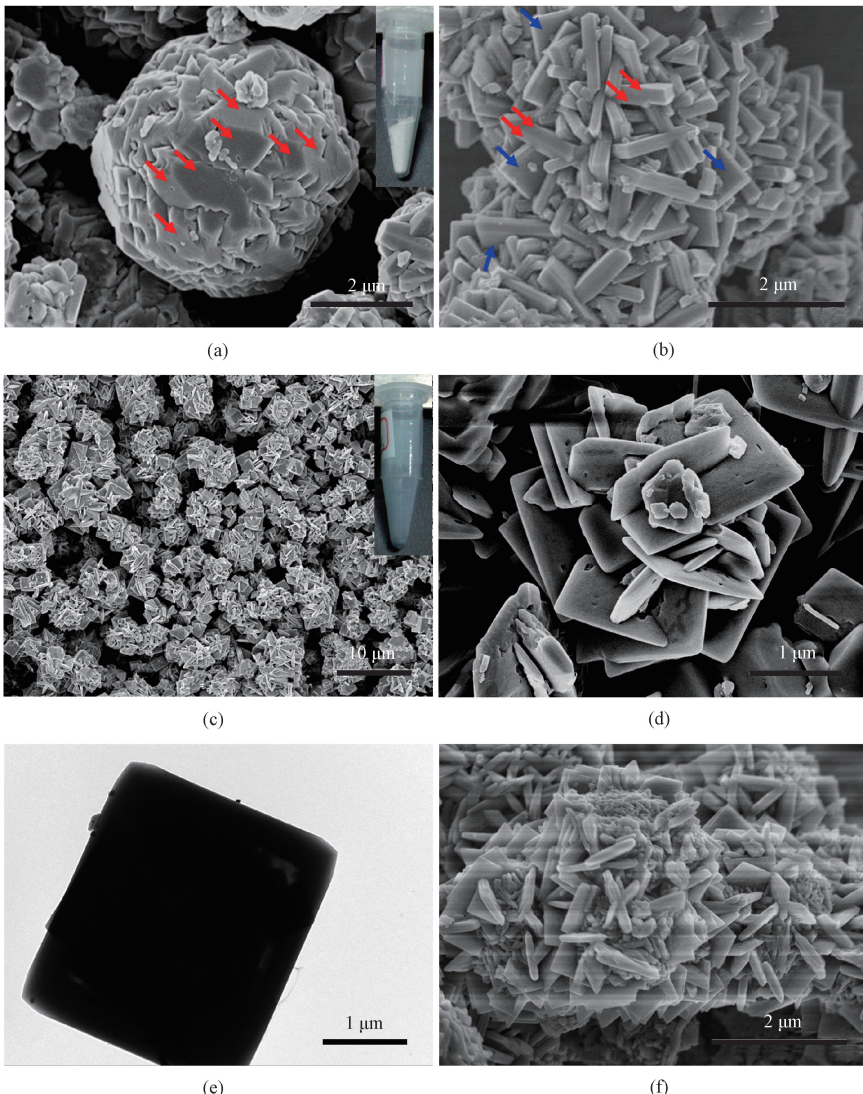


Fig. 2 SEM and TEM images of F-B-TiO₂ samples obtained at different volume ratios of HBF₄ to TiCl₃: (a) SEM image of F-B-TiO₂-0; (b) SEM image of F-B-TiO₂-0.25; (c)-(d) SEM images of F-B-TiO₂-0.50; (e) TEM image of F-B-TiO₂-0.50; (f) SEM image of F-B-TiO₂-0.75

2.3 Photo-responsive properties

The UV-Vis-NIR spectroscopy was utilized to analyze the photo-responsive properties of F-B-TiO₂ samples synthesized at different volume ratios of HBF₄ to TiCl₃. P25 was chosen as a reference material here. The UV-Vis-NIR results shown in Fig. 3(a) indicate that both P25 and all F-B-TiO₂ samples have nearly overlapping absorption spectra below 400 nm, which mainly reflects the intrinsic absorption of anatase TiO₂ materials^[33]. The sample synthesized without adding HBF₄ exhibits a similar absorption spectrum to P25, with absorption mainly concentrated in the UV region and no absorption in the visible and infrared regions. When HBF₄ is added into the synthesis system, the absorption spectra undergo significant changes, exhibiting strong absorption above 400 nm up to the infrared region. This absorption is

mainly caused by the excitation of electrons localized in the defect structure states which are below the conduction band edge of anatase TiO₂, induced by low-energy photon or thermal excitation^[34]. It can also be easily observed that the absorbance of F-B-TiO₂ samples reaches the maximum when the volume ratio of HBF₄ to TiCl₃ is 0.50.

According to previous studies^[35-36], bandgap energies of the obtained samples were determined by

$$\alpha h\nu = A(h\nu - E_g)^p, \quad (1)$$

where α , $h\nu$, A and E_g represent the adsorption coefficient, photon energy, proportionality constant and bandgap energy, respectively; p is the bandgap scaling exponent, with $p = 1/2$ for the direct bandgap and $p = 2$ for the indirect bandgap. Since anatase is an indirect bandgap semiconductor, the bandgap energy can be

estimated by extrapolating the linear portion of $(\alpha h\nu)^{1/2}$ versus $h\nu$ plot in Fig. 3(b). It is found that the co-doping of F and B can reduce the bandgap energy of the samples compared to P25. The lowest bandgap energy with a value of 2.87 eV is achieved for F-B-TiO₂-0.50, which is consistent with UV-Vis-NIR results.

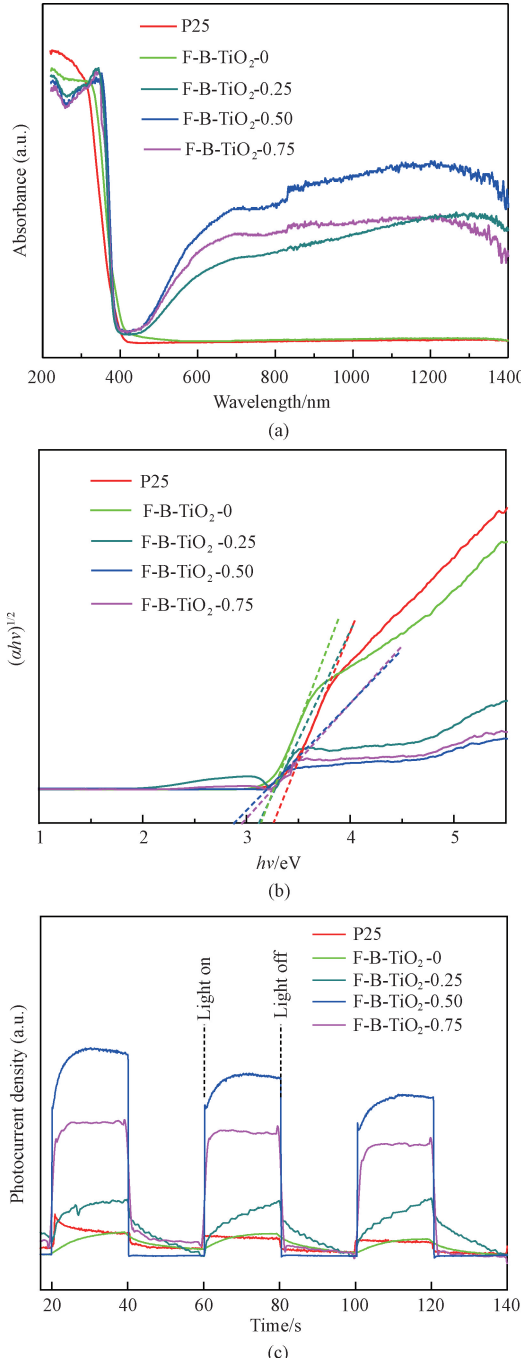


Fig. 3 Photo-responsive properties of P25 and four F-B-TiO₂ samples obtained at different volume ratios of HBF₄ to TiCl₃: (a) UV-Vis-NIR spectra; (b) corresponding bandgap energies; (c) transient photocurrent response

2.4 Photoelectrochemical and surface chemical analyses

Transient photocurrent measurements under chopped light irradiation were conducted on P25 and four F-B-TiO₂ samples by using a xenon lamp as the light source. The results shown in Fig. 3(c) indicate that the photocurrent rapidly rises and falls with the light being switched on and off, indicating a higher charge separation rate under light irradiation. The F-B-TiO₂-0.50 sample displays the maximum photocurrent response for all the tested samples. This significant enhancement illustrates higher separation efficiency of the photogenerated electron-hole pairs, which benefits from the lower reaction barrier and higher photocatalytic activity.

The composition and element state of the F-B-TiO₂-0.50 sample were characterized by using the XPS analysis. The elements presented in the sample mainly include Ti, O, F, B and C as shown in the survey scan in Fig. 4(a). The binding energy of O 1s is located at 528.4 eV (Fig. 4(b)). It is in good agreement with the typical value of lattice oxygen in anatase reported in previous studies^[37-38]. The XPS spectrum of Ti 2p displays two peaks at binding energies of 462.9 and 457.1 eV (Fig. 4(c)), which could be assigned to Ti 2p_{1/2} and Ti 2p_{3/2}, respectively. It is worth noting that these values are slightly lower than those of unmodified TiO₂ (465.0 eV for Ti 2p_{1/2} and 459.5 eV for Ti 2p_{3/2}). This result is probably led by the increase in the electron density with the expected decrease in the oxidation state of Ti atoms, which implies the existence of Ti³⁺ ions. Considering the experimental process, the appearance of Ti³⁺ ions is mainly due to the substitution of F and the generation of oxygen vacancies. Similar process has been reported in a fluorinated TiO₂ system by Czoska et al.^[39]. The XPS spectrum of F 1s has a peak centered at around 682.9 eV (Fig. 4(d)), which is originated from the F species in the form of TiOF₂ and/or ≡Ti—F on the crystal surface of anatase^[11, 40]. There is only one weak peak centered at 192.4 eV in B 1s spectrum (Fig. 4(e)). Two possible reasons have been proposed to explain such a phenomenon in B modified TiO₂ systems, including a low concentration of doped B^[25] and poor XPS measurement sensitivity for B^[41]. The presence of C is also confirmed by XPS (Fig. 4(f)), which is possibly led by the contamination during the synthesis process.

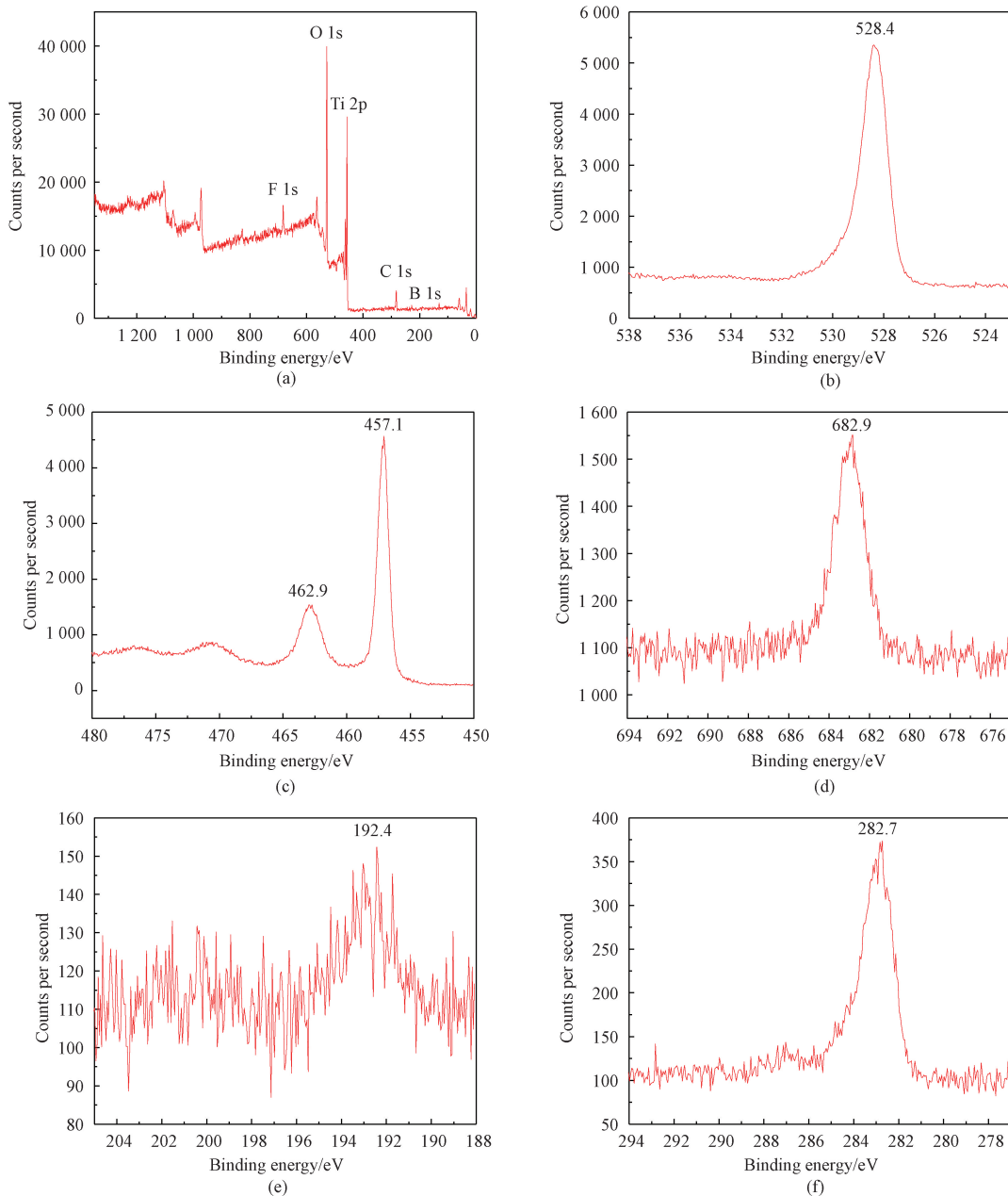


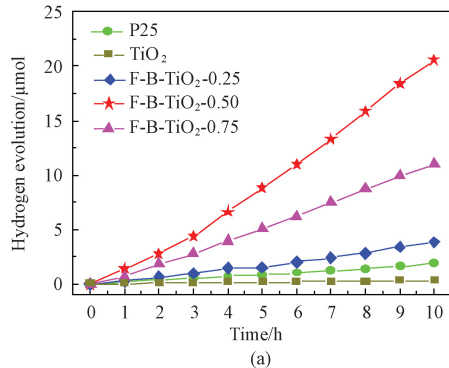
Fig. 4 XPS spectra of F-B-TiO₂-0.50: (a) survey spectrum; (b) O 1s; (c) Ti 2p; (d) F 1s; (e) B 1s; (f) C 1s

2.5 Photocatalytic hydrogen evolution performance

The photocatalytic performance of F-B-TiO₂ samples synthesized under different conditions was evaluated through the photocatalytic hydrogen evolution reaction, where methanol was employed as a sacrificial reductant, and P25 as a reference material. As shown in Fig. 5 (a), the non-doped TiO₂ sample synthesized without additives exhibits the lowest photocatalytic activity. However, the photocatalytic activity of F-B-TiO₂ samples is enhanced due to F-B co-doping, reaching the highest point at a volume ratio of HBF₄ to TiCl₃ of 0.50. After 10 h of UV-Vis light irradiation, the hydrogen evolution of P25 is 1.86 μmol, while the hydrogen evolution of F-B-TiO₂-0.50 reaches 20.57 μmol, more than 10 times that

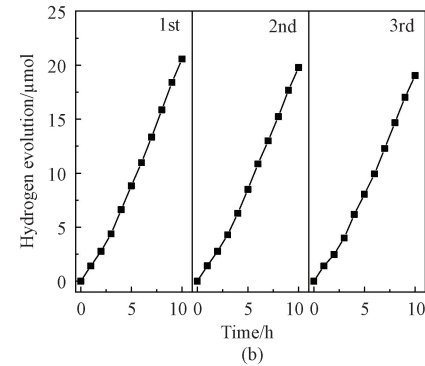
of P25. The photocatalytic activity of F-B-TiO₂ samples synthesized at other volume ratios is significantly lower than that of F-B-TiO₂-0.50. These results are coincident with the UV-Vis absorption properties shown in Fig. 3. The photocatalytic activity of F-B-TiO₂ does not linearly increase with the added amount of HBF₄, which needs further and deeper exploration. In general, the long-term stability and reusability of photocatalysts is a crucial value for their practical applications. Therefore, corresponding experiments were performed. The cyclic test results are shown in Fig. 5 (b). F-B-TiO₂-0.50 possesses excellent photostability, and there is no obvious decrease in the hydrogen evolution after three cycles.

Oxygen vacancies and defect structures also play an important role in enhancing the photocatalytic hydrogen evolution performance of F-B-TiO₂ nanosheets. These vacancies introduce mid-gap states that narrow the bandgap, extending absorption into the visible region, as confirmed by UV-Vis-NIR spectra. The mid-gap states act as shallow electron traps, facilitating charge separation and suppressing recombination, which is further supported by the presence of Ti³⁺ species in the XPS analysis. Additionally, oxygen vacancies serve as active sites for proton adsorption and reduction, lowering the activation energy for hydrogen evolution. The significant enhancement in hydrogen evolution, over



(a)

10 times that of P25, suggests their crucial role in boosting the photocatalytic activity. The correlation between the vacancy concentration and hydrogen evolution, peaking at a volume ratio of HBF₄ to TiCl₃ of 0.50, highlights the need for optimal defect engineering. Furthermore, SEM and TEM analyses reveal porous structures on the anatase (001) facets, providing additional charge trapping sites and enhancing surface reaction kinetics. The synergistic effects of oxygen vacancies, defect structures and F-B co-doping collectively improve charge transfer and hydrogen evolution, demonstrating the importance of defect engineering in optimizing TiO₂-based photocatalysts.



(b)

Fig. 5 Photocatalytic hydrogen evolution by different photocatalysts: (a) comparison of P25 and F-B-TiO₂ obtained at different volume ratios of HBF₄ to TiCl₃; (b) three repeated cycles of F-B-TiO₂-0.50

3 Conclusions

Using TiCl₃ and HBF₄ as precursors, F-B co-doped TiO₂ (F-B-TiO₂) nanosheets were successfully synthesized through a simple one-pot solvothermal method. The addition of HBF₄ significantly suppressed the growth of the less active anatase (101) facets and greatly promoted the exposure of the more active anatase (001) facets, ultimately forming a flower-like structure assembled from F-B-TiO₂ nanosheets bounded with dominant anatase (001) facets. Additionally, F-B co-doping led to the formation of oxygen vacancies and defect structures on the TiO₂ crystal surface, inducing the surface reconstruction of anatase nanosheets. This reconstruction, coupled with the exposed highly active anatase (001) facets and the presence of defect structures, significantly enhanced the photocatalytic performance of F-B-TiO₂, with the hydrogen evolution in photocatalytic water splitting exceeding that of P25 by more than 10 times. These results indicate that F-B-TiO₂ has great potential values in photocatalysis and other related fields such as the photodegradation of organic pollutants, dye-sensitized solar cells and optoelectronic devices.

References

- [1] FUJISHIMA A, HONDA K. Electrochemical photolysis of water at a semiconductor electrode [J]. *Nature*, 1972, 238(5358) : 37-38.
- [2] GUO Q, ZHOU C Y, MA Z B, et al. Fundamentals of TiO₂ photocatalysis: concepts, mechanisms, and challenges [J]. *Advanced Materials*, 2019, 31(50) : e1901997.
- [3] SCHNEIDER J, MATSUOKA M, TAKEUCHI M, et al. Understanding TiO₂ photocatalysis: mechanisms and materials [J]. *Chemical Reviews*, 2014, 114(19) : 9919-9986.
- [4] MA Y, WANG X L, JIA Y S, et al. Titanium dioxide-based nanomaterials for photocatalytic fuel generations [J]. *Chemical Reviews*, 2014, 114(19) : 9987-10043.
- [5] CHEN X B, MAO S S. Titanium dioxide nanomaterials: synthesis, properties, modifications, and applications [J]. *Chemical Reviews*, 2007, 107(7) : 2891-2959.
- [6] WANG S C, LIU G, WANG L Z. Crystal facet engineering of photoelectrodes for photoelectrochemical water splitting [J]. *Chemical Reviews*, 2019, 119(8) : 5192-5247.
- [7] VITTADINI A, SELLONI A, ROTZINGER F P, et al. Structure and energetics of water adsorbed at TiO₂ anatase (101) and (001) surfaces [J]. *Physical Review Letters*, 1998, 81(14) : 2954-2957.
- [8] GONG X Q, SELLONI A. Reactivity of anatase

- TiO₂ nanoparticles: the role of the minority (001) surface [J]. *The Journal of Physical Chemistry B*, 2005, 109(42): 19560-19562.
- [9] LIU S, YU J G, JARONIEC M. Tunable photocatalytic selectivity of hollow TiO₂ microspheres composed of anatase polyhedra with exposed {001} facets [J]. *Journal of the American Chemical Society*, 2010, 132 (34): 11914-11916.
- [10] SELLONI A. Anatase shows its reactive side [J]. *Nature Materials*, 2008, 7(8): 613-615.
- [11] YANG H G, SUN C H, QIAO S Z, et al. Anatase TiO₂ single crystals with a large percentage of reactive facets [J]. *Nature*, 2008, 453(7195): 638-641.
- [12] YANG H G, LIU G, QIAO S Z, et al. Solvothermal synthesis and photoreactivity of anatase TiO₂ nanosheets with dominant {001} facets [J]. *Journal of the American Chemical Society*, 2009, 131(11): 4078-4083.
- [13] HAN X G, KUANG Q, JIN M S, et al. Synthesis of titania nanosheets with a high percentage of exposed (001) facets and related photocatalytic properties [J]. *Journal of the American Chemical Society*, 2009, 131 (9): 3152-3153.
- [14] CHEN J S, TAN Y L, LI C M, et al. Constructing hierarchical spheres from large ultrathin anatase TiO₂ nanosheets with nearly 100% exposed (001) facets for fast reversible lithium storage [J]. *Journal of the American Chemical Society*, 2010, 132(17): 6124-6130.
- [15] QAID S M H, GHATHAN H M, BAWAZIR H S, et al. Successful growth of TiO₂ nanocrystals with {001} facets for solar cells [J]. *Nanomaterials*, 2023, 13(5): 928.
- [16] REN L, MA S S, SHI Y, et al. Insights into the pivotal role of surface defects on anatase TiO₂ nanosheets with exposed {001} facets for enhanced photocatalytic activity [J]. *Materials Research Bulletin*, 2023, 164: 112255.
- [17] LIAO S Q, LIU H, LU Y F, et al. Structural diversity design, four nucleation methods growth and mechanism of 3D hollow box TiO₂ nanocrystals with a temperature-controlled high (001) crystal facets exposure ratio [J]. *ACS Omega*, 2024, 9(1): 1695-1713.
- [18] FU C, LI F, WU Z F, et al. Traces of potassium induce restructuring of the anatase TiO₂ (001)-(1×4) surface from a reactive to an inert structure [J]. *The Journal of Physical Chemistry Letters*, 2023, 14(40): 8916-8921.
- [19] KUBIAK A, GRZEG RSKA A, GABALA E, et al. Unraveling a novel microwave strategy to fabricate exposed {001}/{101} facets anatase nanocrystals: potential for use to the elimination of environmentally toxic metronidazole waste [J]. *Materials Research Bulletin*, 2023, 167: 112438.
- [20] SUN L M, YUAN Y Y, HE X X, et al. Hollow anatase TiO₂ tetrakaidecahedral crystals with an active {001}/{110} redox interface toward high-performance photocatalytic activity[J]. *Chemical Science*, 2024, 15(2): 692-700.
- [21] BASAVARAJAPPA P S, PATIL S B, GANGANAGAPPA N, et al. Recent progress in metal-doped TiO₂, non-metal doped/codoped TiO₂ and TiO₂ nanostructured hybrids for enhanced photocatalysis [J]. *International Journal of Hydrogen Energy*, 2020, 45 (13) : 7764-7778.
- [22] NUR A S M, SULTANA M, MONDAL A, et al. A review on the development of elemental and codoped TiO₂ photocatalysts for enhanced dye degradation under UV-vis irradiation[J]. *Journal of Water Process Engineering*, 2022, 47: 102728.
- [23] WANG C, AO Y H, WANG P F, et al. Preparation, characterization and photocatalytic activity of the neodymium-doped TiO₂ hollow spheres[J]. *Applied Surface Science*, 2010, 257 (1) : 227-231.
- [24] ASAHI R, MORIKAWA T, OHWAKI T, et al. Visible-light photocatalysis in nitrogen-doped titanium oxides[J]. *Science*, 2001, 293(5528): 269-271.
- [25] TEE S Y, KONG J H, KOH J J, et al. Structurally and surficially activated TiO₂ nanomaterials for photochemical reactions [J]. *Nanoscale*, 2024, 16(39): 18165-18212.
- [26] FANG W J, YAN J W, WEI Z D, et al. Account of doping photocatalyst for water splitting [J]. *Chinese Journal of Catalysis*, 2024, 60: 1-24.
- [27] RUAN X W, LI S J, HUANG C X, et al. Catalyzing artificial photosynthesis with TiO₂ heterostructures and hybrids: emerging trends in a classical yet contemporary photocatalyst [J]. *Advanced Materials*, 2024, 36(17): 2305285.
- [28] AYAPPAN C, XING R M, ZHANG X T, et al. TiO₂-based photocatalysts for emerging gaseous pollutants removal: from photocatalysts to reactors design [J]. *Coordination Chemistry Reviews*, 2024, 515: 215960.
- [29] NAKAMURA I, NEGISHI N, KUTSUNA S, et al. Role of oxygen vacancy in the plasma-treated TiO₂ photocatalyst with visible light activity for NO removal[J]. *Journal of Molecular Catalysis A: Chemical*, 2000, 161(1): 205-212.
- [30] JUSTICIA I, ORDEJÓN P, CANTO G, et al. Designed self-doped titanium oxide thin films for efficient visible-light photocatalysis [J].

- [31] Advanced Materials, 2002, 14(19): 1399-1402.
- [31] GONG X Q, SELLONI A, BATZILL M, et al. Steps on anatase TiO₂ (101) [J]. *Nature Materials*, 2006, 5(8): 665-670.
- [32] STRUNK J, Vining W C, BELL A T. A study of oxygen vacancy formation and annihilation in submonolayer coverages of TiO₂ dispersed on MCM-48[J]. *The Journal of Physical Chemistry C*, 2010, 114(40): 16937-16945.
- [33] LIU G, YANG H G, WANG X W, et al. Enhanced photoactivity of oxygen-deficient anatase TiO₂ sheets with dominant {001} facets [J]. *The Journal of Physical Chemistry C*, 2009, 113(52): 21784-21788.
- [34] THOMPSON T L, YATES J T. Surface science studies of the photoactivation of TiO₂ new photochemical processes[J]. *Chemical Reviews*, 2006, 106(10): 4428-4453.
- [35] FAN C Y, CHEN C, WANG J, et al. Black hydroxylated titanium dioxide prepared via ultrasonication with enhanced photocatalytic activity [J]. *Scientific Reports*, 2015, 5: 11712.
- [36] SOURI D, TAHAN Z E. A new method for the determination of optical band gap and the nature of optical transitions in semiconductors [J].
- [37] Applied Physics B, 2015, 119 (2): 273-279.
- [37] REYES-GARCIA E A, SUN Y P, Raftery D. Solid-state characterization of the nuclear and electronic environments in a boron-fluoride co-doped TiO₂ visible-light photocatalyst [J]. *The Journal of Physical Chemistry C*, 2007, 111(45): 17146-17154.
- [38] ZHAO W, MA W H, CHEN C C, et al. Efficient degradation of toxic organic pollutants with Ni₂O₃/TiO_{2-x}B_x under visible irradiation [J]. *Journal of the American Chemical Society*, 2004, 126(15): 4782-4783.
- [39] CZOSKA A M, LIVRAGHI S, CHIESA M, et al. The nature of defects in fluorine-doped TiO₂[J]. *The Journal of Physical Chemistry C*, 2008, 112(24): 8951-8956.
- [40] WANG B, LEUNG M K H, LU X Y, et al. Synthesis and photocatalytic activity of boron and fluorine codoped TiO₂ nanosheets with reactive facets [J]. *Applied Energy*, 2013, 112: 1190-1197.
- [41] LI J Y, LU N, QUAN X, et al. Facile method for fabricating boron-doped TiO₂ nanotube array with enhanced photoelectrocatalytic properties [J]. *Industrial & Engineering Chemistry Research*, 2008, 47(11): 3804-3808.

暴露高活性 (001) 晶面的 F-B 共掺杂锐钛矿 TiO₂ 纳米片及其光催化产氢性能

张梦瑶, 韦 莉, 刘 蕾*

东华大学 先进低维材料中心, 上海 201620

摘要: 通过一步溶剂热合成法制备了暴露 (001) 晶面的 F-B 共掺杂锐钛矿 TiO₂ 纳米片, 并研究了其光催化产氢性能。试验结果表明, 该方法能够有效促进高活性锐钛矿 (001) 晶面的生长, 增强 TiO₂ 对可见光和红外光的吸收, 并进一步诱导形成氧空位。在最优化条件下, 该材料受紫外-可见光照射 10 小时后的产氢量达到 20.57 μmol, 比商品 TiO₂ 纳米颗粒 Degussa P25 高出 10 倍以上。研究结果表明 F-B 共掺杂锐钛矿 TiO₂ 纳米片在光催化领域具有很好的应用潜力。

关键词: F-B 共掺杂; TiO₂; 光催化; 活性晶面; 氧空穴

DOI: 10.19884/j.1672-5220.202412014

Analysis of Three Reactive Dyes and Their Six Derivatives by Capillary Electrophoresis

HUANG Shuqing, SHEN Li*, XU Zhongqi*

College of Chemistry and Chemical Engineering, Donghua University, Shanghai 201620, China

Abstract: Reactive dyes with different reactive groups exhibit different hydrolysis and dyeing behaviors. This is particularly evident in the combination dyeing process, where the competition between hydrolysis and dyeing reactions increases the complexity. Therefore, developing an effective method to monitor the changes in reactive dyes during the dyeing process is important. This study aims to develop a capillary electrophoresis (CE) technique combined with an ultraviolet (UV) detector (CE-UV) for detecting three reactive dyes and their six derivatives (a total of nine analytes). The optimized CE conditions are 20.0 mmol/L sodium tetraborate ($\text{Na}_2\text{B}_4\text{O}_7 \cdot 10\text{H}_2\text{O}$), acetonitrile (ACN) with a volume fraction of 15.0%, 20.0 mmol/L α -cyclodextrin (α -CD), and at a pH value of 9.0 (adjusted with 0.5 mol/L H_3BO_3). The limit of detection (LOD) (a signal-to-noise ratio of 3) for the nine analytes ranges from 1.38 to 5.06 mg/L. The relative standard deviations (RSDs) for peak areas and migration time are 2.19%–4.96% and 0.29%–2.75%, respectively. The method is capable of accurately identifying three reactive dyes and their six derivatives and monitoring alterations in composition and dyeing behavior during single and combination dyeing processes.

Keywords: reactive dye; capillary electrophoresis (CE); hydrolyzed product; combination dyeing

CLC number: O657.8

Document code: A

Article ID: 1672-5220(2025)05-0466-10

Open Science Identity
(OSID)



0 Introduction

Reactive dyes are widely used in the textile industry because of their bright color and excellent color fastness^[1]. Various dye-fiber and dye-dye interactions occur during the dyeing process. In particular, uncontrollable factors occurring during the dyeing process may lead to the production of unsatisfactory results^[2]. Reactive dyes are developed based on acid dyes, and the structural difference between reactive dyes and acid dyes is that reactive dyes contain reactive groups^[3]. The reactive groups react with fiber molecules

through nucleophilic substitution or nucleophilic addition, forming covalent bonds^[4]. When the reactive groups interact with —OH groups in water, they undergo a hydrolysis reaction^[5-6]. In particular, under alkaline conditions, the combination dyeing of fabrics using different reactive dyes results in the production of a great number of hydrolysis products^[7]. These may affect the reproducibility of the dyeing process. This practice not only increases the cost but also pollutes the aquatic ecosystem and soils, which may subsequently impact human health through the food chain^[8-9]. To accurately and rapidly detect the content of reactive dyes and their hydrolysis products in dye solutions, it is necessary to develop an effective detection method.

Haque et al.^[10] analyzed three reactive dyes and measured the absorbance of the post-dye and post-wash liquors by ultraviolet-visible (UV-Vis) spectroscopy, and the solution concentrations were calculated by the Beer-Lambert law. Nevertheless, this method is only capable of determining the total absorbance, and it is not possible to analyze the different structures of the reactive dyes in the mixed solution. The application of the UV-Vis spectroscopy for the determination of multi-component samples necessitates the use of dual-wavelength spectrophotometry, with the maximum absorption wavelength λ_{\max} being determined by solving a set of simultaneous equations based on the Beer-Lambert law^[11-13]. The ensuing calculation process is inherently cumbersome, resulting in poor quantitative accuracy or even inaccurate results. Raman spectroscopy was employed to detect the concentration of reactive dyes with different structures under various dyeing conditions^[14-15]. Javoršek et al.^[16] analyzed the hydrolysis and formation of dye-fiber bonds during the dyeing process by using high-performance liquid chromatography (HPLC). However, HPLC is challenging for analyzing dyes in complex matrices, and inadequate pretreatment or sample preparation may affect the accuracy of the analytical results^[17-19].

Capillary electrophoresis (CE) is driven by a high-voltage direct current electric field, utilizing a capillary

Received date: 2024-12-23

Foundation item: Research Foundation from National Innovation Center of Advanced Dyeing & Finishing Technology, China (No. 2022GCJJ15)

* Correspondence should be addressed to XU Zhongqi, email: chemxzq@dhu.edu.cn; SHEN Li, email: shenli@dhu.edu.cn

Citation: HUANG S Q, SHEN L, XU Z Q. Analysis of three reactive dyes and their six derivatives by capillary electrophoresis[J]. *Journal of Donghua University (English Edition)*, 2025, 42(5): 466-475.

tube as its separation channel, and realizes the separation of the target substances based on the differences in the mobility and partitioning behaviors of the components in the specimen. It has been proven to be capable of quantitatively determining drugs^[20-21], inorganic ions^[22], biogenic amines^[23] and other substances^[24].

Ojstrsek et al.^[25] examined the hydrolysis process of some reactive dyes and analyzed the behavior of color index (C. I.) reactive black 5 in single dyeing. Most of the studies focused on monitoring the hydrolysis reaction of reactive dyes in wastewater by CE, but there were no simultaneous analyses of different reactive dyes or studies on the detection of combination dyeing processes^[26-28].

A previous study from our group has successfully analyzed three heterobifunctional dyes (C. I. reactive red 195, C. I. reactive yellow 145 and C. I. reactive blue 194), as well as single dyeing and combination dyeing processes^[29]. However, combination dyeing uses different dye mixtures, which requires different CE conditions to analyze various processes.

This study aims to analyze three different types of reactive dyes, namely C. I. reactive blue 19 (monofunctional), C. I. reactive black 5 (bifunctional), C. I. reactive red 195 (heterobifunctional), and their activation and hydrolysis forms. When analyzed under the background electrolyte (BGE) conditions used in Ref. [29], the activation form and the hydrolysis form of C. I. reactive blue 19 were found to be poorly separated, and the migration time of the nine analytes was too long. Therefore, there is a need to explore optimized CE conditions. The developed method can be used to evaluate single dyeing and combination dyeing processes, which can help to improve dyeing quality.

1 Materials and Methods

1.1 Materials

Sodium tetraborate ($\text{Na}_2\text{B}_4\text{O}_7 \cdot 10\text{H}_2\text{O}$) was purchased from Sigma-Aldrich (Shanghai) Trading Co., Ltd., China. Boric acid (H_3BO_3) and sodium hydroxide (NaOH) were purchased from Shanghai Lingfeng Chemical Reagent Co., Ltd., China. C. I. reactive black 5 and α -cyclodextrin (α -CD) were purchased from Shanghai Macklin Biochemical Technology Co., Ltd., China. Acetonitrile (ACN) was purchased from Shanghai Adamas Reagent Co., Ltd., China. C. I. reactive blue 19 was purchased from Shanghai Xianding Biotechnology Co., Ltd., China. C. I. reactive red 195 was purchased from Shanghai Yuanye Biotechnology Co., Ltd., China. The area density of the fabric was 115 g/m²; the warp density and weft density of the fabric were 526 ends per 10 cm and 288 picks per 10 cm,

respectively.

1.2 CE conditions

All experiments were conducted on the CE instrument (G1600AX, Agilent Technologies Inc., USA). Bare fused silica capillary was purchased from Yongnian Ruifeng Chromatography Device Ltd., China. The dimension of the capillary was 58.5 cm (50.0 cm to the UV detector) \times 75.0 μm (the inner diameter). The temperature of the capillary cassette was 25 °C. The BGE was a mixture of 20.0 mmol/L $\text{Na}_2\text{B}_4\text{O}_7 \cdot 10\text{H}_2\text{O}$, 20.0 mmol/L α -CD, 15.0% (volume fraction) ACN, at a pH of 9.0 (adjusted with 0.5 mol/L H_3BO_3). New capillary activation was performed by rinsing the capillary with 1.0 mol/L NaOH solution (30 min), water (10 min) and BGE (10 min) at 1.0×10^5 Pa. Before each injection, the capillary was conditioned sequentially with 0.1 mol/L NaOH solution (3 min), water (3 min) and BGE (3 min) at 1.0×10^5 Pa. This procedure eliminated the effect of dye adsorption on the results, thereby ensuring the reproducibility of the experiment. The experimental conditions were set as follows: hydrodynamic injection was performed at a pressure of 3.5×10^3 Pa for a duration of 4.0 s, a separation voltage of 20.0 kV was applied, and a UV detection was carried out at a wavelength of 200.0 nm.

1.3 Preparation of stock solution

Three reactive dye stock solutions were prepared with C. I. reactive blue 19, C. I. reactive black 5 and C. I. reactive red 195 at a mass concentration of 2.0 g/L, respectively. The concentrations of other stock solutions were 50.0 mmol/L for $\text{Na}_2\text{B}_4\text{O}_7 \cdot 10\text{H}_2\text{O}$, 0.5 mol/L for H_3BO_3 , 50.0 mmol/L for α -CD, and 1.0 mol/L for NaOH.

Vinyl sulfone (VS) reactive dyes (activation forms of dyes) and completely hydrolyzed reactive dyes (hydrolysis forms of dyes) were prepared from their respective precursors β -sulfatoethyl sulfone (SES) reactive dyes.

SES can hydrolyze in one or two steps to VS and hydroxyethyl sulfone (HES). The monochlorotriazinyl group (Cl) hydrolyzes to a hydroxytriazinyl group. The procedure for preparing VS reactive dyes was dissolving 10.0 mg dyes in 0.01 mol/L NaOH solution. After the reaction proceeded for a period, the reaction solutions were neutralized with 1.0 mol/L HCl to produce 1.0 g/L stock solutions. The procedure for preparing completely hydrolyzed reactive dyes involved dissolving 0.25 g dyes in 0.1 mol/L NaOH solution and reacting in a water bath at 60 °C. Then, the solutions were cooled to room temperature and neutralized with 1.0 mol/L HCl solution to produce 1.0 g/L stock solutions. The structural formulas of three reactive dyes and their six derivatives are shown in Table 1.

Table 1 Structural formulas of three reactive dyes and their six derivatives

Analyte	Abbreviation	Structure
C. I. reactive black 5	SES-SES-black-5	
Activation form of C. I. reactive black 5	VS-VS-black-5	
Hydrolysis form of C. I. reactive black 5	HES-HES-black-5	
C. I. reactive blue 19	SES-blue-19	
Activation form of C. I. reactive blue 19	VS-blue-19	
Hydrolysis form of C. I. reactive blue 19	HES-blue-19	
C. I. reactive red 195	SES-Cl-red-195	
Activation form of C. I. reactive red 195	VS-Cl-red-195	
Hydrolysis form of C. I. reactive red 195	HES-OH-red-195	

The preparation of the derivatives of C. I. reactive black 5 is shown in Fig. 1. Samples were collected at different time during the preparation process and analyzed by the CE technique combined with an ultraviolet (UV) detector (CE-UV). The electropherograms show that the SES-SES-black-5 peak decreases, while the VS-VS-black-5 peak gradually increases (Fig. 2 (a)). The preparation of the hydrolysis form results in a reaction type II situation, whereby either of the two reactive

groups may be preferentially hydrolyzed, resulting in the production of a partially hydrolyzed product, named HES-VS-black-5 (Fig. 1). The final conversion to the fully hydrolyzed product, named HES-HES-black-5, is shown in Fig. 2 (b). Electropherograms of the preparation of the activation and hydrolysis forms of C. I. reactive blue 19 and C. I. reactive red 195 are shown in Figs. 2 (c)–2(f).

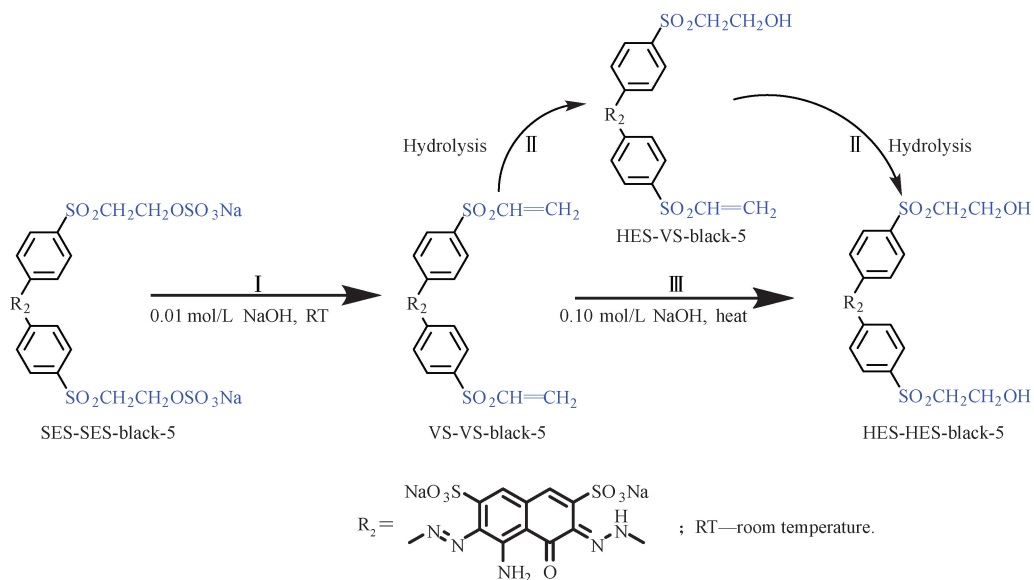


Fig. 1 Preparation routes for activation form and hydrolysis form of C.I. reactive black 5 under different conditions

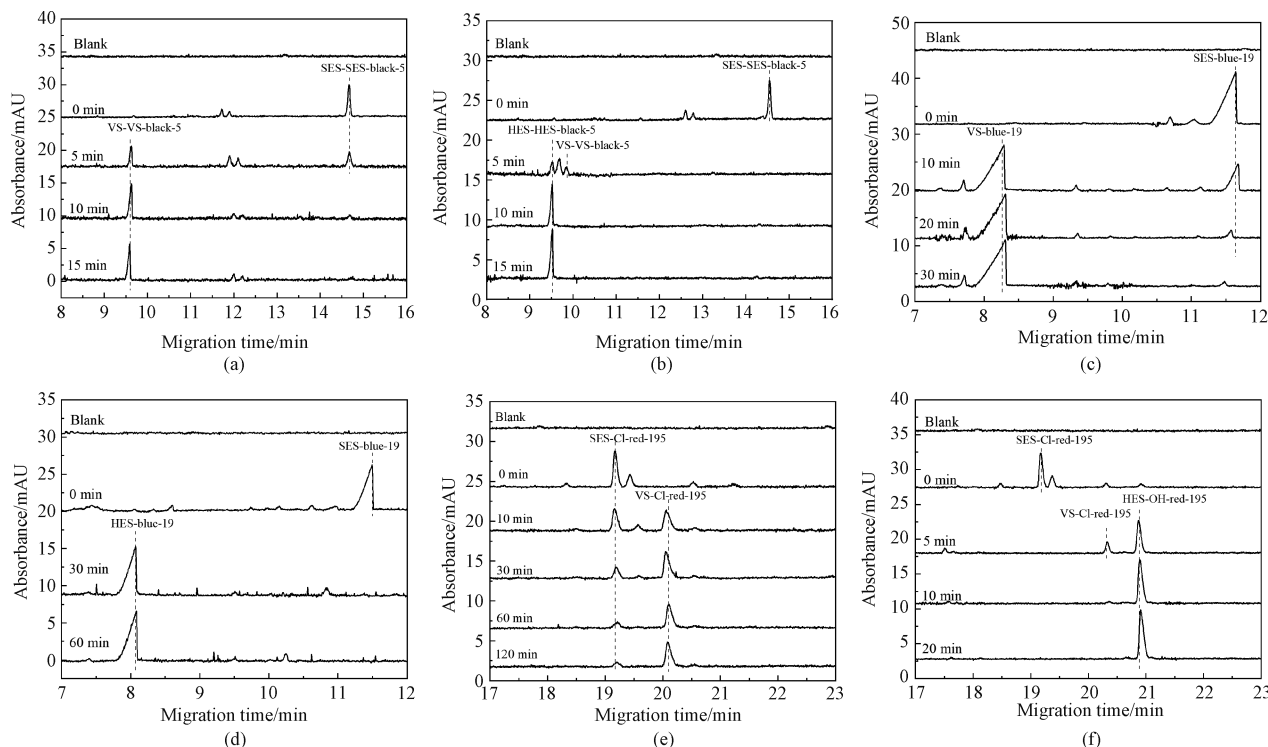


Fig. 2 Electropherograms of analytes in the preparation process at different time: (a) VS-VS-black-5; (b) HES-HES-black-5; (c) VS-blue-19; (d) HES-blue-19; (e) VS-Cl-red-195; (f) HES-OH-red-195

1.4 Dyeing procedure

The formulation for the single dyeing was a dye dosage of 2.0% on-mass of fabric (omf), 5.0 g cotton fabric, and a liquor-to-good ratio of 20:1. The dye was dissolved in 100 mL water, 4.0 g/L Na_2SO_4 was added, and after a certain period of dyeing, Na_2CO_3 was added.

The dyeing procedure is shown in Fig. 3. The formula for the combination dyeing was a dye dosage of 6.0% omf, with a mass ratio of 1:1:1 for the three reactive dyes. The rest of the conditions were the same as those for the single dyeing.

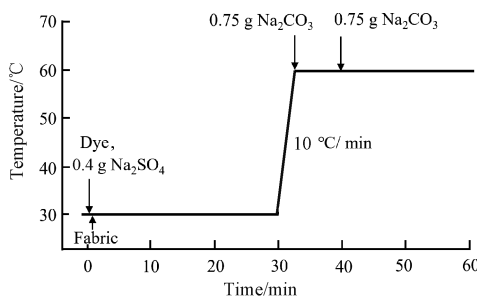


Fig. 3 Dyeing procedure curve

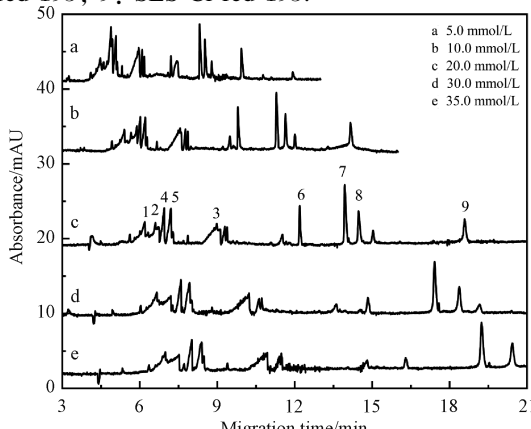
2 Results and Discussion

2.1 Selection and optimization of CE conditions

Adjusting the content of $\text{Na}_2\text{B}_4\text{O}_7 \cdot 10\text{H}_2\text{O}$, α -CD and ACN and the pH of the BGE can enhance the disparity in the flow rates of the neighboring components, thus optimizing the separation. The absorption spectra of three reactive dyes and their six derivatives were measured by UV-Vis spectroscopy. Though λ_{max} of the nine analytes were different in the UV wavelength range, they had high absorption intensity at 200.0 nm. Therefore, the detection wavelength of 200.0 nm was finally selected.

2.1.1 Effect of $\text{Na}_2\text{B}_4\text{O}_7 \cdot 10\text{H}_2\text{O}$ concentration on separation efficiency

The effect of $\text{Na}_2\text{B}_4\text{O}_7 \cdot 10\text{H}_2\text{O}$ concentration on the separation efficiency of nine analytes was investigated. The result is shown in Fig. 4. Increasing the $\text{Na}_2\text{B}_4\text{O}_7 \cdot 10\text{H}_2\text{O}$ concentration within a certain range enhances sample separation. However, beyond this range, further increases reduce the electroosmotic flow (EOF) and slow sample migration without improving the separation efficiency. Excessive $\text{Na}_2\text{B}_4\text{O}_7 \cdot 10\text{H}_2\text{O}$ concentration causes excessive Joule heating, resulting in peak broadening and reducing sensitivity and separation efficiency. Therefore, a $\text{Na}_2\text{B}_4\text{O}_7 \cdot 10\text{H}_2\text{O}$ concentration of 20.0 mmol/L was selected. The corresponding sample peaks are as follows. 1: HES-blue-19, 2: VS-blue-19, 3: SES-blue-19, 4: HES-HES-black-5, 5: VS-VS-black-5, 6: SES-SES-black-5, 7: HES-OH-red-195, 8: VS-Cl-red-195, 9: SES-Cl-red-195.

Fig. 4 Effect of $\text{Na}_2\text{B}_4\text{O}_7 \cdot 10\text{H}_2\text{O}$ concentration on separation efficiency of analytes

2.1.2 Effect of ACN volume fraction on separation efficiency

It is found that organic additives increase the solubility of hydrophobic solutes in the aqueous phase, which affects the retention factor of the analytes and may change the resolution of the analytes^[30]. As the volume fraction of ACN increases, the EOF decreases, resulting in longer migration time for each analyte. When the volume fraction of ACN is higher than 20.0%, the migration time increases significantly, as shown in Fig. 5. Furthermore, an excess volume fraction of ACN has been observed to result in a decline in the BGE stability. Consequently, an ACN volume fraction of 15.0% was selected.

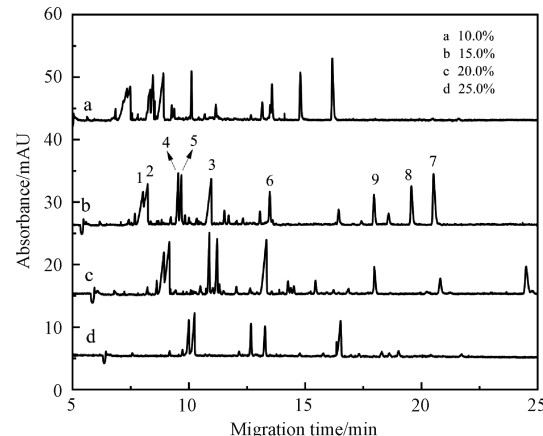
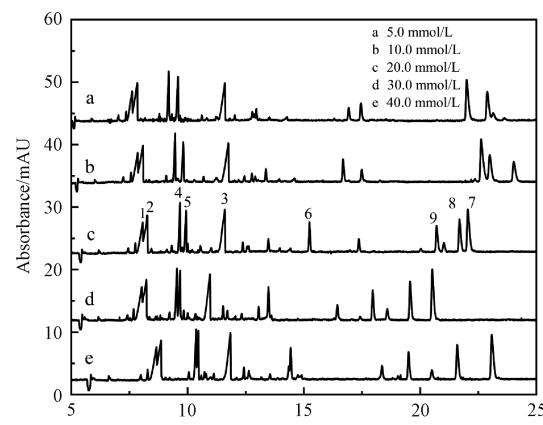


Fig. 5 Effect of ACN volume fraction on separation efficiency of analytes

2.1.3 Effect of α -CD concentration on separation efficiency

The forms of analytes include complexes with α -CD and also have solubilizing effects. The addition of α -CD to the BGE also reduces the interaction between the analytes and the capillary wall, thus increasing the reproducibility of the method and improving the peak shape^[30]. In a concentration range of 5.0 mmol/L to 20.0 mmol/L, the separation improves progressively with increasing the α -CD concentration, as shown in Fig. 6. Consequently, a α -CD concentration of 20.0 mmol/L was selected.

Fig. 6 Effect of α -CD concentration on separation efficiency of analytes

2.1.4 Effect of pH on separation efficiency

For uncoated fused silica capillaries, pH plays an important role in controlling EOF and has a significant impact on the separation process. The pH of the BGE affects the structure and charge of the analytes, increasing the differences between the analytes to be analyzed and thus affecting the separation of the analytes^[31]. When comparing the two pH values (8.5 and 9.0), a higher pH results in an increased EOF and a decreased migration time for analytes, as shown in Fig. 7. However, in a pH range of 9.0–10.0, increasing pH results in longer migration time, but no improvement in the separation efficiency. Consequently, a pH of 9.0 was selected for the BGE.

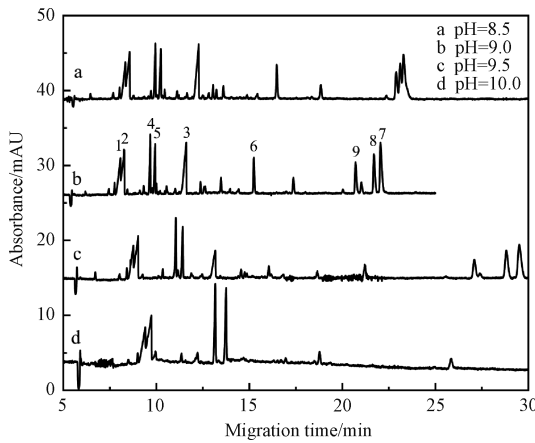


Fig. 7 Effect of pH on separation efficiency of analytes

2.2 Validation of analytical method

The validation parameters for the simultaneous analysis of the three reactive dyes and their activation forms and hydrolysis forms are presented in Table 2. The linear curves obtained for all analytes exhibit a high correlation ($R^2 > 0.995$) and (R^2 is the coefficient of determination). LOD is defined as the minimum concentration that can be detected at a signal-to-noise ratio (S/N) of 3. LQD is the concentration at a S/N of 10. LOD and LQD of nine analytes are found to be in ranges of 1.38–5.06 mg/L and 4.61–16.87 mg/L, respectively. In the mixed standard solution at a mass concentration of 60.0 mg/L for nine analytes, RSD of peak areas ($n = 5$, where n represents the number of parallel experiments conducted for each analyte) is 2.19%–4.14% within one day (intraday) and 3.63%–4.96% within five days (interday), respectively. RSD of migration time ($n = 5$) is 0.29%–0.84% within one day (intraday) and 0.62%–2.75% within five days (interday), respectively. The three reactive dyes and their activation and hydrolysis forms have negative charges, which results in a weak adsorption phenomenon on the capillary surface. Conversely, the rinsing procedure was meticulously executed before each analysis, which effectively minimized the adsorption of the dyes on the capillary surface, thereby ensuring the reproducibility of the analytical method. This indicates that the method can accurately and quantitatively analyze reactive dyes.

Table 2 Linearity, reproducibility and limit of detection of analytical method

Analyte	R^2 (5.0–140.0 mg/L)	LOD/(mg/L)	LQD/(mg/L)	RSD/% ($n=5$)	
				Peak area	Migration time
				Intraday/interday	Intraday/interday
SES-blue-19	0.997 9	1.77	5.91	3.71/4.14	0.39/1.50
VS-blue-19	0.995 7	1.38	4.61	2.19/3.68	0.29/0.62
HES-blue-19	0.997 9	1.80	5.99	3.16/4.58	0.30/0.63
SES-SES-black-5	0.997 4	3.58	11.93	3.70/4.45	0.63/2.49
VS-VS-black-5	0.997 9	2.84	9.48	4.14/4.76	0.37/0.98
HES-HES-black-5	0.997 5	2.11	7.03	2.88/3.63	0.36/0.92
SES-Cl-red-195	0.998 8	5.06	16.87	3.41/4.89	0.79/2.75
VS-Cl-red-195	0.999 4	2.66	8.86	3.24/4.96	0.84/2.30
HES-OH-red-195	0.998 1	2.12	7.05	3.53/4.80	0.84/1.98

2.3 Detection of dyeing process

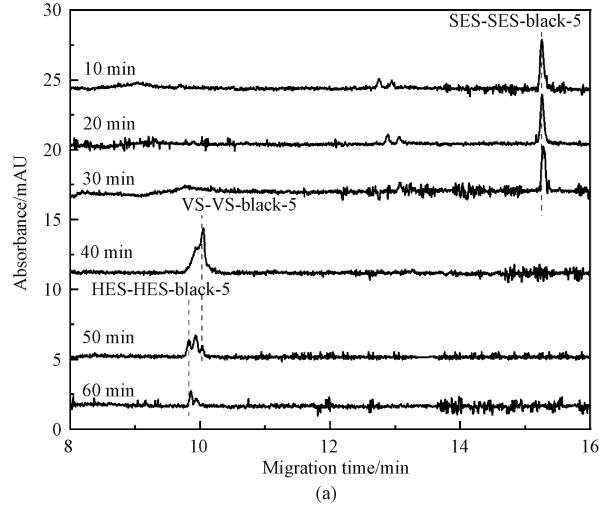
2.3.1 Detection of single dyeing process

Samples were taken every 10 min, after which their pH was adjusted to 7.0 with 0.5 mol/L HCl to stop further hydrolysis, and then the samples were diluted tenfold. Dye-uptake during the single dyeing process was analyzed by CE-UV. For C. I. reactive black 5

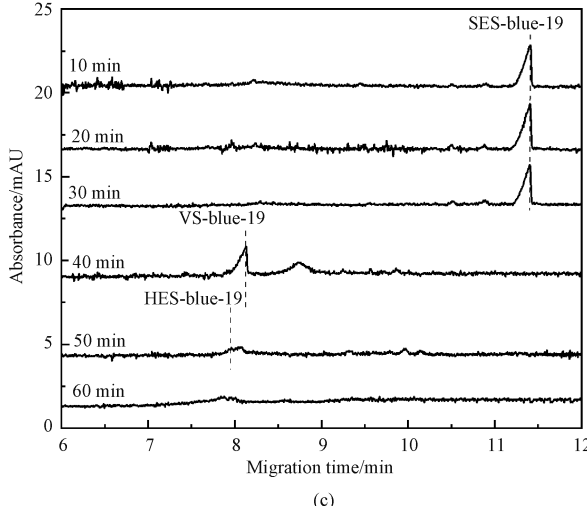
(Fig. 8(a)), during the dye adsorption stage (0–30 min), SES-SES-black-5 remains unchanged. During the dye fixation stage (40–60 min), SES-SES-black-5 converts to VS-VS-black-5, with intermediate hydrolysis products (HES-VS-black-5) appearing, followed by HES-HES-black-5. Similar reaction pathways are also observed for C. I. reactive red 195 and C. I. reactive blue 19, as shown

in Figs. 8 (b) and 8 (c), respectively. The total dye concentration at each time point was determined by summing the concentrations of all forms. The dye-uptake D measured by the CE-UV method is calculated according to

$$D = \frac{C_0 - C_t}{C_0} \times 100\%, \quad (1)$$

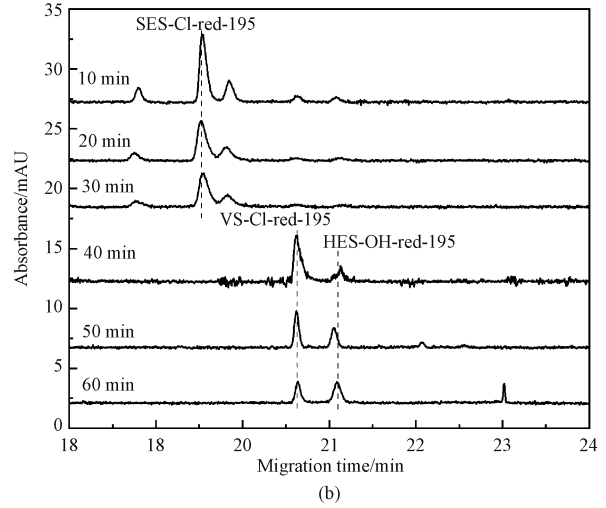


(a)

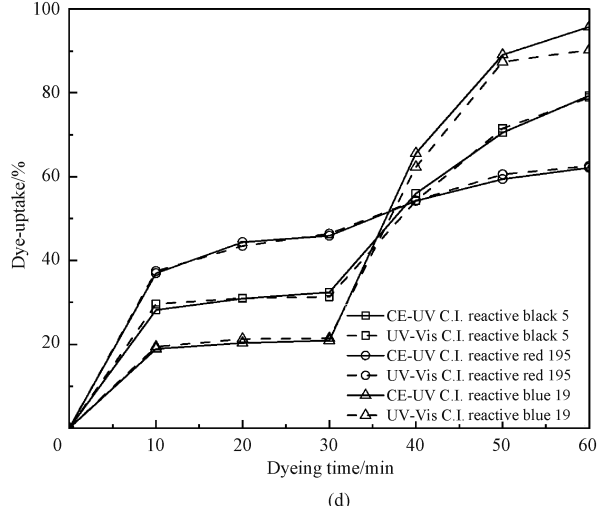


(c)

where C_0 is the initial dye concentration in the dye solution; C_t is the concentration of various forms of dyes taken at time t . The UV-Vis method for detecting the dye-uptake during a single dyeing process is based on GB/T 23976.1—2009 standard. The specific determination method is shown in Ref. [29]. Comparative curves of the dye-uptake measured by the CE-UV method and the UV-Vis method are shown in Fig. 8 (d).



(b)



(d)

Fig. 8 Electropherograms during single dyeing process and comparative curves of dye-uptake measured by two methods: (a) electropherograms of C. I. reactive black 5; (b) electropherograms of C. I. reactive red 195; (c) electropherograms of C. I. reactive blue 19; (d) comparative curves

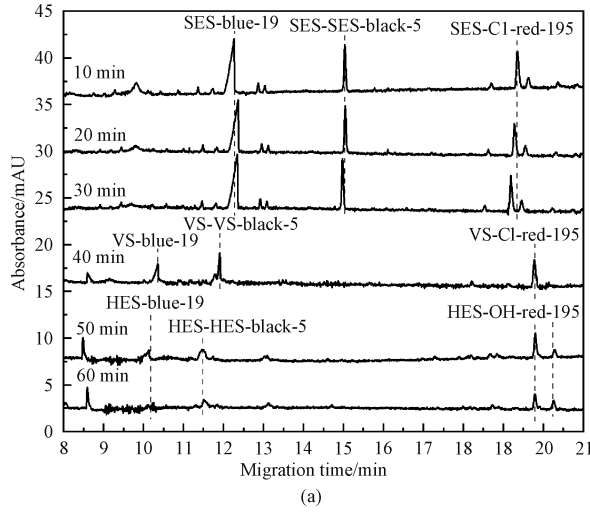
2.3.2 Detection of combination dyeing process

Analyses of the combination dyeing process of C. I. reactive blue 19, C. I. reactive black 5 and C. I. reactive red 195 are shown in Fig. 9. During the adsorption stage, only SES-blue-19, SES-SES-black-5 and SES-Cl-red-195 are presented. During the fixation stage, the reactive dyes are converted to VS-type reactive dyes and intermediate hydrolysis products. The final conversion of these intermediates to completely hydrolyzed reactive dyes is shown in Fig. 9 (a). The dye-uptakes of the three reactive dyes were determined

by using two methods. For the CE-UV method, the relevant parameters were measured via CE, and then the dye-uptakes were calculated by using Eq. (1). For the UV-Vis method, the dye-uptakes were calculated as follows. The absorbance coefficients of the three dyes were measured by using the three-wavelength method. Then, they were used to determine the dye concentration and finally calculate the dye-uptake. The dye concentrations during different stages could be approximately determined by applying three linear equations, enabling the calculation of the dye-uptake for

each dye. The comparative curves of dye-uptake measured by the two methods are shown in Fig. 9 (b). Minor differences are observed between the dye-uptake measured by the two methods. When analyzing the

dyeing process, the UV-Vis method often requires mathematical approaches to compensate for their limitations. The CE-UV method directly detects all forms of reactive dyes, providing more accurate results.



(a)

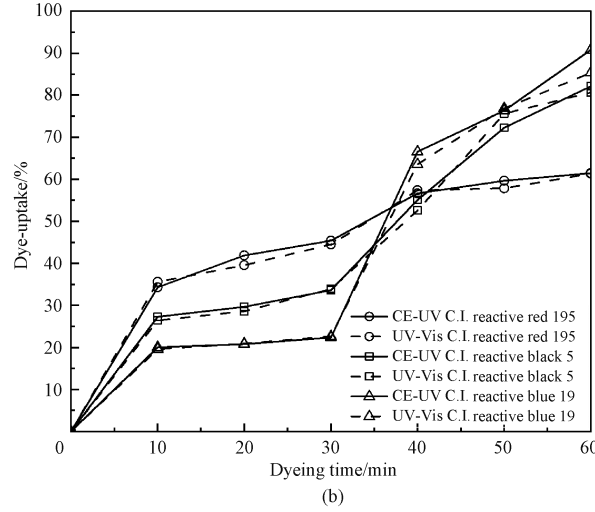


Fig. 9 Electropherograms during combination dyeing process and comparative curves of dye-uptake measured by two methods:
(a) electropherograms; (b) comparative curves

3 Conclusions

In this study, a CE-UV method was developed to achieve simultaneous qualitative and quantitative analysis of three reactive dyes and their activation and hydrolyses derivatives. The method showed good sensitivity and reproducibility. The electropherograms showed that the reactive dyes underwent a transformation process during the dyeing process, specifically, the conversion of the reactive dyes to their activation forms and binding to the fibers, and the hydrolysis reaction to generate hydrolysis products. The dye-uptake of C. I. reactive red 195 and C. I. reactive black 5 remained stable during single dyeing and combination dyeing processes, indicating that its stability in binding to fibers was not easily affected by other dyes. In addition, the dye-uptake of C. I. reactive red 195 during the adsorption stage was higher than that of the other dyes, indicating that its monochlorotriazine group helped to enhance the affinity between the dye and the fiber. Comparing the dye-uptake of C. I. reactive blue 19 during single dyeing and combination dyeing processes, it was found that the dye-uptake of combination dyeing was lower than that of single dyeing. This suggested that the dyeing effect of C. I. reactive blue 19 was affected during the combination dyeing process with bifunctional dyes, resulting in lower dye-uptake. The experimental results verified the existence of competition between hydrolysis and up-dyeing reactions of reactive dyes with different structures during the combination dyeing process. In conclusion,

this study successfully developed a method to analyze reactive dyes and their derivatives by using the CE-UV method and successfully applied it to monitor and analyze the dyeing process.

References

- [1] KAN C W, FONG K W F. A study of reusing vinyl sulfone based reactive dye for dyeing cotton fiber [J]. *Fibers and Polymers*, 2017, 18(11): 2176-2186.
- [2] WANG Y W, YI Q Z, DING Y, et al. Study on the factors influencing the dyeing performance of cotton fabric with vat dyes based on principal component analysis [J]. *The Journal of the Textile Institute*, 2021, 112(9): 1460-1466.
- [3] HE J X. Dye chemistry [M]. Beijing: China Textile Press, 2009. (in Chinese)
- [4] PRUS S, KULPIŃSKI P, MATYJASZGONDEK E, et al. Eco-friendly dyeing of cationised cotton with reactive dyes: mechanism of bonding reactive dyes with CHPTAC cationised cellulose [J]. *Cellulose*, 2022, 29(7): 4167-4182.
- [5] SWATI S S, FARUQUI A N. Investigation on ecological parameters and COD minimization of textile effluent generated after dyeing with mono and bi-functional reactive dyes [J]. *Environmental Technology & Innovation*, 2018, 11: 165-173.
- [6] IRFAN M, XIE K L, HOU A Q. Effect of reactive dye structures and substituents on cellulose fabric dyeing [J]. *Fibers and Polymers*,

- [7] 2020, 21(9) : 2018-2023.
- [8] KLANCNIK M. Influence of temperature on kinetics of hydrolysis of monochlorotriazine reactive dye [J]. *International Journal of Polymeric Materials and Polymeric Biomaterials*, 2000, 47(4) : 735-739.
- [9] AL-TOHAMY R, ALI S S, LI F H, et al. A critical review on the treatment of dye-containing wastewater: ecotoxicological and health concerns of textile dyes and possible remediation approaches for environmental safety [J]. *Ecotoxicology and Environmental Safety*, 2022, 231 : 113160.
- [10] SUI X Y, FENG C C, CHEN Y F, et al. Detection of reactive dyes from dyed fabrics after soil degradation via QuEChERS extraction and mass spectrometry [J]. *Analytical Methods*, 2020, 12(2) : 179-187.
- [11] HAQUE A N M A, MA H N, MASUD RANA M. Compatibility analysis of reactive dyes by exhaustion-fixation and adsorption isotherm on knitted cotton fabric [J]. *Fashion and Textiles*, 2015, 2(1) : 3.
- [12] YANG L L, XU Z X, LI H Q, et al. Synthesis, characterization, and dyeing assessment of reactive dyes containing a benz sulfonamide moiety [J]. *Fibers and Polymers*, 2021, 22(4) : 1000-1008.
- [13] CHEMCHAME Y, POPIKOV I V, SOUFIAOUI M. Study on analytical methods for quantifying the non-adsorbed reactive dye forms in an exhausted dyebath [J]. *Coloration Technology*, 2012, 128(3) : 169-175.
- [14] CHEMCHAME Y, POPIKOV I V, SOUFIAOUI M. Study of analytical methods for quantifying unfixed form of bifunctional reactive dyes used in dyeing cellulosic fibers (cotton) [J]. *Fibers and Polymers*, 2010, 11(4) : 565-571.
- [15] DAI Y M, YANG B F, DING Y S, et al. Real-time monitoring of multicomponent reactive dye adsorption on cotton fabrics by Raman spectroscopy [J]. *Spectrochimica Acta Part A: Molecular and Biomolecular Spectroscopy*, 2020, 230 : 118051.
- [16] DAI Y M, XU H, ZHONG Y, et al. Study on the effect of different dyeing systems on the interaction of multi-component reactive dyes by Raman spectroscopy [J]. *Coloration Technology*, 2021, 137(5) : 520-529.
- [17] JAVORŠEK D, KOVÁČ F, GORENŠEK M. HPLC analysis of monofluoro-S-triazine dye during the dyeing process [J]. *American Journal of Analytical Chemistry*, 2014, 5(4) : 215-224.
- [18] ZOTOU A, ELEFTHERIADIS I, HELI M, et al. Ion-pair high performance liquid chromatographic study of the hydrolysis behaviour of reactive fluorotriazinyl dyes [J]. *Dyes and Pigments*, 2002, 53(3) : 267-275.
- [19] GUO L N, PETIT-RAMEL M, GAUTHIER R, et al. Interaction of vinylsulphone reactive dyes with cellulosic fabrics. Part 1: dyeing mechanism, fibre characterisation and effects of alkaline electrolytes [J]. *Journal of the Society of Dyers and Colourists*, 1993, 109(5/6) : 213-219.
- [20] GUO L N, PETIT-RAMEL M, ARNAUD I, et al. Interaction of vinylsulphone reactive dyes with cellulosic fabrics. Part 2: dye associations and dye surfactant interactions [J]. *Journal of the Society of Dyers and Colourists*, 1994, 110(4) : 149-154.
- [21] REED P A, CARDOSO R M, MUÑOZ R A A, et al. Pyrolyzed cotton balls for protein removal: analysis of pharmaceuticals in serum by capillary electrophoresis [J]. *Analytica Chimica Acta*, 2020, 1110 : 90-97.
- [22] WU X H, CHE X M, QIU Z X, et al. Simultaneous determination of three antituberculosis drugs in the serum of patients with spinal tuberculosis by capillary electrophoresis [J]. *Analytical Methods*, 2021, 13(37) : 4307-4313.
- [23] VAN DER BURG D, WÄTZIG H, DE GRIEND C E S. Analysis of cationic vitamins in cell culture medium samples by capillary zone electrophoresis [J]. *Journal of Analytical Methods in Chemistry*, 2022, 2022 (1) : 2819855.
- [24] KARTSOVA L A, KRAVCHENKO A V, KOLOBOVA E A. Covalent coatings of quartz capillaries for the electrophoretic determination of biologically active analytes [J]. *Journal of Analytical Chemistry*, 2019, 74(8) : 729-737.
- [25] HAMIDLI N, ANDRASI M, NAGY C, et al. Analysis of intact proteins with capillary zone electrophoresis coupled to mass spectrometry using uncoated and coated capillaries [J]. *Journal of Chromatography A*, 2021, 1654 : 462448.
- [26] OJSTRSEK A, DOLISKA A, FAKIN D. Analysis of reactive dyestuffs and their hydrolysis by capillary electrophoresis [J]. *Analytical Sciences*, 2008, 24(12) : 1581-1587.
- [27] TAPLEY K N. Capillary electrophoretic analysis of the reactions of bifunctional reactive dyes under various conditions including a study of the analysis of the traditionally difficult to analyze phthalocyanine dyes [J]. *Journal of Chromatography A*, 1995, 706(1/2) : 555-562.
- [28] HANSA A, PILLAY V L, BUCKLEY C A. Analysis of reactive dyes using high performance capillary electrophoresis [J]. *Water Science and Technology*, 1999, 39(10/11) : 169-172.
- [29] BURKINSHAW S M, GRAHAM C. Capillary zone electrophoresis analysis of chlorotriazinyl reactive dyes in dyebath effluent [J]. *Dyes and Pigments*, 2002, 53(3) : 267-275.

- Pigments*, 1997, 34(4) : 307-319.
- [29] LU Z J, XU J S, XU Z Q, et al. Study of reactive dyes and their hydrolyzed forms in a real trichromatic dyeing process by capillary electrophoresis with UV detection [J]. *Analytical Sciences*, 2024, 40(9) : 1641-1651.
- [30] MA X R, WU Y W, SHEN Q X, et al. One-step admicelle to cyclodextrin sweeping of toxic aristolochic acids by capillary electrophoresis [J]. *Microchemical Journal*, 2024, 200: 110480.
- [31] OUADAH N, MOIRE C, BROTHIER F, et al. Capillary electrophoresis for aluminum ion speciation: optimized separation conditions for complex polycation mixtures [J]. *Journal of Chromatography A*, 2018, 1552: 79-86.

基于毛细管电泳技术的三种活性染料及其六种衍生物分析方法研究

黄书卿, 沈丽*, 徐中其*

东华大学 化学与化工学院, 上海 201620

摘要: 具有不同活性基团的活性染料表现出不同的水解和染色行为。特别是在拼色染色中, 水解和染色反应的竞争使得染色过程变得更加复杂。因此, 开发一种有效的方法来监测染色过程中活性染料的变化显得尤为重要。本研究旨在开发一种毛细管电泳-紫外检测法以用于检测3种活性染料及其6种衍生物(共9种分析物)。毛细管电泳条件: 20.0 mmol/L $\text{Na}_2\text{B}_4\text{O}_7 \cdot 10\text{H}_2\text{O}$, 体积分数为15.0%的乙腈, 20.0 mmol/L α -环糊精, pH 9.0(通过添加0.5 mol/L H_3BO_3 溶液进行调节)。9种分析物的检出限(信噪比为3时)为1.38~5.06 mg/L, 峰面积和迁移时间的相对标准偏差(relative standard deviation, RSD)分别为2.19%~4.96%和0.29%~2.75%。该方法能够准确识别3种活性染料及其6种衍生物, 并检测单色染色和拼色染色过程中成分变化及分析上染行为。

关键词: 活性染料; 毛细管电泳; 水解产物; 拼色染色

DOI: 10.19884/j.1672-5220.202410004

Preparation and Power Frequency Shielding Effectiveness of Stainless Steel Conductive Fabric

YANG Yang¹, ZHANG Yan¹, ZHANG Ruiyun^{1*}, JI Feng¹, LI Wenjun², XU Xiaoyuan³

1. College of Textiles, Donghua University, Shanghai 201620, China

2. Hangzhou Segurmax Textile Co., Ltd., Hangzhou 311215, China

3. China Cotton Textile Association, Beijing 100027, China

Abstract: In order to prepare the shielding fabrics with high efficiency of power frequency (PF) shielding and excellent electrical conductivity, different ratios of aramid/stainless steel fiber blended yarns were used to weave the shielding fabrics with different specifications. The fabric structure, fabric areal density, number of fabric layers, embedding ratio of copper-clad wires wrapped aramid yarns (denoted as CCWWA) and embedding direction were designed, and a total of 34 different types of shielding fabrics were woven for testing. The experiments were mainly conducted to study the influence mechanism of various factors on the PF shielding effectiveness by testing the electrical conductivity and PF shielding effectiveness of the fabrics. The research results indicate that the PF shielding effectiveness improves with increasing fabric areal density and metal fiber content. The fabrics embedded with CCWWA, particularly those with bidirectional embedding, exhibit a significant enhancement in the PF shielding effectiveness, showing an increase of 8 – 20 dB compared to the fabrics without CCWWA. The PF shielding effectiveness varies across different fabric structures, with plain weave fabrics demonstrating the superior PF shielding effectiveness due to their compact structure. Non-conductive base fabric has minimal impact on the PF shielding effectiveness. As the number of fabric layers increases, the PF shielding effectiveness initially improves but then declines, peaking with double-layer fabrics.

Keywords: stainless steel blended fabric; power frequency; shielding effectiveness; conductivity; safety protection

CLC number: TS101.923

Document code: A

Article ID: 1672-5220(2025)05-0476-09

Open Science Identity
(OSID)



0 Introduction

In the highly informatized modern society, electromagnetic waves have extensively permeated various domains of human life^[1-2]. Electronic devices in daily life and working environments generate electromagnetic

waves across different frequency bands^[3-4]. High-frequency electromagnetic waves are primarily emitted by communication equipment, microwave ovens, radar systems and medical devices. Their radiation poses health hazards to humans and causes interference with electronic devices. In the low-frequency electromagnetic spectrum, the most typical interference band is the power frequency (PF) band (50 Hz), mainly generated by industrial and household electricity. Notably, long-term exposure to high-voltage PF electromagnetic environments may induce occupational diseases such as neurophysiological disorders and cardiovascular system abnormalities^[5-9].

In the field of shielding materials, composite films exhibit excellent electromagnetic wave absorption properties, yet they suffer from poor wear comfort and are predominantly applied to high-frequency protection. Conversely, textile-based materials demonstrate favorable wearability but lack sufficient protective performance. To meet long-term wearing requirements, conventional shielding garments predominantly utilize textile-based materials. Consequently, existing protective clothing for high-voltage live-line workers generally provides only basic shielding performance, failing to satisfy the increasingly stringent shielding demands imposed by growing signal transmission intensities.

To address the inadequate PF shielding performance of current protective clothing, this study designs PF shielding fabrics by adjusting yarn types and fabric structural parameters. Through the resistance and the PF shielding effectiveness testing of woven samples, the electrical conductivity and the PF shielding effectiveness of the fabrics with different specifications are comparatively analyzed, providing a reference basis for designing highly conductive and high-performance shielding protective clothing.

1 Materials and Methods

1.1 Materials

The specifications of the yarns used in the

Received date: 2024-10-16

Foundation item: Taishan Industrial Experts Program, China

* Correspondence should be addressed to ZHANG Ruiyun, email: ryzhang@dhu.edu.cn

Citation: YANG Y, Zhang Y, ZHANG R Y, et al. Preparation and power frequency shielding effectiveness of stainless steel conductive fabric [J]. *Journal of Donghua University (English Edition)*, 2025, 42(5): 476-484.

experiment are shown in Table 1. Samples #1 to #4 are blended yarns; sample #5 is a single compositon yarn; sample #6 is a covered yarn.

Table 1 Specifications of yarns

No.	Yarn name	Yarn specification
#1	SS/PMIA/FRV(30/40/30)	36S/2
#2	SS/PMIA(40/60)	30S/2
#3	SS/T(30/70)	36S/2
#4	SS/PMIA(20/80)	36S/2
#5	PMIA	35S/2
#6	CCWWA	200D+35S/1

Notes: SS denotes stainless steel fiber; PMIA represents Nomex yarn; FRV stands for flame retardant viscose fiber; T indicates Tencel fiber; the numbers in parentheses indicate the mass ratio of fibers in the blend; CCWWA is the copper-clad wire-wrapped aramid yarn; D refers to Denier, a fixed-length unit of yarn fineness, while S refers to the English cotton count, a fixed-weight unit of yarn fineness; /1 and /2 indicate that the yarn is made from one and two strands, respectively.

1.2 Fabric preparation

Different blended yarns were selected to weave four types of blended fabrics on an automatic rapier loom. The fabric weave structures were plain and basket. Fabrics with varying metal contents, different metal fiber types, distinct arrangements and diverse woven structures were selected as the raw materials for the experiments. The specifications of the fabrics are detailed in Table 2, and a total of six comparative experiments were designed to analyze the influencing factors. The fabrics are categorized into four classes: A, B, C and D (Table 2). A total of 34 fabrics were designed, with two types of yarns selected for the warp: PMIA and CCWWA yarns. The weft yarns included SS/PMIA/FRV (30/40/30) blended yarn, SS/PMIA (40/60) blended yarn, SS/T (30/70) blended yarn, SS/PMIA (20/80) blended yarn, PMIA yarn and CCWWA covered yarn. The fabric weave structures were plain and basket, and the warp yarn density was set at 20 ends/cm.

Table 2 Fabric parameters

Fabric No.	Warp yarn 1	Warp yarn 2	Warp rod ratio	Weft yarn 1	Weft yarn 2	Weft rod ratio	Warp density/ (ends/cm)	Weft density/ (picks/cm)	Fabric weave structure
A1	PMIA	PMIA	—	SS/PMIA/FRV (30/40/30)	SS/PMIA/FRV (30/40/30)	—	20	20	Plain
A2	PMIA	PMIA	—	SS/PMIA/FRV (30/40/30)	SS/PMIA/FRV (30/40/30)	—	20	15	Plain
A3	PMIA	PMIA	—	SS/PMIA/FRV (30/40/30)	SS/PMIA/FRV (30/40/30)	—	20	10	Plain
A4	PMIA	PMIA	—	SS/PMIA/FRV (30/40/30)	PMIA	1:1	20	25	Plain
A5	PMIA	PMIA	—	SS/PMIA/FRV (30/40/30)	PMIA	1:1	20	20	Plain
A6	PMIA	PMIA	—	SS/PMIA/FRV (30/40/30)	CCWWA	5:1	20	20	Plain
A7	PMIA	PMIA	—	SS/PMIA/FRV (30/40/30)	CCWWA	9:1	20	20	Plain
A8	PMIA	PMIA	—	SS/PMIA/FRV (30/40/30)	CCWWA	15:1	20	20	Plain
A9	PMIA	PMIA	—	SS/PMIA/FRV (30/40/30)	CCWWA	19:1	20	20	Plain
A10	PMIA	PMIA	—	SS/PMIA/FRV (30/40/30)	CCWWA	15:1	20	20	Basket
A11	PMIA	CCWWA	15:1	SS/PMIA/FRV (30/40/30)	CCWWA	15:1	20	20	Plain
A12	PMIA	CCWWA	15:1	SS/PMIA/FRV (30/40/30)	CCWWA	15:1	20	20	Basket
A13	PMIA	PMIA	—	SS/PMIA/FRV (30/40/30)	CCWWA	19:1	20	20	Plain
A14	PMIA	PMIA	—	SS/PMIA/FRV (30/40/30)	CCWWA	38:2	20	20	Plain
A15	PMIA	PMIA	—	SS/PMIA/FRV (30/40/30)	CCWWA	57:3	20	20	Plain

(Table 2 continued)

Fabric No.	Warp yarn 1	Warp yarn 2	Warp rod ratio	Weft yarn 1	Weft yarn 2	Weft rod ratio	Warp density/ (ends/cm)	Weft density/ (picks/cm)	Fabric weave structure
B1	PMIA	PMIA	—	SS/PMIA(40/60)	SS/PMIA(40/60)	—	20	20	Plain
B2	PMIA	PMIA	—	SS/PMIA(40/60)	SS/PMIA(40/60)	—	20	15	Plain
B3	PMIA	PMIA	—	SS/PMIA(40/60)	SS/PMIA(40/60)	—	20	10	Plain
B4	PMIA	PMIA	—	SS/PMIA(40/60)	CCWWA	15:1	20	20	Plain
B5	PMIA	PMIA	—	SS/PMIA(40/60)	CCWWA	15:1	20	20	Basket
B6	PMIA	CCWWA	15:1	SS/PMIA(40/60)	CCWWA	15:1	20	20	Plain
B7	PMIA	CCWWA	15:1	SS/PMIA(40/60)	CCWWA	15:1	20	20	Basket
C1	PMIA	PMIA	—	SS/T(30/70)	SS/T(30/70)	—	20	30	Plain
C2	PMIA	PMIA	—	SS/T(30/70)	SS/T(30/70)	—	20	27	Plain
C3	PMIA	PMIA	—	SS/T(30/70)	SS/T(30/70)	—	20	20	Plain
C4	PMIA	PMIA	—	SS/T(30/70)	CCWWA	15:1	20	20	Plain
C5	PMIA	PMIA	—	SS/T(30/70)	CCWWA	15:1	20	20	Basket
C6	PMIA	CCWWA	15:1	SS/T(30/70)	CCWWA	15:1	20	20	Plain
C7	PMIA	CCWWA	15:1	SS/T(30/70)	CCWWA	15:1	20	20	Basket
D1	PMIA	PMIA	—	SS/PMIA(20/80)	SS/PMIA(20/80)	—	20	30	Plain
D2	PMIA	PMIA	—	SS/PMIA(20/80)	SS/PMIA(20/80)	—	20	27	Plain
D3	PMIA	PMIA	—	SS/PMIA(20/80)	SS/PMIA(20/80)	—	20	20	Plain
D4	PMIA	PMIA	—	SS/PMIA(20/80)	SS/PMIA(20/80)	—	20	17	Plain
D5	PMIA	PMIA	—	SS/PMIA(20/80)	SS/PMIA(20/80)	—	20	15	Plain

Notes: warp rod ratio means the rod ratio of warp yarn 1 to warp yarn 2; weft rod ratio means the rod ratio of weft yarn 1 to weft yarn 2.

1.3 Testing and characterization

1.3.1 Fabric resistance

According to the GB/T 6568—2024 standard, the ring-shaped brass electrodes and a pressurized weight block were used to measure the point-to-point resistance value of fabric specimens. The effective test area of the ring-shaped electrode had an inner diameter of 44 mm and an outer diameter of 144 mm. The test specimen size was 240 mm × 240 mm, and it was cut at least 50 mm away from the fabric edge to avoid edge effects. The pressurized weight block was assembled in a specific sequence to ensure accurate and consistent measurements.

1.3.2 Fabric PF shielding effectiveness

The PF shielding effectiveness (hereinafter referred to as shielding effectiveness) of the fabric was measured according to the GB/T 6568—2024 standard. A voltage generator, brass electrodes, a voltmeter, a rubber plate, a brass plate and an insulating plate were assembled in the specified order. A root mean square (RMS) voltage of 600 V at a frequency of 50 Hz between the electrodes of the measuring device was applied. Following the test procedure, the reference voltage U_0 (without the test specimen) and the output voltage U_1 (with the test specimen) were recorded. The test specimen size was 180 mm × 180 mm, and it was cut at least 50 mm away from the fabric edge. The shielding effectiveness S_E was calculated by using Eq. (1), with the unit expressed in dB^[10-14].

$$S_E = 20 \lg(U_0/U_1). \quad (1)$$

2 Results and Discussion

2.1 Fabric electrical conductivity

Based on the principle of the intrinsic property correlation of electromagnetic shielding materials^[15-17], the resistance is a key factor to reflect the electrical conductivity (hereinafter referred to as conductivity) of fabrics. The lower the resistance, the higher the conductivity. The experimental data shown in Table 3 indicate that the higher the proportion of stainless steel fibers in the yarn, the higher the conductivity. Class B fabrics, with a stainless steel fiber content of 40%, have the higher conductivity among the four types of fabrics. In Class A fabrics, the weft rod ratios of A6, A7, A8 and A9 are 5:1, 9:1, 15:1 and 19:1, respectively; A6 has the highest conductivity and A9 has the lowest. This indicates that when the yarn fiber load and fabric structure are the same, the higher the weft rod ratio of the fabric, the lower its conductivity. Compared with A1, the resistance value of A3 increases by about 18 Ω, which means that when the yarn fiber load and fabric weave structure are the same, the tighter the structure of the fabric, the higher its conductivity. The fabric structures of A8 and A10 are plain weave and basket weave, respectively, with resistance values of 1.72 Ω and 1.93 Ω, respectively. It can be seen that, with other factors being the same, the conductivity of the plain fabric is higher than that of the basket fabric. The reasons for these differences are, on the one hand, the increased load of metal fibers in the fabric forms more continuous conductive networks, and on the other hand, the increased density of yarn interweaving points in the fabric leads to a decrease in contact resistance.

Table 3 PF shielding performance of fabrics

Fabric No.	Shielding effectiveness/dB	Resistance/ Ω
A1	62.11	30.97
A2	57.05	36.91
A3	47.80	49.21
A4	63.02	36.37
A5	55.50	32.27
A6	75.53	0.97
A7	70.18	1.15
A8	68.55	1.72
A9	65.76	2.53
A10	65.42	1.93
A11	87.18	0.41
A12	81.37	0.83
A13	62.02	34.27
A14	64.84	25.67
A15	69.17	13.93
B1	83.35	1.61
B2	80.27	3.09
B3	67.80	12.55
B4	87.85	0.49
B5	85.18	1.28
B6	90.74	0.17
B7	87.86	0.56
C1	58.80	20.37
C2	54.23	24.33
C3	52.78	27.13
C4	74.54	0.89
C5	68.91	1.54
C6	87.02	0.34
C7	83.00	0.76
D1	57.11	59.71
D2	54.97	36.67
D3	49.27	33.73
D4	50.37	32.71
D5	47.38	27.33

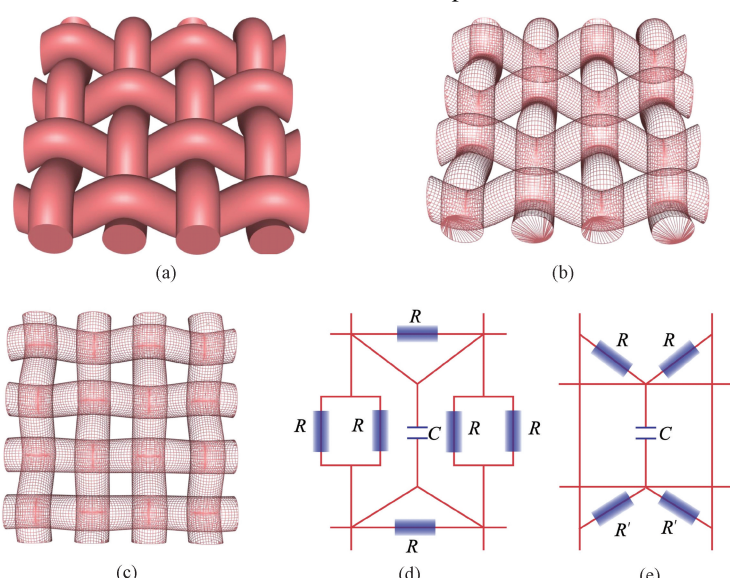


Fig. 1 Equivalent circuit of conductive shielding fabric unit: (a) diagram of plain fabric structure; (b) three-dimensional grid-based analysis diagram of plain fabric; (c) top view of Fig. 1(b); (d) equivalent circuit model for a fabric woven with the same metal yarns in both warp and weft directions; (e) equivalent circuit model for a fabric woven with two different metal yarns in weft direction

2.2 Fabric shielding effectiveness

The conductivity of the material is one of the most important factors affecting the shielding effectiveness of fabrics^[18-20]. The resistance values of the woven fabrics and their corresponding shielding effectiveness are presented in Table 3. A higher shielding effectiveness value indicates better shielding performance. For high-voltage shielding clothing used in electrical work, the Chinese national standard specifies that the shielding effectiveness value must exceed 40 dB.

Figure 1(a) is a diagram of a plain fabric structure. A grid-based analysis (Figs. 1(b) and 1(c)) is used to study the current transmission characteristics of the induced electric field under the action of a vertically incident plane wave. When metal fibers are distributed in both the warp and weft directions of the fabric, the fabric structure can be regarded as a periodic grid system composed of conductive yarns (as shown in Fig. 1(c)). This grid structure can be decomposed into two mutually orthogonal parallel periodic arrays: one parallel array system composed of warp metal yarns and the other parallel array system composed of weft metal yarns. Due to electromagnetic coupling effects, the contact impedance between adjacent conductive yarns can be neglected. Figure 1(d) shows the equivalent circuit model of the unit grid for a fabric woven with the same metal yarns in both the warp and weft directions, while Fig. 1(e) presents the equivalent circuit model for a fabric woven with two different metal yarns in the weft direction. In these equivalent circuits, the resistance R represents the contact resistance between warp and weft yarns, and the capacitance C represents the distributed capacitance generated between parallel conductors^[21-22]. In Fig. 1(e), R' represents the resistance different from R .

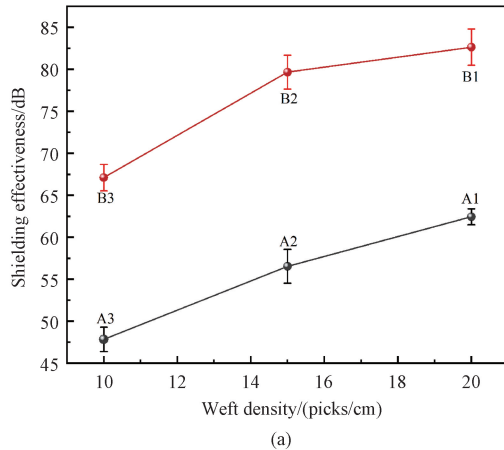
2.2.1 Influence of metal fiber content and fabric areal density on shielding effectiveness

The metal-blended yarns with varying metal fiber contents were used to investigate the effect of metal fiber content on shielding effectiveness. Additionally, the weft density of the fabrics was controlled to analyze the impact of fabric areal density on shielding effectiveness. By controlling the weft density and the type of metal-blended yarns, the effects of these two variables on the shielding effectiveness were analyzed.

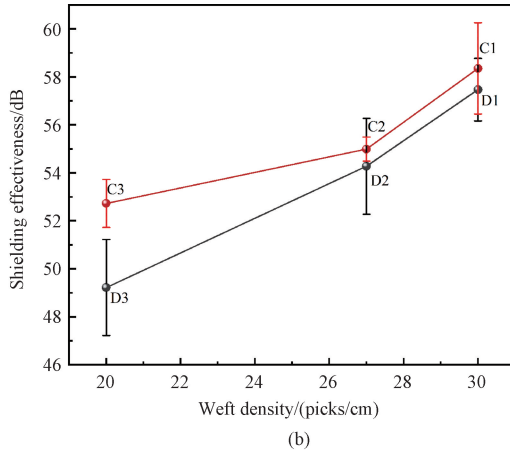
Figure 2(a) shows that the shielding effectiveness of Class B fabrics is consistently higher than that of Class A fabrics, with a difference exceeding 20 dB. This is because the weft yarns in Class B fabrics contain 40% (mass fraction) stainless steel fibers, whereas those in Class A fabrics contain only 30% (mass fraction). A higher metal fiber content improves the conductive network, and enhances the conductivity of the fabric, resulting in higher shielding effectiveness.

Figure 2 shows that as the weft density increases, the shielding effectiveness of the fabric also increases. When the

weft density increases from 10 to 20 picks/cm, the shielding effectiveness rises by approximately 15 dB (Fig. 2(a)). For class C and D fabrics, when the weft density increases from 20 to 30 picks/cm, the shielding effectiveness also increases, but the impact of weft density on shielding effectiveness diminishes. This is primarily because the increase in weft density raises the metal fiber content per unit area, improving the conductivity. As a result, more current is grounded through the fabric, leading to a reduction in the output voltage and an increase in shielding effectiveness. In the experiment, the fabric areal density was adjusted by altering the weft density. Overall, the shielding effectiveness of the fabrics increased gradually with the higher weft density, indicating a positive correlation between fabric areal density and shielding effectiveness. When the metal fiber content is low, the conductive network exhibits poor conductivity, resulting in inferior shielding effectiveness. As the metal fiber content increases, the metal fibers come into closer contact, forming more effective conductive pathways, which significantly enhances the shielding effectiveness.



(a)



(b)

Fig. 2 Curves of shielding effectiveness vs. weft density for fabrics with different metal fiber contents: (a) Class A and B fabrics; (b) Class C and D fabrics

2.2.2 Influence of embedding direction of CCWWA on shielding effectiveness

Three sets of samples, each set with identical fabric structures but varying proportions of stainless steel fiber in the yarns, were selected from the designed samples for shielding effectiveness analysis. These three sets of samples include A1, B1 and C1 without CCWWA; A8, B4 and C4 with CCWWA embedded in the weft direction; A11, B6 and C6 with CCWWA embedded in both the warp and weft directions. Figure 3 shows that B6, with bidirectionally embedded CCWWA, exhibits the best shielding effect, with a shielding effectiveness as high

as 90 dB, representing an approximately 8 dB improvement compared to B1 without CCWWA. When CCWWA are bidirectionally embedded, highly conductive yarns form a highly conductive grid pathway within the fabric, facilitating rapid current flow. In contrast, unidirectional embedding CCWWA creates a low-conductivity grid. The current flows through it resulting in a low shielding effectiveness. For fabrics without CCWWA, the current flows through a much lower-conductivity grid, resulting in slower current flow and lower conductivity. Therefore, samples A1, B1 and C1 without CCWWA exhibit the lowest shielding effectiveness among their class.

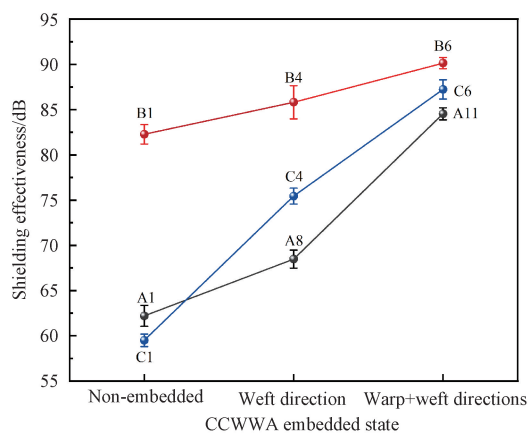


Fig. 3 Shielding effectiveness of fabrics with different CCWWA embedded states

2.2.3 Influence of proportion of CCWWA embedded in weft direction on shielding effectiveness

When the fabric structural pattern remains unchanged and CCWWA are embedded in the weft direction, its shielding effectiveness follows these rules: the greater the number of CCWWA embedded per unit area, the higher the shielding effectiveness; and when the number of CCWWA embedded per unit area is the same, the more wires embedded in the weft direction, the better the

shielding performance. As shown in Fig. 4 (a), the shielding effectiveness value of A6 is the highest, and about 13 dB higher than that of A1. The reason is that the current in a circuit prefers to flow through low-resistance paths. Given that copper fibers have better conductivity than stainless steel fibers, A1, which has no embedded CCWWA, has the lowest conductivity and the lowest shielding effectiveness. As the number of embedded CCWWA increases, the number of highly conductive pathways in the weft direction of the fabric increases, improving current flow and enhancing conductivity, and thus strengthens the fabric's shielding effectiveness. A13, A14 and A15 have the same number of CCWWA embedded per unit area, with weft rod ratios of 19 : 1, 38 : 2 and 57 : 3, respectively. The analysis of their shielding effectiveness (Fig. 4 (b)) shows that the shielding effectiveness of the three-wire parallel sample A15 is about 7 dB higher than that of the single-wire distributed sample A13. According to Holm's contact theory, increasing the number of parallel-embedded conductive yarns can reduce the fabric's equivalent resistance and improve the conductivity of the equivalent circuit. For circuits formed by only one highly conductive yarn, issues such as uneven current density distribution and poor conductivity exist, which can affect the fabric's conductivity and, consequently, its shielding effectiveness.

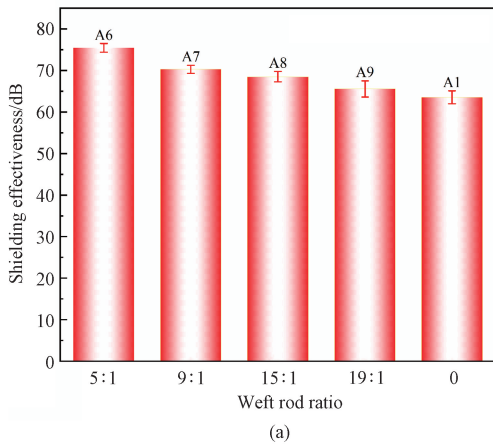
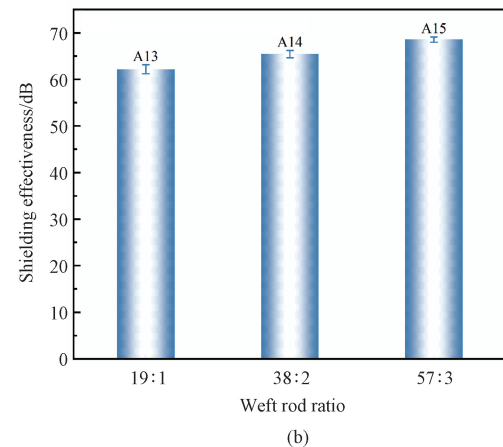


Fig. 4 Shielding effectiveness of fabrics with different weft rod ratios: (a) different number of CCWWA embedded per unit area; (b) same number of CCWWA embedded fabric per unit area



2.2.4 Influence of fabric weave structure on shielding effectiveness

For fabrics in Class A, B and C with the same organizational structure, the shielding effectiveness increases with the rise in stainless steel fiber content. Compared to unidirectional embedding at the same embedding ratio, bidirectional embedding results in an overall improvement in shielding effectiveness. Additionally, for fabrics with different organizational structures, the shielding effectiveness of plain weave fabric

is higher than that of basket weave fabric (Fig. 5). This can be attributed to two main factors: yarn interweaving tightness and structure stability. Tight interweaving increases contact pressure between yarns, leading to better contact and more contact points. Fabrics with higher interweaving tightness exhibit superior shielding effectiveness. The compression during yarn interweaving causes deformation of the inter-yarn apertures, which affects the conductivity of the conductive grid. A more stable fabric structure enhances conductivity and,

consequently, shielding effectiveness.

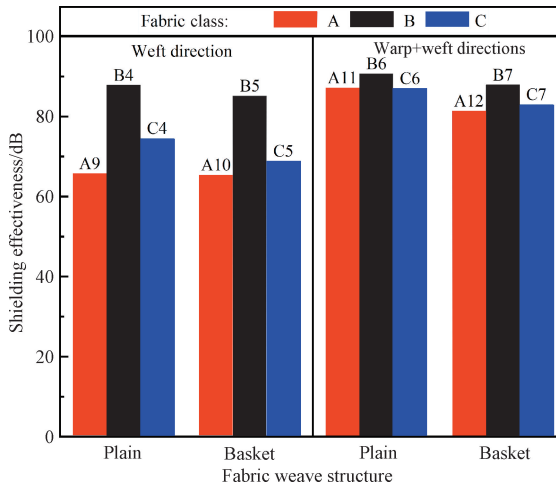


Fig. 5 Shielding effectiveness of fabrics with embedded CCWWA in different fabric weave structures

Plain weaves are the most compact, with the shortest floating length and excellent dimensional stability, resulting in a good shielding performance. In contrast, basket weaves involve two closely interwoven layers, which create non-uniform pore spaces. Under yarn compression, the conductivity of the grid in basket fabrics deteriorates, leading to inferior shielding effectiveness compared to plain weaves.

2.2.5 Influence of base fabric on shielding effectiveness

In the fabric design, A6, A7 and A8 are selected as the surface fabrics, with a pure aramid fabric used as the base fabric. The shielding effectiveness is tested, and the results are shown in Fig. 6. The differences in shielding effectiveness of the surface fabrics with and without the base fabric were not significant. Since the pure aramid fabric is non-conductive, it does not significantly affect shielding effectiveness. The shielding performance is primarily determined by the surface fabrics (A6, A7 and A8), while the addition of a non-conductive base fabric has little impact on the overall shielding effectiveness.

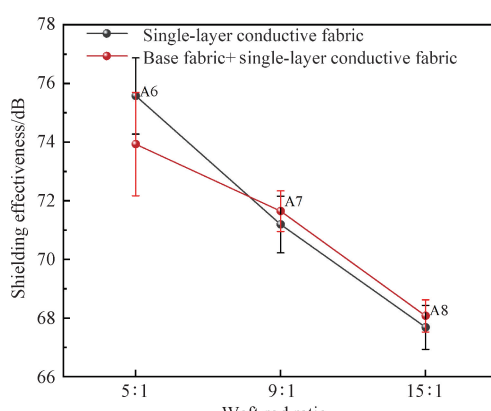


Fig. 6 Shielding effectiveness of fabrics with and without non-conductive base fabric

2.2.6 Influence of number of fabric layers on shielding effectiveness

Fabrics A1, B1 and B6 are selected to investigate the influence of number of fabric layers on shielding effectiveness. As shown in Fig. 7, the shielding effectiveness of a single-layer fabric is lower than that of a double-layer fabric. However, further increasing the number of fabric layers results in a decrease in shielding effectiveness.

The fabrics were made from selected raw materials with consistent conductivity. When two layers were stacked, the shielding effectiveness reached its peak. However, as the number of fabric layers continued to increase, the conductive properties began to decline. This trend occurs because, with a small number of fabric layers, adding more layers introduces additional conductive material into the fabric, thereby enhancing conductivity. However, once the number of layers exceeds a certain threshold, excessive accumulation of conductive material can lead to an uneven distribution within the fabric and a subsequent decline in conductive performance. Additionally, the excessive fabric layers increases internal resistance and capacitance effects, which further destabilize the system and reduce the consistency of the conductive properties. As a result, the shielding effectiveness exhibits a trend of first rising and then gradually declining.

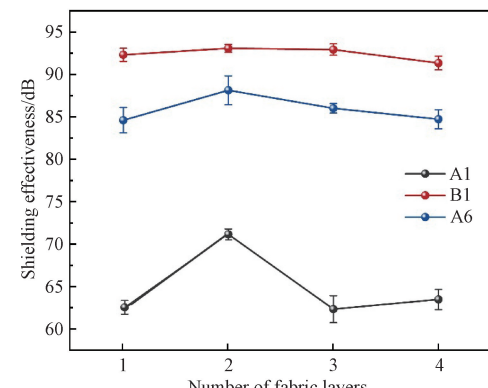


Fig. 7 Curves of shielding effectiveness vs. number of fabric layers

3 Conclusions

In this study, stainless steel blended yarns, aramid yarns and copper-clad wires were used as raw materials to weave shielding fabrics. The influencing factors and specific trends affecting the shielding effectiveness of the electrostatic field in these fabrics were investigated by varying the fabric weave, yarn type, fabric structure and embedded yarn ratios.

1) When the fabric weave and the content of metal wires in the yarn remain unchanged, an increase in weft

density makes the yarns in the fabric become more compact, increasing the contact points. This reduces the surface specific resistance of the fabrics, enhances conductivity, and improves shielding effectiveness.

2) When the fabric structure remains unchanged and metal fibers are embedded in the fabric, the shielding effectiveness of the bidirectionally embedded one is the highest, then the unidirectionally embedded one, and last the no embedding one. For fabrics with CCWWA embedded only in the weft direction, the addition of CCWWA enhances the shielding effectiveness. Among fabrics with different embedding directions of CCWWA, the bidirectionally embedded configuration provides the best shielding effectiveness, showing an improvement of 8–20 dB compared to the fabrics without CCWWA. When CCWWA content per unit area remains constant, arranging CCWWA side by side results in high shielding effectiveness.

3) When the yarn composition and the warp and weft densities of the fabric remain the same, changing the fabric weave results in fabrics with varying shielding effectiveness. The compact structure of the plain fabric provides the best shielding performance, outperforming the basket fabric.

4) The shielding effectiveness of the designed shielding fabric was tested with and without a non-conductive base fabric, and no significant change in the results was observed.

5) Under the same conditions, increasing the number of fabric layers results in the shielding effectiveness increasing first and then decreasing. When the fabric is composed of two layers, the shielding effectiveness of the fabric is the highest.

References

- [1] THENKUMARI K, SANKARAN K S, et al. Design and implementation of frequency reconfigurable antenna for Wi-Fi applications [J]. *Engineered Science*, 2023: 876.
- [2] WU G F, GAO X G, WAN K F. Mobility control of unmanned aerial vehicle as communication relay to optimize ground-to-air uplinks [J]. *Sensors*, 2020, 20(8): 2332.
- [3] JIANG D W, MURUGADOSS V, WANG Y, et al. Electromagnetic interference shielding polymers and nanocomposites: a review [J]. *Polymer Reviews*, 2019, 59(2): 280-337.
- [4] SAID S, MELHAOUI O E, GUETBACH Y, et al. Design of a patch antenna for high-gain applications using 1D-EBG structures [J]. *Engineered Science*, 2024, 27: 1040.
- [5] WEI C H, HE M K, LI M Q, et al. Hollow Co/NC @ MnO₂ polyhedrons with enhanced synergistic effect for high-efficiency microwave absorption [J]. *Materials Today Physics*, 2023, 36: 101142.
- [6] JIA Z X, ZHANG M F, LIU B, et al. Graphene foams for electromagnetic interference shielding: a review [J]. *ACS Applied Nano Materials*, 2020, 3(7): 6140-6155.
- [7] FANG F, LI Y Q, XIAO H M, et al. Layer-structured silver nanowire/polyaniline composite film as a high performance X-band EMI shielding material [J]. *Journal of Materials Chemistry C*, 2016, 4(19): 4193-4203.
- [8] WANG L, CHENG J W, ZOU Y X, et al. Current advances and future perspectives of MXene-based electromagnetic interference shielding materials [J]. *Advanced Composites and Hybrid Materials*, 2023, 6(5): 172.
- [9] ZHENG S N, WU N, LIU Y, et al. Multifunctional flexible, crosslinked composites composed of trashed MXene sediment with high electromagnetic interference shielding performance [J]. *Advanced Composites and Hybrid Materials*, 2023, 6(5): 161.
- [10] XUE Y, LIU J H, YANG Z Q. Current status and development trend of individual security protection in power industry [J]. *Cotton Textile Technology*, 2019, 47(9): 74-78. (in Chinese)
- [11] XU X L, LI Z, LYU D T, et al. Comparison research on measuring methods for materials shielding effectiveness [J]. *Instrument and Equipments*, 2017, 5(4): 95-105. (in Chinese)
- [12] LIU S H, LIU J M, DONG X L. Electromagnetic wave screen dedication and wave-absorbing materials [M]. Beijing: Chemical Industry Press, 2006: 67-71. (in Chinese)
- [13] Standardization Administration of the People's Republic of China. Terminology for electromagnetic shielding materials: GB/T 26667—2021 [S/OL]. (2021-04-30) [2024-09-01] <https://openstd.samr.gov.cn/bzgk/gb/newGbInfo?hcno=F781AC9E998D1E1C5C47CC90A4E90120>. (in Chinese)
- [14] WANG S. Research on electromagnetic wave absorption based on graphene [D]. Changsha: Hunan University, 2019. (in Chinese)
- [15] RONG X. Design and research of high shielding effectiveness multilayer electromagnetic shielding clothing fabric [D]. Zhengzhou: Zhongyuan University of Technology, 2016. (in Chinese)
- [16] ZOU Q, SHI C F, LIU B, et al. Enhanced terahertz shielding by adding rare Ag nanoparticles to Ti₃C₂T_x MXene fiber membranes [J]. *Nanotechnology*, 2021, 32(41): 415204.
- [17] XU L, LU H H, ZHOU Y, et al. Ultrathin, ultralight, and anisotropic ordered reduced graphene oxide fiber electromagnetic interference

- shielding membrane [J]. *Advanced Materials Technologies*, 2021, 6(12) : 2100531.
- [18] MA J H, ZHAO Q L, ZHOU Y X, et al. Hydrophobic wrapped carbon nanotubes coated cotton fabric for electrical heating and electromagnetic interference shielding [J]. *Polymer Testing*, 2021, 100: 107240.
- [19] ZHOU B, LI Z Y, LI Y L, et al. Flexible hydrophobic 2D $Ti_3C_2T_x$ -based transparent conductive film with multifunctional self-cleaning, electromagnetic interference shielding and joule heating capacities [J]. *Composites Science and Technology*, 2021, 201: 108531.
- [20] LOU C W, LIN T A, CHEN A P, et al. Stainless steel/polyester woven fabrics and copper/polyester woven fabrics: manufacturing techniques and electromagnetic shielding effectiveness [J]. *Journal of Industrial Textiles*, 2016, 46(1) : 214-236.
- [21] LIU W L, CHEN C H, HAI W Q, et al. Laser-induced graphene conductive fabric decorated with copper nanoparticles for electromagnetic interference shielding application [J]. *Journal of Donghua University (English Edition)*, 2023, 40(6) : 571-579.
- [22] KRISHNASAMY J, RAMASAMY A, DAS A, et al. Effect of fabric cover and pore area distribution of carbon/stainless steel/polypropylene hybrid yarn-woven fabric on electromagnetic shielding effectiveness [J]. *Journal of Electronic Materials*, 2016, 45(6) : 3087-3100.

不锈钢导电织物的制备及其工频屏蔽效能

杨 阳¹, 张 妍¹, 张瑞云^{1*}, 纪 峰¹, 李文军², 徐潇源³

1. 东华大学 纺织学院, 上海 201620

2. 杭州赛固迈永盛纺织有限公司, 浙江 杭州 311215

3. 中国棉纺织行业协会, 北京 100027

摘要: 为制备兼具高效工频屏蔽效能和优良导电性的屏蔽织物, 采用不同比例的芳纶/不锈钢纤维混纺纱织造不同规格的屏蔽织物。对织物的组织结构、面密度、层数、嵌入铜包覆丝比例及方向进行了设计, 共试织34种成品织物。通过测试织物电导率及工频屏蔽效能, 研究各种因素对工频屏蔽效能的影响机理。研究结果表明: 屏蔽效能随织物面密度与金属纤维含量的增加而增大; 铜包覆丝的嵌入, 特别是双向嵌入, 使织物屏蔽效能得到极大改善, 相较于无嵌入铜包覆丝织物, 嵌入铜包覆丝织物的屏蔽效能提高8~20 dB; 不同结构机织物得到的屏蔽效能不同, 平纹织物因其结构紧密, 屏蔽效能较大; 非导电基布对织物屏蔽效能影响不大; 随织物层数增加屏蔽效能先增大后减小, 双层织物的屏蔽效能最大。

关键词: 不锈钢混纺织物; 工频; 屏蔽效能; 导电性; 安全防护

DOI: 10.19884/j.1672-5220.202403018

Hydrogen Sensing Characteristics of Gas Sensor Based on Pt/Graphene Composite

HOU Tianhao, PENG Yitian, DING Shuyang*

College of Mechanical Engineering, Donghua University, Shanghai 201620, China

Abstract: Graphene has exceptional electrical, optical and thermal properties, and is widely used to create thinner, lighter and faster sensors. In this study, graphene was fabricated by mechanically exfoliating on the SiO₂/Si substrate and the graphene field effect transistor (FET) was prepared by photolithography. Platinum (Pt) particles were doped on the surface of graphene by the hydrazine hydrate reduction method to endow a Pt/graphene sensor with gas-sensing properties. By being tested on a gas detection platform, the characteristics of the electrical (*I-V*) curves and resistance response curves were obtained in different hydrogen environments. The results show that the Pt/graphene sensor exhibits a high sensitivity to hydrogen at room temperature, with a resistance response rate of 33.35% at a hydrogen volume fraction of 1.00%. However, the sensitivity lifetime study shows an essential hysteresis in desorption process, which leads to gradually decreases in the resistance response rate. This research provides an improved production method of graphene-based gas sensors, which has a wide range of potential applications in aero-space industry.

Keywords: graphene; platinum (Pt) particle; hydrogen sensor; chemical adsorption

CLC number: TP212.9

Document code: A

Article ID: 1672-5220(2025)05-0485-09

Open Science Identity
(OSID)



0 Introduction

Hydrogen, as an efficient and environmentally friendly energy source, is expected to be widely used in the future in a number of fields such as transport, construction and electricity^[1]. However, there are certain safety hazards and risks involved in the production and application of hydrogen. Hydrogen is a colorless and odorless gas that is difficult for humans to identify, and excessive concentrations may cause asphyxiation^[2-3]. Hydrogen molecules are extraordinarily small and diffuse through air at a very high rate, enabling them to permeate many materials and inflict irreversible damage^[4]. Accurate detection of the hydrogen volume fraction is therefore essential, and it is one of the key

ways to minimize potential safety risks.

Gas sensors are widely used for resistance-change detection because of their direct measurement principle, simple structure and low manufacturing cost^[5-6]. Numerous studies have confirmed that reducing the dimensionality of a material can increase the sensitivity of a sensor by multiples or even orders of magnitudes^[7-8]. Graphene is considered to be an innovative material that can enhance the performance of sensors due to its larger specific surface area and higher carrier migration rate^[9-10]. Theoretical and experimental results show that intrinsic graphene has a high sensitivity and poor selectivity for a few gases^[11]. Hydrogen adsorbed on unmodified graphene has a low adsorption energy and a low number of charge transfers, so unmodified graphene does not have sensitivity towards hydrogen^[7,12]. In previous studies, to improve the sensitivity and selectivity of graphene sensors to hydrogen, graphene was usually used as a carrier for hydrogen-sensitive materials, and semiconducting metal oxides were doped on graphene^[13-14], metals^[15-17], polymers^[18-19] and composite materials^[20-24].

Platinum (Pt) is a common metal material for modification with a high sensitivity and selectivity to hydrogen. Hydrogen-modified Pt exhibits a higher resistivity than intrinsic Pt, making it better suited for resistance-based detection^[25]. Pt/graphene composites made by Pt-modified graphene show many advantages in hydrogen detection. In theory, adjusting the metal structure at the nanoscale can maximize the sensitivity of metal-based gas sensors^[26]. Yang et al.^[27] explored the possibility of using Pt as a hydrogen sensor and confirmed the specific effect of the Pt sensor on the hydrogen sensing performance.

Graphene essentially exhibits a two-dimensional surface property with a extremely high carrier mobility^[28-29], which makes graphene an ideal material for sensing^[30-32]. In previous studies, researchers have verified the adsorption performance of NH₃ on the surface of Pt-modified graphene sheets^[33] and the interaction mechanism of H₂S with Pt/graphene through the density functional theory (DFT) calculations^[34]. The mechanism of Pt/graphene for gas detection was verified by the

Received date: 2024-03-28

Foundation item: National Natural Science Foundation of China (No. 51905090)

* Correspondence should be addressed to DING Shuyang, email: shuyangding@dhu.edu.cn

Citation: HOU T H, PENG Y T, DING S Y. Hydrogen sensing characteristics of gas sensor based on Pt/graphene composite [J]. *Journal of Donghua University (English Edition)*, 2025, 42(5): 485-493.

adsorption energy and charge transfer. Harley-Trochimczyk's research team^[35] succeeded in creating a low-energy hydrogen sensor by loading functionalized Pt particle polysilicon onto graphene with a high specific surface area. At a hydrogen volume fraction of 0.01%, the sensitivity reached 1.6%; at a temperature of 90 °C, the response and recovery times were relatively shortened, with a detection limit of 0.006 5%. Phan et al.^[36] reported that Pt/palladium (Pd) alloy modified graphene hydrogen sensor had a wide hydrogen detection limit and high sensitivity. Under ambient conditions, the detection sensitivity of the hydrogen sensor was closely related to the hydrogen flow rate.

In this study, we prepare a graphene field effect transistor (FET) by using mechanically exfoliated graphene as a carrier. A Pt/graphene sensor is prepared by depositing Pt particles on the graphene surface with the hydrazine hydrate reduction method. The effect of Pt modification on the properties of graphene is investigated, the hydrogen detection characteristics under environmental conditions are explored, and the resistance response curves of the Pd/graphene sensor are compared. In addition, the basic principle of hydrogen adsorption and desorption is analyzed through the continuity test of the sensor and the resistance response curves.

1 Materials and Methods

1.1 Materials

Graphene was provided by Six Carbon Technology

(Shenzhen, China). SiO_2/Si was supplied by Suzhou Institute of Nano-Tech and Nano-Bionics (SINANO) Chinese Academy of Sciences, China. The ROL-7133 stripped photoresist was supplied by Suzhou Rdmicro Limited Technology Company, China. Pb, H_2PtCl_6 , PEG-400, isopropanol and hydrazine hydrate were provided by Sinopharm Chemical Reagent Co., Ltd., China.

1.2 Methods

1.2.1 Pt/graphene FET preparation

The schematic diagram of Pt/graphene sensor preparation is shown in Fig. 1. Firstly, graphene was prepared by using an optimized mechanical exfoliation method. Graphene was placed on a neutral-viscosity blue film with tweezers and repeatedly folded and pressed for 7–8 times. Then, the blue film was transferred onto a SiO_2/Si substrate (300 nm single-sided SiO_2 oxide layer), and heated on a heating table at 60 °C for 1 min. Graphene was peeled off from the blue film after it was cooled down. After the transfer was completed, the location of the graphene was marked. After the sample was heated at 100 °C for 1 min, the ROL-7133 stripped photoresist was spin-coated on the surface of the sample. After spin-coated, the sample underwent pre-baking, exposure, middle baking, development and glue removing. Then, the graphene FET was prepared by evaporating coatings with lift-off lithography. Finally, the Pt/graphene sensor was prepared by one-step reduction of Pt with the hydrazine hydrate.

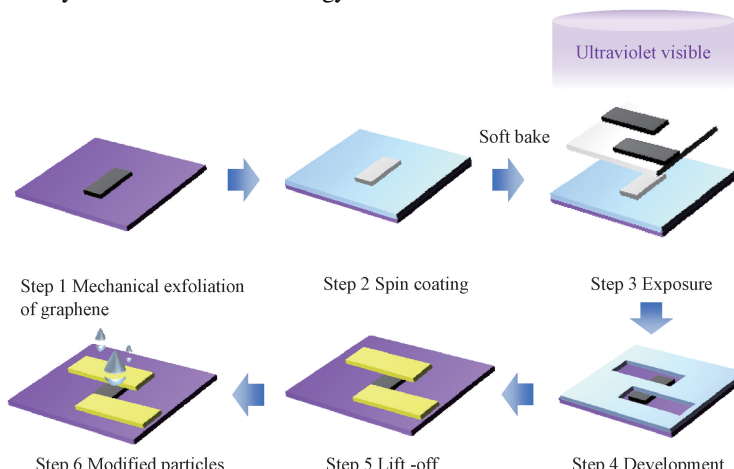


Fig. 1 Schematic diagram of Pt/graphene sensor preparation

1.2.2 Optimized glue removing method by isopropanol

The Pt/graphene sensor was held with tweezers, and the isopropanol was poured into the beaker and heated to 40 °C with magnetic stirring for 3 h. The residual gel on the surface of graphene was removed by isopropanol.

1.2.3 Surface functionalization of graphene

Hydrazine hydrate was used to reduce Pt in H_2PtCl_6 in one step. In order to control the size of the reduced Pt particles and to prevent the agglomeration of the Pt particles, PEG-400 was added as a dispersant. Firstly,

the graphene FET sample treated with isopropanol was cleaned in a plasma cleaner (PDC-32G-2, Harrick Plasma, USA) with the power being selected as high-grade 18 W. The plasma-cleaned sample was taken out and immersed in 0.05 mmol/L H_2PtCl_6 for 3 h. Secondly, the experiment was configured with 10 mL hydrazine hydrate solution (a mass fraction of 10%). The dispersant PEG-400 (300 μL) was added with further ultrasonic for 10 min. Thirdly, 1 μL hydrazine hydrate solution was added dropwise to the graphene

surface. After a few seconds of reaction, the sample was rinsed slowly with isopropanol, and then slowly rinsed with deionized water to obtain the Pt/graphene sensor.

1.3 Characterization of Pt/graphene sensor

The morphology and electrical characterization of the Pt/graphene sensor were performed by an atomic force microscope (MFP-3D, Oxford Instruments, UK) and a source measurement unit (KEITHLEY 2612B, Tektronix, USA), respectively.

The feasibility of the optimized glue removing method by isopropanol was verified, and the Pt particles were characterized by a scanning electron microscope (S-4800, Hitachi, Japan) and energy dispersive spectroscope (AZtec X-Max^N80, Oxford Instruments, USA).

The electrical characteristics and resistance response of the Pt/graphene sensor were tested on a self-built source measurement unit gas detection platform. The high-precision CS200 flow controller and dynamic matching method were adopted, nitrogen was used as the carrier and hydrogen was used as the target gas. The gas flow rate was maintained at $3 \times 10^2 \text{ cm}^3/\text{min}$, and the hydrogen volume fraction varied in the range of 0.08% to 0.12%.

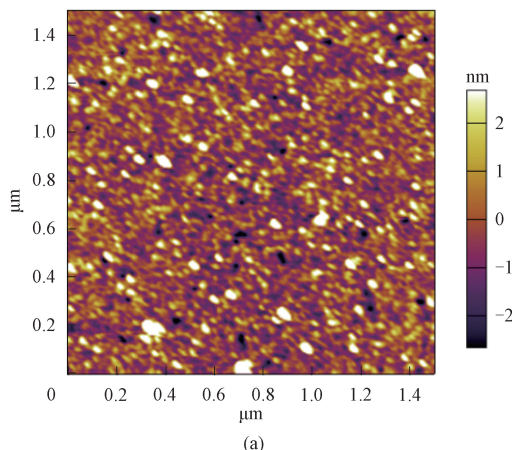


Fig. 2 Graphene surface tested by AFM: (a) before optimization; (b) after optimization by isopropanol

In order to further prove the effectiveness of the optimized glue removing method, the electrical properties of the sample were tested. The results of the electrical properties are shown in Fig. 3. The electrical properties of the sample are altered due to the presence of excess residual glue on the surface, resulting in decrease in the electrical conductivity. At a drain voltage V of 0, the drain current I is $2.51 \mu\text{A}$. The presence of residual glue causes the surface doping of graphene, the I - V curve shifts to the left, and the linearity of the curve is greatly different, resulting in poor electrical properties. After optimization by isopropanol, the I - V curve is closer to the linear curve. At a drain voltage of 0, the drain current of the sample is $0.0031 \mu\text{A}$. The surface doping effect of graphene has been improved. The conductivity of the optimized sample is also improved and the linearity of the I - V curve slope has increased by 4.95 times.

The continuity test of the Pt/graphene sensor was done by continuously controlling the switching of the hydrogen output at a specific hydrogen volume fraction for sensitivity lifetime study. Firstly, before the test, nitrogen ($5 \times 10^2 \text{ cm}^3/\text{min}$) was injected for 300 s and the hydrogen volume fraction was maintained at 1.00%. The hydrogen input was stopped at 150 s and only the nitrogen input was turned on, till the end of the test before resuming nitrogen inject for 300 s, and so on for four cycles. By analyzing the relationship between the current response and the number of tests, we tested the Pt/graphene sensor for current and time variations over a fixed time period.

2 Results and Discussion

2.1 Sample characterization

Figure 2 shows the graphene surface morphology of the graphene FET by the atomic force microscopy (AFM). Isopropanol leaves a visibly adhesive residue on graphene that remains undissolved; nevertheless, the residual glue is reduced, and the adhesive is not dissolved. However, the residual glue on the surface has been reduced.

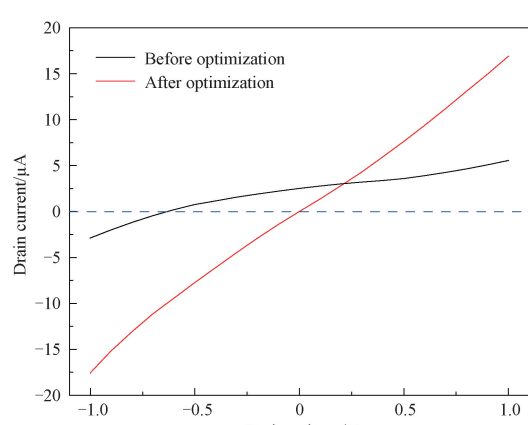
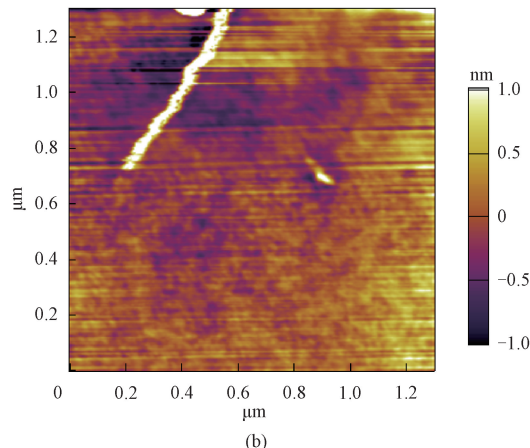


Fig. 3 Electrical properties of graphene FET before and after optimization

Pt element distribution and proportions of elemental contents tested by scanning electron microscopy (SEM) and energy dispersive spectroscopy (EDS) are shown in Figs. 4 (a) and 4 (b), respectively. The surface of graphene after plasma treatment is hydroxylated, and the binding ability of Pt particles to graphene is enhanced,

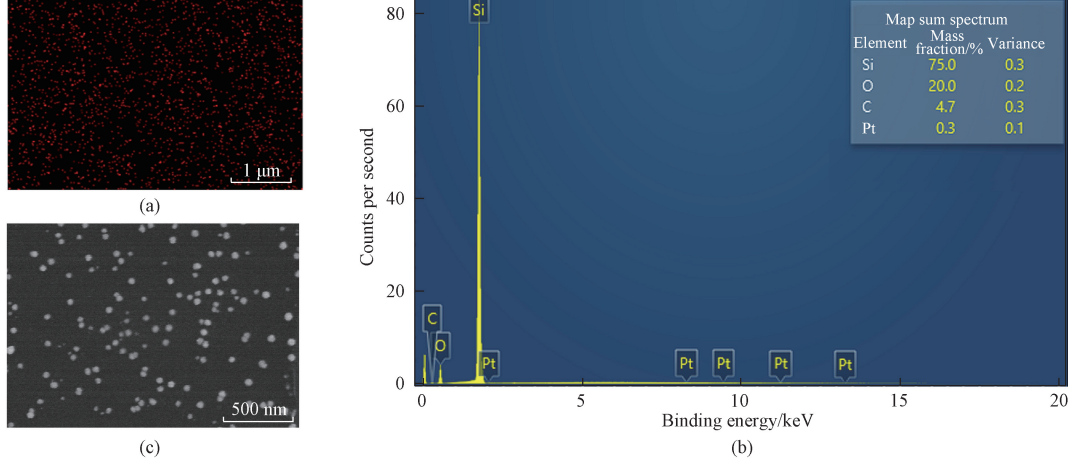


Fig. 4 SEM images and EDS results of Pt/graphene sensor: (a) Pt element distribution; (b) proportions of elemental contents; (c) Pt particle distribution

The I - V curves of the graphene FET and Pt/graphene sensor are shown in Fig. 5. The I - V curve of the graphene FET is almost straight. At the same drain voltage, the Pt/graphene FET has a substantial improvement in the absolute value of the current. According to Wang et al.^[37], metal doping increases the electrical conductivity of graphene. The overlap of electron densities between C and Pt atoms is more obvious than that between C and C atoms, and the bonding ability between atoms is stronger. This shows that doped atoms can enhance electron transfer and improve conductivity. The band gap of the Pt/graphene sensor increases with the increase of the Pt mass fraction, which is beneficial to the conductivity of graphene.

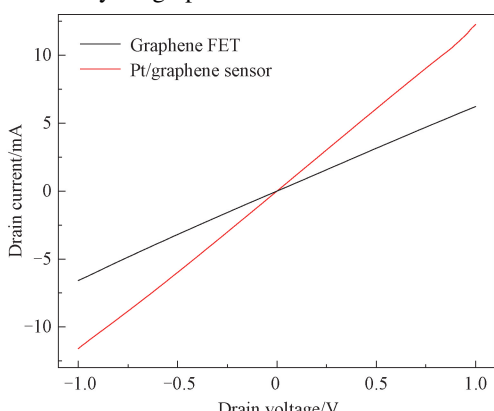


Fig. 5 Electrical property comparison of graphene FET and Pt/graphene sensor

2.2 Hydrogen detection by Pt/graphene sensor

As shown in Fig. 6, at different volume fractions of

making the distribution of Pt on the surface of graphene more uniform as shown in Fig. 4 (a). The mass ratio of Pt to C is 3 : 47, which is relatively high. Figure 4 (c) shows the surface morphology of the Pt/graphene sensor. The Pt particles are uniform in size and distribution.

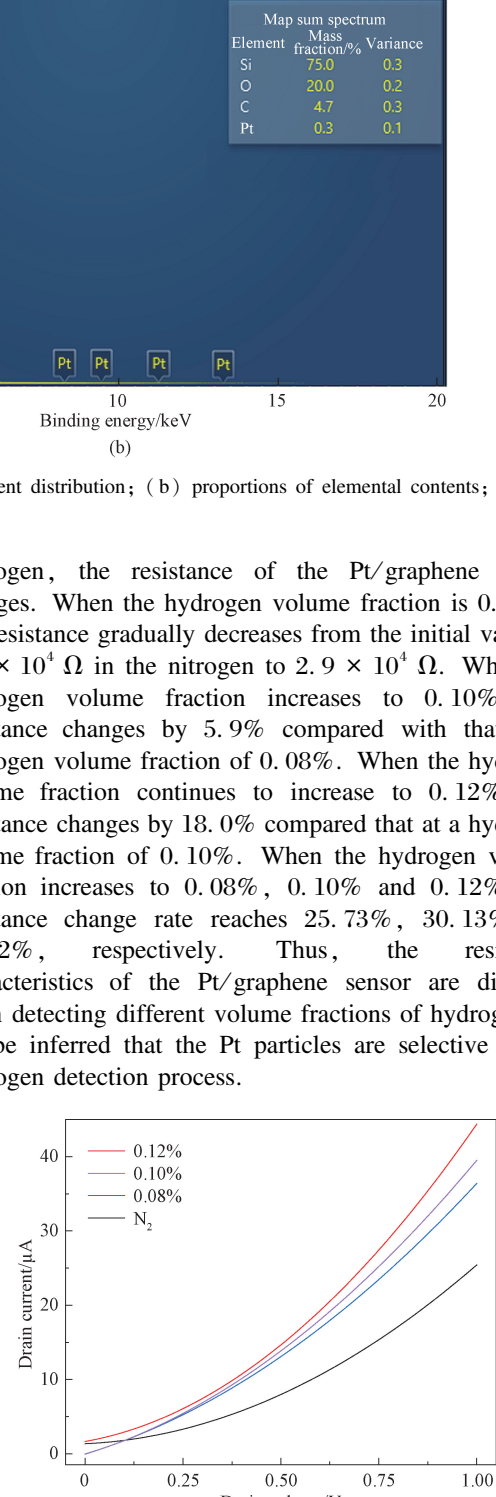


Fig. 6 I - V curves at different volume fractions of hydrogen

The resistance change rate is used to characterize the resistance response sensitivity of the sensor^[38]. It is an important parameter to describe the response rate and stability of the sensor, and can dynamically reflect the resistance change of the sensor. The resistance response curves of the graphene FET and Pt/graphene sensor at a hydrogen volume fraction of 1.00% were compared and tested under constant conditions. As shown in Fig. 7, the graphene FET has low response to hydrogen. The resistance response curve of the Pt/graphene sensor is more pronounced, and after the introduction of hydrogen, the response curve peaks and stabilizes in a short period of time. Due to the limited hydrogen adsorption capacity of Pt, the volume ratio of hydrogen adsorption capacity of Pt is about 60:1 to 70:1. After saturation, a small amount of Pt also adsorbs hydrogen, and the resistance response curve fluctuates, but it is basically stable at about 30%.

Phan et al.^[36] encapsulated the Pt/graphene sensor into a three-dimensional structure through the hydrothermal method. When the volume fraction of the hydrogen is 1.00%, the resistance change rate of the sensor is 15.1%. However, the measurement conditions of the sensing process require a high temperature of 200 °C, which limits the application of the sensor. The Pt/graphene sensor prepared in this study operates at room temperature during the entire experiment process, and has a high resistance change rate to different hydrogen volume fractions. This further confirms the high sensitivity of Pt to hydrogen. When the hydrogen input is turned off, the response curve decreases significantly. However, due to the long time it takes for Pt to desorb hydrogen, the

resistance response curve takes a long time to recover to 90% of the starting resistance. The results show that the Pt/graphene sensor is very sensitive to hydrogen.

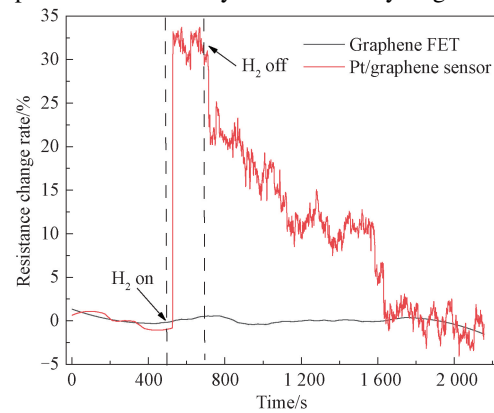


Fig. 7 Resistance response curves of graphene FET and Pt/graphene sensor at hydrogen volume fraction of 1.00%

The sensing characteristics at different hydrogen volume fractions of the Pt/graphene sensor and Pd/graphene sensor are compared as shown in Fig. 8. In Fig. 8(a), after hydrogen injection for 60 s, the resistance decreases significantly and begins to stabilize after reaching saturation with the peak resistance change rate of 20.97% and 33.35% at the hydrogen volume fraction of 0.80% and 1.00%, respectively. However, after reaching the peak, the resistance response curve fluctuates slightly, showing a certain degree of decline. After the hydrogen input is turned off, the resistance response curve decreases significantly, and the resistance begins to rise gradually and returns to the initial state.

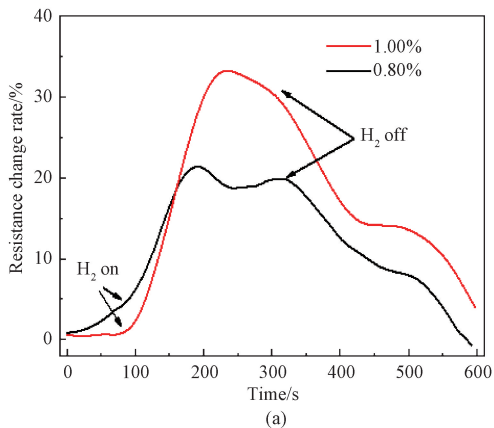


Fig. 8 Hydrogen resistance response curves: (a) Pt/graphene sensor; (b) Pd/graphene sensor

The Pd/graphene sensor was prepared using the same experimental method as that used in the previous preparation of the Pt/graphene sensor, and the same test method was used. The resistance response curve of the Pd/graphene sensor at a hydrogen volume fraction of 1.00% reaches the highest peak of 29.05% at about 600 s. The response time of the Pd/graphene sensor is higher than that of the Pt/graphene sensor.

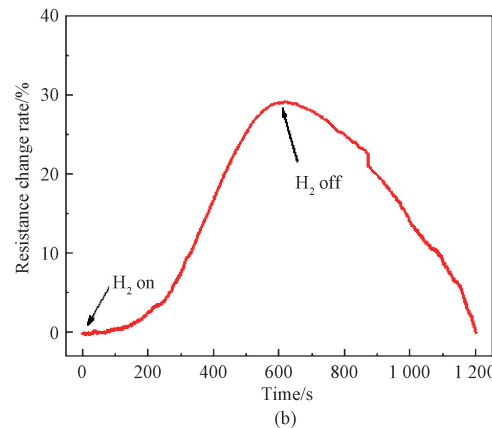
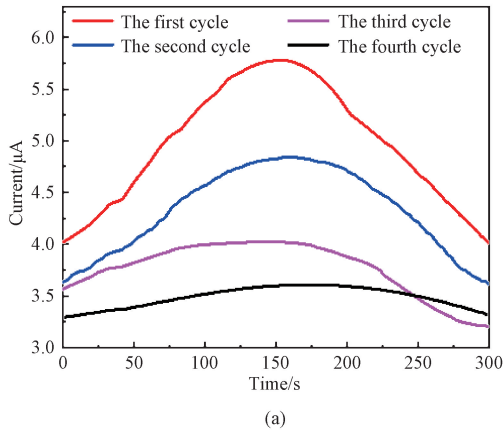


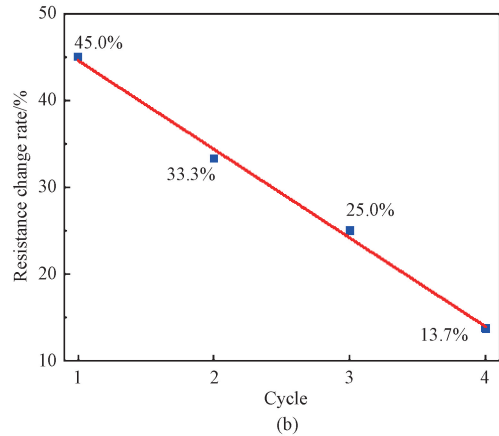
Figure 9 illustrates a comparative plot of the current response of the Pt/graphene sensor at a fixed hydrogen volume fraction of 1.00%. In the first cycle, there is a large change in the current with a pronounced drop in the resistance and a rapid rise in the current. After reaching the set time for testing the hydrogen input, the hydrogen input is turned off, and the current falls rapidly. At the fourth cycle, the fluctuation of the current gradually

stabilizes and is accompanied by a certain hysteresis phenomenon. In order to further verify the effectiveness of the continuity test with a fixed hydrogen volume fraction, the peak resistance response rates of the four



(a)

tests are compared, as shown in Fig. 9 (b). From the continuity test results, the Pt/graphene FET releases hydrogen at a relatively slow rate, which adversely affects the subsequent hydrogen detection.



(b)

Fig. 9 Hydrogen continuous response: (a) current; (b) resistance change rate

2.3 Hydrogen detection mechanism of Pt/graphene sensor

The hydrogen adsorption of the Pt/graphene sensor include physical adsorption and chemical adsorption. The formation of hydrides affects the structure, bonding and strength between atoms, influencing the change in the resistance of the Pt/graphene sensor. In physical adsorption, hydrogen attaches to the surface of the Pt particles, decomposes into hydrogen molecules or atoms,

and then interacts with the Pt particles through van der Waals forces. The chemical adsorption is a process in which dissociated hydrogen atoms bind to Pt particles via covalent bonds to form metal hydrides. The hydrogen sensor continuity test mechanism is shown in Fig. 10. During the cyclic hydrogen test, hydrogen atoms that are adsorbed on the Pt surface fail to desorb in time. Thus, as the number of tests increases, the resistance response rate shows a gradual downwards trend.

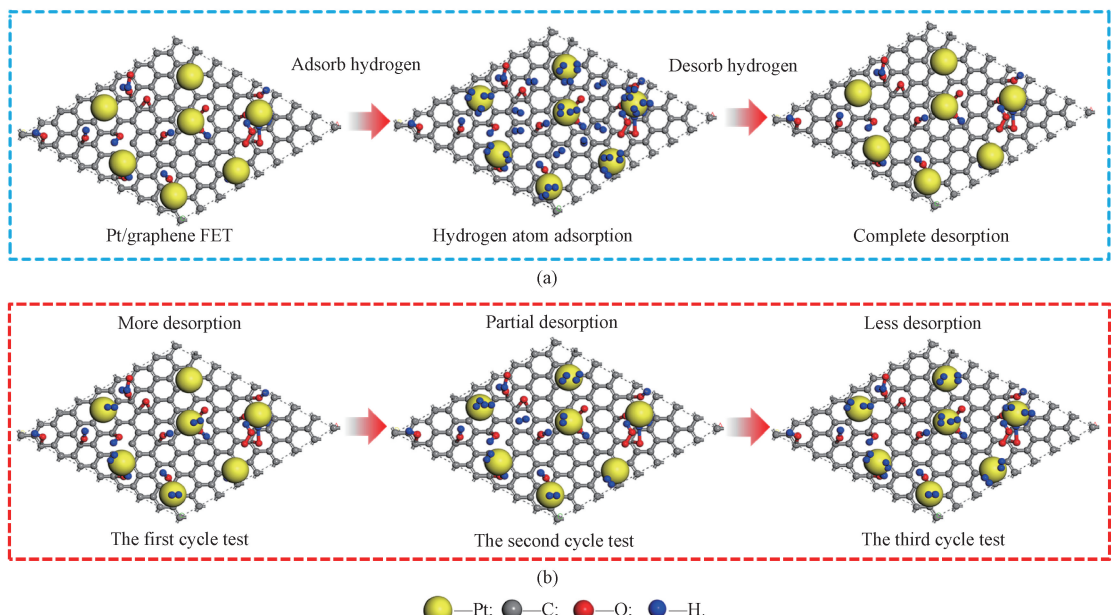
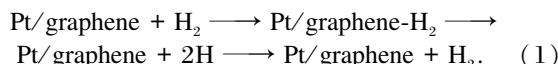


Fig. 10 Hydrogen sensor continuity test mechanism: (a) under ideal conditions with hydrogen being completely desorbed; (b) actual hydrogen atom desorption in different cycles

In the hydrogen adsorption process, hydrogen atoms are adsorbed on the Pt surface, and the Gibbs free energy of the adsorption reaction is positive, much higher than that of the desorption reaction. Hydrogen cannot be

bound to Pt in the form of a molecule on the Pt surface, and it is easy to dissociate into hydrogen atoms^[39]. The generation of Pt—H leads to a decrease of Pt and the migration of electrons from Pt—H to graphene. The rise

in the electron volume fraction enhances its conductivity and results in a decrease in the resistance of the hydrogen sensor. The overall can be described as



Most of the Pt—H produced by the reaction can be stabilized^[37]. Since Pt atoms form chemical bonds with hydrogen atoms, it takes a lot of energy to break these bonds. The desorption process is therefore relatively difficult and takes a long time. When saturation is reached, the time required for desorption exceeds the time required for hydrogen adsorption. Part of the Pt/graphene sensor surface is saturated in adsorption, and hysteresis in the sensor testing occurs in a confined environment with continuous hydrogen emission.

3 Conclusions

In this study, a Pt/graphene hydrogen detection sensor is successfully prepared by an optimized glue removing method by isopropanol. The conductivity of the optimized samples is also improved and the linearity of the I - V curve slope has increased by 4.95 times. The Pt/graphene sensor produced in this study has a high selectivity and sensitivity for hydrogen detection. The resistance characteristics are affected by the hydrogen volume fraction. The resistance response with Pt modification exhibits a higher sensitivity than that with Pd modification. The hydrogen chemical adsorption leads to a significant hysteresis during the continuity tests. Covalent Pt—H bonds make hydrogen desorption from the saturated surface slow and complex. This sensor shows a highly linearity of electrical properties. The findings would provide useful guidance for the rational design and further optimization of hydrogen sensors and promote its application in the aero-space industry.

References

- [1] SOHAIL AHMAD M, INOMATA Y, KIDA T. Energy application of graphene based membrane: hydrogen separation [J]. *The Chemical Record*, 2024, 24(1) : e202300163.
- [2] JABALLAH S, DAHMAN H, GHILOUFI I, et al. Facile synthesis of Al-Mg co-doped ZnO nanoparticles and their high hydrogen sensing performances [J]. *International Journal of Hydrogen Energy*, 2020, 45(58) : 34268-34280.
- [3] LI Z, YAO Z J, ALI HAIDRY A, et al. Resistive-type hydrogen gas sensor based on TiO₂: a review [J]. *International Journal of Hydrogen Energy*, 2018, 43(45) : 21114-21132.
- [4] MIRZAEI A, YOUSEFI H R, FALSAFI F, et al. An overview on how Pd on resistive-based nanomaterial gas sensors can enhance response toward hydrogen gas [J]. *International Journal of Hydrogen Energy*, 2019, 44 (36) : 20552-20571.
- [5] HÜBERT T, BOON-BRETT L, BLACK G, et al. Hydrogen sensors: a review [J]. *Sensors and Actuators B: Chemical*, 2011, 157(2) : 329-352.
- [6] LI X P, GU Z Y, CHO J, et al. Tin-copper mixed metal oxide nanowires: synthesis and sensor response to chemical vapors [J]. *Sensors and Actuators B: Chemical*, 2011, 158(1) : 199-207.
- [7] XIANG C L, ZOU Y J, QIU S J, et al. Nanocarbon-based materials for hydrogen sensor [J]. *Progress in Chemistry*, 2013, 25: 270. (in Chinese)
- [8] LIU W L, CHEN C H, HAI W Q, et al. Laser-induced graphene conductive fabric decorated with copper nanoparticles for electromagnetic interference shielding application [J]. *Journal of Donghua University (English Edition)*, 2023, 40 (6) : 571-579.
- [9] XIANG R F, CHEN X Y, LIU Y, et al. Porous graphene-based electrodes for fiber-shaped supercapacitors with good electrical conductivity [J]. *Journal of Donghua University (English Edition)*, 2023, 40(2) : 134-141.
- [10] ZHONG X J, LI W L, GAO X, et al. Preparation and output performance of triboelectric nanogenerator based on electrospun PVDF/GO composite nanofibers [J]. *Journal of Donghua University (Natural Science)*, 2024, 50(3) : 15-22. (in Chinese)
- [11] SCHEDIN F, GEIM A K, MOROZOV S V, et al. Detection of individual gas molecules adsorbed on graphene [J]. *Nature Materials*, 2007, 6: 652-655.
- [12] WOLLANDT T, MANGEL S, KUSSMANN J, et al. Charging and electric field effects on hydrogen molecules physisorbed on graphene [J]. *The Journal of Physical Chemistry C*, 2023, 127 (8) : 4326-4333.
- [13] FEDORENKO G, OLEKSENKO L, MAKSYMOVYCH N. Oxide nanomaterials based on SnO₂ for semiconductor hydrogen sensors [J]. *Advances in Materials Science and Engineering*, 2019, 2019: 5190235.
- [14] CHOO T F, SAIDIN N U, KOK K Y. Hydrogen sensing enhancement of zinc oxide nanorods via voltage biasing [J]. *Royal Society Open Science*, 2018, 5(5) : 172372.
- [15] DEL ORBE D V, YANG H, CHO I, et al. Low-power thermocatalytic hydrogen sensor based on electrodeposited cauliflower-like nanostructured Pt black [J]. *Sensors and Actuators B: Chemical*, 2021, 329: 129129.
- [16] TIAN J W, JIANG H C, ZHAO X H, et al. A Pb-level hydrogen sensor based on activated Pd

- nanoparticles loaded on oxidized nickel foam [J]. *Sensors and Actuators B: Chemical*, 2021, 329: 129194.
- [17] YANG Z H, DU X Q, YE X Q, et al. The free-standing nanoporous palladium for hydrogen isotope storage [J]. *Journal of Alloys and Compounds*, 2021, 854: 157062.
- [18] NUGROHO F A A, DARMADI I, CUSINATO L, et al. Metal-polymer hybrid nanomaterials for plasmonic ultrafast hydrogen detection [J]. *Nature Materials*, 2019, 18: 489-495.
- [19] ÖSTERGREN I, POURRAHIMI A M, DARMADI I, et al. Highly permeable fluorinated polymer nanocomposites for plasmonic hydrogen sensing [J]. *ACS Applied Materials & Interfaces*, 2021, 13(18): 21724-21732.
- [20] YE Z, LI Z, DAI J X, et al. Hydrogen sensing performance investigations with optical heating and sensing element surface modification [J]. *International Journal of Hydrogen Energy*, 2021, 46(1): 1411-1419.
- [21] DAS S, ROY S, BHATTACHARYA T S, et al. Efficient room temperature hydrogen gas sensor using ZnO nanoparticles-reduced graphene oxide nanohybrid [J]. *IEEE Sensors Journal*, 2021, 21(2): 1264-1272.
- [22] SEO M H, KANG K, YOO J Y, et al. Chemo-mechanically operating palladium-polymer nanograting film for a self-powered H₂ gas sensor [J]. *ACS Nano*, 2020, 14(12): 16813-16822.
- [23] PARK S, YANG J, LEE H M, et al. Effect of the position of amine groups on the CO₂, CH₄, and H₂ adsorption performance of graphene nanoflakes [J]. *Industrial & Engineering Chemistry Research*, 2023, 62(12): 5230-5240.
- [24] LIU X L, YANG X M, CUI J W, et al. Ni coated with N-doped graphene layer as active and stable H₂ evolution cocatalysts for photocatalytic overall water splitting [J]. *ACS Catalysis*, 2023, 13(21): 14314-14323.
- [25] JAISWAL J, DAS A, CHETRY V, et al. Vertically aligned porous V_xO_y nanofilms with Pt decoration for sub-ppm H₂ gas sensors [J]. *ACS Applied Nano Materials*, 2023, 6(4): 2646-2657.
- [26] KOO W T, CHO H J, KIM D H, et al. Chemiresistive hydrogen sensors: fundamentals, recent advances, and challenges [J]. *ACS Nano*, 2020, 14(11): 14284-14322.
- [27] YANG F, DONAVAN K C, KUNG S C, et al. The surface scattering-based detection of hydrogen in air using a platinum nanowire [J]. *Nano Letters*, 2012, 12(6): 2924-2930.
- [28] NOVOSELOV K S, GEIM A K, MOROZOV S V, et al. Two-dimensional gas of massless Dirac fermions in graphene [J]. *Nature*, 2005, 438: 197-200.
- [29] ZHANG Y B, TAN Y W, STORMER H L, et al. Experimental observation of the quantum Hall effect and Berry's phase in graphene [J]. *Nature*, 2005, 438: 201-204.
- [30] POTYRAILO R A, SURMAN C, NAGRAJ N, et al. Materials and transducers toward selective wireless gas sensing [J]. *Chemical Reviews*, 2011, 111(11): 7315-7354.
- [31] RUMYANTSEV S, LIU G X, SHUR M S, et al. Selective gas sensing with a single pristine graphene transistor [J]. *Nano Letters*, 2012, 12(5): 2294-2298.
- [32] SINGH A K, UDDIN M A, TOLSON J T, et al. Electrically tunable molecular doping of graphene [J]. *Applied Physics Letters*, 2013, 102(4): 043101.
- [33] RAD A S, PAZOKI H, MOHSENI S, et al. Surface study of platinum decorated graphene towards adsorption of NH₃ and CH₄ [J]. *Materials Chemistry and Physics*, 2016, 182: 32-38.
- [34] CHEN D C, ZHANG X X, TANG J, et al. Adsorption and dissociation mechanism of SO₂ and H₂S on Pt decorated graphene: a DFT-D3 study [J]. *Applied Physics A*, 2018, 124(6): 404.
- [35] HARLEY-TROCHIMCZYK A, CHANG J Y, ZHOU Q, et al. Catalytic hydrogen sensing using microheated platinum nanoparticle-loaded graphene aerogel [J]. *Sensors and Actuators B: Chemical*, 2015, 206: 399-406.
- [36] PHAN D T, UDDIN A S M I, CHUNG G S. A large detectable-range, high-response and fast-response resistivity hydrogen sensor based on Pt/Pd core-shell hybrid with graphene [J]. *Sensors and Actuators B: Chemical*, 2015, 220: 962-967.
- [37] WANG L L, LI W, CAI Y, et al. Characterization of Pt- or Pd-doped graphene based on density functional theory for H₂ gas sensor [J]. *Materials Research Express*, 2019, 6(9): 095603.
- [38] LI H Y, WANG H L, WEI F Y, et al. Research progress of flexible wearable humidity sensors [J]. *Technical Textiles*, 2023, 41(9): 1-12. (in Chinese)
- [39] HU S, TANG L J, ZHU Z H, et al. Dissociative adsorption study of hydrogen isotopes on metal platinum surface by thermodynamic computation [J]. *Journal of Atomic and Molecular Physics*, 2008, 25(2): 287-292. (in Chinese)

基于 Pt/石墨烯复合材料气体传感器的氢传感特性

侯天浩，彭倚天，丁树杨*

东华大学 机械工程学院，上海 201620

摘要：石墨烯具有卓越的电学、光学和热学特性，可用于制备更薄、更轻和响应更快的传感器。该文在 SiO_2/Si 衬底上使用机械剥离方法制备石墨烯，并通过光刻法制备石墨烯场效应晶体管；通过水合肼还原法对石墨烯表面进行 Pt 颗粒修饰，以赋予 Pt/石墨烯传感器气敏特性；通过气体检测平台可获得不同氢气环境下的电学曲线和电阻响应曲线的特性。研究结果表明，Pt/石墨烯气体传感器在室温下对氢气表现出较高的灵敏度，在氢气体积分数为 1.00% 时，电阻响应率高达 33.35%。然而在灵敏度寿命测试中发现，解吸过程存在本质滞后现象，这使得连续测试的电阻响应率出现明显下降。该文提供了一种基于石墨烯的气体传感器的改进制备方法，该方法将在航空航天中具有广泛的潜在应用。

关键词：石墨烯；Pt 颗粒；氢传感器；化学吸附

MLGIA: Recognition of Traffic Panel Information Based on PaddlePaddle

JI Yukai, GE Huayong*, MENG Yaqun, LI Sisi

College of Information Science and Technology, Donghua University, Shanghai 201620, China

Abstract: To address the challenge of recognizing small target information on traffic panels, a model named MLGIA is proposed based on PaddlePaddle. MLGIA is composed of MobilenetV3 with lightweight GhostBlock (LGB) and an improved augmented feature pyramid network (IAFPN). In this model, LGB improves MobilenetV3 by optimizing the convolutional structure and employing linear transformations to extract sufficient feature maps; IAFPN enhances feature representation through pruning techniques and channel-reduction convolutions. Additionally, knowledge distillation compresses the model and improves its accuracy, while the match category information (MCI) method further optimizes the processing of the detected category information. Experimental results demonstrate that MLGIA outperforms MobilenetV3. MLGIA achieves a detection accuracy comparable to YOLOv8n, with significantly lower resource consumption. Therefore, MLGIA is a strong complement in the traffic panel information recognition domain.

Keywords: convolutional neural network; object detection; feature fusion; knowledge distillation; lightweight

CLC number: TP183

Document code: A

Article ID: 1672-5220(2025)05-0494-09

Open Science Identity
(OSID)



0 Introduction

With the rapid development of the intelligent new energy vehicle industry, autonomous driving has seen widespread commercial applications. Lidar and infrared sensors can effectively capture information about spatial positions and reference objects^[1-2]. However, these sensors have significant limitations in obtaining visual information, such as road lane markings and traffic signs. As a result, there is growing interest in extracting traffic information from RGB (a standard color encoding method that uses varying intensities of red, green and blue light to represent a wide array of colors) images.

Thanks to advancements in deep learning, many algorithmic frameworks have been proposed for traffic sign detection^[3-5], achieving increasingly high accuracy. These methods primarily focus on simple traffic signs but

lack recognition of traffic panels. The complex signs on traffic panels contain both textual and road topology information. The target regions in traffic panels are also small, making the above methods unsuitable for traffic panel recognition. The text recognition framework of traffic signs proposed by Dinesh et al.^[6] is an excellent inspiration for us to improve the recognition of traffic panels. SignParser proposed by Guo et al.^[7] identifies road topology and the connections between regions of interest within panels. An improved YOLOv5 proposed by Khalid et al.^[8] achieves impressive accuracy in panel detection under adverse weather conditions. However, recognizing traffic panels requires vehicle deployment, which demands a highly lightweight model.

Therefore, we introduce an object detection model named MLGIA under the PaddlePaddle framework. The model employs a backbone network named MobilenetV3_LGB, which is built upon MobilenetV3^[9] with an added lightweight GhostBlock (LGB). An improved augmented feature pyramid network (IAFPN) is further introduced to enhance its feature fusion capabilities. Knowledge distillation^[10] is employed to improve the accuracy of the lightweight model, and the match category information (MCI) method is used to process the obtained information. Through these innovations, we aim to comprehensively detect various information on traffic panels with high accuracy while reducing model computational complexity and parameters, enhancing lightweight performance, and providing necessary support for developing intelligent transportation systems.

1 Methods

We refer to the modified network as MobileNetV3_LGB. It is divided into five feature layers with different receptive fields, as shown in Fig. 1. The first layer is a depthwise separable convolution (DW conv). The second and third layers use Mobileblock, while the fourth and fifth layers employ LGB. In this section, we focus on explaining the principles and implementation details of the algorithm, including the implementation of MobilenetV3_LGB for feature extraction, the fusion of feature information by using IAFPN, the parameter

Received date: 2024-09-08

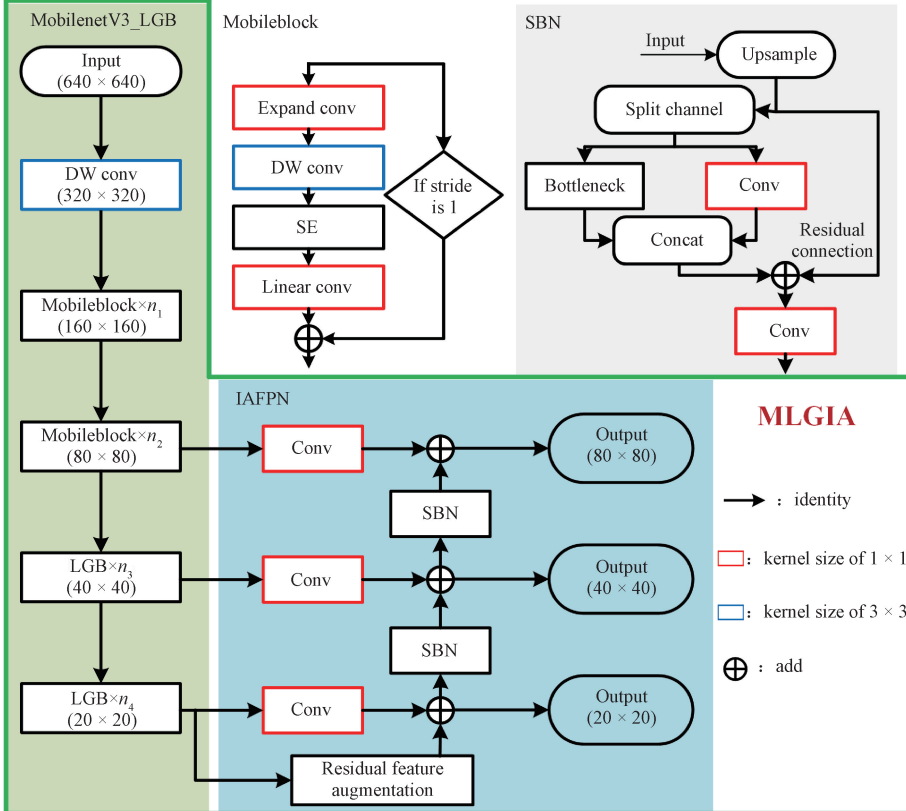
Foundation item: National Natural Science Foundation of China (No. 62372100)

* Correspondence should be addressed to GE Huayong, email: gehuayong@dhu.edu.cn

Citation: JI Y K, GE H Y, MENG Y Q, et al. MLGIA: recognition of traffic panel information based on PaddlePaddle[J]. *Journal of Donghua University (English Edition)*, 2025, 42(5): 494-502.

design and knowledge distillation training of MLGIA, and the use of MCI to obtain traffic panel information after achieving object detection. The complete MLGIA network with the detailed structural information primarily

consists of Mobilenet_LGB and IAFPN, highlighted in Fig. 1 with the green box. Mobileblock and squeeze-and-bottleneck (SBN) are the essential modules within the model.



n_i ($i=1, 2, \dots, 4$)—the number of repetitions of each module, corresponding to the model's parameter design;

conv—convolution; concat—concatenation; SE—squeeze-and-excitation.

Fig. 1 Framework of MLGIA network structure

1.1 MobilenetV3_LGB feature extraction network

1.1.1 Lightweight improved GhostConv^[11] (Gconv)

Gconv begins by using a convolution operation to obtain feature maps for some channels. Then, a linear transformation is applied to these feature maps to generate the remaining channels. Finally, two sets of feature maps are concatenated to complete the convolution. This structure extracts semantic information from similar feature maps and enhances feature extraction capability.

For mobile devices, a lightweight design is a crucial criterion for convolutional neural networks. To further reduce the network's computational load and improve feature extraction efficiency, we improved the activation function used in Gconv. The original Gconv utilizes the SiLU^[12] function, defined as

$$F_{\text{SiLU}}(x) = x \cdot \sigma(x), \quad (1)$$

where x is the input; $\sigma(x) = (1 + e^{-x})^{-1}$. However, the SiLU function has a relatively high computational cost and is unsuitable for resource-constrained scenarios. Inspired by the H-swish activation function of MobilenetV3^[9], Gconv is expressed as

$$F_G(x) = \frac{1}{6}x \cdot \min(\max(0, x + 3), 6). \quad (2)$$

We define an adaptive H-swish linear unit (AL_HSLU) as

$$F_A(x) = \frac{1}{6}x \cdot \max\left(0, \min\left(0, -\frac{2x}{\lg R_L} + 3\right), 6\right), \quad (3)$$

where R_L is the learning rate of the network, which adjusts with the number of training epochs. The definition and gradient of AL_HSLU are shown in Fig. 2.

This activation function has a simple form and low computational cost, and is suitable for lightweight models, offering a high computational efficiency and a high training speed. During the early stages of training, when network parameters are relatively random, a higher learning rate increases the derivative of the activation function at zero, thereby accelerating the activation speed and network convergence. In contrast, when the network gradually converges during the later stages of training, a lower learning rate allows for more precise extraction of high-level semantic information, helping the model improve the accuracy.

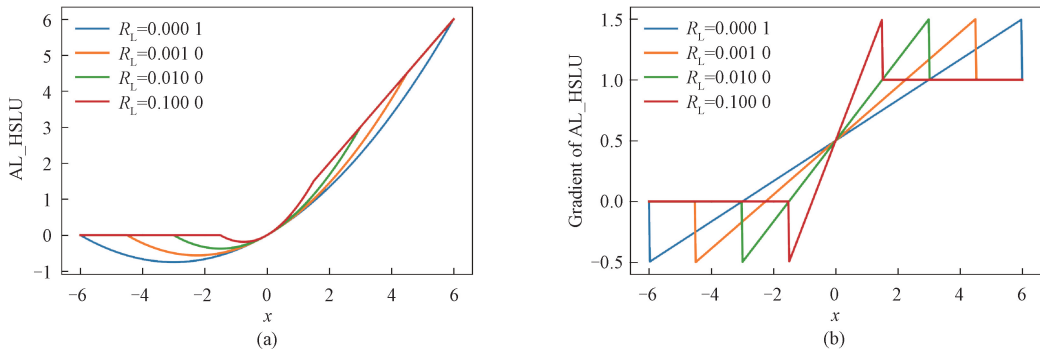


Fig. 2 Functions of AL_HSLU: (a) definition; (b) gradient

1.1.2 LGB enhancement of MobilenetV3

LGB is implemented by using the lightweight ghost convolution (LG conv), which enhances the complexity

of the features, as shown in Fig. 3. LG conv is implemented by using AL_HSLU.

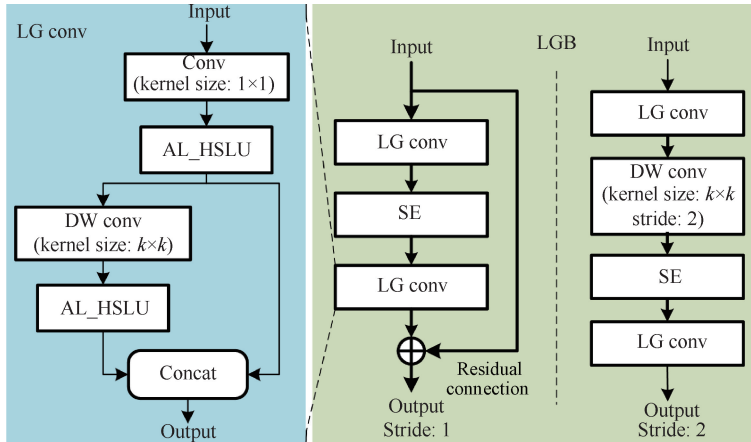


Fig. 3 Framework of LGB and LGconv

When the stride is 1, we construct the LGB with two LG conv separated by an SE^[13] block and a residual connection. When the stride is 2, LGB adds a DW conv after the first LG conv to achieve downsampling. We use LGB only in the deeper layers because the number of channels is relatively small in the shallow layers of a convolutional network, and the feature maps are relatively simple. In such cases, LGB generates feature maps that do not change significantly, which prevents the extraction of sufficient feature information. In the deeper layers of the network, where more semantic information is present, LGB can capture more complex features, and its linear transformations can also reduce computational costs.

1.2 IAFPN feature fusion network

The IAFPN feature fusion network enhances feature fusion by introducing a residual connection to adjust and improve AugFPN^[14]. AugFPN faces issues such as compressing features during layer fusion, which can result in insufficient and incomplete high-level semantic information. We improved the structure, parameters and layer connections to develop IAFPN.

1.2.1 Channel adjustment and layer selection

AugFPN reduces the number of channels in deeper layers to match the shallower layers when fusing features,

which lowers feature complexity and impacts network performance. To address this, we increased the output channels in the deeper layers to match the input channels. This adjustment enhances the network's non-linear transformation capability, ensuring effective feature extraction and increasing feature diversity.

AugFPN utilizes feature maps with downsampling factors of 4, 8, 16 and 32. To ensure adequate information transfer from deeper to shallower layers and achieve multi-scale fusion during training, we only used downsampling factors of 8, 16 and 32 in IAFPN. The feature maps with downsampling factor of 4 cannot sufficiently learn complex data patterns and features, so removing this layer helps reduce network loss.

1.2.2 Enhanced feature fusion

Inspired by bottleneck^[15], we improve feature fusion by incorporating SBN. The bottleneck structure first reduces the input channel number to a lower dimension by using a 1×1 convolution, then captures spatial features with a 3×3 convolution, and finally expands the channel number again with another 1×1 convolution, followed by a residual connection for output. We commonly use this approach to enhance network performance and efficiency.

The SBN structure, as shown in Fig. 1, divides the input feature map into two parts by channels. One part uses the bottleneck layer, and the other uses a 1×1 convolution layer. After concatenation and residual connection, the final convolution completes the feature fusion of each layer. The cross-connection between the bottleneck layer and the 1×1 convolution layer reduces the computational load and facilitates information transfer and sharing between different features. The final convolution introduces non-linear transformations, enhancing the feature fusion performance. This design not only reduces network parameters and computational

loads but also improves the feature extraction efficiency and addresses issues such as gradient vanishing and exploding during the training of deep neural networks.

1.3 MLGIA parameter design and knowledge distillation

Since traffic panel recognition is deployed on vehicles, the application scenario imposes specific requirements for lightweight models with strict cost constraints for deployment. To address this challenge, inspired by MobilenetV3^[9], we designed two networks, namely MobilenetV3_LGB_large and MobilenetV3_LGB_small, as shown in Table 1.

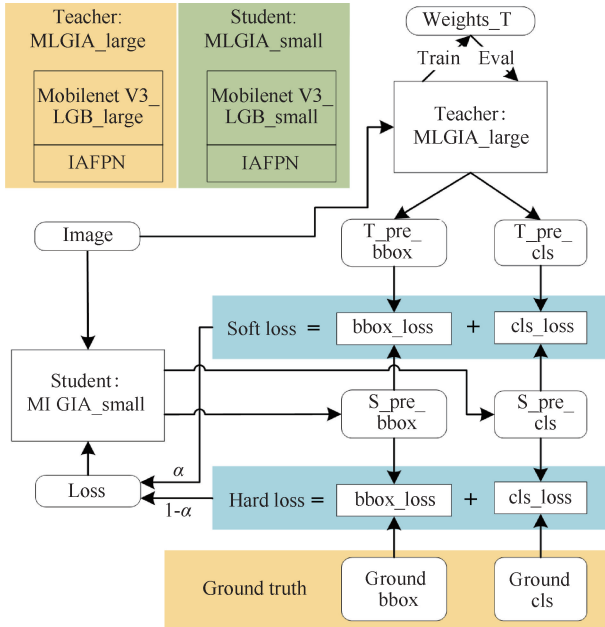
Table 1 Network parameters for MLGIA

Network	Block	Kernel	Number of expansion channels	Number of out channels	SE	Activation	Stride
MobilenetV3_LGB_large	DW conv	3	–	16	0	ReLU	2
	Mobileblock	3	16	16	0	ReLU	1
	Mobileblock	3	64	24	0	ReLU	2
	Mobileblock	3	72	24	0	ReLU	1
	Mobileblock	5	72	40	1	ReLU	2
	Mobileblock	5	120	40	1	ReLU	1
	Mobileblock	5	120	40	1	ReLU	1
	LGB	3	240	80	0	AL_HSLU	2
	LGB	3	200	80	0	AL_HSLU	1
	LGB	3	184	80	0	AL_HSLU	1
	LGB	3	184	80	0	AL_HSLU	1
	LGB	3	480	112	1	AL_HSLU	1
	LGB	3	672	112	1	AL_HSLU	1
	LGB	5	672	160	1	AL_HSLU	2
	LGB	5	960	160	1	AL_HSLU	1
	LGB	5	960	160	1	AL_HSLU	1
MobilenetV3_LGB_small	DW conv	3	–	16	0	ReLU	2
	Mobileblock	3	16	16	1	ReLU	2
	Mobileblock	3	72	24	0	ReLU	2
	Mobileblock	3	88	24	0	ReLU	1
	LGB	5	96	40	1	AL_HSLU	2
	LGB	5	240	40	1	AL_HSLU	1
	LGB	5	240	40	1	AL_HSLU	1
	LGB	5	120	48	1	AL_HSLU	1
	LGB	5	144	48	1	AL_HSLU	1
	LGB	5	288	96	1	AL_HSLU	2
	LGB	5	576	96	1	AL_HSLU	1
	LGB	5	576	96	1	AL_HSLU	1

We combined MobilenetV3_LGB_large with IAFPN to create MLGIA_large as the teacher model and combined MobilenetV3_LGB_small with IAFPN to create MLGIA_small as the student model for knowledge distillation training, as shown in Fig. 4. We first trained the teacher model to obtain the weight file Weights_T, then switched it to an evaluation mode

to provide soft labels to the student model. During training, the student model learned not only from the true labels but also from the soft labels provided by the teacher model. We calculated the loss by merging soft loss and hard loss at a ratio of $\alpha/(1 - \alpha)$, which helped the student model capture comprehensive feature information and significantly improved the model's

performance. The MLGIA_small model, trained in this way, maintains high performance while achieving model compression and acceleration, facilitating lightweight deployment.



bbox—bounding box; cls—classification; $S_{\text{pre_bbox}}$ —bounding box predicted by student model; $T_{\text{pre_bbox}}$ —bounding box predicted by teacher model; $S_{\text{pre_cls}}$ —classification probabilities predicted by student model; $T_{\text{pre_cls}}$ —classification probabilities predicted by teacher model.

Fig. 4 Framework of knowledge distillation

1.4 MCI

The MCI algorithm links the various regions of information obtained from the object detection system to derive the final traffic panel information. The MCI algorithm involves three main components: text information extraction, road information extraction and panel information matching. We used the text recognition module from PaddleOCR^[16] to achieve accurate text extraction.

An improved thinning method is utilized in the road information extraction algorithm to extract information about road intersections. Traditional thinning algorithms rely on small rectangular boxes for judgments, which can lead to biases in global information assessment. Since intersections are composed of geometric shapes, and the Hough transform^[17] can effectively capture geometric information, we improved the thinning algorithm using the Hough transform, as detailed in Algorithm 1. This improvement enhances the utilization of global information, enabling effective road information extraction.

The panel information matching algorithm determines the final traffic panel information based on the regions' coordinates and area information. In Algorithm 1, the data obtained from the road information extraction is used and combined with the positional information and

words of the text regions. Each text box is matched with the corresponding road intersection to link the traffic panel information and achieve traffic panel recognition.

Algorithm 1 Road information extraction

Input:

Img : road region image

$thresh$: threshold to determine lines and circles

Output:

$roadout$: road information

Begin:

1. Convert Img to a grayscale image G_Img .
2. Apply a circular filter to G_Img to remove edge noise; apply erosion and dilation to remove salt-and-pepper noise. The resulting image is D_Img .
3. Convert D_Img to a binary image B_Img .
4. Thin B_Img results in T_Img . Calculate image width W , height H , diagonal length R , and maximum angle Θ .
5. For (x, y) in (W, H) :

For (ρ, θ) in (R, Θ) :

Compute $nums$: the number of points at each length ρ and angle θ .

6. If $nums > thresh$: filter out lines or circles, integrate similar data and compute the intersection points of road endpoints. Return $roadout$.

End.

2 Experiments

Starting with the experimental environment configuration, the operating system used in this paper is Ubuntu 18.04, with an Intel® Xeon® Gold 6330 CPU, NVIDIA GeForce RTX 3090 24 G GPU, and CUDA and CuDNN versions of 11.2 and 8.4.1, respectively. The deep learning framework used is PaddlePaddle 2.5.1.

The evaluation metrics used in this study include computational complexity, number of parameters (Params), mAP_{50} , and $mAP @ [.5 : .95]$. The computational complexity of the model is measured in giga floating-point operations per second (GFLOPS). Params represents the model's storage and memory requirements. mAP_{50} indicates the mean average precision (mAP) at an intersection over the union (IoU) threshold of 50%, assessing the detection accuracy at a fixed threshold. $mAP @ [.5 : .95]$ represents the average of the mAP values across multiple IoU thresholds (from 0.50 to 0.95 with a step size of 0.05), providing a more comprehensive evaluation of the model's detection performance. These metrics reflect the model's efficiency and effectiveness.

The dataset used in this experiment is supported by the National Natural Science Foundation of China (NSFC) and is the Traffic Panel Database (TPD) from China. The TPD includes 1 525 traffic images with

13 657 labels covering various traffic panels. These images are collected under different conditions, such as varying weather, lighting, and other environments. We categorized and annotated the images from the TPD dataset into nine categories based on road intersections, text, and directional information: text region, road sign, forward north, forward south, forward east, forward west, forward, left turn, and right turn.

The hyperparameters for the experiment were set as follows to achieve better training results. The model input size was 640×640 pixels, with an initial learning rate of 0.010. The Adam optimizer was used to adjust the model parameters. Due to the limited dataset, the model was pre-trained for 150 epochs on the COCO dataset^[18],

achieving a mAP@ [.5 : .95] of 34.2%. Subsequently, the TPD dataset was split into training, validation, and test sets at 8:1:1, and the model was trained for 300 epochs.

3 Results and Analyses

The effectiveness of the proposed improvements to the MobilenetV3 network was validated through a series of ablation experiments. These experiments evaluated the improvements of LGB, IAFPN, and knowledge distillation based on MobilenetV3 _ large and MobilenetV3 _ small networks. The results were then compared with the proposed MLGIA network, as presented in Table 2.

Table 2 Ablation experiment results

Network	Computational complexity/GFLOPS	Params/ 10^6	mAP ₅₀ /%	mAP@ [.5 : .95]/%
MobilenetV3_large	1.89	2.85	89.1	52.5
MobilenetV3_large+LGB	1.59	2.43	93.3	55.8
MobilenetV3_large+IAFPN	2.14	3.08	97.2	59.7
MobilenetV3_large+LGB+IAFPN	1.74	2.66	98.9	62.1
MobilenetV3_small	0.49	0.88	76.8	43.2
MobilenetV3_small+LGB	0.42	0.73	83.4	47.6
MobilenetV3_small+IAFPN	0.53	0.96	88.2	52.2
MobilenetV3_small+LGB+IAFPN	0.47	0.81	92.8	55.6
MobilenetV3_small+LGB+IAFPN+KD	0.47	0.81	96.4	59.3

Notes: MobilenetV3 _ small + LGB + IAFPN and MobilenetV3 _ large + LGB + IAFPN denote large and small models of MLGIA, respectively; MobilenetV3 _ small+LGB+IAFPN+KD represents MLGIA _ small model trained by knowledge distillation from MLGIA _ large as teacher model.

The results show that the unmodified MobilenetV3 performs poorly. Adding LGB reduces both computational complexity and parameter count and improves detection accuracy, demonstrating that LGB supports lightweight model implementation. Although IAFPN increases the computational complexity, it significantly improves detection accuracy. This is due to the efficient feature extraction by the bottleneck layers and enhanced feature representation enabled by the residual connections. Finally, knowledge distillation yielded absolute improvements of 3.6% (from 92.8% to 96.4%) in mAP₅₀ and 3.7% (from 55.6% to 59.3%) in mAP@ [.5 : .95] for the small model.

The optimized models from the above training were compared with high-performance object detection networks. The experimental results are shown in Table 3. MLGIA _ large demonstrates significantly higher mAP₅₀ and mAP@ [.5 : .95] compared to MobilenetV3 and GhostNet networks. Among other high-performing networks, MLGIA performs slightly worse than PPYOLOE + _ s in detection accuracy but outperforms YOLOv5n. MLGIA _ small _ KD shows slightly lower detection accuracy than YOLOv8n. However, our network vastly outperforms other networks in terms of lightweight design. Thus, MLGIA _ small _ KD is an excellent lightweight network for traffic panel object detection.

Table 3 Comparative experiment results

Network	Computational complexity/GFLOPS	Params/ 10^6	mAP ₅₀ /%	mAP@ [.5 : .95]/%
MobilenetV3_large	1.89	2.85	89.1	52.5
MobilenetV3_small	0.49	0.88	76.8	43.2
GhostNet	5.54	4.26	92.0	57.4
YOLOv5n	2.11	1.79	95.0	54.2
YOLOv8n	4.07	3.01	98.4	62.3
PPYOLOE+_s ^[19]	8.17	7.68	99.1	65.8
MLGIA_large	1.74	2.66	98.9	62.1
MLGIA_small_KD	0.47	0.81	96.4	59.3

Notes: MLGIA _ large is an abbreviation for MobilenetV3 _ large+LGB+IAFPN; MLGIA _ small _ KD is an abbreviation for MobilenetV3 _ large+LGB+IAFPN+KD.

The MLGIA_small_KD model detects objects on traffic panel images from various environments to validate visualizations of experimental results, as shown in Fig. 5. In Fig. 5, TR refers to the text region, and RS refers to the road sign. The numbers following them denote the corresponding confidence scores. It demonstrates that MLGIA performs well in daylight environments. However, dark and rain-fog conditions require higher image quality due to the impact of underexposure and water droplet obstructions.

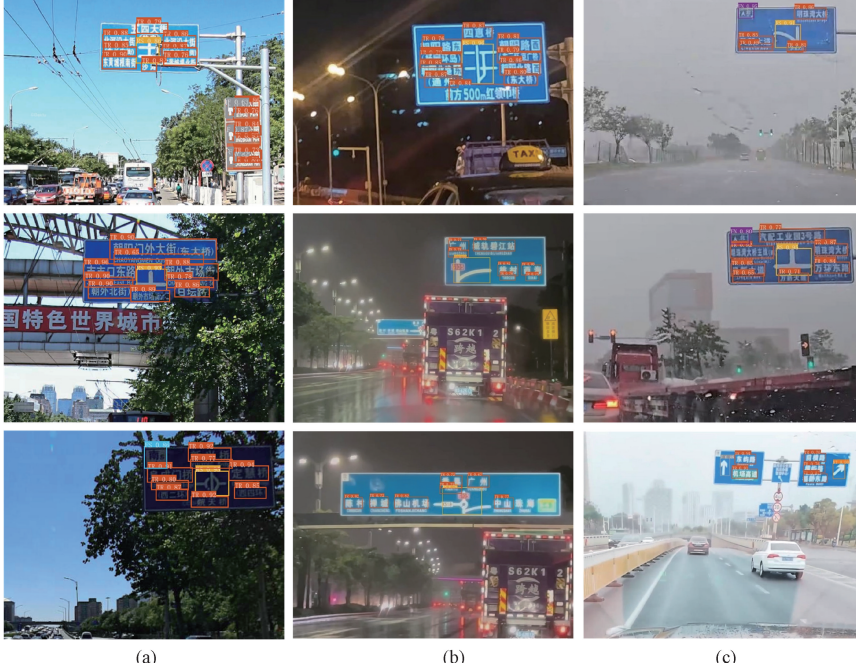


Fig. 5 Visualization of object detection by MLGIA_small_KD model in different environments: (a) daylight; (b) dark; (c) rain-fog

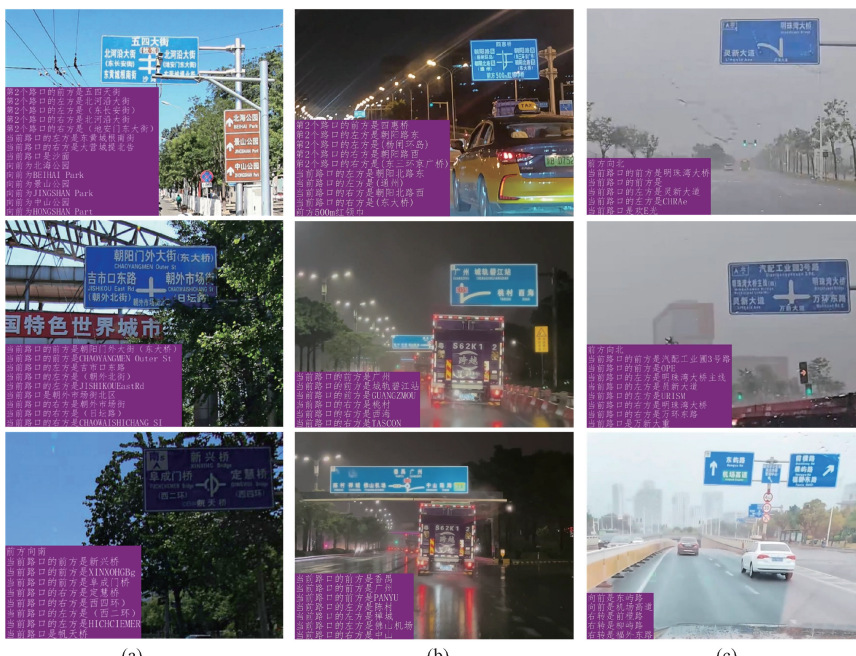


Fig. 6 Visualization of traffic panel information recognition by MLGIA with MCI method in different environments: (a) daylight; (b) dark; (c) rain-fog

After completing object detection, the MCI method was used to recognize traffic panel information and obtain complete information. The results in Fig. 6 indicate that with the MCI method, MLGIA performs well in extracting traffic panel information, thereby providing reliable data for vehicle navigation. However, MLGIA's performance in text recognition remains limited under occlusions, primarily due to its inability to leverage contextual cues (e.g., word association) to infer adjacent text.

4 Conclusions

The recognition of traffic panel information has significant practical value. This paper proposes MLGIA, a model specifically designed for detecting small targets in traffic panels, based on the PaddlePaddle framework. MLGIA improves the backbone feature extraction and neck feature fusion components, and utilizes the MCI method to achieve comprehensive traffic panel information recognition. The algorithm makes the network more lightweight and improves the extraction of the directional and road layout information, thereby refining the panel information extraction capabilities. Experimental comparisons show that MLGIA achieves high average detection accuracy. Overall, MLGIA exhibits more robust performance, more effective information extraction, and a more straightforward structure. Future work will focus on enhancing MLGIA's contextual reasoning capabilities to overcome its current limitations in handling occlusions.

References

- [1] LI Y, IBANEZ-GUZMAN J. Lidar for autonomous driving: the principles, challenges, and trends for automotive lidar and perception systems [J]. *IEEE Signal Processing Magazine*, 2020, 37(4) : 50-61.
- [2] DAI X R, YUAN X, WEI X Y. TIRNet: object detection in thermal infrared images for autonomous driving [J]. *Applied Intelligence*, 2021, 51(3) : 1244-1261.
- [3] TABASSUM A, VAIDEH K. Traffic sign recognition for an intelligent vehicle: a review [J]. *Turkish Online Journal of Qualitative Inquiry*, 2021, 12(6) : 6209-6215.
- [4] TIAN Y, GELERNTER J, WANG X, et al. Traffic sign detection using a multi-scale recurrent attention network [J]. *IEEE Transactions on Intelligent Transportation Systems*, 2019, 20 (12) : 4466-4475.
- [5] HAQUE W A, AREFIN S, SHIHAVUDDIN A S M, et al. DeepThin: a novel lightweight CNN architecture for traffic sign recognition without GPU requirements [J]. *Expert Systems with Applications*, 2021, 168: 114481.
- [6] DINESH N, MATHI S. Optical character recognition-based signboard detection [C]// Disruptive Technologies for Big Data and Cloud Applications. Singapore: Springer Nature Singapore, 2022: 447-455.
- [7] GUO Y F, FENG W, YIN F, et al. SignParser: an end-to-end framework for traffic sign understanding [J]. *International Journal of Computer Vision*, 2024, 132(3) : 805-821.
- [8] KHALID S, SHAH J H, SHARIF M, et al. A robust intelligent system for text-based traffic signs detection and recognition in challenging weather conditions [J]. *IEEE Access*, 2024, 12: 78261-78274.
- [9] HOWARD A, SANDLER M, CHEN B, et al. Searching for MobileNetV3 [C]//2019 IEEE/CVF International Conference on Computer Vision (ICCV). New York: IEEE, 2019: 1314-1324.
- [10] HINTON G, VINYALS O, DEAN J. Distilling the knowledge in a neural network [EB/OL]. (2015-3-9) [2024-08-16]. <https://arxiv.org/abs/1503.02531>.
- [11] HAN K, WANG Y H, TIAN Q, et al. GhostNet: more features from cheap operations [C]//2020 IEEE/CVF Conference on Computer Vision and Pattern Recognition (CVPR). New York: IEEE, 2020: 1577-1586.
- [12] ELFWING S, UCHIBE E, DOYA K. Sigmoid-weighted linear units for neural network function approximation in reinforcement learning [J]. *Neural Networks*, 2018, 107: 3-11.
- [13] HU J, SHEN L, ALBANIE S, et al. Squeeze-and-excitation networks [J]. *IEEE Transactions on Pattern Analysis and Machine Intelligence*, 2020, 42(8) : 2011-2023.
- [14] GUO C X, FAN B, ZHANG Q, et al. AugFPN: improving multi-scale feature learning for object detection [C]//2020 IEEE/CVF Conference on Computer Vision and Pattern Recognition (CVPR). New York: IEEE, 2020: 12592-12601.
- [15] HE K M, ZHANG X Y, REN S Q, et al. Deep residual learning for image recognition [C]// 2016 IEEE Conference on Computer Vision and Pattern Recognition (CVPR). New York: IEEE, 2016: 770-778.
- [16] DU Y N, LI C X, GUO R Y, et al. PP-OCR: a practical ultra lightweight OCR system [EB/OL]. (2020-10-15) [2024-08-16]. <https://arxiv.org/abs/2009.09941>.
- [17] BALLARD D H. Generalizing the Hough transform to detect arbitrary shapes [J]. *Pattern Recognition*, 1981, 13(2) : 111-122.
- [18] LIN T Y, MAIRE M, BELONGIE S, et al. Microsoft COCO: common objects in context [C]//Computer Vision-ECCV 2014. Cham: Springer International Publishing, 2014: 740-755.
- [19] XU S L, WANG X X, LV W Y, et al. PP-YOLOE: an evolved version of YOLO [EB/OL]. (2022-12-12) [2024-08-16]. <https://arxiv.org/abs/2203.16250>.

MLGIA：基于 PaddlePaddle 的交通面板信息识别

吉宇凯，葛华勇^{*}，孟亚群，李思思

东华大学 信息科学与技术学院，上海 201620

摘要：为应对交通标志牌小目标信息识别的挑战，基于 PaddlePaddle 框架提出了 MLGIA 模型。MLGIA 由轻量级 GhostBlock (lightweight GhostBlock, LGB) 改进的 MobilenetV3 与增强型特征金字塔网络 (improved augmented feature pyramid network, IAFPN) 构建。在该模型中，LGB 通过优化卷积结构并结合线性变换以充分提取特征图，从而实现对 MobilenetV3 的改进；IAFPN 通过剪枝与通道缩减卷积技术增强了对图形特征的表达。此外，知识蒸馏技术被运用于实现模型压缩和精度提升；信息类别匹配 (match category information, MCI) 方法进一步优化检测到的类别信息的处理流程。实验结果表明，MLGIA 性能优于 MobilenetV3，其检测精度与 YOLOv8n 相当，资源消耗更少。因此，MLGIA 模型是对交通标志牌信息识别领域的一个重要补充。

关键词：卷积神经网络；目标检测；特征融合；知识蒸馏；轻量级

DOI: 10.19884/j.1672-5220.202411003

Security Defenses for Cross-Technology Communication in IoT Control System

LI Tianyun, ZHANG Anqi, ZHANG Guanglin*

College of Information Science and Technology, Donghua University, Shanghai 201620, China

Abstract: To solve security problems in cross-technology communication (CTC), we take the Internet of Things (IoT) control system as an example, and propose a comprehensive solution against the attack on the physical layer CTC from ZigBee to Wi-Fi. Specifically, we propose a noise interference strategy by adding an appropriate amount of dedicated noise signals, which can interfere with the eavesdropping and simulation of ZigBee signals without affecting the reception of the receiver. Moreover, we also propose a regression modeling strategy which collects data, extracts features, and trains a binary logistic regression model so that the receiver can actively distinguish simulated attack signals. We build the experimental platform by using GNU Radio and USRP devices. Experimental results demonstrate that the security defense strategies can identify and distinguish the signals from the attacker with a high accuracy, effectively solving the signal emulation attack on the physical layer CTC from ZigBee to Wi-Fi.

Keywords: cross-technology communication; Internet of Things (IoT); intelligent control; security defense strategy

CLC number: TN918.91

Document code: A

Article ID: 1672-5220(2025)05-0503-10

Open Science Identity
(OSID)



0 Introduction

Wi-Fi^[1-2], ZigBee^[3-4], Bluetooth^[5], LoRa^[6], RFID^[7] and other wireless technologies are widely used in various fields such as smart home, smart wearable, smart medical and smart industry. However, due to their operation in the same frequency band, the coexistence of these technologies in the same application field often leads to serious interference problems such as channel competition, signal collision and throughput reduction. As shown in Fig. 1, especially in the 2.4 GHz frequency band, the spectrum overlap phenomenon of various wireless signals is severe. It has been proven that Wi-Fi and ZigBee interfere with each other in the real-world environment, and the packet loss rate of ZigBee fluctuates between 0% and 85% depending on various Wi-Fi traffic loads^[8].

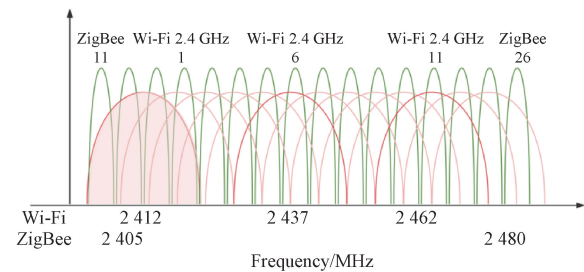


Fig. 1 Spectrum distribution of Wi-Fi and ZigBee in 2.4 GHz frequency band

Cross-technology communication (CTC) is emerged to solve the above interference problem that is caused by the coexistence of multiple technologies, and to achieve the connection and collaborative work between different wireless technologies without the need for gateways. Recently, CTC has shown broad application prospects in various fields.

Specifically, Wi-Fi access points in a smart home environment can dynamically assign priorities to sensor nodes based on different scenarios, effectively managing and coordinating the coexistence of multiple heterogeneous wireless devices^[9-10]. The PTrack platform of health monitoring utilizes CTC to not only accelerate the upload speed of health data, but also broaden the monitoring scope^[11].

Although CTC has brought many conveniences to the development of the Internet of Things (IoT), it still has new security risks. Specifically, CTC allows heterogeneous devices to communicate without gateway authentication, such as bypassing the gateway to invade the smart home system and opening the smart door lock. Moreover, a malicious device would mimic normal devices in CTC, making it impossible to distinguish between homogeneous devices and heterogeneous devices. For example, in agricultural automatic control systems, attackers can eavesdrop on and mimic ZigBee signals from sensors, which causes the Wi-Fi receiver to obtain incorrect parameters and thus make wrong decisions.

Recently, most related works have studied the security issue in CTC. JamCloak raised security and privacy issues such as advertisement pushing and data

Received date: 2024-11-05

* Correspondence should be addressed to ZHANG Guanglin, email: glzhang@dhu.edu.cn

Citation: LI T Y, ZHANG A Q, ZHANG G L. Security defenses for cross-technology communication in IoT control system [J]. *Journal of Donghua University (English Edition)*, 2025, 42(5): 503-512.

stealing^[12]. Attackers can also use heterogeneous communication technique to conduct mimicry attacks, stealing or tampering with sensor data to control IoT devices, which can lead to serious security issues^[13]. As shown in Fig. 2, an attacker can use Wi-Fi to imitate ZigBee signals and tamper with the data collected by sensors, causing the Wi-Fi control device to obtain incorrect information and then issue wrong instructions after intelligent decision-making. In Fig. 2, quadrature amplitude modulation (QAM) is a modulation method that modulates the amplitude of two orthogonal carriers.

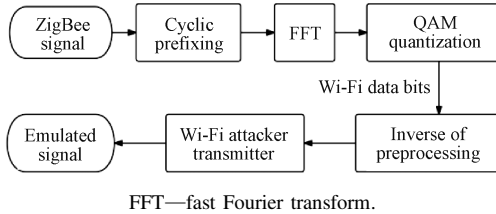


Fig. 2 Signal simulation attack in IoT

Existing CTC research focuses on the enhancement of the data transmission rate, synchronisation capability, and anti-jamming capability in data sharing and fusion of wireless heterogeneous devices. Strip-Comm^[14] and FreeBee^[15] employed strategies such as Manchester coding and folding technologies to resist noise, respectively. AdaComm^[16] and C-chirp^[17] improved the reliability of channel state information (CSI). PRComm adopted a related decoding strategy to improve the synchronization and anti-interference of CTC^[18]. X-burst contributed to optimizing the energy transmission efficiency of CTC^[19]. G-Bee was proposed to synchronize the transmission of ZigBee signals^[20]. NETCTC provided a feedback mechanism for cross protocol data transmission^[21]. However, these related studies focus on the implementation and optimization of CTC, and neglect the security issue, which is our main consideration.

Based on these, we propose a strategy combining noise interference and detection to defend against cross-technology signal emulation attacks. The noise interference uses ZigBee's direct sequence spread spectrum (DSSS) coding error tolerance, misleading attackers into eavesdropping on distorted signals after QAM quantization. The regression modeling strategy extracts features from signals using time-domain cyclic prefix and frequency-domain constellation features, training a binary logistic regression model. This model recognizes signal sources at the Wi-Fi receiver, continuously improves performance, and distinguishes emulated signals. The GNU Radio 3.8, USRP 2953R and DHT11 sensor are used in the experiment, and the data from the DHT11 sensor is transmitted through a ZigBee transmitter.

Our contributions are summarized as follows.

1) We present a comprehensive solution against cross-technology attacks in IoT intelligent control

systems, which can significantly reduce the risk of receiving imitation data from attackers at the decision-making end and improve the security and reliability of data transmission.

2) We employ a noise interference strategy to interfere with the eavesdropping of attackers. Meanwhile, we employ a regression modeling strategy to enable the Wi-Fi receiving decision devices to distinguish attack signals.

3) We conduct experiments on GNU Radio 3.8 and USRP 2953R devices to verify the effectiveness and practicality of the proposed security defense strategies by simulating the CTC process.

1 Related Work

1.1 Packet-level CTC

Packet-level CTC utilizes packet-level features to construct a side channel that can effectively communicate data information across protocols between heterogeneous devices by simultaneously addressing both the sender and receiver.

1.1.1 CTC based on received signal strength indicator (CTC-RSSI)

The transmitter and receiver create recognizable sequences by using the signal strength for cross-technology data. Packet energy, length, interval, etc., are adjusted to form received signal strength indicator (RSSI) features. Wi-Fi transmit packet transmission causes ZigBee to receive a 1-bit high RSSI, and no transmission results in a 0-bit low RSSI. WiZig boosts data rates by varying Wi-Fi transmit power^[22]. HoWiES establishes a mapping table between the sender and receiver^[23]. EMF alters the signal duty cycle by the packet order, using the Morse code for bit transfer^[24].

1.1.2 CTC based on channel state information (CTC-CSI)

The overlapping of heterogeneous wireless signals in the frequency domain supports CTC based on CSI. Wi-Fi 802.11a/g/n uses 20 MHz channels that are divided into 64 sub-channels, with CSI indicating states (amplitude and phase) on sub-carriers^[25]. CSI is more stable and resistant to interference than RSSI. CTC via CSI features, waveform and frequency bias at Wi-Fi Rx is feasible. The use of support vector machines to make judgments on CSI sequences is proposed in ZigFi^[25]. C-chirp sends packets on ZigBee channels, varying the CSI linearly at the Wi-Fi receiver within 60 m^[17].

However, packet-level CTC is relatively simple and compatible, and its data transmission rate is significantly limited, i. e., only a few hundred bits per second to a few kilobits per second. In our paper, we focus on physical-layer-level CTC, which can further improve the transmission efficiency and has been widely studied in recent years.

1.2 Physical-layer-level CTC

Transparent CTC at the receiver side is a method that

allows the receiver side to directly decode other heterogeneous wireless signals without any modifications. WeBee provided a physical-layer waveform simulation-based approach^[26]. If the transmitter does not require any modifications, it is a transparent CTC on the transmitter. It fully utilizes the computing power of the receiver to achieve reverse transmission of CTC from low-end wireless devices to high-end wireless devices, and its core idea is cross mapping^[27]. Non-transparent CTC is the scenario in which both the transmitter and the receiver make hardware modifications or firmware upgrades. These techniques can be used to improve the performance of CTC or to achieve concurrent transmission of multiple cross-technology data. For TwinBee, the distribution of symbol errors was explored by decoding Wi-Fi analogue signals at the ZigBee receiver side, and a code-slice combining approach was proposed to recover the erroneous decoded bits at the receiver side^[28].

In practice, the physical-layer-level CTC may cause decoding errors once it receives the waveform or phase effects of noise and attacks. Therefore, it is more susceptible to noise or attacks. Unfortunately, these related studies do not consider the security issue in CTC.

2 Background

2.1 Transparent CTC on transmitter

Transparent CTC at the transmitter end implies that the transmitter requires no modifications and fully leverages the computing power of the receiver to achieve reverse cross-technology information transmission from low-end wireless devices to high-end wireless devices. The core idea of this technology is cross-mapping^[27], which realizes the transmission and decoding of cross-technical information through the mapping relationship between the signal at the transmitter and the signal decoded by the receiver. SymBee is a novel ZigBee-to-Wi-Fi CTC method with symbolic-level encoding^[29]. It is one of the transparent CTC at the transmitter end. After investigating the existing research at home and abroad, it is found that the scenario of imitating ZigBee to attack ZigBee data link through Wi-Fi has occurred from time to time. This attack technique has been described in detail in the IoT house published by Zhang et al.^[13]. It can be inferred that SymBee also has the risk of ZigBee being imitated.

2.2 Software and hardware platform construction

GNU Radio is a framework designed to assist wireless communication developers in designing, building and implementing wireless communication systems.

It offers comprehensive processing modules for complex signal processing applications. GNU Radio has been applied to a wide range of practical systems, including audio processing, mobile communications, satellite communications, radar systems and software-defined radio systems.

USRP is a software defined radio device that can be used to flexibly build individual signal processing functions. The USRP 2953R used in this paper (shown in Fig. 3) provides high bandwidth and high dynamic processing capability, consists of a Xilinx field programmable gate array (FPGA) module, dual analog-to-digital converters (ADCs) with a transmission rate of 200 million samples per second (MS/s), dual digital-to-analog converters (DACs) with a transmission rate of 200 MS/s and Gigabit Ethernet ports or 10 Gigabit Ethernet ports. The device is capable of operating between 1.2 GHz and 6.0 GHz, and can be extended to support multiple-input multiple-output (MIMO) configurations. We use the 120 MHz version for the system.



Fig. 3 USRP 2953R used in experiment

3 IoT Intelligent Control System Design

Most existing IoT intelligent control systems rely on gateways to convert different communication protocols and restrict the access of illegal devices. Gateways can effectively prevent information leakage and malicious tampering, thereby ensuring the security of IoT intelligent control systems. However, in this paper, the IoT intelligent control system that we design is based on the SymBee CTC mode without gateways, which increases the risk of being attacked.

We illustrate a general diagram of IoT intelligent control system in Fig. 4. In an IoT intelligent control system, the ZigBee transmitters of ZigBee sensors (such as temperature sensors and humidity sensors) utilize the SymBee CTC method to send the collected data to the Wi-Fi receiver (such as smartphones) for processing and analysis.

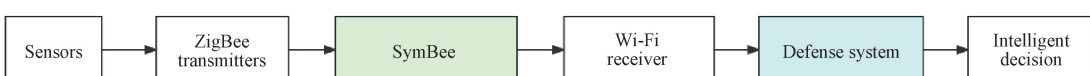


Fig. 4 General diagram of IoT intelligent control system

3.1 ZigBee transmitters

In the IoT intelligent control system, the sensors use

the ZigBee transmitters to send collected data to the Wi-Fi receiver for processing and analysis.

1) Data source. DHT11 is a digital sensor that can detect humidity and temperature simultaneously. The internal structure of DHT11 is demonstrated in Fig. 5. GND represents ground. VDD provides positive voltage to the power supply. MCU is an integrated circuit chip.

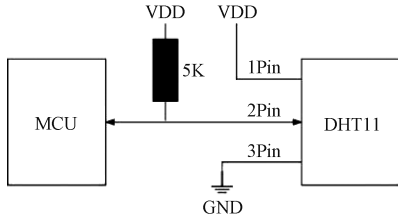
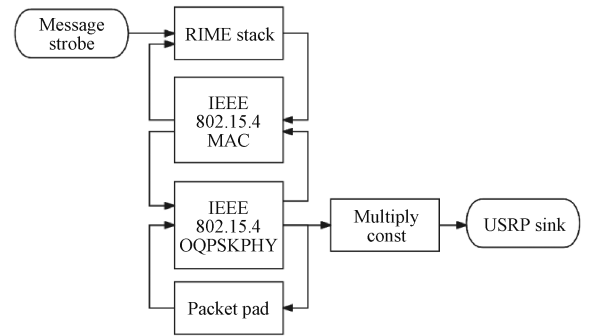


Fig. 5 Internal structure of DHT11

2) ZigBee signal transmission. The data format is specifically composed of unencoded binary data output by sensors^[30]. When processing the data, each part is processed separately by the GNU Radio companion (GRC) of the ZigBee transmitter that we built on the GNU Radio platform as shown in Fig. 6.



RIME— a layered protocol stack; const—constant;
OQPSKPHY—offset quadrature phase shift keying physical layer.

Fig. 6 Structure diagram of ZigBee transmitter

3.2 Wi-Fi receiver

At the receiving end of the system, the Wi-Fi receiver processes the received signal and loads the data into smart devices for analysis and decision-making.

1) Wi-Fi signal reception. A Wi-Fi signal's symbol is 80-bit complex data consisting of 16-bit cyclic prefix data and 64-bit valid data. Figure 7 shows the flowchart of the Wi-Fi receiver built for the test environment in GNU Radio.

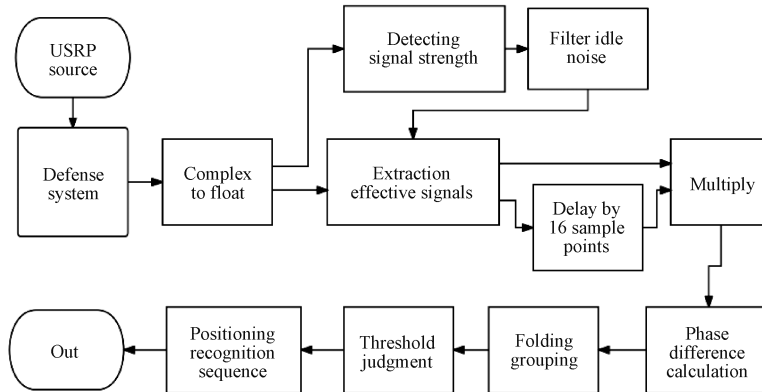
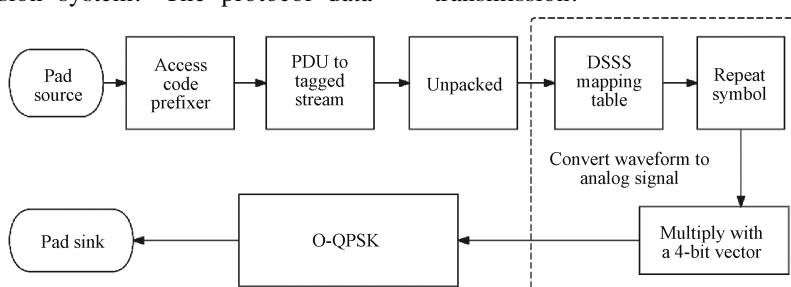


Fig. 7 Flowchart of Wi-Fi receiver

The testing environment was built by using two USRP 2953R and GNU Radio 3.8 in the Ubuntu virtual machine of VMware Workstation. One USRP 2953R is used as a ZigBee transmitter, and the other is used as a Wi-Fi receiver. Figure 8 shows the physical layer of the transmission system. The protocol data

unit (PDU) refers to a single unit of information transmitted between peer entities in a computer network. Offset quadrature phase shift keying (O-QPSK) is an improved QPSK modulation method that uses phase modulated reference signals for data transmission.



DSSS—direct sequence spread spectrum.

Fig. 8 Physical layer flowchart of transmission system

2) Intelligent decision. Received data are sent to the monitor node's program entry and visualized via

matplotlib plots; an easy GUI is used for the user interface and Pickle is used for variable serialization. As

shown in Fig. 9, the entered temperature threshold is displayed as a straight line on the interface at runtime. When the temperature exceeds the set threshold, a warning is given by adding a label. The intelligent decision-making system can send the corresponding instructions to the ZigBee node to respond to the operation through the Wi-Fi transmitter.

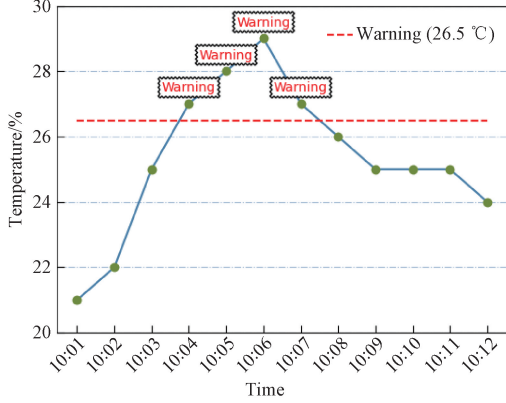


Fig. 9 Temperature interface

4 Defense against Cross-Technology Attacks

We focus on the security issues during the signal transmission in Fig. 4 and design two security defense strategies to ensure the signal is not tampered by attackers.

4.1 Noise interference strategy

Based on the carrier frequency offset characteristics of attacks, this section proposes a physical-layer defense scheme. By introducing additive white Gaussian noise (AWGN) during signal transmission, attackers can eavesdrop on and simulate ZigBee signals, resulting in significant quantization errors after Fourier transform and quantization, leading to signal distortion and reducing the success rate of attacks.

1) AWGN. AWGN represents a common communication noise model. It has a uniform power spectral density and Gaussian power distribution, and is widely used in simulating real communication environments. AWGN is generated by configuring Gaussian noise source parameters in our experiment.

2) FFT. FFT is a highly efficient algorithm for performing the discrete Fourier transform (DFT). It is a basic tool for analyzing signal transformation from the time domain to the frequency domain^[20].

$$Z'(m, n) = Z(m, n) + N_z(m, n), \quad (1)$$

where $Z(m, n)$ represents the frequency-domain

expression of the ZigBee signal after FFT; $N_z(m, n)$ represents the added AWGN noise; $Z'(m, n)$ represents the frequency-domain expression of the ZigBee signal after applying noise interference strategy. Figure 10 shows the image of the noisy ZigBee signal sent in our experiment after FFT.

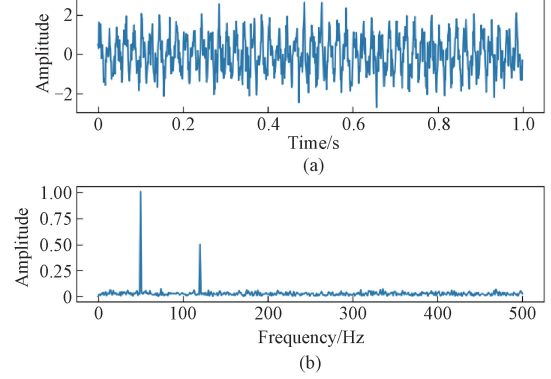


Fig. 10 Images of ZigBee signal: (a) time-domain signal with noise; (b) frequency-domain signal after FFT

3) QAM quantization error. The FFT processed signals $Z(m, n)$ and $Z'(m, n)$ are quantized, and the quantized constellation coordinates are denoted as $Q(m, n)$ and $Q'(m, n)$. After quantification, the quantization errors are labelled as $e(m, n)$ and $e'(m, n)$, respectively:

$$e(m, n) = (Z_{\text{Re}}(m, n) - \alpha Q_{\text{Re}}(m, n))^2 + (Z_{\text{Im}}(m, n) - \alpha Q_{\text{Im}}(m, n))^2, \quad (2)$$

$$e'(m, n) = (Z_{\text{Re}}(m, n) - \alpha Q'_{\text{Re}}(m, n))^2 + (Z_{\text{Im}}(m, n) - \alpha Q'_{\text{Im}}(m, n))^2, \quad (3)$$

where $Z_{\text{Re}}(m, n)$ and $Z_{\text{Im}}(m, n)$ represent the real part and imaginary part of the FFT signals, respectively; α is the optimal scalar; $Q_{\text{Re}}(m, n)$ and $Q_{\text{Im}}(m, n)$ are the real part and imaginary part of the quantized constellation coordinates without AWGN, respectively; $Q'_{\text{Re}}(m, n)$ and $Q'_{\text{Im}}(m, n)$ are the real part and imaginary part of the quantized constellation coordinates with AWGN, respectively. They can be used to compare the differences in the presence or absence of AWGN. Moderate AWGN noise can cause signals to be quantized to different QAM points, resulting in larger quantization errors.

4.2 Regression modeling strategy

Wi-Fi attackers possess sufficient computing power to execute signal emulation attacks through exhaustive searches of their constellations. Consequently, this subsection introduces a regression modeling strategy designed to differentiate in real time between signals from Wi-Fi attackers and those from ZigBee transmitters, as illustrated in Fig. 11.

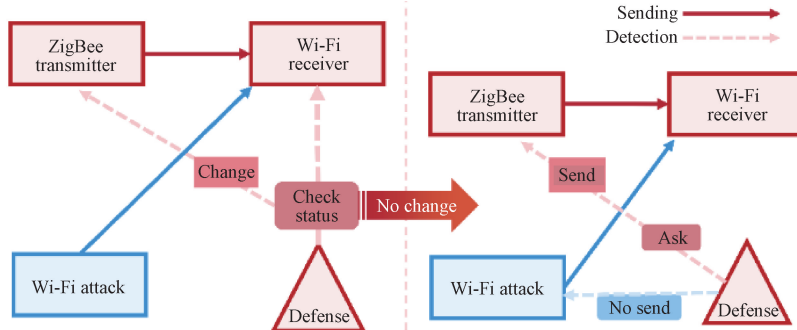


Fig. 11 Flowchart of regression modeling strategy

1) Feature extraction. The regression modeling strategy leverages wireless network protocol traits. To differentiate ZigBee from attacks, the receiver analyzes time and frequency features. In the time domain, cyclic prefix of Wi-Fi is verified by the cosine distance and high cosine distance values mean strong similarity. Comparing the average distance can analyze whether it is an attack signal. In the frequency domain, eavesdropped signals differ in constellation structure from analog ones.

2) Data collection and labeling. At the beginning of the run, the system records whether the transmitter sends a signal when the receiver receives a signal, so that the system can continuously classify it based on the historical learning results, as shown in Fig. 11. When receiving a signal, the first step is to check for any changes in the Wi-Fi receiver. If no change occurs, the signal is deemed an analog signal. If a signal has already been sent, the ZigBee transmitter is queried. If the sensor indicates that no signal is transmitted, the signal is classified as the analog. If a transmitter on the sensor side sends a signal, it is identified as the source.

3) The logistic regression model. The regression model categorizes data by formulating a boundary based on features^[31]. Advantages of logistic regression in this paper are easy implementation due to simple formulas and clear parametric models, high efficiency with a fast calculation speed and low delay, and rich output offering probabilities for different events instead of an absolute 0 or 1.

The receiver in this paper needs to divide the sources of the received signal into two categories, so the binary logistic regression model is used. By comparing the magnitude of the two probabilities to determine the signal source, it can be determined that the signal comes from the transmitter with a higher probability.

$$P(Y = 1 | \mathbf{x}) = \frac{\exp(\hat{\mathbf{w}} \cdot \mathbf{x} + \hat{b})}{1 + \exp(\hat{\mathbf{w}} \cdot \mathbf{x} + \hat{b})}, \quad (4)$$

$$P(Y = 0 | \mathbf{x}) = \frac{1}{1 + \exp(\hat{\mathbf{w}} \cdot \mathbf{x} + \hat{b})}, \quad (5)$$

where event “ $Y = 1$ ” indicates that the signal is from a Wi-Fi attacker; event “ $Y = 0$ ” indicates the transmitter; \mathbf{x} denotes a feature vector; $\hat{\mathbf{w}}$ is the estimated weight vector, and $\hat{\mathbf{w}} \in \mathbf{R}^n$; \hat{b} is the estimated bias term obtained by maximizing log-likelihood.

4.3 Selection design

To verify the performance of the proposed security defense strategies, this section shows the defense system selection design set in GRC, which can easily and quickly select the security defense strategy to be compared. We use the variables above to select the defense strategy.

In this system, after selecting the security defense strategies, the two selectors in the system will be synchronized, and open the corresponding port to receive data streams. To select the security defense strategies to be used, the route of the data flow can be automatically selected, simplifying the complexity of the GRC flow diagram, and avoiding repeated operations and excessive equipment performance consumption.

5 Performance Analysis of Security Defense Strategies

5.1 Experiment setup

We use one USRP 2953R equipped with IEEE 802.15.4 physical layer to send messages and another USRP 2953R equipped with IEEE 802.11 PHY to receive messages and perform a signal emulation attack on them in the GNU Radio 3.8 environment. The USRP 2953R receives the wireless signals through the radio frequency (RF) front-end and converts them into a digital signal stream for transmission to the connected computers.

5.2 Interference performance

After interference by noise, the signal emulated by the Wi-Fi attacker is quantized to a different constellation point than the one emitted by the transmitter. Figure 12 shows the original constellation performance. After adding AWGN, points that are more reddish indicate points with higher quantification errors, while green ones are points with lower quantification errors, as shown in Fig. 13.

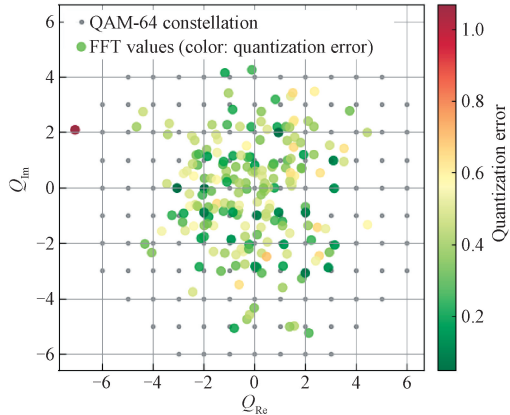


Fig. 12 Original constellation performance

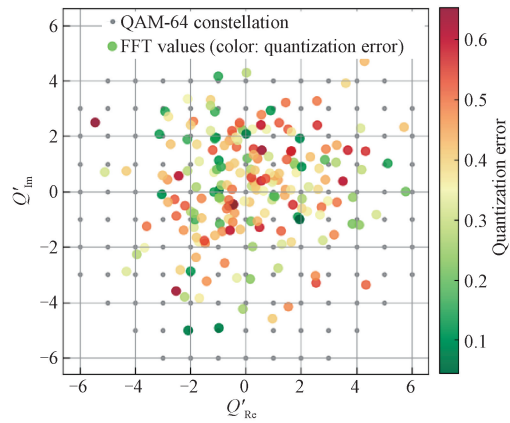


Fig. 13 New constellation performance

The QAM points on the constellation are shown in Table 1. For example, considering the point $m = 10$, when no noise is present, the point m quantizes to the QAM point $-1 + j$; however, after adding noise, it quantizes to $-1 - j$, deviating from the original FFT point. This erroneous quantization results in increased quantization errors, demonstrating that adding AWGN to the ZigBee transmit signal amplifies the quantization error in the attacker's simulation.

Table 1 Comparison of constellation performance

Sub-carrier	$Q(m, n)$	$e(m, n)$	$Q'(m, n)$	$e'(m, n)$
10	$-1 + j$	0.647 8	$-1 - j$	2.625 4
11	$-1 + 2j$	0.387 8	$-1 + j$	0.648 1
12	$-1 + 5j$	0.121 7	$-1 + 5j$	0.122 3
13	$1 + j$	0.831 5	$1 - j$	1.812 5
14	$1 + 2j$	0.501 3	$1 + 2j$	0.524 5
15	$1 + 5j$	0.451 4	$1 + 4j$	0.625 1
16	$2 + 3j$	0.544 7	$2 + 2j$	0.924 5
17	$5 - 3j$	1.104 2	$5 - 3j$	1.135 4
18	$-7 + j$	0.425 1	$-5 + j$	2.512 4

5.3 Recognition performance

The trained model of the regression modeling strategy predicts points in the sample space, observes classifications, draws category boundaries and creates a decision boundary graph. In binary classification, this graph splits the vector space into two parts, and the decision boundary is a straight line, serving as the binary classification threshold. We use Matplotlib and SciKit-Learn to calculate prediction probabilities on a grid, set a threshold to distinguish attacker and sensor signals, and draw the decision boundary, as shown in Fig. 14.

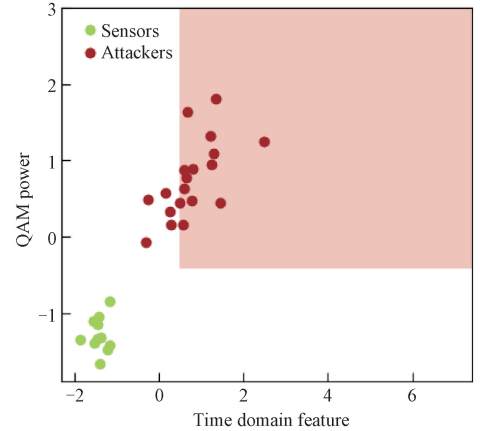


Fig. 14 Model decision boundary of regression modeling strategy

Signals are received continuously in the application, so a large number of fast data input and processing speeds need to be considered to distinguish signal sources in time based on the feature classification learned by the model. The accuracy of the model gradually tends to "1" with the increase of the amount of model training data. Figure 15 shows the accuracy of the model of the regression modeling strategy.

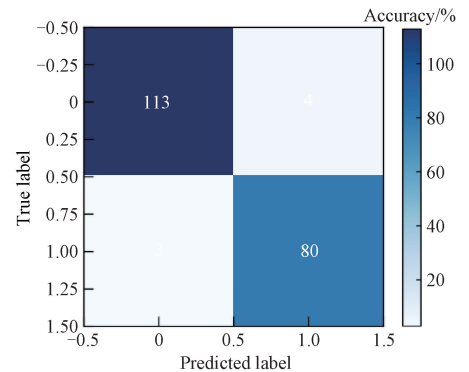


Fig. 15 Model performance accuracy

To verify the stability of the security defense strategies under different network loads, a series of tests are conducted within the traffic rate range of the ZigBee transmitter. The control of the traffic rate is achieved by adding a throttle module to the ZigBee transmitter. The results are shown in Fig. 16. From the experimental results, it can be seen that our security defense strategies

have good stability under heavy traffic conditions.

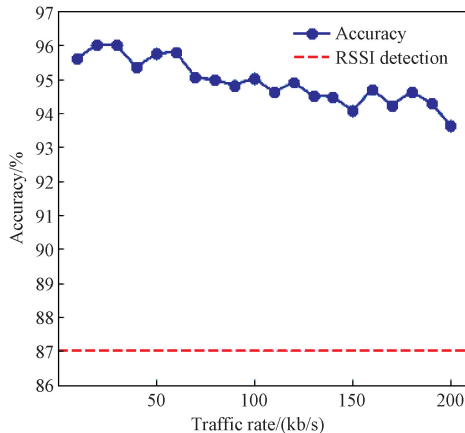


Fig. 16 Accuracy on different traffic rates

6 Conclusions

In this paper, a comprehensive solution is proposed, which combines a noise interference strategy and a regression modeling strategy to counteract CTC attacks at the physical-layer communication from ZigBee to Wi-Fi. On the receiver side, dedicated noisy signals are added to raw signals. Subsequently, data collection and feature extraction are performed. By training a binary logistic regression model, the recognition ability of attackers' simulated signals is continuously enhanced. Exhaustive experiments verify the superior defense performance of our proposed strategies, which plays an important role in the secure and reliable development of IoT. In future research, the processing efficiency and other performance of the regression model can be further improved to defend against replay attacks and DoS attacks. At the same time, conducting in-depth research on the characteristics of Bluetooth and long-term evolution signals and identifying parameters that can be used for feature extraction can help to apply the security defense strategies to more situations of heterogeneous wireless signals coexist.

References

- [1] IEEE Standard Association. IEEE Standard 802.11[S]. New York: IEEE, 2012.
- [2] ZHANG D A, WANG J X, JANG J, et al. On the feasibility of Wi-Fi based material sensing [C]//The 25th Annual International Conference on Mobile Computing and Networking. New York: ACM, 2019: 1-16.
- [3] IEEE Standard Association. IEEE Standard 802.15.4[S]. New York: IEEE, 2003.
- [4] PARK Y, HA J H, KIM H, et al. Enabling sensor network to smartphone interaction using software radios[J]. *ACM Transactions on Sensor Networks*, 2017, 13(1) : 1-26.
- [5] SHESHADRI R, SUNDARESAN K, CHAI E. BLU: blueprinting interference for robust LTE access in unlicensed spectrum [C]//Proceeding of the 13th ACM CONEXT. New York: ACM, 2017: 15-27.
- [6] SEMTECH R. LoRa Standard [EB/OL]. [2020-10-12] (2024-10-11). <https://lora-alliance.org>.
- [7] HAN J S, DING H, QIAN C, et al. CBID: a customer behavior identification system using passive tags [J]. *ACM Transactions on Networking*, 2016, 24(5) : 2885-2898.
- [8] ANGRISANI L, BERTOCCHI M, FORTIN D, et al. Experimental study of coexistence issues between IEEE 802.11b and IEEE 802.15.4 wireless networks [J]. *IEEE Transactions on Instrumentation and Measurement*, 2008, 57(8) : 1514-1523.
- [9] CHI Z C, LI Y, HUANG Z C, et al. Simultaneous bi-directional communications and data forwarding using a single ZigBee data stream [C]//2019 IEEE Conference on Computer Communications. New York: IEEE, 2019: 577-585.
- [10] JIANG W C, YIN Z M, KIM S M, et al. Transparent cross-technology communication over data traffic [C]//2017 IEEE Conference on Computer Communications. New York: IEEE, 2017: 1-9.
- [11] LIU R F, YIN Z M, JIANG W C, et al. WiBeacon: expanding BLE location-based services via WiFi [C]//Proceedings of the 27th Annual International Conference on Mobile Computing and Networking. New York: ACM, 2021: 83-96.
- [12] CHEN G L, DONG W. JamCloak: reactive jamming attack over cross-technology communication links [C]//2018 IEEE 26th International Conference on Network Protocols (ICNP). New York: IEEE, 2018: 34-43.
- [13] ZHANG X N, YU S H, ZHOU H S, et al. Signal emulation attack and defense for smart home IoT[J]. *IEEE Transactions on Dependable and Secure Computing*, 2023, 20 (3) : 2040-2057.
- [14] ZHENG X L, HE Y, GUO X Z. Strip-Comm: interference-resilient cross-technology communication in coexisting environments [C]//Proceeding of IEEE INFOCOM. New York: IEEE, 2018: 171-179.
- [15] KIM S M, HE T. FreeBee: cross-technology communication via free side-channel [C]//Proceeding of the 21st ACM MobiCom. New York: ACM, 2015: 317-330.
- [16] WANG W G, ZHENG X L, HE Y, et al. AdaComm: tracing channel dynamics for reliable cross-technology communication [C]//2019 16th

- [17] Annual IEEE International Conference on Sensing, Communication, and Networking (SECON). New York: IEEE, 2019: 1-9.
- [18] XIA D, ZHENG X L, LIU L, et al. C-chirp: towards symmetric cross-technology communication over asymmetric channels [C]//2020 17th Annual IEEE International Conference on Sensing, Communication, and Networking (SECON). New York: IEEE, 2020: 1-9.
- [19] WANG W, HE D S, JIA W, et al. PRComm: anti-interference cross-technology communication based on pseudo-random sequence [C]//Proceedings of the 20th International Conference on Information Processing in Sensor Networks. New York: ACM, 2021: 163-175.
- [20] HOFMANN R, BOANO C A, ROMER K. X-burst: enabling multi-platform cross-technology communication between constrained IoT devices [C]//2019 16th Annual IEEE International Conference on Sensing, Communication, and Networking (SECON). New York: IEEE, 2019: 1-9.
- [21] CHAE Y, WANG S, KIM S M. Exploiting WiFi guard band for safeguarded ZigBee [C]//Proceedings of the 16th ACM Conference on Embedded Networked Sensor Systems. New York: ACM, 2018: 172-184.
- [22] WANG S, YIN Z M, LI Z J, et al. Networking support for physical-layer cross-technology communication [C]//2018 IEEE 26th International Conference on Network Protocols (ICNP). New York: IEEE, 2018: 259-269.
- [23] GUO X Z, ZHENG X L, HE Y. WiZig: cross-technology energy communication over a noisy channel [C]//Proceeding of IEEE INFOCOM. New York: IEEE, 2020: 2449-2460.
- [24] ZHANG Y F, LI Q. HoWiES: a holistic approach to ZigBee assisted WiFi energy savings in mobile devices [C]//2013 Proceedings IEEE INFOCOM. New York: IEEE, 2013: 1366-1374.
- [25] CHI Z C, HUANG Z C, YAO Y, et al. EMF: embedding multiple flows of information in existing traffic for concurrent communication among heterogeneous IoT devices [C]//IEEE INFOCOM 2017-IEEE Conference on Computer Communications. New York: IEEE, 2017: 1-9.
- [26] GUO X Z, HE Y, ZHENG X L, et al. ZIGFI: harnessing channel state information for cross-technology communication [C]//IEEE INFOCOM 2018-IEEE Conference on Computer Communications. New York: IEEE, 2018: 360-368.
- [27] LI Z J, HE T. WeBee: physical-layer cross-technology communication via emulation [C]//Proceeding of the 23rd ACM MobiCom. New York: ACM, 2017: 2-14.
- [28] LI L G, CHEN Y R, LI Z J. Physical-layer cross-technology communication with narrowband decoding [C]//Proceeding of the 27th IEEE ICNP. New York: IEEE, 2019: 1-2.
- [29] CHEN Y R, LI Z J, HE T. TwinBee: reliable physical-layer cross-technology communication with symbol-level coding [C]//IEEE INFOCOM 2018-IEEE Conference on Computer Communications. New York: IEEE, 2018: 153-161.
- [30] WANG S, KIM S M, HE T. Symbol-level cross-technology communication via payload encoding [C]//2018 IEEE 38th International Conference on Distributed Computing Systems (ICDCS). New York: IEEE, 2018: 500-510.
- [31] HIDAYAT T, MAHARDIKO R, SIANTURI TIGOR F D. Method of systematic literature review for Internet of Things in ZigBee smart agriculture [C]//2020 8th International Conference on Information and Communication Technology (ICoICT). New York: IEEE, 2020: 1-4.
- [32] CHEN Y R, WANG S, LI Z J, et al. Reliable physical-layer cross-technology communication with emulation error correction [J]. *ACM Transactions on Networking*, 2020, 28(2): 612-624.

物联网控制系统中跨技术通信的安全防御

李天韵, 张安琪, 张光林*

东华大学 信息科学与技术学院, 上海 201620

摘要: 为解决跨技术通信 (cross-technology communication, CTC) 安全问题, 以物联网 (Internet of Things, IoT) 智能控制系统为例, 提出了一种从 ZigBee 到 Wi-Fi 的物理层 CTC 攻击综合解决方案。具体而言, 提出了一种噪声干扰策略, 通过添加适量的专有噪声信号来干扰攻击者对 ZigBee 信号的窃听和仿真, 而不影响接收端的信号接收; 提出了一种回归建模策略来收集数据、提取特征, 并训练二进制逻辑的回归模型, 使接收器能够主动区分模拟的攻击信号。使用 GNU Radio 和 USRP 设备构建了一个实验平台。实验结果表明, 所提出的安全防御策略能够高精度地识别和区分攻击者的信号, 有效地防御了从 ZigBee 到 Wi-Fi 的物理层 CTC 上的信号仿真攻击。

关键词: 跨技术通信; 物联网; 智能控制; 安全防御策略

DOI: 10.19884/j.1672-5220.202406009

Select-and-Answer Prompting: Facilitating LLMs for Improving Zero-Shot Reasoning

WANG Yufang¹, TANG Xuesong^{1, 2*}, HAO Kuangrong^{1, 2}

1. College of Information Science and Technology, Donghua University, Shanghai 201620, China

2. Engineering Research Center of Digitized Textile & Fashion Technology, Ministry of Education, Donghua University, Shanghai 201620, China

Abstract: Large language models (LLMs) have demonstrated remarkable generalization abilities across multiple tasks in natural language processing (NLP). For multi-step reasoning tasks, chain-of-thought (CoT) prompting facilitates step-by-step thinking, leading to improved performance. However, despite significant advancements in LLMs, current CoT prompting performs suboptimally on smaller-scale models that have fewer parameters. Additionally, the common paradigm of few-shot CoT prompting relies on a set of manual demonstrations, with performance contingent on the quality of these annotations and varying with task-specific requirements. To address these limitations, we propose a select-and-answer prompting method (SAP) to enhance language model performance on reasoning tasks without the need for manual demonstrations. This method comprises two primary steps: guiding the model to conduct preliminary analysis and generate several candidate answers based on the prompting; allowing the model to provide final answers derived from these candidate answers. The proposed prompting strategy is evaluated across two language models of varying sizes and six datasets. On ChatGLM-6B, SAP consistently outperforms few-shot CoT across all datasets. For GPT-3.5, SAP achieves comparable performance to few-shot CoT and outperforms zero-shot CoT in most cases. These experimental results indicate that SAP can significantly improve the accuracy of language models in reasoning tasks.

Keywords: zero-shot learning; large language model (LLM); reasoning problem; chain-of-thought (CoT) prompting

CLC number: TP3-05

Article ID: 1672-5220(2025)05-0513-10

Document code: A

Open Science Identity
(OSID)



0 Introduction

Large language models (LLMs)^[1] have achieved remarkable success across a wide range of natural language processing tasks. Compared to previous large

pre-trained language models (PLMs)^[2], LLMs offer stronger performance in many areas. When confronted with complex tasks that demand multi-step reasoning, PLMs exhibit limited reasoning abilities^[3], although PLMs have parameters reaching the scale of billions. The size of these parameters makes fine-tuning extremely expensive. Furthermore, the parameters and architectures of most PLMs are not released as open source^[4]. Thus, LLMs are often applied to solve multi-step reasoning problems.

Various approaches have been proposed to improve the reasoning capabilities of LLMs. Previous efforts include supervised fine-tuning methods, which involve fine-tuning LLMs with large amounts of training data^[5]. Studies have also explored iterative refinement of answers and knowledge enhancement through retrieval from external knowledge bases^[6]. Wei et al.^[7] introduced chain-of-thought (CoT) prompting. This technique comprises two main methods. The first is zero-shot CoT, which involves adding a single prompt after the question, such as “Let’s think step by step”, to facilitate LLMs’ reasoning process generation. This approach does not require input-output demonstrations. The second method, known as few-shot CoT, provides LLMs with step-by-step reasoning examples instead of standard question-answer pairs. In practice, few-shot CoT has achieved stronger performance than zero-shot CoT^[8]. The differences between zero-shot CoT and few-shot CoT are shown in Fig. 1. However, these reasoning examples depend on human annotation, requiring consistent formatting for different types of tasks like arithmetic and commonsense reasoning. Additionally, CoT prompting proves effective only in models with hundreds of billions of parameters; neither few-shot CoT nor zero-shot CoT benefits smaller models^[9].

To address the reliance on human annotation and improve the reasoning abilities of smaller models, we propose a select-and-answer prompting method (SAP). The core motivation behind SAP is to enhance the

Received date: 2024-06-21

Foundation item: National Natural Science Foundation of China (No. 62176052)

* Correspondence should be addressed to TANG Xuesong, email: tangxs@dh.edu.cn

Citation: WANG Y F, TANG X S, HAO K R. Select-and-answer prompting: facilitating LLMs for improving zero-shot reasoning [J]. *Journal of Donghua University (English Edition)*, 2025, 42(5): 513-522.

performance of LLMs in reasoning tasks without requiring extensive manual intervention. SAP introduces a two-step process that integrates reasoning with answer extraction in a structured manner, enabling models to handle complex

reasoning tasks more efficiently. Thus, SAP bridges the gap between the need for human involvement in CoT prompting and the limitations of smaller models in handling reasoning tasks.

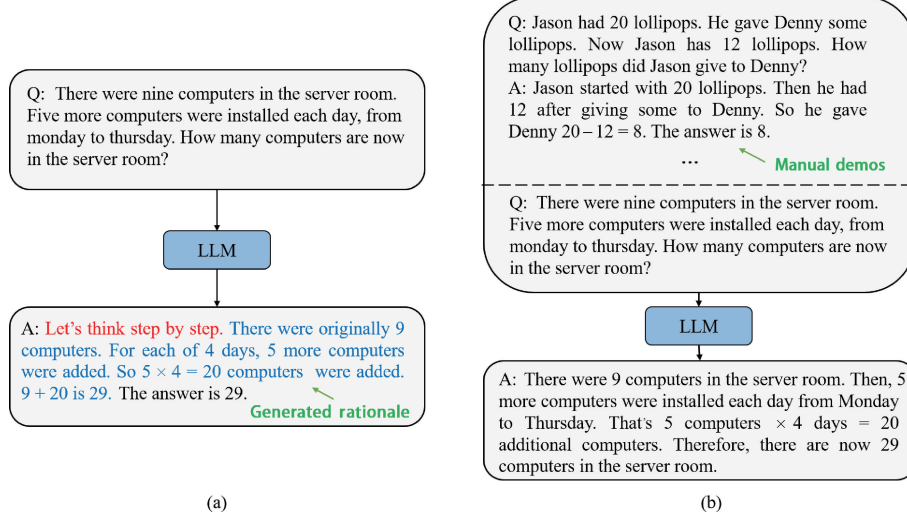


Fig. 1 Sample inputs and outputs of common CoT prompting methods for LLMs: (a) zero-shot CoT; (b) few-shot CoT

SAP consists of two primary steps. 1) The “select” prompt uses a modified version of zero-shot CoT, directing LLMs to perform a preliminary analysis of the problem and generate multiple candidate answers. The instruction prompt has been extended from “Let’s think step by step” to include the directive “give several candidate answers”, establishing a clear format for LLMs’ outputs. 2) The “answer” prompt combines the original question with the generated candidates, enabling the model to select the most accurate answer from these candidates. However, the two-step process still appears somewhat redundant and could be further optimized in future research.

SAP offers three key advantages.

1) It eliminates the need for human-annotated examples, making it more scalable across different reasoning tasks.

2) It simplifies the reasoning process by structuring candidate answers, which in turn enables the efficient extraction of correct responses.

3) It significantly enhances reasoning performance without requiring billions of parameters, making it suitable for smaller LLMs.

We evaluate SAP on six benchmark datasets across three reasoning tasks: arithmetic reasoning (GSM8K^[10], AddSub^[11], SingleEq and SVAMP^[12]), commonsense reasoning (CommonsenseQA^[13]), and symbolic reasoning (last letter concatenation). Our experiments demonstrate that SAP matches or outperforms few-shot CoT in GPT-3.5 and significantly outperforms it in ChatGLM-6B^[14] across all tasks. This suggests that SAP can effectively transfer prompt-based reasoning capabilities to smaller models, improving both efficiency

and accuracy.

1 Related Work

1.1 Reasoning task

Solving multi-step reasoning tasks has been an active research area in the past few years. Researchers have proposed benchmarks for many reasoning tasks. These include commonsense reasoning (requiring common sense knowledge) and multi-hop reasoning^[15] (requiring context understanding and multi-step inferences). Other types are arithmetic reasoning^[16], involving mathematical concepts, and logical reasoning, based on rule comprehension and logical judgment. To enhance the precision of language models in reasoning tasks, researchers have pursued various strategies. One approach involves fine-tuning LLMs to directly generate the ultimate answer. For instance, Geva et al.^[17] trained an NLP model by utilizing an interpretation produced by a fine-tuned GPT model. Experimental findings indicate that this trained model exhibits improved accuracy, particularly on CSQA datasets. A more advanced and widely adopted method is the introduction of CoT prompting, which guides the model through a step-by-step reasoning process to arrive at the final answer, rather than generating the result directly.

1.2 In-context learning (ICL)

ICL is pivotal to LLM reasoning^[18]. It enhances output accuracy by introducing examples into the input, allowing the LLM to cope with a variety of tasks^[19]. Research centered on ICL has outlined various avenues for refining LLM performance. Rubin et al.^[20] proposed the ability to retrieve demonstrations relevant to the test

instance, dynamically providing relevant training examples for a given test input. Mishra et al. [21] suggested expanding examples by refining information, such as embedding task instructions, thereby enriching the learning process. Additionally, adjusting the output probabilities of the LLM, rather than directly calculating the likelihood probability of the target label, is also an effective method. However, the research by Liu et al. [22] indicates that the effectiveness of ICL can be significantly influenced by the context of the selected examples. Specifically, fluctuations in performance are closely related to the format, order, and wording of prompts. In contrast, Min et al. [23] suggest that using incorrect labels in examples only slightly reduces performance, raising questions about the strict paradigm of input-output mapping.

1.3 CoT prompting

The proposal of CoT has ushered LLMs into a new stage of reasoning ability. CoT prompting represents a gradient-free technique, guiding LLMs to generate a series of coherent intermediate reasoning steps that ultimately lead to the solution of a problem^[24]. Kojima et al. [25] paved the way for generating reasoning steps without the need for manual demonstration. They posited that LLMs are adept zero-shot reasoners, with the most prominent method involving appending the prompt “Let’s think step by step” after a reasoning question. The CoT reasoning, often denoted as few-shot CoT, revolves around the key idea of inserting multi-step reasoning paths before generating the final answer to achieve the desired outcome and stimulate emergent reasoning abilities^[26]. Various methods were proposed to enhance CoT prompting, including representing the reasoning process using programming language, complex structures such as trees and graphs, as well as task decomposition and combining different prompts. In least-to-most prompting^[27], complex problems are reduced to sub-problems, and then the sub-problems are solved sequentially. The other trend is to vote over multiple reasoning paths for a test question^[28]. Zelikman et al. [29] suggested using prompts to enhance the fundamental principles of train carriages. Lu et al. [30] combined CoTs and error analysis to propose a new prompt method, EAPrompt. Jiang et al. [31] proposed LongLLMLingua, which improved the perception ability of LLMs in long context scenarios through prompt compression. However, such approaches typically require large LLMs with more than 100 billion (B) parameters, making them challenging to directly apply to small LLMs.

2 Methods

2.1 Overview

To overcome these limitations and to improve the reasoning performance of smaller models, we propose SAP, which is a new type of zero-shot prompting method and consists of two main steps. In Step 1, appropriate

prompting statements are used to elicit reasoning in the LLM, generating possible candidate answers. In Step 2, the candidate answers obtained from the previous step, together with the prompting statements, are used to guide the LLM in reanalyzing the original question and evaluating the candidate answers.

2.2 Two-step reasoning strategy

In the process of generating candidate answers, our primary goal is to improve the accuracy of the LLM analysis to ensure that the resulting candidate answers contain the correct answers. At the same time, we need to clearly define tasks for the LLM so that it can provide answers in a specific format to facilitate subsequent steps. When constructing prompt statements, we should follow two criteria. First, we ensure that the prompts do not affect the analysis of the original question and allow the LLM to understand the subtask that comes up with multiple candidate answers. Second, we need to provide a clear template so that candidate answers can be provided in a fixed format. We refer to the method proposed in zero-shot CoT, where specific prompt-triggering sentences are used to convert input data into prompts with simple templates. Meanwhile, the construction of the template should consider inducing the LLM to generate the intermediate inference process to improve the reliability of the output candidate answers, as shown in Algorithm 1.

Algorithm 1: SAP

Given: question Q ; prompt p_{generate} for generating candidate answers; LLM for generating candidate answers $\text{LLM}_{\text{generate}}$; LLM for deriving final answers $\text{LLM}_{\text{answer}}$; answer prompt p_{answer} .

Step 1: generate candidate answers

Input: Q , p_{generate} , and $\text{LLM}_{\text{generate}}$.

Process: Use $\text{LLM}_{\text{generate}}$ with p_{generate} to generate several candidate answers $[a_1, a_2, \dots, a_n]$, along with their corresponding rationales, based on Q .

Output: rationale and $[a_1, a_2, \dots, a_n]$.

Step 2: obtain final answers

Input: Q , p_{answer} , $[a_1, a_2, \dots, a_n]$ and $\text{LLM}_{\text{answer}}$.

Process: Use $\text{LLM}_{\text{answer}}$ with p_{answer} to analyze $[a_1, a_2, \dots, a_n]$ and derive the final answer A .

Output: A .

Specifically, we use a simple template to modify the input question x into prompt x' in Step 1: “ $Q: [X]. A: [T]$ ”, where $[X]$ is the input slot for the input question, and $[T]$ is the handcrafted trigger sentence slot for triggering the LLM to generate a post-ordered inference process. In this task, the reasoning process involves initial analysis of the question and the presentation of candidate answers. In zero-shot CoT, the

instructions in the input slot $[T]$ include the trigger instruction “Let’s think step by step”. As shown in Fig. 2, SAP follows the above template. To implement this, we manually design a set of trigger prompts as follows: “Q: $[X]$. A: Let’s analyze the problem step by step and give several candidate answers at the end of the answer, starting with: Possible candidate answers”.

Referring to zero-shot CoT, SAP defaults to generating output with a greedy decoding strategy (1 output chain). In addition, when considering the design of the trigger sentence, we give detailed thought to the instructions. Specifically, in the trigger sentence, referring to zero-shot CoT, we use the sentence “Let’s analyze the problem step by step” to require the LLM to

perform analytical reasoning in as much detail as possible, enhancing the LLM’s ability to generate relevant and important reasoning steps. To ensure that the output of the LLM follows a fixed format, we emphasize the sentence “at the end of the answer, starting with: Possible candidate answers” to explicitly instruct the LLM not to ignore tasks that output possible candidate answers. Adding important trigger sentences increases the credibility of the generated candidate answers. As shown in Fig. 2 (a), at the end of Step 1, the LLM generates inference text that contains the answer. In general, the strategy of adding specific descriptions to trigger sentences provides a new way to improve the zero-shot performance of complex reasoning.

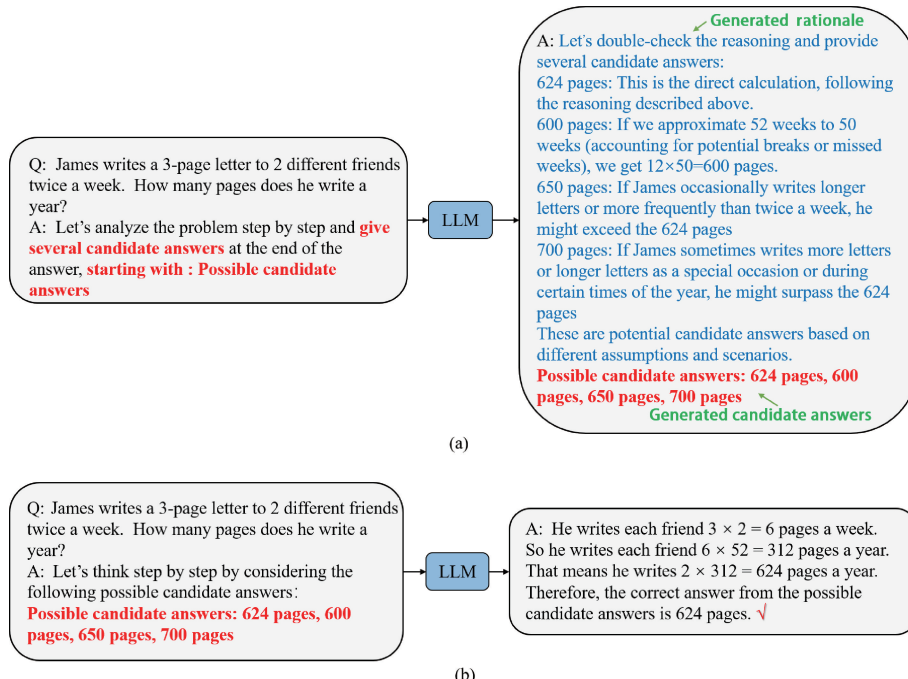


Fig. 2 Example inputs and outputs of GPT-3.5 with SAP: (a) reasoning for generating candidate answers; (b) final answer based on selected candidate options

We designed another prompt trigger sentence for the second reasoning step, enabling the LLM to consider the candidate answer generated in Step 1 in the reasoning of the next step. In addition to inducing the LLM to consider candidate answers during reasoning, the prompt also includes the answers generated in the first step. Since we designed a fixed prompt format in Step 1: “Possible candidate answers”, we can extract the desired instruction information from the first prompt answer in Step 2. This allows the LLM to return the final answer by considering the candidate answers, as shown in Fig. 2 (b).

For models with hundreds of billions of parameters, such as GPT-3.5, we used the above approach to simply build templates. For a smaller model, such as ChatGLM-6B, we initially adopted an LLM to generate the first step inference responses that might improve the performance of the smaller model. To achieve this, we selected a

small subset of the dataset and followed a manually constructed trigger prompt to an LLM (GPT-3.5 in this paper) to generate the answer to the question in Step 1. This includes intermediate reasoning steps and possible candidate answers in a fixed format. We ensured the reasonableness of the chain of reasoning steps by checking whether the candidate answers generated by the large model contained ground truth answers. With this approach, we obtained an enhanced dataset. In this dataset, a subset of the problem is paired with a candidate that leads to correct reasoning and a high-confidence answer. Therefore, we can refine the reasoning power into smaller models by fine-tuning the generated intermediate steps.

In Step 2, models with hundreds of billions of parameters are processed in the same way as smaller LLMs. Specifically, the trigger sentence for reasoning in

Step 2, along with the reasoning result from Step 1, is input into the unfine-tuned LLM to get the final answer.

3 Experimental Setup

3.1 Datasets

SAP is evaluated on six baseline datasets from three types of reasoning problems. Arithmetic reasoning includes the following datasets: 1) GSM8K, a high-quality multilingual dataset of primary-level math word problems created by human authors; 2) SVAMP, derived by extending an existing dataset; 3) AddSub, a dataset covering the addition and subtraction arithmetic word

problem; 4) SingleEq, a dataset containing a single equation elementary algebra word problem that performs multiple mathematical operations on non-rational numbers and a variable. For commonsense reasoning, the assessment set includes CSQA, requiring the application of different types of commonsense knowledge to obtain correct answers on multiple-choice questions. For symbolic reasoning, the evaluation covers the last letter concatenation dataset (named Last Letters), which is required to solve problems connecting the last letter of a word in a name, e.g., “James Brown” to “sn”. The datasets used in the experiment are summarized in Table 1.

Table 1 Details of datasets used in experiment

Dataset	Answer	Samples	Avg words	Data split (filename)
GSM8K	Number	1 319	46. 9	Test.jsonl
SVAMP	Number	600	31. 8	SVAMP.json
AddSub	Number	395	31. 5	AddSub.json
SingleEq	Number	508	27. 4	Questions.json
CSQA	Option	1 221	27. 8	dev_rand_split.jsonl
Last Letters	String	500	15. 0	-

Notes: “Answer” indicates the expected format of the model’s output; “Samples” denotes the number of test instances in each dataset; “Avg words” indicates the average number of words per question; “Data split (filename)” specifies the exact file used for evaluation, ensuring reproducibility.

3.2 Baselines and implementations

We compare our approach to three baseline approaches: zero-shot, zero-shot CoT, and few-shot CoT. The zero-shot baseline connects the test question with the prompt “Yes” as LLM input, generating an answer to a given question without the need for an intermediate step. Among them, the zero-shot CoT appends “Let’s think step by step” to the prompt. Few-shot CoT specifically uses the manual-CoT method, which creates eight hand-crafted examples for demonstration.

We use GPT-3.5 (GPT-3.5-turbo version) as the baseline model. As a backbone language model, it is one of the most widely used LLMs and provides a standard application programming interface (API) for easy integration. We chose this LLM because it has the strongest CoT inference performance among public LLMs. It is easy to evaluate our approach on large models and provide intermediate reasoning steps needed to fine-tune smaller models. For a smaller LLM, we choose ChatGLM-6B of version 2, because the model’s parameters are public and downloadable, and the model is large enough to generate the rationale for non-trivial mass. In our experiment with the greedy decoding strategy, the temperature is set to 0. For few-shot CoT, the number of examples k used in arithmetic reasoning data is set to 8. For the commonsense reasoning class data set, k is set to 7. In symbolic reasoning data sets, k is set to 4.

4 Results and Discussion

4.1 Discussions on main results

The accuracy of SAP, the existing zero-shot CoT and few-shot CoT on six reasoning datasets is listed in Table 2.

1) SAP enhances performance effectively and robustly by bootstrapping candidate answers across various settings of difficulty and tasks in most datasets. For instance, using GPT-3.5, we achieved an accuracy of 79.3% on GSM8K and 84.0% on SVAMP. Across most datasets, SAP consistently matches or surpasses the accuracy compared to the few-shot CoT that requires manual demonstration. On the commonsense reasoning dataset CSQA, the accuracy of SAP (76.3%) outperforms that of zero-shot (60.9%) and zero-shot CoT (67.2%), and it slightly trails behind few-shot CoT (78.2%). Nonetheless, SAP offers more flexibility and stronger task adaptability: no manual construction of examples is required for each dataset.

2) SAP demonstrates significant improvements on smaller LLMs like ChatGLM-6B. For example, with ChatGLM-6B, the accuracy of SAP on GSM8K is 38.0%, much higher than that of zero-shot (10.7%). Additionally, although the SAP performance of the smaller ChatGLM-6B model is not as good as that of GPT-3.5, the improvements brought by SAP on smaller LLMs significantly exceed those on larger LLMs.

Table 2 Accuracies of methods on six datasets

Model	Method	Accuracy/%					
		GSM8K	SVAMP	CSQA	SingleEq	AddSub	Last Letters
GPT-3.5	Zero-shot	68.4	71.1	60.9	74.0	73.6	54.8
	Zero-shot CoT	73.2	78.8	67.2	83.6	78.2	60.3
	Few-shot CoT	78.9	82.4	78.2	86.1	87.3	64.2
	SAP (ours)	79.3	84.0	76.3	88.4	83.1	71.6
ChatGLM-6B	Zero-shot	10.7	30.3	24.8	68.7	54.8	18.3
	Zero-shot CoT	28.0	34.3	28.9	70.2	58.2	25.1
	Few-shot CoT	32.4	33.1	31.2	66.5	60.9	28.9
	SAP (ours)	38.0	40.5	39.1	72.1	69.2	36.7

4.2 Self-consistency analysis

Self-consistency reduces the randomness of LLMs' outputs by generating N inference results and determining the final answer through majority voting. With self-consistency, consistent and improved results are typically expected from the method. Our goal is to investigate the impact of self-consistency on SAP, and whether they are mutually compatible. We evaluated the self-consistency of SAP and few-shot CoT on the GSM8K and CSQA datasets. Experiments were conducted with varying the number of sampling paths at a fixed temperature of 0.7. The results for few-shot CoT and SAP were obtained under identical conditions, and the results of all samples were aggregated

through majority voting to derive final answers.

One limitation of self-consistency is that it incurs higher computational costs. We attempt a small number of sampling paths (five in this experiment) as a starting point to achieve most of the benefits without incurring excessive costs, as performance tends to saturate after a certain number of sampling paths in most cases (Fig. 3). Our research findings suggest that for ChatGLM-6B, SAP consistently outperforms few-shot CoT in most cases, while for GPT-3.5, SAP achieves comparable or superior performance to few-shot CoT. The results indicate a significant improvement in performance with our approach on smaller LLMs.

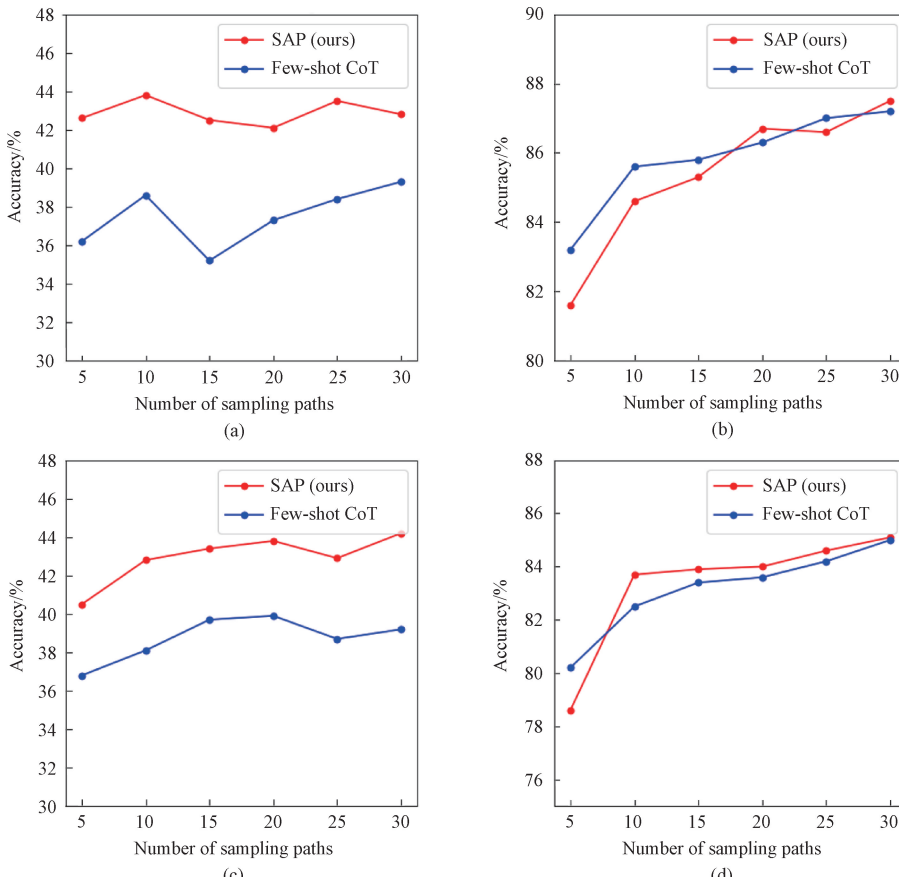


Fig. 3 Self-consistency analysis with varying number of sampling paths: (a) tested on GSM8K for ChatGLM-6B; (b) tested on GSM8K for GPT-3.5; (c) tested on CSQA for ChatGLM-6B; (d) tested on CSQA for GPT-3.5

4.3 Performance of prompts

Table 3 shows the performance comparison of five different input prompts, specifically the answer accuracy on the datasets GSM8K and CSQA, when the five input prompts are used in the first step. All these input prompts are variants of trigger sentences used in Step 1 of the SAP prompt strategy, and greedy decoding is employed. We observe that the accuracy is lower when the prompt sentence does not involve the task of guiding the model

step-by-step through prompts and explicitly providing candidate answers. However, when we add more sentences regarding the intermediate thinking steps and the format of the task of providing candidate answers, the prompts perform the task better. These results indicate that when prompts include more detailed instructions for guiding LLMs, LLMs can generate high-quality reasoning text.

Table 3 Performance comparison of prompts with GPT-3.5 on GSM8K and CSQA

No.	Prompt sentence	Accuracy/%	
		GSM8K	CSQA
1	Understand the problem and propose several candidate answers.	70.5	62.5
2	Please analyze the problem step by step and give several candidate answers.	72.8	63.7
3	Let's think step by step and give several candidate answers.	74.3	64.8
4	Firstly, understand the problem, then give several candidate answers at the end of the answer, starting with: Possible candidate answers.	75.2	66.1
5	Let's analyze the problem step by step and give several candidate answers at the end of the answer, starting with: Possible candidate answers.	76.7	68.2

4.4 Effects of prompt selection

We also conducted ablation experiments and analyses to explore the key factors contributing to the significant improvements of SAP compared to the baseline, with the complete results shown in Fig. 4. Unlike previously proposed CoT methods, our main innovation lies in presenting an efficient answer selection strategy. This method guides the model to first select and then respond through a two-step prompt selection. Therefore, for the ablation experiments on the GSM8K dataset, we used few-shot CoT as the baseline and compared it with SAP without the prompt selection module (PSM) and the complete SAP. Additionally, we compared the reasoning path and direct answers of the self-consistency method, with the number of paths set to 10. The experimental results in Table 2 show that SAP's performance improvement is more significant on smaller LLMs than on larger ones, which is why we select ChatGLM-6B as the experimental model for the ablation experiments. Table 3 shows that relying solely on the second-step prompt or using only sampling decoding cannot achieve optimal performance. In other words, combining the first-step prompt selection with the reasoning path can lead to the best results.

Figure 4 demonstrates that SAP without PSM and the complete SAP can enhance performance compared to few-shot CoT. Additionally, the complete SAP outperforms all other methods, indicating the effectiveness of the PSM. Relying solely on the second-step prompt or using only sampling decoding does not yield optimal performance.

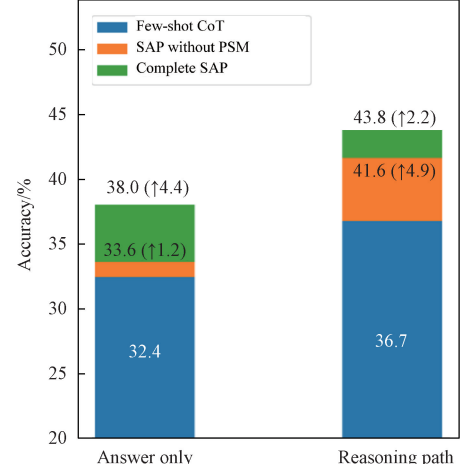


Fig. 4 Ablation study on GSM8K dataset with ChatGLM-6B

5 Conclusions

Previous research has demonstrated that LLMs exhibit reasoning abilities when guided by CoT prompting. However, the manual construction of CoT prompts relies heavily on expert craftsmanship. To alleviate this manual design burden, we propose the select-and-answer prompting method, SAP. It guides LLMs to conduct preliminary analysis, generate several candidate answers for the task, and then complete the original task based on these candidate answers. Evaluation on six datasets, covering three reasoning tasks, reveals that SAP outperforms previous zero-shot

baselines and consistently matches or exceeds the performance of few-shot CoT on multiple datasets. Our findings suggest that SAP can generate several high-confidence candidate answers, and SAP has the potential to outperform few-shot CoT prompting that requires manual demonstration, which could spark further developments of new CoT prompting methods.

References

- [1] BROWN T B, MANN B, RYDER N, et al. Language models are few-shot learners [C]// Conference on Neural Information Processing Systems, NIPS ' 20: 34th International Conference on Neural Information Processing Systems, Vancouver, BC, Canada. New York: NIPS, 2020: 1877-1901.
- [2] LU P, QIU L, YU W H, et al. A survey of deep learning for mathematical reasoning [C]// Proceedings of the 61st Annual Meeting of the Association for Computational Linguistics (Volume 1: Long Papers). Stroudsburg: ACL, 2023: 14605-14631.
- [3] SUN T, SHAO Y, QIAN H, et al. Black-box tuning for language-model-as-a-service [C]// Proceedings of the 39th International Conference on Machine Learning. New York: PMLR, 2022: 20841-20855.
- [4] BAO K Q, ZHANG J Z, ZHANG Y, et al. Tallrec: an effective and efficient tuning framework to align large language model with recommendation [C]//Proceedings of the 17th ACM Conference on Recommender Systems. New York: ACM, 2023: 1007-1014.
- [5] HSIEH C Y, LI C L, YEH C K, et al. Distilling step-by-step! Outperforming larger language models with less training data and smaller model sizes [C]//Findings of the Association for Computational Linguistics: ACL 2023. Stroudsburg: ACL, 2023: 8003-8017.
- [6] GAO Y F, XIONG Y, GAO X Y, et al. Retrieval-augmented generation for large language models: a survey [EB/OL]. (2023-12-18) [2024-06-02]. <https://arxiv.org/abs/2312.10997v5>.
- [7] WEI J, WANG X Z, SCHUURMANS D, et al. Chain-of-thought prompting elicits reasoning in large language models [C]//Proceedings of the 36th Conference on Neural Information Processing Systems. New York: NIPS, 2022: 24824-24837.
- [8] STOLFO A, JIN Z J, SHRIDHAR K, et al. A causal framework to quantify the robustness of mathematical reasoning with language models [C]//Proceedings of the 61st Annual Meeting of the Association for Computational Linguistics (Volume 1: Long Papers). Stroudsburg: ACL,
- [9] HENDRYCKS D, BURNS C, KADAVATH S, et al. Measuring mathematical problem solving with the MATH dataset[EB/OL]. (2021-03-05) [2024-06-02]. <https://arxiv.org/abs/2103.03874>.
- [10] COBBE K, KOSARAJU V, BAVARIAN M, et al. Training verifiers to solve math word problems [EB/OL]. (2021-10-27) [2024-06-02]. <https://arxiv.org/abs/2110.14168>.
- [11] HOSSEINI M J, HAJISHIRZI H, ETZIONI O, et al. Learning to solve arithmetic word problems with verb categorization[C]//Proceedings of the 2014 Conference on Empirical Methods in Natural Language Processing (EMNLP). Stroudsburg: ACL, 2014: 523-533.
- [12] PATEL A, BHATTAMISHRA S, GOYAL N. Are NLP models really able to solve simple math word problems? [C]//Proceedings of the 2021 Conference of the North American Chapter of the Association for Computational Linguistics: Human Language Technologies, Online. Stroudsburg: ACL, 2021: 2080-2094.
- [13] TALMOR A, HERZIG J, LOURIE N, et al. CommonsenseQA: a question answering challenge targeting commonsense knowledge [C]//Proceedings of the 2019 Conference of the North American Chapter of the Association for Computational Linguistics: Human Language Technologies. Stroudsburg: ACL, 2019: 4149-4158.
- [14] DU Z X, QIAN Y J, LIU X, et al. GLM: general language model pretraining with autoregressive blank infilling [C]//Proceedings of the 60th Annual Meeting of the Association for Computational Linguistics (Volume 1: Long Papers). Stroudsburg: ACL, 2022: 320-335.
- [15] JI H Z, KE P, HUANG S H, et al. Language generation with multi-hop reasoning on commonsense knowledge graph [C]// Proceedings of the 2020 Conference on Empirical Methods in Natural Language Processing (EMNLP), Online. Stroudsburg: ACL, 2020: 725-736.
- [16] LING W, YOGATAMA D, DYER C, et al. Program induction by rationale generation: learning to solve and explain algebraic word problems[C]//Proceedings of the 55th Annual Meeting of the Association for Computational Linguistics (Volume 1: Long Papers). Stroudsburg: ACL, 2017: 158-167.
- [17] GEVA M, KHASHABI D, SEGAL E, et al. Did Aristotle use a laptop? A question answering benchmark with implicit reasoning strategies[J]. *Transactions of the Association for Computational Linguistics*, 2021, 9: 346-361.
- [18] RADFORD A, WU J, CHILD R, et al. 2023: 545-561.

- Language models are unsupervised multitask learners [EB/OL]. (2019-02-14) [2024-06-02]. <https://openai.com/research/language-unsupervised>.
- [19] GUU K, LEE K, TUNG Z, et al. Retrieval augmented language model pre-training [C]// Proceedings of the 37th International Conference on Machine Learning. New York: PMLR, 2020: 3929-3938.
- [20] RUBIN O, HERZIG J, BERANT J. Learning to retrieve prompts for in-context learning [C]// Proceedings of the 2022 Conference of the North American Chapter of the Association for Computational Linguistics: Human Language Technologies. Stroudsburg: ACL, 2022: 2655-2671.
- [21] MISHRA S, KHASHABI D, BARAL C, et al. Cross-task generalization via natural language crowdsourcing instructions [C]// Proceedings of the 60th Annual Meeting of the Association for Computational Linguistics (Volume 1: Long Papers). Stroudsburg: ACL, 2022: 3470-3487.
- [22] LIU H K, TAM D, MUQEETH M, et al. Few-shot parameter-efficient fine-tuning is better and cheaper than in-context learning [C]// Proceedings of the 36th International Conference on Neural Information Processing Systems. New York: NIPS, 2022: 1950-1965.
- [23] MIN S, LEWIS M, HAJISHIRZI H, et al. Noisy channel language model prompting for few-shot text classification [C]// Proceedings of the 60th Annual Meeting of the Association for Computational Linguistics (Volume 1: Long Papers). Stroudsburg: ACL, 2022: 5316-5330.
- [24] SUZGUN M, SCALES N, SCHÄRLI N, et al. Challenging BIG-bench tasks and whether chain-of-thought can solve them [C]// Findings of the Association for Computational Linguistics: ACL 2023. Stroudsburg: ACL, 2023: 13003-13051.
- [25] KOJIMA T, GU S S, REID M, et al. Large language models are zero-shot reasoners [C]// Proceedings of the 36th International Conference on Neural Information Processing Systems. New York: NIPS, 2022: 22199-22213.
- [26] JIN M, YU Q K, SHU D, et al. The impact of reasoning step length on large language models [C]// Findings of the Association for Computational Linguistics: ACL 2024. Stroudsburg: ACL, 2024: 1830-1842.
- [27] ZHOU D, SCHÄRLI N, HOU L, et al. Least-to-most prompting enables complex reasoning in large language models [EB/OL]. (2022-05-21) [2024-06-02]. <https://arxiv.org/abs/2205.10625>.
- [28] ZHU X Y, WANG J J, ZHANG L, et al. Solving math word problems via cooperative reasoning induced language models [C]// Proceedings of the 61st Annual Meeting of the Association for Computational Linguistics (Volume 1: Long Papers). Stroudsburg: ACL, 2023: 4471-4485.
- [29] ZELIKMAN E, WU Y, MU J, et al. Star: bootstrapping reasoning with reasoning [C]// Proceedings of the 36th International Conference on Neural Information Processing Systems. New York: NIPS, 2022: 15476-15488.
- [30] LU Q Y, QIU B P, DING L, et al. Error analysis prompting enables human-like translation evaluation in large language models [C]// Findings of the Association for Computational Linguistics: ACL 2024. Stroudsburg: ACL, 2024: 8801-8816.
- [31] JIANG H Q, WU Q H, LUO X F, et al. LongLLMLingua: accelerating and enhancing LLMs in long context scenarios via prompt compression [C]// Proceedings of the 62nd Annual Meeting of the Association for Computational Linguistics (Volume 1: Long Papers). Stroudsburg: ACL, 2024: 1658-1677.

选择与回答提示：引导大型语言模型提升零样本推理能力

王煜芳^{1, 2*}, 唐雪嵩^{1, 2}, 郝矿荣^{1, 2}

1. 东华大学 信息科学与技术学院, 上海 201620

2. 东华大学 数字化纺织服装技术教育部工程研究中心, 上海 201620

摘要：大型语言模型 (large language model, LLM) 在自然语言处理 (natural language processing, NLP) 的多项任务中展示出显著的泛化能力。对于多步骤推理任务，思维链 (chain-of-thought, CoT) 提示有助于逐步思考，从而提升性能。然而，尽管 LLM 取得了重大进展，但目前的 CoT 提示技术在参数规模较小的模型上仍表现不佳。此外，常见的少样本思维链 (few-shot CoT) 提示依赖于一组人工编写的示例，其性能取决于这些示例的质量，并随任务的具体要求而变化。为了解决这些局限性，提出了一种名为“选择-回答提示” (select-and-answer prompting, SAP) 的方法，以在无需人工编写示例的情况下增强语言模型在推理任务上的表现。该方法分为两步：引导模型进行初步分析，并基于提示生成多个候选答案；让模型从这些候选答案中选出最终答案。该文提出的提示策略针对 2 种不同规模的语言模型和 6 个数据集进行了评估。试验结果表明，在 ChatGLM-6B 上，SAP 的性能在全部数据集上均优于 few-shot CoT；在 GPT-3.5 上，SAP 的性能与 few-shot CoT 相当，且在大多数情况下优于 zero-shot CoT。这些结果表明，SAP 能显著提升语言模型在推理任务中的准确性。

关键词：零样本学习；大型语言模型；推理问题；思维链提示

Subgraph Matching on Multi-Attributed Graphs Based on Contrastive Learning

LIU Bozhi, FANG Xiu, SUN Guohao*, LU Jinhua

School of Computer Science and Technology, Donghua University, Shanghai 201620, China

Abstract: Graphs have been widely used in fields ranging from chemical informatics to social network analysis. Graph-related problems become increasingly significant, with subgraph matching standing out as one of the most challenging tasks. The goal of subgraph matching is to find all subgraphs in the data graph that are isomorphic to the query graph. Traditional methods mostly rely on search strategies with high computational complexity and are hard to apply to large-scale real datasets. With the advent of graph neural networks (GNNs), researchers have turned to GNNs to address subgraph matching problems. However, the multi-attributed features on nodes and edges are overlooked during the learning of graphs, which causes inaccurate results in real-world scenarios. To tackle this problem, we propose a novel model called subgraph matching on multi-attributed graph network (SGMAN). SGMAN first utilizes improved line graphs to capture node and edge features. Then, SGMAN integrates GNN and contrastive learning (CL) to derive graph representation embeddings and calculate the matching matrix to represent the matching results. We conduct experiments on public datasets, and the results affirm the superior performance of our model.

Keywords: subgraph matching; graph neural network (GNN); multi-attributed graph; contrastive learning (CL)

CLC number: TP339.1

Document code: A

Article ID: 1672-5220(2025)05-0523-11

Open Science Identity
(OSID)



0 Introduction

In recent years, there has been extensive research on graph-related problems, with applications ranging from chemical informatics to social network analysis. Graph-related problems become increasingly significant, with subgraph matching standing out as one of the most challenging tasks. Subgraph matching aims to find all subgraphs in the data graph that are isomorphic to the query graph. Figure 1 illustrates a subgraph matching application in social network analysis. Consider a scenario where a work group requires its member A to be acquainted with both individuals B and C , where A , B and C can represent labels for family members, jobs, geographic locations, etc. We can formulate a query graph and utilize a subgraph matching algorithm to search

for the groups meeting the specified conditions in a known extensive social network graph. As shown in Fig. 1, the algorithm finds two matching subgraphs: one consisting of A_1 , B_1 and C , and another consisting of A_2 , B_2 and C . E and F are other unrelated nodes in the data graph.

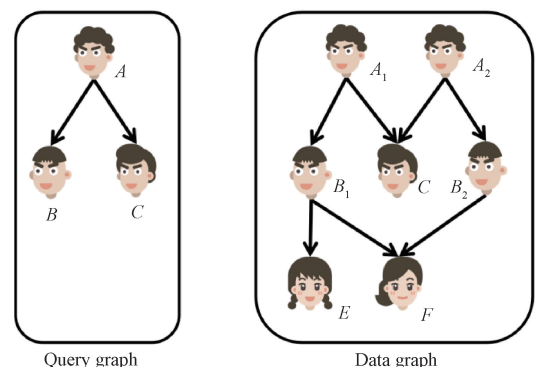


Fig. 1 Subgraph matching applied in social network analysis

Subgraph matching is a challenging NP-complete problem. Traditional methods typically utilize search strategies to analyze the neighbor structure of nodes and sequentially match all nodes, presenting a substantial computational challenge, especially when dealing with extensive real datasets. Therefore, researchers seek more efficient alternatives. The advent of graph neural networks (GNNs) has spurred the development of several GNN-based methods for subgraph matching, including Sub-GMN^[1], AEDNet^[2] and DMPNN^[3]. These methods derive embedding representations by learning graph features, followed by predicting the matching matrix. The robust learning capabilities of GNNs ensure accurate predictions, while the parallel processing prowess of GPUs ensures efficient computations.

While existing GNN-based methods have made some progress in subgraph matching, they focus mainly on basic structural matching. However, real-world graphs are intricate, with multiple attributes on nodes and edges. Figure 2 provides an example of subgraph matching on multi-attributed graphs, displaying nodes with diverse attribute details and multiple interconnections among them. Considering both attribute and structure

information, the matching results will be the subgraph consisting of A_1 , B_1 and C , while the subgraph consisting of A_2 , B_2 and C can not match the query graph. The existing GNN-based methods focus only on structural

matching, and in this case, the subgraph consisting of A_2 , B_2 and C will appear in their matching results. Hence, innovative approaches are required to address subgraph matching on multi-attributed graphs.

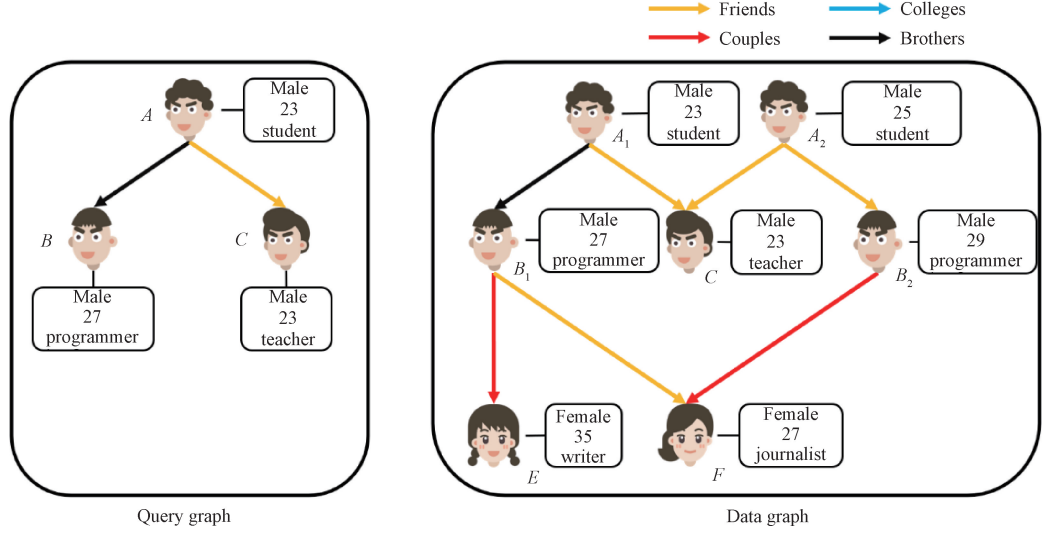


Fig. 2 Example of subgraph matching on multi-attributed graphs

The concept of line graph was first proposed in the graph theory^[4] to address various graph theoretic problems in mathematical modeling, including the shortest path and the minimum spanning tree problems. In a line graph, edges are transformed into vertices, representing the adjacency of edges in the original graph. In recent years, researchers have utilized the line graph to enrich the learned features of GNNs, enabling them to tackle diverse graph-related tasks such as node classification^[5] and link prediction^[6]. We realize that the line graph offers a convenient way to acquire abstract edge information, addressing previous limitations of ignoring the attribute information on the nodes and edges when matching subgraphs. In our proposed model, we adopt the line graph to acquire attribute information. Contrastive learning (CL)^[7] has been applied in many scenarios, such as computer vision (CV)^[8] and graph data mining^[9]. CL effectively improves the embedding quality by minimizing the distance between positive pairs in the embedding space. As a typical learning method, CL can mine the intrinsic features of data to improve the downstream task^[10]. We recognize that subgraph matching inherently involves contrastive relationships between nodes (matching nodes and mismatching nodes). Utilizing these contrastive relationships can improve the quality of the embeddings learned by GNNs, thereby improving the matching accuracy. Existing methods tend to ignore these contrastive relationships contained in subgraph matching, which can lead to less robust model prediction performance. Therefore, in our proposed model, we apply CL to improve the quality of the embeddings learned by GNNs.

While the line graph can acquire attribute

information, it may lead to information loss and an increase in graph complexity, affecting the learning of graphs. Therefore, the first challenge in our method is how to enhance the line graph to avoid information loss and an increase in graph complexity. In addition, the key to CL is generating appropriate anchors, positive and negative instances. Inappropriate positive and negative instances will directly lead to low-quality embeddings. Hence, the second challenge is how to construct a CL framework to select appropriate contrastive pairs and improve the quality of embeddings. To address these challenges, our model adds reverse edges when transforming the line graph and utilizes the matching relationship between nodes in the query graph and data graph.

Overall, we summarize the main contributions of this research as follows.

1) To obtain complete and accurate features on edges, we propose an improved line graph. The new line graph adds reverse edges to those edges in the original graph. This ensures the converted line graph retains complete information, allowing our model to capture comprehensive edge features while maintaining the low complexity of the line graph structure.

2) To improve the quality of embeddings, we construct a CL framework in our model. To our knowledge, it is the first to incorporate CL into subgraph matching.

3) We conduct experiments on three public datasets, and the experimental results show that our model outperforms existing models, proving the effectiveness of our model.

In the first section of this paper, the related work on

subgraph matching is presented; in the second section, problem definition and preliminaries are described; in the third section, the methodology and the model proposed in this paper are presented; in the fourth section, the experimental results are presented.

1 Related Work

The existing methods to deal with subgraph matching problems can be divided into two categories: traditional search-based methods and GNN-based methods. We review the related work based on these two categories.

1.1 Traditional search-based methods

Traditional methods mainly employ a search strategy to analyze the neighbor structure of nodes and match all nodes sequentially. The first subgraph isomorphism algorithm proposed by Ullmann^[11] uses a depth-first search strategy to enumerate subgraphs in the data graph that match the query graph. VF^[12] makes improvements in the matching order and pruning strategy. Since then, many improved algorithms have been proposed that consider more complex substructure features to prune the results, thereby speeding up the search process. For example, GraphQL^[13] utilizes a depth-first search spanning tree to filter candidate nodes. These algorithms enhance candidate node filtering from various perspectives, effectively reducing the frequency of backtracking during the search process. In addition, some index-based matching algorithms have been proposed. Among them, GraphGrep^[14] is a typical path-based indexing algorithm that enumerates paths in the graph with lengths lower than a predefined value as indexed features and uses the indices to reduce the search space. To achieve distributed processing, the approach in Ref. [15] decomposes the query graph based on node degrees, thus leveraging the resulting subqueries as an index. By reusing indexing information, they significantly reduce the indexing load, which becomes crucial in scenarios where multiple queries are issued simultaneously. Most of the methods proposed in recent years focus on filtering candidate sets. G-finder^[16] employs two key techniques: a novel auxiliary data structure for efficiently indexing candidate vertices, and a dynamic filtering and refinement strategy to early prune false candidates. CECI^[17] introduces three unique techniques: BFS-based filtering and reverse-BFS-based refinement for early pruning of unpromising candidates; set intersection for faster candidate verification; search cardinality-based cost estimation for proactive detection and division of large embedding clusters. GuP^[18] proposes a subgraph matching algorithm with pruning based on guards. By attaching a guard to each candidate vertex and edge, GuP adaptively filters out unnecessary candidates depending on the search state at each step. MGSM^[19] presents a new matching algorithm called Tps, which is noted for its strategic vertex searching order. To achieve efficient graph indexing, a graph indexing scheme is introduced in

Ref. [20], which operates by monotonically counting path and cycle features under relaxed semantics.

All of the traditional search-based methods face the common problem that they have very high computational complexity and are hard to apply to large-scale datasets. What's more, they do not consider the attribute information in the graph, which means that they cannot be applied to the subgraph matching problem on multi-attributed graphs.

1.2 GNN-based methods

With the rising popularity of GNNs, researchers have advocated for using neural network models to address subgraph matching problems. Sub-GMN directly forces node-level embeddings of two matched nodes to be close to each other and makes the corresponding node-level embeddings similar by combining GCN^[21] and NTN^[22]. NeuroMatch^[23] decomposes query and data graphs into small subgraphs, training the model to capture geometric constraints corresponding to subgraph relations, and then performing subgraph matching directly in the embedding space. AEDNet^[24] proposes an adaptive edge-deleting mechanism to remove extra edges to ensure consistency of the adjacency structure of matched nodes. DMPNN^[25] starts from a particular edge-to-vertex transform and exploits the isomorphism property in the edge-to-vertex dual graphs.

In other graph-related scenarios, researchers have developed models to extract features from multi-attributed graphs. GATNE^[24] divides the node embedding into two parts to learn different types of information, respectively, and finally combines them to obtain node representations containing comprehensive information. For graphs containing different edge relationships, RGCN^[25] employs a dedicated aggregation strategy for each edge type, applying distinct transformations based on the type of edge. CompGCN^[26] leverages a variety of composition operations from knowledge graph embedding techniques^[27] to jointly embed both nodes and relations in a graph.

Compared with the traditional search-based methods, the existing GNN-based methods can achieve better matching efficiency because of the robust learning of GNNs and the parallel processing ability of GPUs. The ways of learning feature information lead to differences in the performance of subgraph matching accuracy. In our model, we apply the CL to learn feature information and improve the quality of the embeddings, thereby improving the subgraph matching accuracy.

2 Problem Definition and Preliminaries

2.1 Problem definition

A graph is denoted as a tuple $\{V, E, F^n, F^e\}$, where V is the node set, E is the edge set, and F^n and F^e are feature functions that map each node and each edge to feature vectors, respectively. In this paper, $Q = \{V_Q, E_Q, F_Q^n, F_Q^e\}$ represents a query graph, and $G = \{V_G, E_G, F_G^n, F_G^e\}$ stands for a data graph.

The subgraph matching on multi-attributed graphs is an injection function $m: V_Q \rightarrow V_G$ which satisfies:

- 1) $\forall u \in V_Q, m(u) \in V_G$ and $F^m(u) = F^m(m(u))$;
- 2) $\forall (u_a, u_b) \in E_Q, (m(u_a), m(u_b)) \in E_G$ and $F^e(u_a, u_b) = F^e(m(u_a), m(u_b))$.

Here, u denotes a node; u_a and u_b represent two distinct nodes. There may be multiple mappings from V_Q to V_G . We use $M(Q, G) = \{m_1, m_2, \dots, m_k\}$ for the set of all mappings. The subgraph matching problem is to find the set of all mappings $M(Q, G)$ for a given pair of graphs.

2.2 Line graph

The line graph H of a data graph G represents the adjacencies between edges of G with an edge-to-vertex map denoted as $g: E_G \rightarrow V_H$.

A line graph H of a data graph G is obtained by associating a vertex $v' \in V_H$ with each edge $e \in E_G$ and connecting two vertices $u', v' \in V_H$ with an edge from u' to v' if and only if the destination of the corresponding edge d in the data graph G is exactly the source of e . Formally, we have the following conclusions.

- 1) $\forall e = (u, v) \in E_G, Y_G(e) = X_H(g(e))$;
- 2) $\forall v' \in V_H, X_H(v') = Y_G(g^{-1}(v'))$;
- 3) $\forall d, e \in E_G, u' = g(d) \in V_H, v' = g(e) \in V_H$;
- 4) $\forall e' = (u', v') \in E_H, d = g^{-1}(u') \in E_G, e = g^{-1}(v') \in E_G$.

Here, e and d denote different edges; v denotes a node; Y_G denotes the edge feature function of the data graph G ; X_H denotes the node feature function of the line graph H . Figure 3 demonstrates the process of converting an original graph into a line graph. In the line graph, each node denotes an edge of the original graph. If the destination of an edge connects to the source of another edge in the original graph, an edge is formed in the line graph, corresponding to node b in the original graph.

This process continues for the remaining edges in the line graph. Undirected graphs can be considered as special cases of bidirectional graphs.

However, this type of line graph may pose some problems, such as the loss of information for nodes a and c as depicted in the original graph. In this paper, we propose a new way of line graph construction to avoid such problems.

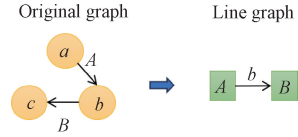


Fig. 3 Example of converting an original graph to a line graph

3 Methodology

3.1 Overview

Our proposed model, subgraph matching on multi-attributed graph network (SGMAN), mainly consists of four modules: a graph transform module, a message passing module, an embedding contrast module, and a result prediction module. Figure 4 shows an overview of SGMAN. Firstly, in the graph transform stage, the original graphs convert into line graphs. Secondly, in the message passing stage, input original graphs and line graphs, employing convolutional operations to learn graph features (where h and z represent embeddings). Thirdly, in the embedding contrast stage, we utilize the contrastive relationships between nodes to construct contrastive pairs, aiming to improve the quality of embeddings by minimizing the distance between anchors and positives and maximizing the distance between anchors and negatives. Finally, in the result prediction stage, compute the matching matrix as a prediction.

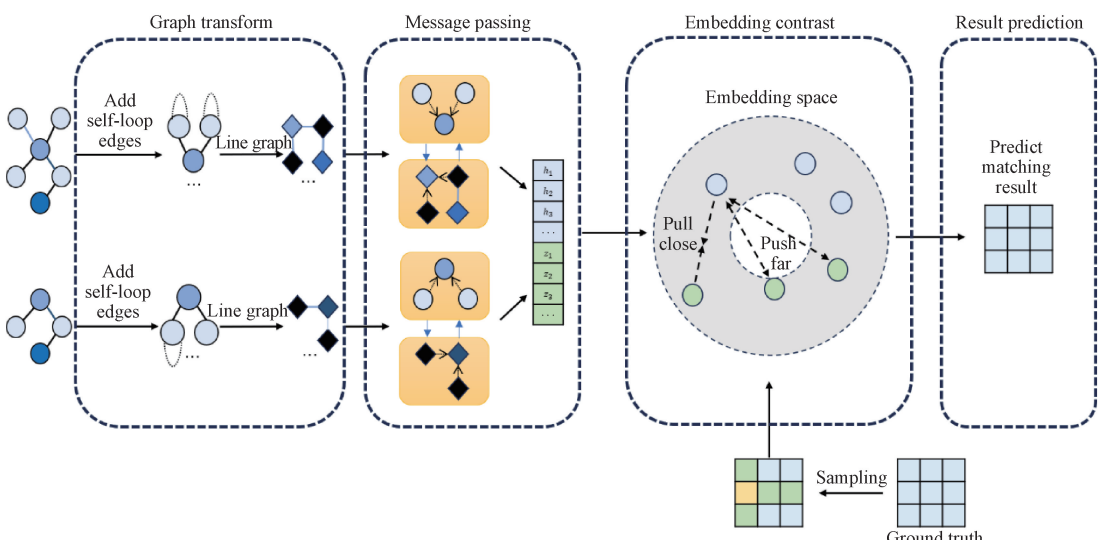


Fig. 4 Model overview of SGMAN

3.2 Graph transform

In the graph transform stage, we first convert the original graphs to line graphs. However, as mentioned in subsection 2.2, the way of constructing line graphs will lead to the problem of information loss, and in the subgraph matching process, such information loss will result in two non-isomorphic graphs having isomorphic line graphs.

Figure 5 is an example of problems caused by line

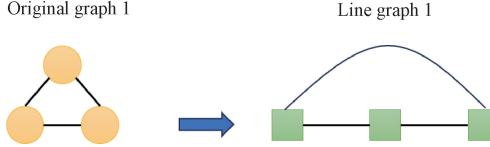


Fig. 5 Example of problems caused by line graphs

DMPNN realizes this problem and proposes to add reverse edges to each edge of the original graph to prevent information loss in the line graph. However, this method introduces significant redundancy. As shown in Fig. 6(a), there are four edges b in the line graph, and such redundancy will limit the performance of graph learning tasks. To deal with the above-mentioned problems, we propose a new way to construct a line graph. First, we add self-loop edges to nodes with a degree of 1. This operation ensures that all nodes have a degree higher than 1. Then, we convert the new graph to the improved line graph. Figure 6(b) is an example of our way. The advantages of our improved line graph can be summarized below.

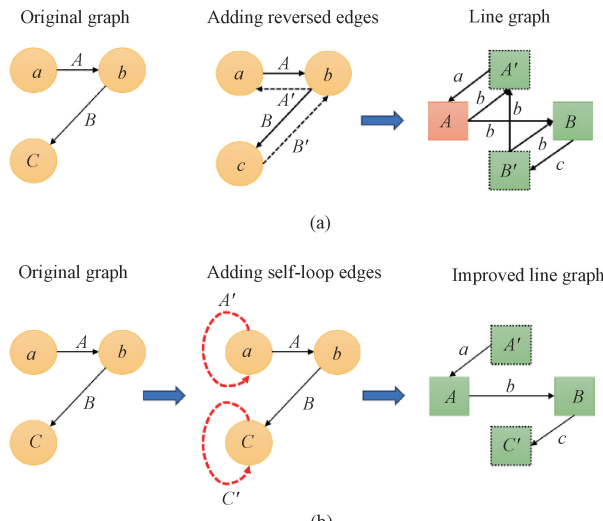


Fig. 6 Comparison of line graphs construction between DMPNN and our method; (a) construction of line graph in DMPNN; (b) construction of line graph in our method

1) Preserve the integrity of information. Our improved line graph avoids the loss of node information by introducing self-loop edges, ensuring that nodes with a degree of 1 are retained, thus maintaining the completeness of graph information.

graphs. The original graph 1 and original graph 2 are two non-isomorphic graphs, but they have isomorphic line graphs. We identify that the problem arises from the omission of nodes with a degree of 1 in the original graph during the conversion to a line graph. Neglecting this situation and directly employing line graphs to capture node and edge features will result in the model learning inaccurate features, thereby leading to poor performance in subgraph matching tasks.

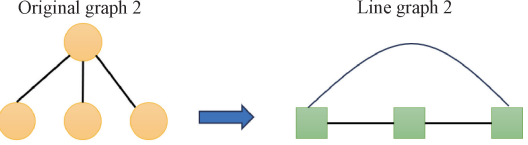


Fig. 5 Example of problems caused by line graphs

2) Reduce graph complexity. Compared to DMPNN, our improved line graph significantly reduce graph complexity and eliminates redundant information. This facilitates the following graph learning process, enhancing overall efficiency.

3.3 Message passing

After obtaining the improved line graph, we apply convolution to learn the graph features in the message passing stage. Figure 7 is a description of this stage. In the original graph, a node obtains information from its neighbor nodes, and at the same time, obtains information from the corresponding nodes in the line graph.

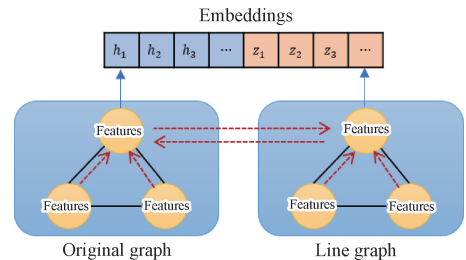


Fig. 7 Schematic of message passing process between original graph and line graph

In our model, the edge embeddings in the original graph are the node embeddings in the corresponding line graph. To ensure that nodes in the original graph capture features from edges, we combine the embeddings of nodes in the line graph with the embeddings of nodes in the original graph as the new embeddings in the next layer. We then apply similar operations in the line graph, allowing its nodes to learn features from the original graph. By doing so, nodes can aggregate new information from neighbor structures in the next layer.

The convolution equation is given as

$$\mathbf{h}^{l+1} = (\gamma_0 + \gamma_1) \mathbf{h}^l + \frac{2\gamma_1}{\lambda} (\mathbf{D} + \mathbf{I}_m) \mathbf{h}^l + \frac{\gamma_1}{\lambda} \mathbf{B}^T \mathbf{z}^l, \quad (1)$$

where \mathbf{D} is the degree matrix; \mathbf{I}_m is the identity matrix; \mathbf{B} is the oriented incidence matrix; \mathbf{h}^l is the feature vector

corresponding to nodes in the original graph in the l th layer; \mathbf{z}' is the feature vector corresponding to nodes in the line graph in the l th layer; γ denotes the trainable parameter; λ is the scaling parameter.

3.4 Embedding contrast

After message passing, in the embedding contrast module, we utilize the contrastive relationships of nodes to improve the quality of embedding by minimizing the distance of anchors and positives while simultaneously maximizing the distance of anchors and negatives in the embedding space.

We employ the exact subgraph matching algorithm VF3^[28] to generate the binary ground truth, denoted as g , for the query graph with j nodes and the data graph with k nodes, and $g[j][k] = 1$ means a match for the j th node in the query graph and the k th node in the data graph. We set the k th node in the data graph with $g[j][k] = 1$ as the positive instance for the j th node in the query graph, and the remaining nodes in the data graph with $g[j][k] = 0$ as negative instances.

It is worth noting that a query graph may match multiple matching subgraphs in the data graph, and therefore, one node in a query graph can have multiple matching nodes in a data graph. In such cases, one node will have multiple positive instances. Therefore, different from self-supervised CL, the contrastive loss in our method will consider multiple positive instances. The formula for calculating the contrastive loss L is

$$L = \sum_{i \in I} \frac{-1}{|P(i)|} \sum_{p \in P(i)} \frac{\exp(\mathbf{h}_i \cdot \mathbf{h}_p / \tau)}{\sum_{a \in A(i)} \exp(\mathbf{h}_i \cdot \mathbf{h}_a / \tau)}, \quad (2)$$

where the index i is the anchor; I contains all data in a batch; $P(i)$ is the set of indices of all positives in the batch, the other indices are negatives, and $|P(i)|$ is its cardinality; $A(i)$ represents $I \setminus \{i\}$; τ is a scalar temperature parameter; \mathbf{h} denotes embedding vectors in different layers; \cdot denotes the inner (dot) product. The purpose of this loss function is to minimize the distance between the matching nodes in the embedding space while maximizing the distance between mismatching nodes. Calculating the loss in this way offers the following advantages.

1) Attractive power with multiple positives. We utilize the matching relationship between nodes to construct multiple positive instances. The loss encourages the nodes and positives to close in the embedding space, resulting in a better quality of the embedding.

2) Contrastive power with many negatives. This property is crucial for representation learning using CL, as several studies have demonstrated improved performance with an increased number of negatives. Therefore, we regard all mismatching nodes as negatives to enhance the performance of CL.

3.5 Result prediction

In the result prediction stage, the model outputs the

prediction results for subgraph matching. Following the preceding steps, we obtain embeddings of nodes. We calculate the similarity between the embeddings of the nodes in the query graph and the data graph as the similarity matrix. This matrix reflects the matching results of specific nodes between the two graphs, serving as the output of the model.

4 Experiments

We conduct extensive experiments on three publicly available datasets and compare the performance with state-of-the-art GNN-based methods to validate our proposed model. Our goal is to answer the following questions.

Q1: How does SGMAN perform compared to other GNN-based methods?

Q2: How do different parts of SGMAN contribute to the final performance?

Q3: How do different parameter settings affect the performance of SGMAN?

Q4: How does the performance improve when incorporating the proposed components into other graph models?

4.1 Experimental setup

In this section, we introduce the datasets used in the experiment, the baselines for comparison, the evaluation metrics and the implementation details.

4.1.1 Datasets

Tables 1 and 2 show the statistics of three datasets: the dataset Regular, which uses 3-stars, triangles, tailed triangles and chordal cycles as patterns; the mutagenic compound dataset Mutag with 24 patterns; the heterogeneous dataset Complex with 75 random patterns. Train, valid and test denote the number of graphs in the corresponding dataset, respectively. DMPNN provides these datasets, and to ensure a fair comparison, we follow the same processing method as DMPNN for dividing the train, valid and test sets in the dataset, and the details are shown in Table 1. In Table 2, $|p|$ and $|g|$ correspond to query graphs and data graphs, $|V|$ is the number of vertexes, $|E|$ is the number of edges, $|X|$ is the number of labeled types of nodes, $|Y|$ is the number of labeled types of edges. Max and avg represent the maximum and average values of the number of nodes in all graphs in the dataset, respectively.

Table 1 Distribution of graphs across dataset

Dataset	Train	Valid	Test
Regular	6 000	4 000	10 000
Mutag	1 400	1 500	1 500
Complex	358 000	44 000	44 000

Table 2 Statistics of graph features

Metric	Regular		Mutag		Complex	
	Max	Avg	Max	Avg	Max	Avg
$ V_p $	4.0	3.8	4.0	3.5	8.0	5.2
$ E_p $	10.0	7.5	3.0	2.5	8.0	5.9
$ X_p $	1.0	1.0	2.0	1.5	8.0	3.4
$ Y_p $	1.0	1.0	2.0	1.5	8.0	3.8
$ V_g $	30.0	18.8	28.0	17.9	64.0	32.6
$ E_g $	90.0	62.7	66.0	39.6	256.0	73.6
$ X_g $	1.0	1.0	16.0	9.0	7.0	3.3
$ Y_g $	1.0	1.0	16.0	9.4	4.0	3.0

4.1.2 Baselines

We select the competitive network models capable of handling multi-relational graphs as baselines, including TXL, RGCN, RGIN, CompGCN and DMPNN. TXL is a 6-layer transformer encoder with additional memory. RGCN is a 3-layer RGCN with the block-diagonal decomposition. We follow the same setting in DMPNN to use mean-pooling in the message propagation part. RGIN combines GIN and RGCN: adding a 2-layer MLP^[29] after each relational convolutional layer and using the sum aggregator. These models are versatile for learning multi-relational graph data. We use the obtained graph representations to calculate the matching matrix, which is then compared with the ground truth obtained from the VF3 exact matching algorithm.

4.1.3 Evaluation metrics

Our main focus is to evaluate the performance of different graph models in predicting subgraph matching. We consider subgraph matching as a regression problem and compare the prediction results with the ground truth, calculating the mean absolute error (MAE), root mean square error (RMSE)^[30] and accuracy (ACC). MAE represents the average of the absolute errors of the predicted and actual matching results. RMSE represents the sample standard deviation of the difference between the correctly predicted and actual matching results. ACC represents the accuracy

of the matching results. Lower MAE and RMSE values indicate better performance, while higher ACC values signify improved accuracy.

4.1.4 Implementation details

We first perform a complexity analysis. In the phase of converting the graph into a line graph, the complexity is $O(n + e)$. In the phase of message passing and embedding contrast, the complexity is $O(n)$.

To ensure a fair comparison, we maintain the uniformity in embedding dimensions, hidden sizes and filter numbers, setting them all to 64. The segment size and memory size in TXL are 128, based on the computational complexity consideration. We use MSE to train the model and select the best model based on the results of the development set. The optimizer is AdamW^[31] with a base learning rate of 1×10^{-3} and a weight decay coefficient of 1×10^{-5} . LeakyReLU serves as the activation function across all modules. Training and evaluations of models are done on an NVIDIA 4090 GPU under the PyTorch and DGL frameworks.

4.2 Overall performance (Q1)

We compare the performance of SGMAN with baselines. Table 3 shows the performance of each model on the three datasets. The best performance is shown in bold. Imp represents the improvement in performance between SGMAN and other models; w/o represents without in the ablation experiment.

Table 3 Overall performance comparison

Model	Regular			Mutag			Complex		
	MAE	RMSE	ACC	MAE	RMSE	ACC	MAE	RMSE	ACC
TXL	10.721	15.263	0.819	0.830	1.895	0.912	9.576	43.055	0.762
RGCN	12.676	15.833	0.847	0.227	1.043	0.947	8.939	27.842	0.805
RGIN	10.074	15.578	0.872	0.203	0.545	0.957	6.377	24.231	0.836
CompGCN	11.790	16.478	0.865	0.211	0.809	0.956	7.714	26.134	0.817
DMPNN	10.016	15.680	0.878	0.167	0.474	0.961	3.186	22.778	0.847
SGMAN	8.332	13.229	0.896	0.046	0.145	0.992	2.465	17.634	0.877
Imp	0.168	0.156	0.018	0.724	0.694	0.031	0.226	0.226	0.030
w/o CL&loop	9.944	15.566	0.858	0.191	0.440	0.958	3.982	28.392	0.801
w/o CL	8.833	13.778	0.884	0.070	0.426	0.965	2.519	20.015	0.852
w/o loop	8.736	13.234	0.887	0.079	0.431	0.963	2.848	20.237	0.849

Based on the data presented in Table 3, SGMAN outperforms other models across all evaluation metrics and datasets, highlighting the efficacy of our approach. As the complexity of graph attributes increases, SGMAN demonstrates the best performance compared to other models, particularly in Mutag and Complex datasets. This is because line graphs leverage their significant advantage on multi-attributed graphs, and combined with CL, provide higher-quality embeddings, resulting in better matching results. Even on the Regular dataset where graph attributes are simple, SGMAN performs well by capturing higher-order information, outperforming baselines.

4.3 Analysis of ablation experiments (Q2)

We conduct ablation experiments to assess the contribution of each component to the model. Our study comprises two primary components: adding self-loop edges to the original graph and transforming the original graph into a line graph; integrating CL into the model and utilizing the contrastive relationships between nodes to improve the quality of embeddings. The ablation experiment is categorized into three parts: removing only loop from the model, removing only CL, and removing both self-loop and CL. The results are presented in the last three rows of Table 3.

The performance of the model decreases when specific components are excluded, highlighting the effectiveness of our proposed method. Notably, the model exhibits a poorer performance when both loop and CL are removed. In addition, on the Mutag and Complex datasets containing multiple attributes, models without CL perform slightly better than those without line graphs. This is because line graphs offer significant advantages in capturing features on multi-attributed graphs, and the

benefits of CL are built upon the rich feature information obtained from line graphs.

4.4 Parameter analyses (Q3)

We conduct experiments on the Regular and Mutag datasets to investigate how the temperature parameter τ impacts subgraph matching accuracy. The results are depicted in Fig. 8. The model achieves optimal results when τ is between 0.075 and 0.125. According to Ref. [7], a smaller temperature parameter is more beneficial for training, allowing a greater focus on learning from hard negative instances. This facilitates the separation of similar node embeddings in the embedding space. Conversely, a higher temperature parameter makes distinguishing hard negative instances from positive instances challenging, resulting in lower-quality embeddings. Therefore, selecting an appropriate temperature parameter ensures a more uniform distribution in the embedding space, leading to better results.

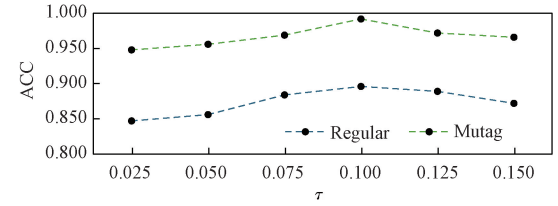


Fig. 8 Impact of temperature parameter on ACC of Mutag and Regular datasets

4.5 Performance on other models (Q4)

We assess the impact of improved line graphs and CL on baseline models, focusing our evaluation on Regular and Mutag datasets for efficiency. The results are shown in Tables 4 and 5, and w/ represents with in the ablation experiment.

Table 4 Performance comparison after introducing self-loop edges on datasets

Model	Regular			Mutag		
	MAE	RMSE	ACC	MAE	RMSE	ACC
TXL	w/o loop	10.721	15.263	0.819	0.830	1.895
	w/ loop	9.578	14.251	0.836	0.622	1.122
RGCN	w/o loop	12.676	15.833	0.847	0.227	1.043
	w/ loop	9.910	14.621	0.858	0.145	0.570
RGIN	w/o loop	10.074	15.578	0.872	0.203	0.545
	w/ loop	9.632	15.309	0.882	0.075	0.248
CompGCN	w/o loop	11.790	16.478	0.865	0.211	0.809
	w/ loop	10.364	14.568	0.876	0.106	0.440
DMPNN	w/o loop	10.016	15.680	0.878	0.167	0.474
	w/ loop	9.541	14.504	0.888	0.083	0.378

Table 5 Performance comparison after introducing CL on datasets

Model	Regular			Mutag		
	MAE	RMSE	ACC	MAE	RMSE	ACC
TXL	w/o CL	10.721	15.263	0.819	0.830	1.895
	w/ CL	9.988	14.322	0.842	0.722	1.013
RGCN	w/o CL	12.676	15.833	0.847	0.227	1.043
	w/ CL	10.697	15.378	0.857	0.210	0.556
RGIN	w/o CL	10.074	15.578	0.872	0.203	0.545
	w/ CL	9.929	15.091	0.889	0.123	0.357
CompGCN	w/o CL	11.790	16.478	0.865	0.211	0.809
	w/ CL	10.561	15.283	0.874	0.126	0.489
DMPNN	w/o CL	10.016	15.680	0.878	0.167	0.474
	w/ CL	9.975	15.204	0.892	0.121	0.341
						0.970

As depicted in Table 4, introducing line graphs enhances subgraph matching accuracy and reduces matching errors across all models. Similarly, the results presented in Table 5 demonstrate a performance boost in predicting subgraph matching problems through the application of CL. Through comparisons, we observe that on the Mutag dataset, which contains multi-attributed graphs, the improvement from incorporating line graphs is greater than the improvement from introducing CL. However, on the Regular dataset, which does not include multi-attributed graphs, introducing CL yields better results. This further illustrates the effectiveness of the line graph in leveraging its advantages on multi-attributed graphs, bringing abundant information into graph networks to achieve better results.

5 Conclusions

In this research, we propose a novel model for subgraph matching on multi-attributed graphs. We improve line graphs to acquire the features on nodes and edges, and construct a CL framework to enhance the quality of embeddings, thus improving the model's ability to predict subgraph matches. Experimental results confirm the feasibility and effectiveness of our approach.

References

- [1] LAN Z X, YU L M, YUAN L L, et al. Sub-GMN: the subgraph matching network model [EB/OL]. (2019-03-15) [2024-09-10]. <https://arxiv.org/abs/2104.00186v3>.
- [2] LAN Z X, MA Y, YU L M, et al. AEDNet: adaptive edge-deleting network for subgraph matching[J]. *Pattern Recognition*, 2023, 133: 109033.
- [3] LIU X, SONG Y Q. Graph convolutional networks with dual message passing for subgraph isomorphism counting and matching [J]. *Proceedings of the AAAI Conference on Artificial Intelligence*, 2022, 36(7): 7594-7602.
- [4] BARNES J A, HARARY F. Graph theory in network analysis[J]. *Social Networks*, 1983, 5(2): 235-244.
- [5] XIAO S X, WANG S P, DAI Y F, et al. Graph neural networks in node classification: survey and evaluation[J]. *Machine Vision and Applications*, 2021, 33(1): 4.
- [6] HANG M H, CHEN Y X. Link prediction based on graph neural networks[EB/OL]. (2018-02-27) [2024-09-10]. <https://arxiv.org/abs/1802.09691v1>.
- [7] PRANNAY K, PIOTR T, CHEN W, et al. Supervised contrastive learning [J]. *Advances in Neural Information Processing Systems*. 2020, 33: 18661-18673.
- [8] HE K M, FAN H Q, WU Y X, et al. Momentum contrast for unsupervised visual representation learning [C]//2020 IEEE/CVF Conference on Computer Vision and Pattern Recognition (CVPR). New York: IEEE, 2020: 9726-9735.
- [9] HAFIDI H, GHOGHO M, CIBLAT P, et al. GraphCL: contrastive self-supervised learning of graph representations [EB/OL]. (2020-08-25) [2024-09-10]. <https://arxiv.org/abs/2007.08025>.
- [10] QIU J Z, CHEN Q B, DONG Y X, et al. GCC: graph contrastive coding for graph neural network pre-training[C]//Proceedings of the 26th ACM SIGKDD International Conference on Knowledge Discovery & Data Mining. New York: ACM,

- 2020: 1150-1160.
- [11] ULLMANN J R. An algorithm for subgraph isomorphism [J]. *Journal of the ACM*, 1976, 23(1): 31-42.
- [12] CORDELLA L P, FOGGIA P, SANSONE C, et al. A (sub) graph isomorphism algorithm for matching large graphs [J]. *IEEE Transactions on Pattern Analysis and Machine Intelligence*, 2004, 26(10): 1367-1372.
- [13] ZOU L, CHEN L, YU J X, et al. A novel spectral coding in a large graph database [C]// Proceedings of the 11th International Conference on Extending Database Technology Advances in Database Technology-EDBT '08. New York: ACM, 2008: 181-192.
- [14] SHASHA D, WANG J T L, GIUGNO R. Algorithmics and applications of tree and graph searching [C]// Proceedings of the Twenty-First ACM SIGMOD-SIGACT-SIGART Symposium on Principles of Database Systems. New York: ACM, 2002: 39-52.
- [15] CHOI D, LEE H, LIM J, et al. Efficient continuous subgraph matching scheme considering data reuse [J]. *Knowledge-Based Systems*, 2023, 282: 111120.
- [16] LIU L H, DU B X, XU J J, et al. G-finder: approximate attributed subgraph matching [C]// 2019 IEEE International Conference on Big Data. New York: IEEE, 2019: 513-522.
- [17] BHATTARAI B, LIU H, HUANG H H. CECI: compact embedding cluster index for scalable subgraph matching [C]// Proceedings of the 2019 International Conference on Management of Data. New York: ACM, 2019: 1447-1462.
- [18] ARAI J, FUJIWARA Y, ONIZUKA M. GuP: fast subgraph matching by guard-based pruning [J]. *Proceedings of the ACM on Management of Data*, 2023, 1(2): 1-26.
- [19] MA Y X, XU B M, YIN H F. Tps: a new way to find good vertex-search order for exact subgraph matching [J]. *Multimedia Tools and Applications*, 2024, 83(27): 69875-69896.
- [20] HE J Z, CHEN Y X, LIU Z Y, et al. Optimizing subgraph retrieval and matching with an efficient indexing scheme [J]. *Knowledge and Information Systems*, 2024, 66(11): 6815-6843.
- [21] YANG F, ZHANG H Y, TAO S M. Semi-supervised classification via full-graph attention neural networks [J]. *Neurocomputing*, 2022, 476: 63-74.
- [22] SOCHER R, CHEN D Q, MANNING C D, et al. Reasoning with neural tensor networks for knowledge base completion [J]. *Advances in Neural Information Processing Systems*, 2013, 12: 926-934.
- [23] YING R, LOU Z Y, YOU J X, et al. Neural subgraph matching [EB/OL]. (2020-07-06) [2024-09-10]. <https://arxiv.org/abs/2007.03092>.
- [24] CEN Y K, ZOU X, ZHANG J W, et al. Representation learning for attributed multiplex heterogeneous network [C]// Proceedings of the 25th ACM SIGKDD International Conference on Knowledge Discovery & Data Mining. New York: ACM, 2019: 1358-1368.
- [25] SCHLICHTKRULL M, KIPF T N, BLOEM P, et al. Modeling relational data with graph convolutional networks [M]// Lecture Notes in Computer Science. Cham: Springer International Publishing, 2018: 593-607.
- [26] VASHISHTH S, SANYAL S, NITIN V, et al. Composition-based multi-relational graph convolutional networks [EB/OL]. (2019-11-08) [2024-09-10]. <https://arxiv.org/abs/1911.03082v2>.
- [27] CAO J H, FANG J Y, MENG Z Q, et al. Knowledge graph embedding: a survey from the perspective of representation spaces [J]. *ACM Computing Surveys*, 2024, 56(6): 1-42.
- [28] CARLETTI V, FOGGIA P, SAGGESE A, et al. Introducing VF3: a new algorithm for subgraph isomorphism [C]// International Workshop on Graph-Based Representations in Pattern Recognition. Cham: Springer, 2017: 128-139.
- [29] TAUD H, MAS J F. Multilayer perceptron (MLP) [M]// Geomatic Approaches for Modeling Land Change Scenarios. Cham: Springer, 2018: 451-455.
- [30] OKU H, ISHIKAWA M. High-speed liquid lens with 2 ms response and 80.3 nm root-mean-square wavefront error [J]. *Applied Physics Letters*, 2009, 94(22): 221108.
- [31] LOSHCHILOV I, HUTTER F. Decoupled weight decay regularization [EB/OL]. (2019-01-04) [2024-09-11]. <https://doi.org/10.48550/arxiv.1711.05101>.

基于对比学习的多属性图子图匹配

刘博智，方秀，孙国豪^{*}，陆金虎

东华大学 计算机科学与技术学院，上海 201620

摘要：图被广泛应用于从化学信息学到社会网络分析等领域。与图相关的问题变得越来越重要，子图匹配是其中最具挑战性的任务之一。子图匹配的目的是在数据图中找到与查询图同构的所有子图。传统的搜索方法大多依赖于计算复杂度高的搜索策略，难以用于大规模的真实数据集。随着图神经网络（graph neural network, GNN）的出现，研究人员开始用其来解决子图匹配问题。然而，在图的学习过程中，忽略了节点和边上的属性特征，这导致在现实场景中匹配结果的不准确。为解决这个问题，我们提出了一种新模型，即多属性图子图匹配网络（subgraph matching on multi-attributed graph network, SGMAN）。SGMAN首先利用改进的线图来捕获节点和边上的特征，进而将GNN和对比学习（contrastive learning, CL）相结合，得到图的嵌入表示，并计算匹配矩阵以表示匹配结果。在公开数据集上的实验结果证实了该模型的优越性能。

关键词：子图匹配；图神经网络；多属性图；对比学习

Graph-Based Transform and Dual Graph Laplacian Regularization for Depth Map Denoising

MENG Yaqun, GE Huayong*, HOU Xinxin, JI Yukai, LI Sisi

College of Information Science and Technology, Donghua University, Shanghai 201620, China

Abstract: Owing to the constraints of depth sensing technology, images acquired by depth cameras are inevitably mixed with various noises. For depth maps presented in gray values, this research proposes a novel denoising model, termed graph-based transform (GBT) and dual graph Laplacian regularization (DGLR) (DGLR-GBT). This model specifically aims to remove Gaussian white noise by capitalizing on the nonlocal self-similarity (NSS) and the piecewise smoothness properties intrinsic to depth maps. Within the group sparse coding (GSC) framework, a combination of GBT and DGLR is implemented. Firstly, within each group, the graph is constructed by using estimates of the true values of the averaged blocks instead of the observations. Secondly, the graph Laplacian regular terms are constructed based on rows and columns of similar block groups, respectively. Lastly, the solution is obtained effectively by combining the alternating direction multiplication method (ADMM) with the weighted thresholding method within the domain of GBT.

Keywords: depth map; graph signal processing; dual graph Laplacian regularization (DGLR); graph-based transform (GBT); group sparse coding (GSC)

CLC number: TN911.73

Document code: A

Article ID: 1672-5220(2025)05-0534-09

Open Science Identity
(OSID)



0 Introduction

The depth camera captures information regarding the position of an object in three-dimensional (3D) space, where each pixel value indicates the distance from the corresponding object to the camera. Depth maps captured with active sensors such as time-of-flight (ToF)-based cameras and structure light (SL)-based cameras suffer from various types of intrinsic artifacts^[1]. There is some recent work on denoising of depth maps, where the availability of both color and texture images is assumed, and their correlations are exploited for denoising^[2-8]. We do not assume the availability of color images in this work. As a practical matter, it is difficult to obtain high-

quality color images in challenging environments with unreliable lighting conditions, such as darkrooms. Denoising methods for depth maps presented in gray values are analogous to those for gray-scale images. Pioneering researchers tended to adopt a filter-based method^[9-11] to filter depth maps. The biggest advantage of this type of method is that it is fast and efficient. However, its disadvantage is quite obvious: the denoising effect is not satisfactory. Based on the Bayesian assumption, the problem of solving the original image X according to the maximum a posteriori probability can be formulated as

$$X = \arg \min_x \|Y - X\|_2^2 + \psi\varphi(X), \quad (1)$$

where Y represents the noisy image; $\varphi(X)$ represents the prior term; ψ represents the parameter. Compared with the filter-based method, the prior-based image denoising method^[12-21] possesses higher accuracy and robustness. A suitable prior is indeed crucial in image denoising tasks. Among the currently available best models, the low-rank (LR) based models have shown good performance in image denoising. For instance, the weighted nuclear norm minimization (WNNM) model^[12] is a classical one leveraging the LR prior. The rank residual constraint (RRC) model^[13] is another example. It reconceptualizes the rank minimization problem in terms of matrix approximation. Specifically, it tries to progressively approximate the underlying LR matrix by minimizing the rank residuals. The LR regularized group sparse coding (LR-GSC) model^[14] also plays a significant role. It is proposed by exploiting the nonlocal self-similarity (NSS) of natural images. This model bridges the gap between group sparse coding (GSC) and joint sparsity (JS). It takes advantage of both the sparsity and the LR property of the dictionary domain coefficients of each group of similar patches. Likewise, the low-rankness guided group sparse representation (LGSR) model^[15], which also utilizes the NSS of natural images, jointly exploits the sparsity and the LR prior knowledge of each group of similar patches within a unified framework. This further enriches the ways to use such priors for improving

Received date: 2024-09-10

Foundation item: National Natural Science Foundation of China (No. 62372100)

* Correspondence should be addressed to GE Huayong, email: gehuayong@dhu.edu.cn

Citation: MENG Y Q, GE H Y, HOU X X, et al. Graph-based transform and dual graph Laplacian regularization for depth map denoising [J].

Journal of Donghua University (English Edition), 2025, 42(5): 534-542.

denoising results. However, these LR-based models have a common drawback. They are poor at restoring texture details. The main reason is that they focus primarily on minimizing the nuclear norm to capture the LR nature of the data. In this process, they often overlook the fine-grained information related to texture details. As a result, some crucial high-frequency components essential for representing texture details may be inadvertently discarded or weakened.

When these LR-based models are applied to depth maps, the problem remains. For example, when we try to enhance a depth map of an indoor scene captured by a 3D sensor, these models can effectively reduce noise in the depth data. But they fail to accurately restore the fine details like the edges of furniture or the textures of the walls. This is due to their inherent focus on the LR nature of the data, causing them to sacrifice the high-frequency components crucial for depicting these texture details.

In contrast, there are models that specialize in depth map processing, and these models are excellent at preserving texture details. The nonlocal graph-based transform (NLGBT) model^[16] uses graph-based signal processing techniques. It constructs graph structures based on image pixels and utilizes the relationships between pixels to better capture texture details. The group-based nuclear norm and learning graph (GNNLG) model^[17] also has its unique features. It integrates graph signals with the LR property. Specifically, it embeds the graph topology by utilizing streaming Laplacian matrices and then combines it with the kernel norm. However, both models are more limited in terms of the amount of available data and the noise level in the images. They perform poorly on depth maps rich in more texture details with higher levels of noise.

Inspired by the above models, we propose to combine graph-based transform (GBT) with dual graph Laplacian regularization (DGLR) for eliminating high-frequency components while preserving texture details in depth map denoising tasks. The main reason for this combination lies in the unique properties of GBT and DGLR. The GBT provides a flexible framework for manipulating the image data while maintaining its structural information. By transforming the image into a graph domain, we can leverage the relationships between pixels (represented as nodes in the graph) to better understand and handle the image's texture details. When combined with the DGLR, it allows us to selectively suppress the identified high-frequency components that are likely to be noise, while safeguarding the texture details that are crucial for the visual quality and semantic understanding of the depth map. Specifically, within each group, the graph is constructed by using estimates of the true values of the averaged blocks instead of the observations. Next, in particular, the graph Laplacian regularity terms are constructed based on rows and columns of similar block groups, respectively. Finally, a combination of the alternating direction multiplication

method (ADMM) and the weighted thresholding method within the domain of GBT is used to attain a rapid and effective solution.

1 Proposed DGLR-GBT Model

1.1 Graph spectra and graph-based dictionaries

Graph signal processing generalizes the signal processing task to signals living on a non-Euclidean domain, whose structure can be captured by a weighted graph^[22]. We define a weighted undirected graph $\mathbf{g} = (V, E, W)$, where V , E and W represent the vertex set, edge set and weight matrix, respectively. For an image, blocks of pixels in the image are generally considered as the vertices of the graph, and the weights of the weight matrix W are often computed with a Gaussian kernel. The degree matrix $D = \text{diag}(d_1, d_2, \dots, d_n)$, where d_i is the sum of elements in the i th row of the weight matrix W . Here $d_i = \sum_j w_{ij}$, where w_{ij} represents the element in the i th row and j th column of the weight matrix W . The graph Laplacian matrix L is defined as $L = D - W$. Specifically, L can be decomposed as

$$L = U\Lambda U^T, \quad (2)$$

where U is the matrix consisting of the eigenvectors; Λ is the diagonal matrix of eigenvalues. For a given signal s , the graph signal smoothness is defined as $s^T L s$.

The graph Fourier transform (GFT) of s is $S = U^T s$, where S is the frequency component of s in the spectral domain. Obviously, the corresponding inverse GFT (IGFT) can also be obtained, which is expressed as $s = US$. From another point of view, U can be viewed as a dictionary, called a graph-based dictionary. For natural images, it is observed that the energy of the frequency components of the graph signal is concentrated in the low-frequency components. This characteristic enables us to utilize the low-frequency components for the sparse representation of the graph signal. Through the above analysis, it becomes clear that the GBT can be effectively combined with the sparse representation optimization problem. When performing graph dictionary construction, the element w_{ij} of the weight matrix W is defined as

$$w_{ij} = \exp(\text{dist}(i, j)/\sigma_w^2), \quad (3)$$

where σ_w^2 is the Gaussian kernel; $\text{dist}(i, j)$ represents a distance between the node i and the node j . In the context of distance metric application, the general distance metric often utilizes its observed value y_i . For instance, it defines the distance between two points i and j as $\hat{\text{dist}}(i, j) = \sum_{k=1}^K [y_k(i) - y_k(j)]^2/K$, where K is the number of nearest neighbors. However, this approach ignores the effect of noise. When the noise level is relatively high, the matching accuracy based on this distance metric will be significantly reduced. To address

this issue, we propose to use the modified true value \mathbf{x}_i instead of \mathbf{y}_i to redefine the distance metric. Specifically, $\text{dist}(i, j) = \sum_{k=1}^K [\mathbf{x}_k(i) - \mathbf{x}_k(j)]^2 / K$. We consider the difference $\{\mathbf{y}_k(i) - \mathbf{y}_k(j)\}_{k=1}^K$ to be the K sample values of the random variable $\{\mathbf{x}_k(i) - \mathbf{x}_k(j)\}_{k=1}^K$. According to the law of large numbers, we can establish the relationship that $\{\mathbf{y}_k(i) - \mathbf{y}_k(j)\}_{k=1}^K = \{\mathbf{x}_k(i) - \mathbf{x}_k(j)\}_{k=1}^K + e$. Here, the random variable e obeys a Gaussian distribution with a mean of 0. We use $E[\mathbf{y}_k(i) - \mathbf{y}_k(j)] - e$ in place of $E[\mathbf{x}_k(i) - \mathbf{x}_k(j)]$ and $D[\mathbf{y}_k(i) - \mathbf{y}_k(j)]$ in place of $D[\mathbf{x}_k(i) - \mathbf{x}_k(j)]$. So, $\text{dist}(i, j) = \frac{1}{K} \sum_{k=1}^K [\mathbf{x}_k(i) - \mathbf{x}_k(j)]^2 = E[(\mathbf{x}_k(i) - \mathbf{x}_k(j))^2] = E[\mathbf{x}_k(i) - \mathbf{x}_k(j)] + D[\mathbf{x}_k(i) - \mathbf{x}_k(j)] \approx E[\mathbf{y}_k(i) - \mathbf{y}_k(j)] + e^2 + D[\mathbf{y}_k(i) - \mathbf{y}_k(j)] = \text{dist}(i, j) + e^2$.

The GBT-specific build process^[16] proceeds as follows. Firstly, similar blocks are grouped and averaged to get an average block. This averaging process serves multiple purposes: 1) it smooths out small variations or noise within the individual similar blocks; 2) it yields a stable and representative description of the common features present in those blocks; 3) it provides a single entity that encapsulates the key characteristics of the grouped similar regions. Next, the pixels of this average block as the nodes of the graph and connected to the four nearest neighbors in the patch to form a four-connected graph. Given the connectivity graph, we can compute the adjacency matrix \mathbf{A} and the degree matrix \mathbf{D} . The adjacency matrix \mathbf{A} is a fundamental representation of the graph's structure. It records the presence or absence of

edges between nodes. In our four-connected graph context, if there is an edge connecting two pixels (nodes), the corresponding entry in the adjacency matrix \mathbf{A} will be 1, and 0 otherwise. The weight matrix \mathbf{W} of the constructed graph is measured by the square of the intensity difference between neighboring pixels. Subsequently, we can obtain the Laplacian matrix \mathbf{L} . The eigenvectors of the Laplacian matrix \mathbf{L} carry valuable information about the frequency components and spatial patterns within the graph structure, which forms the basis for constructing the GBT dictionary. Finally, we use the eigenvectors of the Laplacian matrix \mathbf{L} to construct the GBT dictionary \mathbf{U} . By using these eigenvectors as the basis vectors for the dictionary, we can represent the image data in a transformed domain that captures both the local and global characteristics of the image.

1.2 DGLR

An image block group is the basic processing unit for image denoising. As shown in Fig. 1, given a clean image \mathbf{x} , we divide it into J overlapping image patches $\{\mathbf{x}_i\}_{i=1}^{i=J}$ of size $n \times n$. For each image patch, the K nearest neighbor method is used to find its most similar $K - 1$ nearest neighbors to get the similar patches \mathbf{x}_i^K , where the similarity between two image blocks is measured by the Euclidean distance. Since each image block can be expanded into an $\mathbf{R}^{n \times 1}$ column vector, then each similar block group can be denoted as $\mathbf{G}_i^{r \times c} \in \mathbf{R}^{n \times K}$, where r and c represent the row and column indices of the matrix consisting of the similar block group, respectively. We normalize the K similar blocks, i.e., the rows of the group $\mathbf{G}_i^{r \times c}$, to obtain J normalized blocks denoted as \mathbf{x}_i .

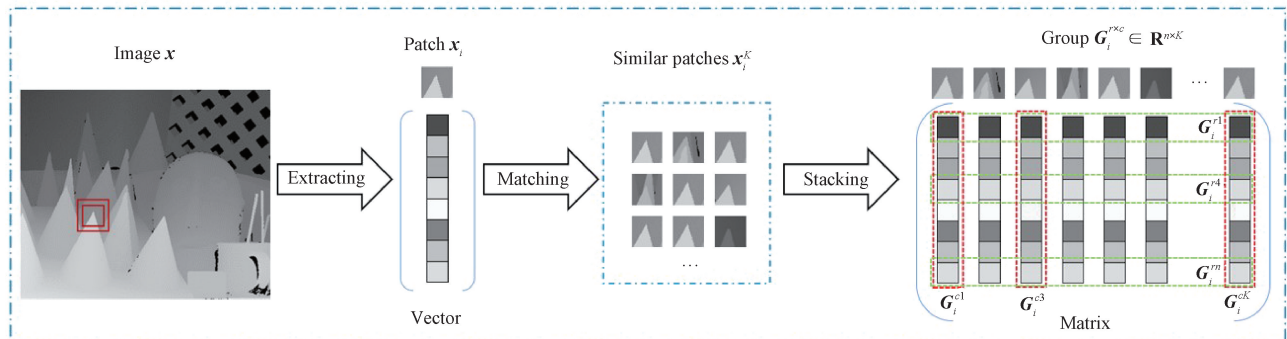


Fig. 1 Schematic diagram of group acquisition

A feature of the above group is that similar patches are usually sparse. Thus, \mathbf{x} can be expressed as $\mathbf{x} = \mathbf{U}\boldsymbol{\alpha}$, where $\boldsymbol{\alpha}$ denotes the correlation coefficient. When we get the dictionary \mathbf{U} , the sparse coding can be expressed as

$$\begin{aligned} \min_{\boldsymbol{\alpha}} & \| \mathbf{y} - \mathbf{x} \|_2^2 + \theta \| \boldsymbol{\alpha} \|_0 \\ \text{s. t. } & \mathbf{x} = \mathbf{U}\boldsymbol{\alpha}, \end{aligned} \quad (4)$$

where \mathbf{y} represents the noisy image; θ represents the regularization parameter. After solving the sparse coding problem, we can get the noise reduction group $\mathbf{x} = \mathbf{U}\boldsymbol{\alpha}$ from the obtained $\boldsymbol{\alpha}$.

For simplicity, we use the subscript r and subscript c to represent rows and columns, respectively. We regard the rows of the similar block group $\mathbf{G}_i^{r \times c}$ as the vertices V_r of the graph $\mathbf{g}_r = (V_r, E_r, W_r)$, where $E_r \subset V_r \times V_r$, and the weights W_r are solved by Eq. (3). Next, we can get the row graph Laplacian matrix $\mathbf{L}_r = \mathbf{D}_r - \mathbf{W}_r$, where \mathbf{D}_r is the row degree matrix. Based on this, the row graph Laplacian regular term $\text{tr}(\boldsymbol{\alpha}^T \mathbf{L}_r \boldsymbol{\alpha})$ can be obtained from Eq. (2). In the same way, we can also obtain the column graph Laplacian regular term $\text{tr}(\boldsymbol{\alpha} \mathbf{L}_c \boldsymbol{\alpha}^T)$.

2 Proposed Solution

Group-based methods have received much attention in image denoising. However, the existing methods, with a predominant focus on sparsity or LR property, might impose limitations on the performance of image

denoising. In this research, we propose a model integrating GBT and DGLR under sparsity constraints, which is denoted as DGLR-GBT. Figure 2 illustrates the framework structure of the proposed model DGLR-GBT. Here t_w is a new weighted threshold; μ , λ and θ are regularization parameters.

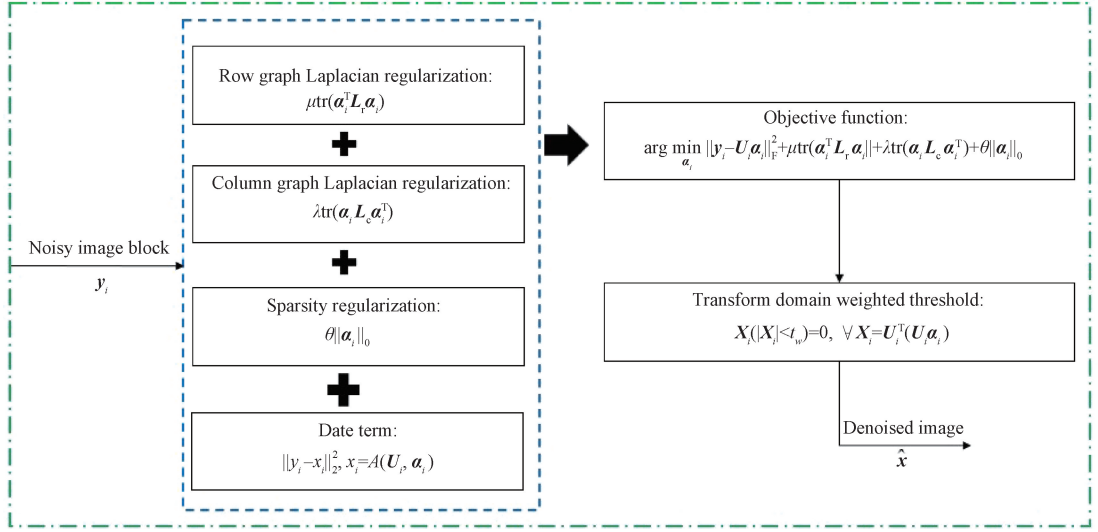


Fig. 2 Framework structure of DGLR-GBT

2.1 Dual graph regularized sparse coding

A single prior is difficult to effectively utilize all the properties of depth maps, and there are local differences in the statistical properties of the noise in the matrix. Therefore, in this research, we introduce the row-graph Laplacian regularization term to enhance the local smoothness of the depth map. Meanwhile, we also introduce the column-graph Laplacian regularization term to make full use of the NSS prior to the natural image. Since two Laplacian regularization terms are added to GBT, it is named DGLR-GBT and can be composed as

$$\arg \min_{\alpha_i} \|y_i - U_i \alpha_i\|_F^2 + \mu \text{tr}(\alpha_i^T L_r \alpha_i) + \lambda \text{tr}(\alpha_i^T L_c \alpha_i^T) + \theta \|\alpha_i\|_0. \quad (5)$$

With α_i , the reconstructed image can be expressed by $x_i = U_i \alpha_i$. We provide an algorithm based on ADMM, enabling the simultaneous update of all columns of α_i . For simplicity and without loss of generality, the subscript i is omitted in the derivation. The denoising Problem (5) is reformulated as

$$\arg \min_{\alpha} \|y - U \alpha\|_F^2 + \mu \text{tr}(\alpha^T L_r \alpha) + \lambda \text{tr}(\alpha^T L_c \alpha^T) \quad (6)$$

s.t. $\alpha = Z$ $\|z_j\|_0 \leq T \forall j$.

The augmented Lagrangian function of Problem (6) is $L_\rho(\alpha, Z, V) = F(\alpha) + I(Z) + \rho \|\alpha - Z + V\|_2^2$. Here Z is the dyadic variable; V denotes the scaled dual form variable; $F(\alpha) = \|y - Z \alpha\|_F^2 + \mu \text{tr}(\alpha^T L_r \alpha) + \lambda \text{tr}(\alpha^T L_c \alpha^T)$, for an indicator function; $I(Z) = I(\|z_j\|_0 \leq T \forall j)$

$T, \forall j$) returns 1 if the condition is satisfied and 0 otherwise; T is the sparsity parameter, which limits the upper bound of the number of non-zero elements in each z_j ; ρ is the augmented Lagrangian parameter. Specifically, by applying the ADMM scheme, Problem (6) can be converted into

$$\alpha^{\xi+1} = \arg \min_{\alpha} L_\rho(\alpha, Z^\xi, V^\xi), \quad (7)$$

$$Z^{\xi+1} = \arg \min_Z L_\rho(\alpha^{\xi+1}, Z, V^\xi), \quad (8)$$

$$V^{\xi+1} = V^\xi + \alpha^{\xi+1} - Z^{\xi+1}, \quad (9)$$

where ξ is the iteration number. Based on the ADMM algorithm, an efficient solution can be obtained for each subproblem.

2.2 Transform domain weighted threshold

Upon accomplishing the determination of the graph dictionary and resolving the sparse coding issue, we proceed to further threshold the denoising group. The traditional empirical threshold^[16] is defined as $t = \sigma \sqrt{2 \log(n^2 K)}$, where σ represents the noise level, and it will be updated iteratively. While the traditional empirical threshold performs satisfactorily when the noise level is relatively low, it is prone to inducing excessive smoothing of the image in the presence of high noise levels, thereby impairing the edge information of the image. To address this issue, we introduce a weighting factor w_σ to the traditional empirical threshold t to alleviate the over-smoothing effect when the noise level is high.

This method can balance the effect of the noise level to some extent and improve the effectiveness of thresholding. The weighting factor w_σ is configured as

$$w_\sigma = \begin{cases} -0.01\sigma^{(0)} + 0.95 + 0.05\text{sign}(30 - \sigma^{(0)}), & \sigma^{(0)} \leq 50, \\ 0.4, & \sigma^{(0)} > 50, \end{cases} \quad (10)$$

where $\sigma^{(0)}$ denotes the initial value of the standard deviation of the noise. It is evident that the magnitude of the weights is adaptive to the noise level. Specifically, as the noise level escalates, a greater amount of interfering information affects the image edges. However, concomitantly, the more high-frequency values present in the frequency domain, the smaller the weights. The complete DGLR-GBT encoding is presented in Algorithm 1. The full code related to this study can be accessed at <https://github.com/mengyaqun/DGLR-GBT.git>.

Algorithm 1 Depth map denoising via DGLR-GBT

Input: Noisy image y , Noise level σ

Initialization: $y^{(1)} = y$

for $i = 1$ to $iter$ **do**

1. Block clustering, as shown in Fig. 1
2. GBT dictionary construction is carried out based on Eq. (2) to obtain U
3. Graph Laplacian regular term construction: $\text{tr}(\alpha^T L_i \alpha)$, $\text{tr}(\alpha L_c \alpha^T)$
4. Problem (6) is solved by the ADMM algorithm
5. Transform spectrum shrinkage: the new threshold $w_\sigma \times t$ according to Eq. (10)

Output: The denoised depth map \hat{x}

3 Experimental Results

3.1 Experimental setup

For the assessment of the quality of denoised images, the peak signal-to-noise ratio (PSNR) and the structure similarity (SSIM) are employed as evaluation metrics. All experiments are conducted in the MATLAB R2022b environment and executed on an Intel (R) Core (TM) i5-10210U CPU @ 1.60 GHz 2.11 GHz processor. Subsequently, the parameter settings within our proposed method are deliberated. The regularization parameters μ , λ and θ are set as 1, 1 and 1, respectively, and the weighted threshold t_w is set as $w_\sigma \times t$. Other parameters, such as the block size n , the number of similar blocks K , and the relaxation parameter δ for iterative regularization with the noise variance updating parameter η are assigned values as presented in Table 1.

Table 1 Parameter settings

σ/dB	n	K	δ	η
$\sigma \leq 20$	5	25	0.13	0.63
$20 < \sigma \leq 30$	6	30	0.09	0.63
$30 < \sigma \leq 40$	7	50	0.08	0.65
$40 < \sigma \leq 50$	8	60	0.08	0.67
$50 < \sigma$	9	80	0.08	0.67

3.2 Objective evaluation

The widely used Middlebury stereo datasets^[23-25] for depth map denoising are employed in our experiments. These datasets include the 2003, 2005 and 2006 versions. An additive Gaussian white noise with a standard deviation of 10–50 is superimposed onto these images. Several comparison algorithms are employed, including block-matching and 3D filtering algorithm (BM3D)^[11], NLGBT^[16], WNNM^[12], RRC^[13], LR-GSC^[14], multi-scale weighted group sparse coding (MS-WGSC) model^[17] and LGSR^[15]. Tables 2 and 3 display the average values of PSNR and SSIM for all the depth maps within the Middlebury stereo datasets. The optimal and sub-optimal performances are indicated by red bold and green text, respectively.

As can be seen from Table 2, DGLR-GBT surpasses all the state-of-the-art algorithms in terms of the average PSNR. This encompasses even the powerful LGSR^[15] and WNNM^[12]. From Table 3, it is evident that both LGSR^[15] and DGLR-GBT achieve the optimal results in nearly all the average values of SSIM for all the depth maps. It is worth highlighting that LGSR^[15] represents the latest and most advanced denoising algorithm that combines the sparse and LR priors. However, it is conspicuous that the SSIM values of LGSR decline compared to those of the other models when the noise levels are high, particularly when the noise levels fall within a range of 40–50 dB. This is due to the fact that some pseudo-structures are introduced into the noisy image when the noise level is high, which diminishes the structural similarity of the image and consequently restricts the denoising performance.

To further validate the effectiveness of our algorithm, we conduct comparative experiments with two classic denoising algorithms: the feed-forward denoising convolutional neural network (DnCNN)^[26], and the fast and flexible denoising convolutional neural network (FFDNet)^[27]. Additionally, to verify the robustness of our algorithm, we evaluate it on a real-world depth dataset, RGBM. The results are presented in Tables 4 and 5, respectively, with the best values highlighted in bold. As shown in Table 4, DGLR-GBT outperforms DnCNN and achieves comparable performance to FFDNet in terms of denoising quality. Furthermore, Table 5 demonstrates that DGLR-GBT maintains a stable advantage over other depth map datasets.

Table 2 PSNR comparison of various algorithms on Middlebury stereo datasets

σ/dB	PSNR							
	BM3D	NLGBT	WNNM	RRC	LR-GSC	MS-WGSC	LGSR	DGLR-GBT
10	42.603 7	43.979 3	44.011 2	42.968 8	43.462 1	43.871 6	44.058 0	44.514 6
15	39.560 0	40.740 0	41.092 1	40.361 1	39.111 4	40.957 8	40.874 3	41.399 9
20	37.543 1	38.166 6	38.972 2	38.408 8	38.818 7	38.876 6	38.988 8	39.401 1
25	36.080 4	36.149 2	37.398 3	36.931 0	36.772 0	37.161 8	37.371 0	37.585 0
30	35.027 7	34.634 6	36.187 0	35.786 8	36.197 7	35.950 5	36.245 0	36.263 7
40	33.402 9	32.260 9	34.380 7	34.076 0	34.606 2	34.128 8	34.510 3	34.631 6
50	32.140 0	31.048 9	33.196 8	32.776 7	33.332 5	33.393 9	33.242 0	33.427 1
Average	36.622 5	36.711 4	37.891 2	37.329 9	37.471 5	37.763 0	37.898 5	38.174 7

Table 3 SSIM comparison of various algorithms on Middlebury stereo datasets

σ/dB	SSIM							
	BM3D	NLGBT	WNNM	RRC	LR-GSC	MS-WGSC	LGSR	DGLR-GBT
10	0.987 8	0.988 6	0.990 2	0.989 9	0.990 7	0.989 7	0.9922	0.991 0
15	0.979 6	0.980 4	0.982 6	0.984 1	0.968 5	0.981 9	0.985 9	0.983 7
20	0.970 4	0.967 6	0.973 5	0.977 2	0.978 3	0.972 3	0.980 3	0.979 1
25	0.961 0	0.950 6	0.967 1	0.972 9	0.965 6	0.963 9	0.975 7	0.975 7
30	0.950 8	0.936 1	0.957 7	0.966 9	0.969 1	0.953 5	0.970 4	0.969 4
40	0.930 9	0.935 1	0.937 5	0.955 6	0.960 0	0.930 9	0.957 8	0.963 9
50	0.925 6	0.923 4	0.934 4	0.943 8	0.950 9	0.951 2	0.949 4	0.957 1
Average	0.958 0	0.954 5	0.963 3	0.9701	0.969 0	0.963 3	0.973 1	0.974 3

Table 4 PSNR and SSIM comparison of DnCNN, FFDNet and DGLR-GBT on Middlebury stereo datasets

σ/dB	DnCNN		FFDNet		DGLR-GBT	
	PSNR	SSIM	PSNR	SSIM	PSNR	SSIM
10	43.114 6	0.988 6	43.689 0	0.991 0	44.514 6	0.991 0
20	38.785 9	0.974 1	39.312 0	0.982 5	39.401 1	0.979 1
30	36.214 3	0.958 1	36.727 3	0.972 7	36.263 7	0.969 4
40	34.640 2	0.948 6	35.026 5	0.953 5	34.631 6	0.963 9
50	33.469 0	0.936 2	33.804 6	0.953 5	33.427 1	0.957 1
Average	37.244 8	0.961 1	37.711 9	0.970 6	37.647 6	0.972 1

Table 5 PSNR and SSIM comparison of various algorithms on RGBM datasets

σ/dB	Metric	Algorithm							
		BM3D	NLGBT	WNNM	RRC	LR-GSC	MS-WGSC	LGSR	DGLR-GBT
30	PSNR	33.374 6	33.124 0	33.970 0	33.849 9	33.837 7	34.066 3	33.829 3	34.245 1
	SSIM	0.945 7	0.946 6	0.956 6	0.967 5	0.964 3	0.952 3	0.966 3	0.971 2
50	PSNR	30.164 7	28.913 6	30.825 2	30.743 6	30.760 3	31.249 0	30.677 2	31.259 0
	SSIM	0.920 3	0.936 4	0.932 8	0.946 0	0.943 7	0.949 3	0.942 3	0.955 2

3.3 Subjective evaluation

Figures 3, 4 and 5 present the visual comparison among the competing denoising methods on depth maps Art, Teddy and Rocks2 at noise levels of 15, 30 and 50 dB, respectively. As depicted in Fig. 3, when the noise level is relatively low, all denoising methods yield satisfactory recovery results. Nevertheless, as the noise level escalates, WNNM^[12], MS-WGSC^[17], LR-GSC^[14] and LGSR^[15] begin to generate some undesirable

artifacts, while BM3D^[11], NLGBT^[16] and RRC^[13] result in some over-smoothing outcomes, as demonstrated in Figs. 4 and 5. Only DGLR-GBT performs stably in denoising tasks at different noise levels. This stability can be attributed to two key aspects of its design. On the one hand, DGLR-GBT incorporates a dual graph Laplacian structure that enables it to effectively analyze the spectral characteristics of the image in both local and global aspects. By doing so, it can precisely distinguish between

noise-related high-frequency components and those crucial texture details, regardless of the noise level. On the other hand, the GBT method allows it to adaptively adjust the

denoising process according to the specific characteristics of different images and noise levels, ensuring that it neither generates artifacts nor causes over-smoothing.

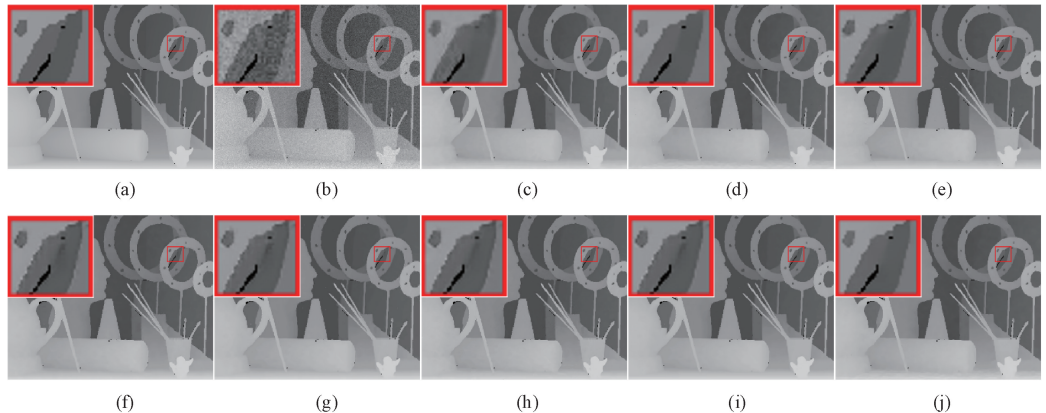


Fig. 3 Denoising results on depth map Art by different methods (noise level: 15 dB): (a) ground truth; (b) noisy image; (c) BM3D; (d) NLGBT; (e) WNNM; (f) RRC; (g) LR-GSC; (h) MS-WGSC; (i) LGSR; (j) DGLR-GBT

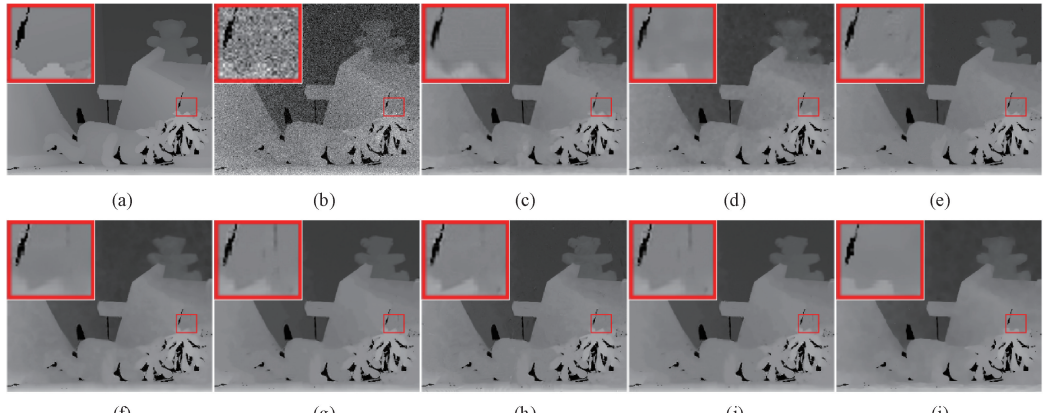


Fig. 4 Denoising results on depth map Teddy by different methods (noise level: 30 dB): (a) ground truth; (b) noisy image; (c) BM3D; (d) NLGBT; (e) WNNM; (f) RRC; (g) LR-GSC; (h) MS-WGSC; (i) LGSR; (j) DGLR-GBT

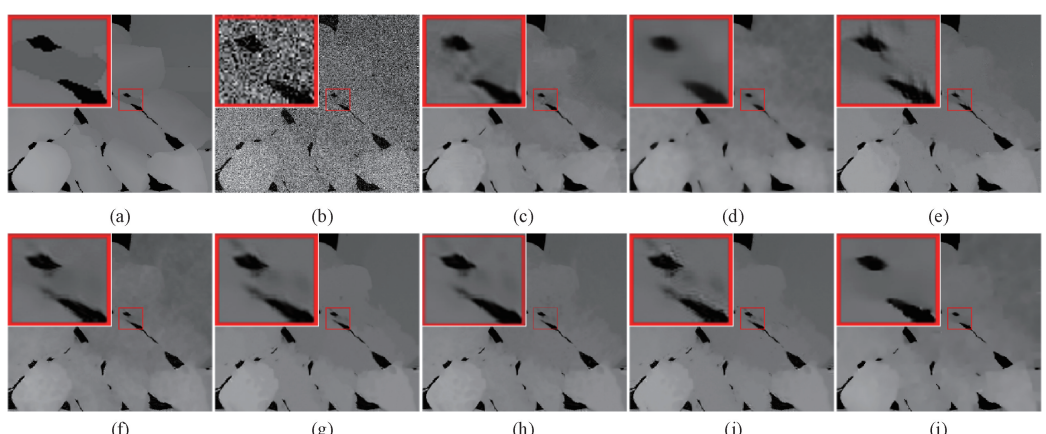


Fig. 5 Denoising results on depth map Rocks2 by different methods (noise level: 50 dB): (a) ground truth; (b) noisy image; (c) BM3D; (d) NLGBT; (e) WNNM; (f) RRC; (g) LR-GSC; (h) MS-WGSC; (i) LGSR; (j) DGLR-GBT

3.4 Algorithm complexity analysis

Considering the feasibility in practical applications, especially in real-time processing scenarios, a low

computational cost is of crucial importance for depth map denoising. The complexity of the proposed algorithm is analyzed in the following manner. Firstly, an image with

a size of $N \times N$ is divided into overlapping image blocks with a size of $n \times n$. For each of these blocks, the construction of the graph and the solution process of the ADMM algorithm are the two main time-consuming operations. The time for these two operations are denoted by T_1 and T_2 , respectively. Specifically, T_1 refers to the time required for generating the adjacency matrix \mathbf{A} , the degree matrix \mathbf{D} , and the Laplacian matrix \mathbf{L} . Through theoretical analysis and relevant calculation, it can be derived that $T_1 = O(n^2)$. As for T_2 , it represents the time spent on solving the model presented in Problem (6). More precisely, T_2 can be decomposed into $t_1 + t_2$, where t_1 is the time taken for solving the α -subproblem, and t_2 is the time needed for solving the Z -subproblem. Consequently, $T_2 = O(n^3)$. Based on the above analysis, the complexity of reconstructing the entire image can be expressed as $O(n^3)$. It is worth highlighting that parallel algorithms can be designed to reduce the elapsed time. Moreover, with the continuous development of hardware, particularly CPUs and GPUs, parallel computing can be readily implemented^[8].

4 Conclusions

Group-based methodologies have attracted significant attention within the domain of image denoising. Nevertheless, the majority of the extant methods predominantly center around sparsity or LR property, which might potentially impede the performance of image denoising. In this research, we introduce a graph-based denoising framework that exhibits particular efficacy for depth maps. We propose a model that combines the graph dictionary and the dual graph Laplacian within the context of sparsity constraints. This model fully exploits NSS and the piecewise smoothness of the depth maps to eliminate noise. Concurrently, more comprehensive and detailed information is retained during the noise removal process via the combination of the ADMM and the GBT domain weighted thresholding.

References

- [1] IBRAHIM M M, LIU Q, KHAN R, et al. Depth map artefacts reduction: a review [J]. *IET Image Processing*, 2020, 14(12): 2630-2644.
- [2] ZHONG Z W, LIU X M, JIANG J J, et al. Guided depth map super-resolution: a survey [J]. *ACM Computing Surveys*, 2023, 55 (14Sup.): 1-36.
- [3] ZHANG Y B, FENG Y H, LIU X M, et al. Color-guided depth image recovery with adaptive data fidelity and transferred graph Laplacian regularization [J]. *IEEE Transactions on Circuits and Systems for Video Technology*, 2020, 30 (2): 320-333.
- [4] WANG Z X, YAN Z Q, YANG J. SGNet: structure guided network via gradient-frequency awareness for depth map super-resolution [J]. *Proceedings of the AAAI Conference on Artificial Intelligence*, 2024, 38(6): 5823-5831.
- [5] ZHONG Z W, LIU X M, JIANG J J, et al. Deep attentional guided image filtering [J]. *IEEE Transactions on Neural Networks and Learning Systems*, 2023, 35(9): 12236-12250.
- [6] ZHAO Z X, ZHANG J S, XU S, et al. Discrete cosine transform network for guided depth map super-resolution [C]//2022 IEEE/CVF Conference on Computer Vision and Pattern Recognition (CVPR). New York: IEEE, 2022: 5687-5697.
- [7] WANG K, ZHAO L J, ZHANG J J, et al. Joint depth map super-resolution method via deep hybrid-cross guidance filter [J]. *Pattern Recognition*, 2023, 136: 109260.
- [8] ZHANG Y Y, HE X H, CHEN H G, et al. Depth map super-resolution via learned nonlocal model and enhanced local regularization [J]. *Signal Processing*, 2024, 218: 109368.
- [9] BUADES A, COLL B, MOREL J M. A non-local algorithm for image denoising [C]//2005 IEEE Computer Society Conference on Computer Vision and Pattern Recognition (CVPR '05). New York: IEEE, 2005: 60-65.
- [10] GASTAL E S L, OLIVEIRA M M. Adaptive manifolds for real-time high-dimensional filtering [J]. *ACM Transactions on Graphics*, 2012, 31 (4): 1-13.
- [11] DABOV K, FOI A, KATKOVNIK V, et al. Image denoising by sparse 3-D transform-domain collaborative filtering [J]. *IEEE Transactions on Image Processing*, 2007, 16(8): 2080-2095.
- [12] GU S H, ZHANG L, ZUO W M, et al. Weighted nuclear norm minimization with application to image denoising [C]//2014 IEEE Conference on Computer Vision and Pattern Recognition. New York: IEEE, 2014: 2862-2869.
- [13] ZHA Z Y, YUAN X, WEN B H, et al. From rank estimation to rank approximation: rank residual constraint for image restoration [J]. *IEEE Transactions on Image Processing*, 2019, 29: 3254-3269.
- [14] ZHA Z Y, WEN B H, YUAN X, et al. Image restoration via reconciliation of group sparsity and low-rank models [J]. *IEEE Transactions on Image Processing*, 2021, 30: 5223-5238.
- [15] ZHA Z Y, WEN B H, YUAN X, et al. Low-rankness guided group sparse representation for image restoration [J]. *IEEE Transactions on Neural Networks and Learning Systems*, 2023, 34 (10): 7593-7607.
- [16] HU W, LI X, CHEUNG G, et al. Depth map denoising using graph-based transform and group sparsity [C]//2013 IEEE 15th International

- Workshop on Multimedia Signal Processing (MMSP). New York: IEEE, 2013: 1-6.
- [17] YAN C G, LI Z S, ZHANG Y B, et al. Depth image denoising using nuclear norm and learning graph model [J]. *ACM Transactions on Multimedia Computing, Communications, and Applications*, 2020, 16(4): 1-17.
- [18] OU Y, SWAMY M N S, LUO J Q, et al. Single image denoising via multi-scale weighted group sparse coding [J]. *Signal Processing*, 2022, 200: 108650.
- [19] LI F, RU Y M, LV X G. Patch-based weighted SCAD prior for rician noise removal [J]. *Journal of Scientific Computing*, 2021, 90(1): 26.
- [20] LIU S Q, HU Q, LI P F, et al. Speckle suppression based on weighted nuclear norm minimization and grey theory [J]. *IEEE Transactions on Geoscience and Remote Sensing*, 2019, 57(5): 2700-2708.
- [21] LIU S Q, GAO L L, LEI Y, et al. SAR speckle removal using hybrid frequency modulations [J]. *IEEE Transactions on Geoscience and Remote Sensing*, 2021, 59(5): 3956-3966.
- [22] MARTINS W A, LIMA J B, RICHARD C, et al. A primer on graph signal processing [M]// Signal Processing and Machine Learning Theory. Cambridge, Massachusetts: Academic Press, 2024: 961-1008.
- [23] SCHARSTEIN D, SZELISKI R. High-accuracy stereo depth maps using structured light [C]// 2003 IEEE Computer Society Conference on Computer Vision and Pattern Recognition. New York: IEEE, 2003, 1: 195-202.
- [24] SCHARSTEIN D, PAL C. Learning conditional random fields for stereo [C]// 2007 IEEE Conference on Computer Vision and Pattern Recognition. New York: IEEE, 2007, 1-8: 1688.
- [25] HIRSCHMULLER H, SCHARSTEIN D. Evaluation of cost functions for stereo matching [C]// 2007 IEEE Conference on Computer Vision and Pattern Recognition. New York: IEEE, 2007, 1-8: 2134.
- [26] ZHANG K, ZUO W M, CHEN Y J, et al. Beyond a Gaussian denoiser: residual learning of deep CNN for image denoising [J]. *IEEE Transactions on Image Processing*, 2017, 26(7): 3142-3155.
- [27] ZHANG K, ZUO W M, ZHANG L. FFDNet: toward a fast and flexible solution for CNN based image denoising [J]. *IEEE Transactions on Image Processing*, 2018, 27(9): 4608-4622.

基于图变换和对偶图拉普拉斯正则化的深度图像去噪

孟亚群, 葛华勇*, 侯鑫鑫, 吉宇凯, 李思思
东华大学 信息科学与技术学院, 上海 201620

摘要: 由于深度传感技术的限制, 深度相机获取的图像不可避免地会掺杂各种噪声。针对以灰度值呈现的深度图, 该研究提出了一种新的去噪模型, 称为基于图变换和对偶图拉普拉斯正则化。该模型利用深度图固有的非局部自相似性和分段平滑性等特性, 专门去除高斯白噪声。在组稀疏编码框架内, 实现了基于图变换和对偶图拉普拉斯正则化的结合。首先, 在每个组内, 使用平均块真实值的估计值而不是观测值来构建图。其次, 分别基于相似块组的行和列构建图拉普拉斯正则项。最后, 将交替方向乘法与图变换域内的加权阈值相结合来有效地求解模型。

关键词: 深度图; 图信号处理; 对偶图拉普拉斯正则化; 图变换; 组稀疏编码

DOI: 10.19884/j.1672-5220.202407005

Static Characteristic Analysis of Aerostatic Porous Bearing with a Restricted Layer

YU Zhe^{1, 2}, YAN Ruzhong^{1, 2*}, MA Xiaojian^{1, 2}, ZHANG Haojie^{1, 2}

1. College of Mechanical Engineering, Donghua University, Shanghai 201620, China

2. Engineering Research Center of Advanced Textile Machinery, Ministry of Education, Donghua University, Shanghai 201620, China

Abstract: To enhance the gas-damping effect and improve the bearing performance, a restricted layer is applied on the surface of aerostatic porous bearings. Based on the gas lubrication theory, a mathematical model of an aerostatic porous bearing with a restricted layer is established, and two proportional coefficients, a permeability ratio δ and a thickness ratio γ , are proposed. Critical values of δ and γ are determined through sensitivity analyses of complex restriction-layer parameters. The static characteristics of aerostatic porous bearings with a restricted layer or an unrestricted layer are comparatively analyzed by using Fluent simulation. The results show that when $\delta \approx 0.005$ and $\gamma \approx 0.010$, the load capacity and static stiffness of the restricted-layer aerostatic porous bearing are high; compared with the unrestricted-layer aerostatic porous bearing, the restricted-layer aerostatic porous bearing has a lower sensitivity to changes in the air supply area. The existence of the restricted layer not only enhances the throttling effect and reduces the mass flow rate, but also effectively improves the static stiffness of the bearing.

Keywords: aerostatic porous bearing; restricted layer; static characteristic; critical coefficient

CLC number: TH133.36

Document code: A

Article ID: 1672-5220(2025)05-0543-07

Open Science Identity
(OSID)



0 Introduction

The porous material in aerostatic porous bearings has a uniform structure, and its throttle holes are made up of thousands of tiny air holes with uniform internal fluid movement. Compared with traditional hydrostatic aerostatic bearings, the aerostatic porous bearing has a higher static stiffness and load capacity, and it is the key component of rotary spindles and moving guides for precision machine tools^[1-3].

Many researchers have studied the static characteristics of aerostatic porous bearings. Wang et al.^[4] investigated the relationship between the air supply pressure, material thickness, elastic modulus and the deformation of the porous bearing, and found that the

deformation was directly proportional to the air supply pressure and inversely proportional to the material thickness and elastic modulus. Yan et al.^[5] analyzed the static and dynamic characteristics of the vacuum preloaded porous aerostatic bearing. San Andrés et al.^[6] built a test rig for the porous tilting pad bearing and tested the effects of the pressure and rotational speed on the static and dynamic characteristics of the bearing. Kang et al.^[7] used Fluent simulation to analyze the temperature and pressure distributions of the flow field of the porous mass radial bearing, and the results showed that the maximum temperature occurred at the gas film outlet.

However, due to the compressibility of air, aerostatic porous bearings are prone to pneumatic hammer instability, which causes problems such as increased vibration and noise, shortened bearing life, and impact on bearing stability and accuracy^[8-10]. A restricted layer is usually coated on the surface of the aerostatic porous bearing to improve the gas-damping effect and bearing stability and stiffness. Miyatake et al.^[11] proposed a bearing with a restricted layer being coated on aerostatic porous material and proved that it could improve the stability of the bearing. Cui et al.^[12] proposed that the flow of fluid over the aerostatic porous material and surface restriction layer obeyed Darcy's law and experimentally verified the theoretical model. Saha et al.^[13] theoretically analyzed the static characteristics of two-layer (coarse layer) aerostatic porous bearings. The presence of the restricted layer reduced the friction and mass flow in the bearing. Yoshimoto et al.^[14] discussed the effect of the restricted layer on the static characteristics of the aerostatic porous bearing under symmetric and coupled loads, respectively, and introduced the surface confinement ratio associated with the restricted layer. Feng et al.^[15] analyzed the temperature field of the restricted-layer aerostatic porous bearing. Under high speed and heavy load conditions, the high-temperature heat generated by the air film would be transferred to the rotating spindle, and the thermal expansion and thermal deformation would have a significant effect on the performance of the bearing.

Received date: 2024-07-20

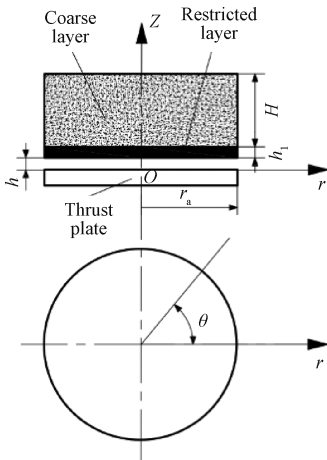
* Correspondence should be addressed to YAN Ruzhong, email: yanrz@dh.edu.cn

Citation: YU Z, YAN R Z, MA X J, et al. Static characteristic analysis of aerostatic porous bearing with a restricted layer [J]. *Journal of Donghua University (English Edition)*, 2025, 42(5): 543-549.

Although some results have been achieved in the study of the aerostatic porous bearing with a restricted layer, they mainly focus on the influence of restricted-layer coefficients on the static characteristics of the bearing, and there is a lack of comparative analyses of the static characteristics of aerostatic porous bearings with a restricted layer or an unrestricted layer, unable to reflect the superiority of the structure and performance of the restricted-layer aerostatic porous bearing. Therefore, based on the gas lubrication theory, this paper establishes a mathematical model of the restricted-layer aerostatic porous bearing and proposes two proportional coefficients, a permeability ratio δ and a thickness ratio γ , to study the influence of complex restricted-layer parameters on the static characteristics of the aerostatic porous bearing. Through the sensitivity analyses, two critical values of δ and γ are obtained, and the influence of the restricted layer on the static characteristics of the aerostatic porous bearing is obtained by using Fluent simulation. The static characteristics of the restricted-layer aerostatic porous bearing and the unrestricted-layer aerostatic porous bearing are compared and analyzed to verify the superiority of the restricted-layer aerostatic porous bearing in terms of the structure and its static characteristics.

1 Mathematical Model

The schematic diagram of the restricted-layer aerostatic porous bearing is shown in Fig. 1. Pressurized gas is fed into the porous material through the upper surface of the coarse-layer porous material. The thin restricted-layer porous material has a lower permeability than that of the coarse-layer porous material. In the theoretical analysis, it is assumed that the gas flows in both the coarse layer and the restricted layer of the porous material obey Darcy's law^[16].



h —bearing clearance; H —thickness of coarse layer;

h_1 —thickness of restricted layer; r_a —radius of bearing.

Fig. 1 Schematic diagram of restricted-layer aerostatic porous bearing

The analysis is carried out under some assumptions for simplicity.

1) The gas flow is under the isothermal and laminar flow condition and the inertia effect is negligible in the bearing clearance.

2) The cross-film pressure gradient is negligible on the account of the extremely thin gas film.

3) The porous material is deemed to be isotropic, that is, the permeability of the porous material in all directions is equivalent.

Based on the above-mentioned assumptions, the mass flow rates of gases in three directions are

$$m_\theta = -\rho \frac{\varphi}{\mu} \frac{\partial p}{\partial \theta} dr dz, \quad (1)$$

$$m_r = -\rho \frac{\varphi}{\mu} \frac{\partial p}{\partial r} rd\theta dz, \quad (2)$$

$$m_z = -\rho \frac{\varphi}{\mu} \frac{\partial p}{\partial z} r dr d\theta, \quad (3)$$

where m_θ , m_r and m_z are the mass flow rates of gases in the θ , r and z directions; ρ is the gas density in the external atmosphere; φ is the permeability of the coarse-layer porous material; p is the gas pressure in the bearing clearance; μ is the dynamic viscosity of the gas.

In the numerical calculations, the mathematical model is discretized in three directions (i , j and k), as shown in Fig. 2, and the governing equation of pressure distribution is derived from the continuity of the mass flow in a small element.

According to the law of conservation of masses,

$$m_{\theta\text{in}} - m_{\theta\text{out}} + m_{r\text{in}} - m_{r\text{out}} + m_{z\text{in}} - m_{z\text{out}} = 0, \quad (4)$$

where the subscripts in and out represent the inflow and outflow of gases into and out of the coarse-layer porous material.

Substituting Eqs. (1)–(3) into Eq. (4), we can get the pressure distribution in the coarse-layer porous material:

$$\begin{aligned} & -\rho_b \frac{\varphi}{\mu} \frac{\partial p_b}{\partial \theta} \Big|_{\text{in}} dr dz + \rho_b \frac{\varphi}{\mu} \frac{\partial p_b}{\partial \theta} \Big|_{\text{out}} dr dz - \\ & \rho_b \frac{\varphi}{\mu} \frac{\partial p_b}{\partial r} \Big|_{\text{in}} \left(r + \frac{dr}{2}\right) d\theta dz + \rho_b \frac{\varphi}{\mu} \frac{\partial p_b}{\partial r} \Big|_{\text{out}} \left(r - \frac{dr}{2}\right) d\theta dz - \\ & \rho_b \frac{\varphi}{\mu} \frac{\partial p_b}{\partial z} \Big|_{\text{in}} r dr d\theta + \rho_b \frac{\varphi}{\mu} \frac{\partial p_b}{\partial z} \Big|_{\text{out}} r dr d\theta = 0, \end{aligned} \quad (5)$$

where the subscript b represents the coarse-layer porous material.

Considering the compressibility of an ideal gas $p_b/\rho_b = gRT$, where R is the universal gas constant and T is the gas thermodynamic temperature, Eq. (5) can be transformed as

$$\begin{aligned} & -p_b \frac{\varphi}{\mu} \frac{\partial p_b}{\partial \theta} \Big|_{\text{in}} dr dz + p_b \frac{\varphi}{\mu} \frac{\partial p_b}{\partial \theta} \Big|_{\text{out}} dr dz - \\ & p_b \frac{\varphi}{\mu} \frac{\partial p_b}{\partial r} \Big|_{\text{in}} \left(r + \frac{dr}{2}\right) d\theta dz + p_b \frac{\varphi}{\mu} \frac{\partial p_b}{\partial r} \Big|_{\text{out}} \left(r - \frac{dr}{2}\right) d\theta dz - \\ & p_b \frac{\varphi}{\mu} \frac{\partial p_b}{\partial z} \Big|_{\text{in}} r dr d\theta + p_b \frac{\varphi}{\mu} \frac{\partial p_b}{\partial z} \Big|_{\text{out}} r dr d\theta = 0. \end{aligned} \quad (6)$$

Introducing the boundary conditions:

$$p_b = p_s \text{ at } z = h + H,$$

$$p_b = p_t \text{ at } z = h + \gamma H,$$

$$\frac{\partial p_b}{\partial r} = 0 \text{ at } r = r_a,$$

where γ is the thickness ratio; p_s is the gas supply pressure; the subscript t represents the restricted layer of the porous material.

Due to the circumferential sealing of the coarse layer, the integrating gives the pressure expression in the coarse layer.

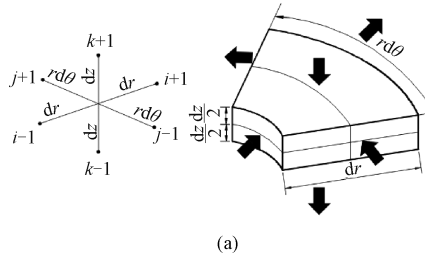
Figure 2 (b) shows the boundary between the restricted-layer and the coarse-layer porous material. The axial gas flow in the restricted layer can be ignored for simplicity considering the negligible thickness, and then the mass flow in the θ and r directions are expressed as

$$m_{\theta t} = -\rho \frac{h^3}{12\mu} \frac{\partial p}{r \partial \theta} dr, \quad (7)$$

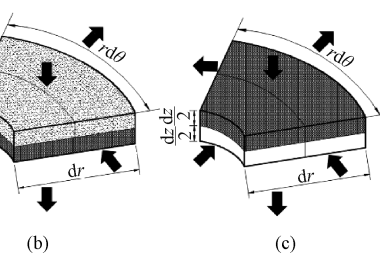
$$m_{rt} = -\rho \frac{h^3}{12\mu} \frac{\partial p}{\partial r} rd\theta. \quad (8)$$

Similarly, the corresponding pressure distribution equation can be obtained:

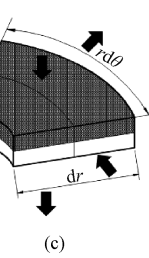
$$-\rho \frac{\partial p_t}{r \partial \theta} |_{in} drdz + p_t \frac{\partial p_t}{r \partial \theta} |_{out} drdz -$$



(a)



(b)



(c)

Fig. 2 Element structures and continuity of mass flow rates: (a) discrete element of porous material; (b) small element in boundary between coarse layer and restricted layer; (c) small element in boundary between restricted layer and bearing clearance

After integrating the pressure distribution over the bearing thrust surface, the bearing stiffness is defined as the rate of change of the load with clearance.

The conventional approach for acquiring performance parameters typically requires solving a set of complex differential governing equations, a process that often entails substantial computational overhead and significant time costs. With the rise and development of finite element software, these troubles could be circumvented by applying a computational fluid dynamics (CFD) approach^[17].

2 Numerical Simulation based on Fluent

2.1 Parameters of restricted-layer aerostatic porous bearing

For the restricted-layer aerostatic porous bearing, the

$$p_t \frac{\partial p_t}{\partial r} \Big|_{in} \left(r + \frac{dr}{2} \right) d\theta dz - p_t \frac{\partial p_t}{\partial r} \Big|_{out} \left(r - \frac{dr}{2} \right) d\theta dz - \\ 2p_t \frac{\partial p_t}{\partial z} \Big|_{in} rd\theta dr + 2\delta p_t \frac{\partial p_t}{\partial z} \Big|_{out} rd\theta dr = 0, \quad (9)$$

where δ represents the permeability ratio.

Introducing the boundary conditions:

$$p_t = p \text{ at } z = h,$$

$$\frac{\partial p_t}{\partial r} = 0 \text{ at } r = r_a.$$

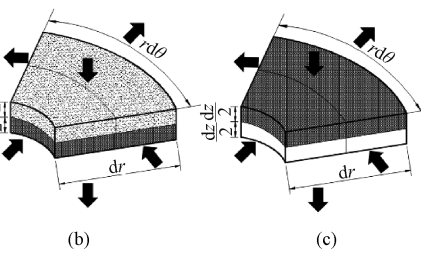
The junction of the restricted layer and the gas film is shown in Fig. 2 (c). The pressure in the bearing clearance can be expressed as

$$-p \frac{\partial p}{r \partial \theta} \Big|_{in} h^3 dr + p \frac{\partial p}{r \partial \theta} \Big|_{out} h^3 dr - \\ p \frac{\partial p}{\partial r} \Big|_{in} \left(r + \frac{dr}{2} \right) h^3 d\theta + p \frac{\partial p}{\partial r} \Big|_{out} \left(r - \frac{dr}{2} \right) h^3 d\theta - \\ 12\delta\varphi p \frac{\partial p}{\partial z} \Big|_{in} rd\theta dr = 0. \quad (10)$$

The load capacity is obtained by substituting the boundary conditions:

$$p = p_a \text{ at } r = r_a,$$

where p_a is the pressure of the external atmosphere.



permeability and thickness of the restricted layer are principle parameters, and are listed in Table 1. In this paper, the correlation between the parameters of the coarse layer and the restricted layer is taken into account innovatively, introducing the permeability ratio δ and the thickness ratio γ of the restricted layer:

$$\begin{cases} \gamma = \frac{h_1}{H}, \\ \delta = \frac{\varphi'}{\varphi}, \end{cases} \quad (11)$$

where φ' is the permeability of surface-restricted layer.

Table 1 Principal parameters of restricted-layer aerostatic porous bearing

Parameter	r_a/mm	H/mm	φ/m^2	δ	γ	p_a/MPa	T/K	p_s/MPa	$h/\mu\text{m}$
Value	15	5	10^{-12}	Variate	Variate	0.1	293	0.5	Variate

2.2 Sensitivity analysis of restricted-layer coefficients

At an air film thickness of 10 μm , the relationship among coefficients (δ and γ) and the bearing performance is obtained. As seen in Fig. 3, as δ increases, the load capacity and the mass flow rate of the bearing increase first and then flatten out at the demarcation value of 0.005, while the static stiffness consistently declines.

Furthermore, the higher γ is, the lower the load capacity and the mass flow are, and the slightly higher the static stiffness is. The multi-objective optimization based on CFD made a compromise with bearing performance. It recommends a set of candidate data, namely $\delta \approx 0.005$ and $\gamma \approx 0.010$, where the relatively high load capacity and static stiffness of the bearing can be obtained.

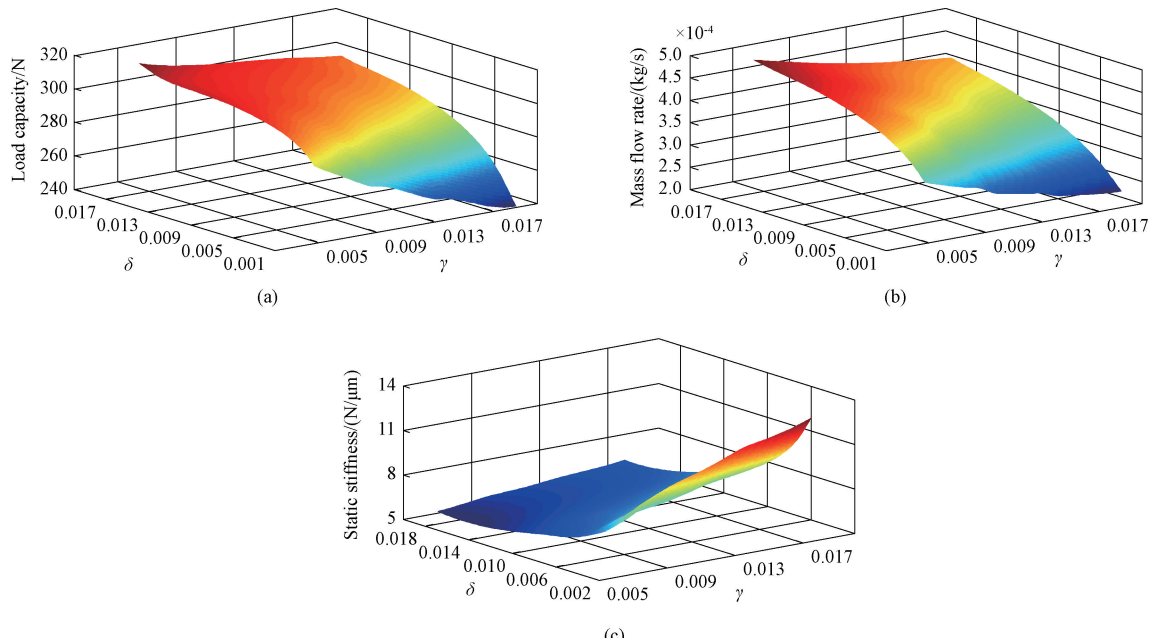


Fig. 3 Relationship among restricted-layer coefficients and static characteristics of bearing: (a) relationship among restricted-layer coefficients and load capacity; (b) relationship between restricted-layer coefficients and mass flow rate; (c) relationship among restricted-layer coefficients and static stiffness

2.3 Performance comparison between restricted-layer and unrestricted-layer aerostatic porous bearings

To achieve both high load capacity and static stiffness in the aerostatic porous bearing, a comparative analysis of bearing performance with varying permeability levels should be conducted, with particular emphasis on the role of the coarse layer. Drawing on the foregoing discussed values of δ and γ , the performance comparison between bearings with a restricted layer and those with different permeabilities in case of different bearing clearances is made. Figure 4 illustrates that the load capacity and static stiffness decrease but the mass flow rate increases with the bearing clearance increasing. The lower the permeability of the coarse-layer porous material, the greater the decline of the load capacity for the unrestricted-layer aerostatic porous bearing. The unrestricted-layer aerostatic porous bearing with a permeability of 10^{-12} m^2 presents a rather low static

stiffness and considerably high mass flow rate, though its load capacity is superior to other bearings. Additionally, the unrestricted-layer aerostatic porous bearing with a permeability of 10^{-14} m^2 exhibits a high static stiffness when the bearing clearance is less than 9 μm . Nevertheless, this inevitably requires operation under extremely narrow bearing clearance conditions, which requires considerably high manufacturing accuracy. By comparison, the restricted-layer aerostatic porous bearing not only retains a relatively higher load capacity but also has a lower mass flow rate. In particular, when the bearing clearance is higher than 15 μm , the static stiffness of the restricted-layer aerostatic porous bearing steadily exceeds that of other bearings, while the load capacity and static stiffness of the unrestricted-layer aerostatic porous bearing at a permeability of 10^{-14} m^2 gradually become inferior. Therefore, the bearing with a restricted layer takes on better practicality and superiority in terms of applicable bearing clearance.

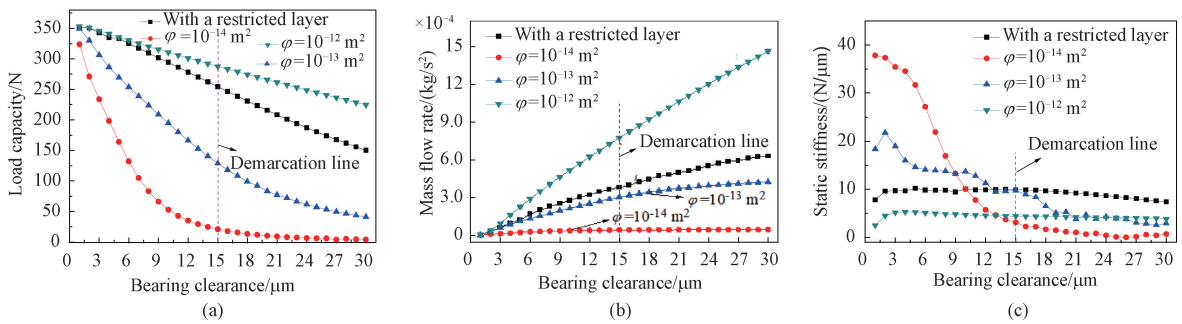


Fig. 4 Static characteristic comparison among bearings with different materials: (a) relationship between bearing clearance and load capacity; (b) relationship between bearing clearance and mass flow rate; (c) relationship between bearing clearance and static stiffness

Figure 5 shows the pressure contour plots on the section through the axis of the coarse layer, which reflects the pressure drop in the porous material. When the compressed gas is fed to the bearing, the pressure drops due to the viscous flow across the porous restrictor. It is obvious that the pressure drop across the unrestricted layer of the porous material gradually aggravates with the permeability decreasing. Furthermore, the higher the

bearing clearance is, the sharper the pressure drop in the coarse-layer porous material. In contrast, a large percentage of the pressure drop occurs in the restricted layer of porous material, considerably reducing the viscous loss. Thus, the researchers have the freedom to adjust the geometry of the coarse layer to meet the mechanical requirements.

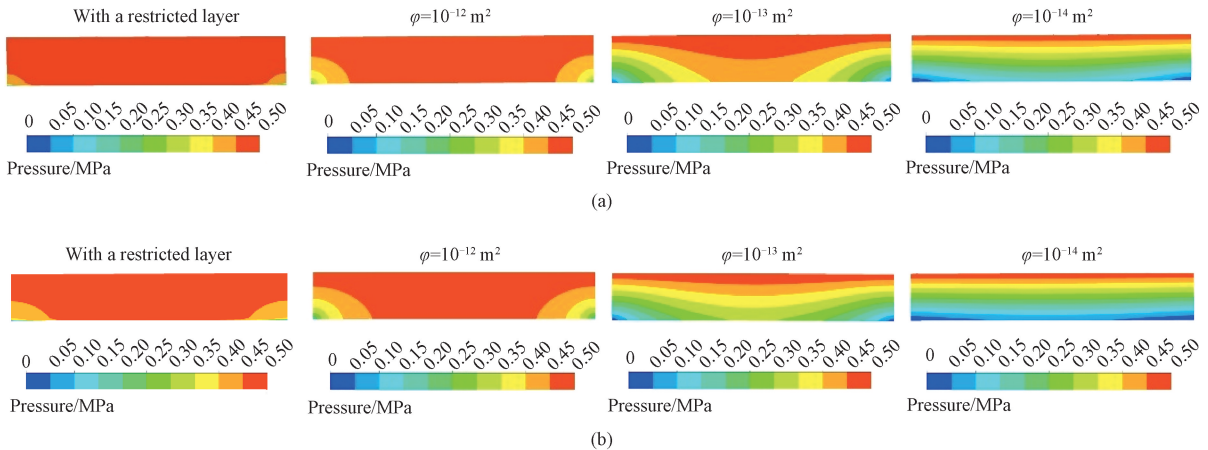


Fig. 5 Comparison of pressure contour plots of different bearings: (a) pressure contour plots at h of $10 \mu\text{m}$; (b) pressure contour plots at h of $15 \mu\text{m}$

The static characteristics of the bearing are obtained when the bearing clearance is $20 \mu\text{m}$ and subtracted from that of the bearing with a full gas supply. Figure 6 reveals that the bearing with a low permeability generally shows a relatively low sensitivity to the bearing clearance. Figure 6(c) conveys the abnormal message that when the bearing clearance is less than $12 \mu\text{m}$, the mass flow rate difference increases first and then decreases with the increase of the permeability, and the mass flow rate

difference of the unrestricted-layer aerostatic porous bearing with a high permeability increases rapidly. In conclusion, the restricted-layer aerostatic porous bearing highlights a small performance difference except for the unrestricted-layer aerostatic porous bearing with a permeability of 10^{-14} m^2 when the gas supply area changes, and especially with the increase of the bearing clearance, the static stiffness difference of all bearings becomes subtle.

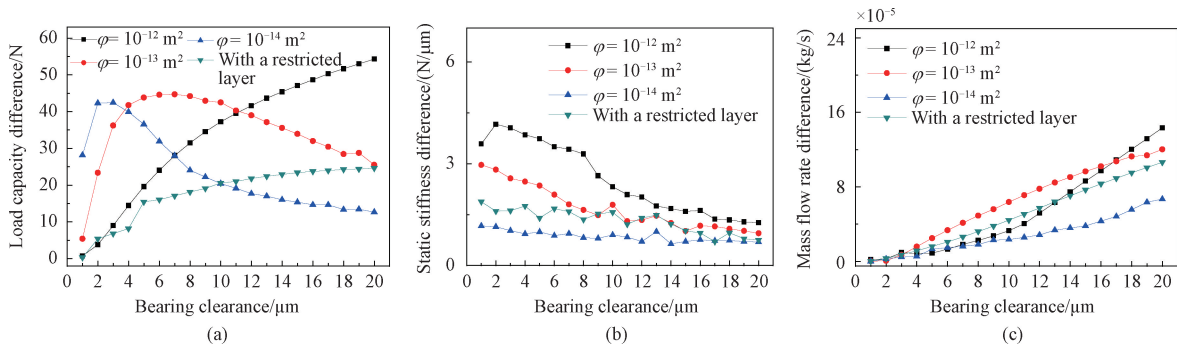


Fig. 6 Bearing performance comparison among bearings with different bearing clearances: (a) relationship between bearing clearance and load capacity difference; (b) relationship between bearing clearance and static stiffness difference; (c) relationship between bearing clearance and mass flow rate difference

3 Conclusions

In this paper, the static characteristics of the restricted-layer aerostatic porous bearing such as the load capacity, static stiffness and mass flow rate are analyzed by theory and Fluent simulation. The conclusions are as follows.

1) Two proportional coefficients, a permeability ratio δ and a thickness ratio γ , are proposed, and a parametric sensitivity analysis shows that when $\delta \approx 0.005$ and $\gamma \approx 0.010$, the load capacity and static stiffness of the restricted-layer aerostatic porous bearing are higher.

2) Compared with the unrestricted-layer aerostatic porous bearing, the existence of the restricted layer not only enhances the throttling effect and reduces the mass flow rate, but also effectively improves the static stiffness of the bearing.

3) The pressure drop mainly occurs on the surface of the restricted layer, which greatly reduces the viscous loss. Thus, the restricted-layer aerostatic porous bearing allows researchers to freely adjust the geometry of the coarse layer to meet the mechanical requirements.

4) The low permeability bearing is less sensitive to changes in the bearing clearance. When the gas supply area changes, the restricted-layer aerostatic porous bearing has a lower difference in performance change than the unrestricted-layer aerostatic porous bearing, and has superior load capacity and static stiffness.

References

- [1] CHEN G D, JU B F, FANG H, et al. Air bearing: academic insights and trend analysis [J]. *The International Journal of Advanced Manufacturing Technology*, 2020, 106 (3): 1191-1202.
- [2] ZHANG K, HU H D, GUO M H, et al. Effects from O-rings on the stability of a rotor-porous air journal bearing test-rig [J]. *Journal of Mechanical Engineering*, 2024, 60: 1-9. (in Chinese)
- [3] GU Y D, MARTIN B, ARTUR S, et al. Aerostatic bearing with porous restrictor: research status and future perspectives [J]. *Journal of Drainage and Irrigation Machinery Engineering*, 2021, 39(8) : 818-825. (in Chinese)
- [4] WANG W, CHENG X H, ZHANG M, et al. Effect of the deformation of porous materials on the performance of aerostatic bearings by fluid-solid interaction method [J]. *Tribology International*, 2020, 150: 106391.
- [5] YAN R Z, ZHANG Y B. Static and dynamic characteristics of vacuum preloaded porous aerostatic bearings [J]. *Journal of Donghua University (English Edition)*, 2024, 41(1) : 81-88.
- [6] SAN ANDRÉS L, YANG J, MCGOWAN R. Measurements of static and dynamic load performance of a 102 MM carbon-graphite porous surface tilting-pad gas journal bearing [J]. *Journal of Engineering for Gas Turbines and Power*, 2021, 143(11) : 111017.
- [7] KANG L, ZHANG X N, LOU J J, et al. Conjugate heat transfer study on porous media gas lubricated bearing [J]. *Journal of Engineering for Thermal Energy and Power*, 2020, 35(3) : 158-166. (in Chinese)
- [8] YAMADA K, ONISHI N, SEKIYA K, et al. Permeability control method with laser for porous bushings of aerostatic bearings [J]. *International Journal of Precision Engineering and Manufacturing*, 2013, 14(5) : 779-784.
- [9] PANZERA T H, CHRISTOFORO A L, CAMPOS RUBIO J C, et al. Evaluation of compacted cementitious composites for porous bearings [J]. *International Journal of Applied Ceramic Technology*, 2013, 10(3) : 474-483.
- [10] DA SILVA L J, PANZERA T H, VIEIRA L M, et al. Carbon nanotubes and superplasticizer reinforcing cementitious composite for aerostatic porous bearing [J]. *Proceedings of the Institution of Mechanical Engineers, Part J: Journal of Engineering Tribology*, 2017, 231(11) : 1397-1407.

- [11] MIYATAKE M, YOSHIMOTO S, SATO J. Whirling instability of a rotor supported by aerostatic porous journal bearings with a surface-restricted layer [J]. *Proceedings of the Institution of Mechanical Engineers, Part J: Journal of Engineering Tribology*, 2006, 220(2): 95-103.
- [12] CUI C, ONO K. Theoretical and experimental investigation of an externally pressurized porous annular thrust gas bearing and its optimal design [J]. *Journal of Tribology*, 119(3): 486-492.
- [13] SAHA N, MAJUMDAR B C. Study of externally-pressurized gas-lubricated two-layered porous journal bearings: a steady state analysis [J]. *Proceedings of the Institution of Mechanical Engineers, Part J: Journal of Engineering Tribology*, 2002, 216(3): 151-158.
- [14] YOSHIMOTO S, TOZUKA H, DAMBARA S. Static characteristics of aerostatic porous journal bearings with a surface-restricted layer [J]. *Proceedings of the Institution of Mechanical Engineers, Part J: Journal of Engineering Tribology*, 2003, 217(2): 125-132.
- [15] FENG K, LI W J, HUO Y W, et al. Thermal characteristic analysis of aerostatic porous journal bearings with surface-restricted layer [J]. *Journal of Mechanical Engineering*, 2018, 54(12): 216-224. (in Chinese)
- [16] OTSU Y, MIYATAKE M, YOSHIMOTO S. Dynamic characteristics of aerostatic porous journal bearings with a surface-restricted layer [J]. *Journal of Tribology*, 2011, 133(1): 011701.
- [17] LI Y F, YIN Y H, YANG H, et al. Modeling for optimization of circular flat pad aerostatic bearing with a single central orifice-type restrictor based on CFD simulation [J]. *Tribology International*, 2017, 109: 206-216.

带有限制层多孔质空气轴承静态特性分析

余 哲^{1, 2}, 闫如忠^{1, 2*}, 马晓建^{1, 2}, 张豪杰^{1, 2}

1. 东华大学 机械工程学院, 上海 201620

2. 东华大学 纺织装备教育部工程研究中心, 上海 201620

摘要: 为增强气体阻尼效果并提高轴承性能, 可在多孔质空气轴承的表面增加限制层。基于气体润滑理论, 建立了带有限制层多孔质空气轴承的数学模型, 提出了渗透率比 δ 和厚度比 γ 两个比例系数。通过对复杂的限制层参数进行参数敏感性分析得到 δ 和 γ 的临界系数。利用 Fluent 仿真对带有限制层多孔质空气轴承和非限制层多孔质空气轴承的静态特性进行了对比分析。结果表明: 当 $\delta \approx 0.005$ 、 $\gamma \approx 0.010$ 时, 带有限制层多孔质空气轴承的承载能力和静刚度较大; 与非限制层多孔质空气轴承相比, 带有限制层多孔质空气轴承对供气区域变化的敏感度较低。限制层的存在不仅能增强节流效果, 降低空气质量流率, 还能有效提高轴承静刚度。

关键词: 多孔质空气轴承; 限制层; 静态性能; 临界系数

Automated Bionic Wig Weaving Process Design and Weaving Path Planning

LYU Hongzhan*, YOU Jia, LI Junjie, LU Licheng, SUN Zhihong

College of Mechanical Engineering, Donghua University, Shanghai 201620, China

Abstract: The traditional production of bionic wigs through manual weaving is a complex process characterized by high labor intensity, making automation challenging. To address this issue, an automated weaving process for bionic wigs is proposed and the design of an automated bionic wig weaving machine is presented based on an analysis of manual weaving principles and processes. Furthermore, according to the characteristics of the weaving machine and the distribution pattern of weaving nodes, the minimum weaving duration of a single hairnet is taken as the optimization goal, and a continuous weaving path planning for the weaving process of the mixed scheme is conducted. The weaving duration for various weaving paths are calculated and compared, and the results indicate that the duration of the S-shaped weaving path is always the shortest in different weaving regions. The designed automated weaving process and the weaving path planning provide a theoretical foundation and experimental data for achieving automated weaving of bionic wigs.

Keywords: bionic wig; weaving process; wig weaving machine; path planning

CLC number: TS9

Document code: A

Article ID: 1672-5220(2025)05-0550-08

Open Science Identity
(OSID)



0 Introduction

China is a leading producer and exporter of wigs. In the year of 2022, global wig market has reached nearly 100 billion USD, with China accounting for 80% of worldwide exports^[1]. Bionic wigs, primarily worn as aesthetic prostheses, are fabricated by manually weaving individual hair strands into lace hairnet^[2], making the manual weaving process both time-consuming and labor-intensive. This time-consuming task has led to steadily rising labor costs. As the market demand for bionic wigs continues to surge, the need for automation in wig weaving is becoming increasingly urgent.

There has been extensive research on the automated wig weaving machines. It is disclosed in Ref. [3] that there is a motor-driven crochet in the experimental device to move hair. The principle is simple, but the device is

large and exhibits low automation, and the continuity and precision of weaving cannot be guaranteed. Hiroshi^[4] proposed an automated hair-transplant machine that utilized a vacuum generator to adhere artificial hair strands to the base of a hairnet. The hair strands were woven onto the hairnet by the up-and-down movement of a specialized crochet hook. However, due to its limited adsorption capabilities, the machine could only use artificial hair strands as raw materials in the weaving process. Kuang et al.^[5] designed a wig weaving machine that employed a double cam mechanism to plan the crochet trajectory, and the weaving path of the machine was designed by adjusting the hairnet position with a two-dimensional numerical control table. However, the design remains semi-automatic, and manual adjustments and coordination are needed. Mitsuhiro et al.^[6] introduced a manipulator with dual clamping mechanisms in the wig weaving. However, the absence of continuous path planning and the uncontrolled distribution of loose hair strands prevent the continuous weaving.

With the research on automated wig weaving machines, the wig weaving process has undergone continuous improvement and development. Lin^[7] proposed a three-layer hairnet wig-making process, which involved weaving on two layers of the interlaced hairnet and then sewing them together at the bottom. Although this three-layer hairnet is sturdy, its breathability is very poor, and its unique structure is difficult to manufacture. Tao et al.^[8] enhanced the traditional weaving process by adding elastic ropes to the folded ends of the hair strands, increasing the firmness of the hair knots. However, the steps are complicated and it is difficult for automation. Sun et al.^[9] introduced a new wig weaving process suitable for automated weaving machines, utilizing a latch needle to complete the knotting action and produce double knots. This method is more suitable for automated weaving machines.

In summary, the concept of automated weaving machine for bionic wigs is still at the patent level, and there is currently no wig weaving device that can achieve automation in wig weaving. In this paper, the manual bionic wig weaving process is analyzed to enhance the

Received date: 2024-09-27

Foundation item: Yuzhou Olandi Arts & Crafts Co., Ltd., Project of Development and Research of Wig Planting Equipment, China (No. HX103210723)

* Correspondence should be addressed to LYU Hongzhan, email: lvhz@dh.edu.cn

Citation: LYU H Z, YOU J, LI J J, et al. Bionic wig automated weaving process design and weaving path planning[J]. *Journal of Donghua University (English Edition)*, 2025, 42(5): 550-557.

design of an automated bionic wig weaving process based on existing manual wig weaving machines. Additionally, path planning during the weaving process is designed for the weaving machine.

1 Manual Bionic Wig Weaving Process

The manual bionic wig weaving consists of three key elements: a crochet, a hairnet and hair strands. The crochet is a specialized manual weaving tool with a barb on the front of the crochet. The hairnet is made of polyester lace and is composed of interwoven meshes with a height of 0.8 mm. The polyester lace material not only ensures adequate tension and elasticity but also possesses a degree of toughness which aids in crocheting and enhances the wig's durability^[10]. Most ordinary wigs on the market are made from synthetic fibers^[11] on the consideration of

costs. However, the strength and texture of wigs made from these fibers are subpar^[12], and their shaggy appearance significantly differs from that of human hair. Consequently, human hair is selected as a raw material for bionic wigs to achieve a more realistic effect. Combining the above three key elements, the final bionic wig product maintains a high degree of consistency with the human hair growth in terms of shape, smoothness and imitation.

In manual weaving, the worker coils the hair into a circle with one hand and operates the crochet with the other. Then the worker continuously twists the wrist to adjust the position of the crochet, and weaves the hair strands into knots along the common edge of the hairnet meshes. The double knot weaving process^[13] is utilized in manual weaving, which employs the reverse half-buckle method to create double knots. The manual double knot weaving process is illustrated in Fig. 1.

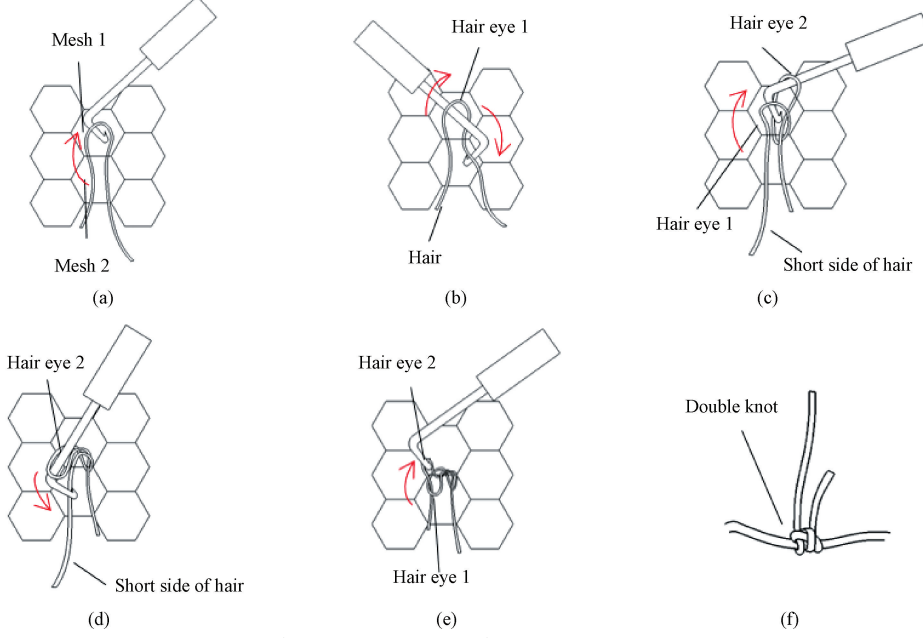
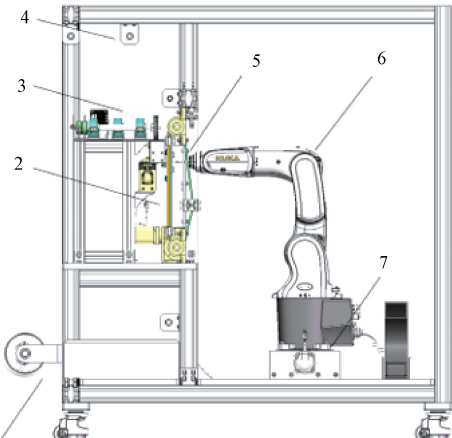


Fig. 1 Double knot weaving process: (a) crochet first feed; (b) hair eye 1 formation and crochet second feed; (c) hair eye 2 formation; (d) crochet third feed; (e) hook through hair eye 2; (f) double knot formation

2 Automated Bionic Wig Weaving Principle and Process Design

2.1 Automated bionic wig weaving machine and principle

To achieve the automation of the weaving process, an automated bionic wig weaving machine^[14] is designed, as illustrated in Fig. 2. The weaving machine is primarily divided into three devices: the crochet drive device^[15], the hairnet transmission device^[16] and the hair conveying device^[17]. These three devices correspond to the three essential elements of manual weaving: the crochet, the hairnet and the hair strands. During the weaving process, the crochet weaving action, continuous hairnet conveying and hair feeding are performed, respectively.



1—winder; 2—hairnet transmission device; 3—hair conveying device; 4—roller; 5—latch needle; 6—corobot; 7—ground rail.
Fig. 2 Model of automated bionic wig weaving machine

Figure 3 is the schematic diagram of the automated bionic wig weaving machine. According to the requirements of manual weaving, improvements are made to address the complex weaving actions involved in the crochet. The hairnet is repositioned vertically, and the original barbed crochet is replaced with a latch needle, which is now placed at the front of the hairnet. The hair conveying device organizes the hair strands into a uniform and evenly distributed curtain which is positioned at the rear end of the hairnet. When the weaving machine is in operation, the corobot controls the latch needle to execute a series of knotting actions, and the process is modularized. The ground rail is located at the bottom of the corobot, and it drives the corobot to move horizontally to complete the horizontal weaving of the hairnet. The hairnet transmission device longitudinally moves the hairnet to complete the longitudinal weaving.

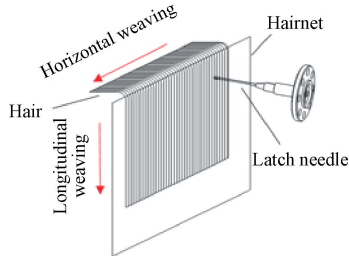


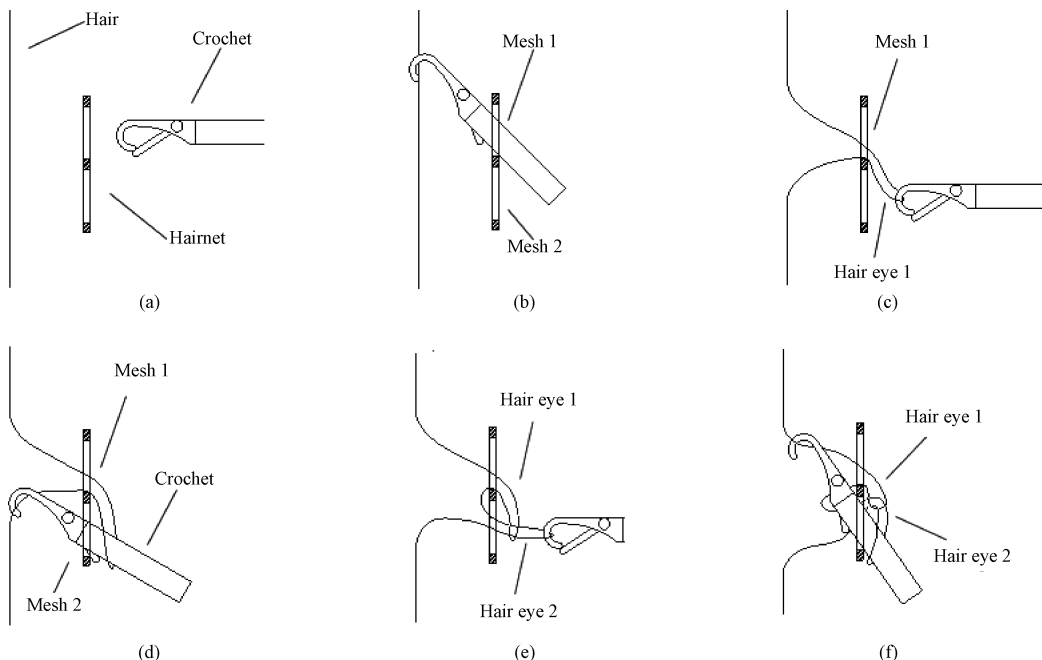
Fig. 3 Schematic diagram of automated bionic wig weaving machine

2.2 Automated bionic wig weaving process design

In order to ensure the efficiency and quality of automated weaving, the automated weaving process is

designed based on the double knot weaving process. The relative movement of the crochet and hairnet in the weaving process of a double knot is shown in Fig. 4. The movement of the crochet in the automated process is divided into nine decomposition actions to achieve the automated weaving of a double knot.

The weaving of a double knot involves two adjacent meshes, namely mesh 1 and mesh 2. The entire automated bionic wig weaving process can be divided into four phases. In the first phase, the crochet is inserted diagonally through mesh 1 to pick up the hair strands and pull them out, as shown in Figs. 4(a)–4(c). The hair strands create a loop at the common edge of the two meshes, referred to as hair eye 1. In the second phase, the crochet hooks the long edge of the hair through mesh 2, forming a loop with hair eye 1, which is designated as hair eye 2, as shown in Figs. 4(d)–4(e). In the third phase, the crochet hooks the short edge of the hair completely out of mesh 2 from hair eye 2, as shown in Figs. 4(f)–4(g). In the fourth phase, the long edge of the hair is fully extracted, resulting in a double knot, as shown in Figs. 4(h)–4(i). Compared with the manual weaving process, the automated weaving process only alters the initial layout of key elements. In the step of forming a double knot, both the two processes involve two adjacent meshes, and the composition of hair eye 1 and hair eye 2 formed during weaving is the same. Therefore, the double knot produced in the automated weaving process is consistent in quality with that produced in the manual weaving process.



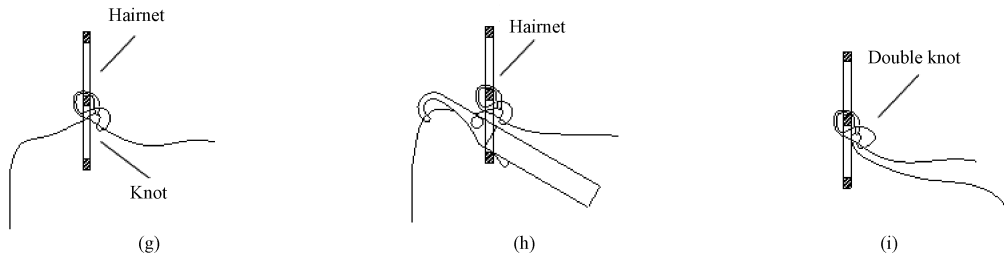


Fig. 4 Automated bionic wig weaving process: (a) initial placement; (b) crochet first feed; (c) hair eye 1 formation; (d) crochet second feed; (e) hair eye 2 formation; (f) crochet third feed; (g) knot formation; (h) crochet fourth feed; (i) double knot formation

3 Automated Bionic Wig Weaving Path Planning

To achieve continuous weaving of the entire hairnet, it is essential to plan the weaving path. The hairnet is staggered by a grid of regular hexagons, and the weaving nodes are located along the common sides of the hexagons. The distance between adjacent transverse weaving nodes is 1.386 mm, while the vertical distance between two longitudinal weaving nodes is 0.800 mm. All the weaving nodes on the hairnet collectively form a single area shaped like a hairnet, as illustrated in Fig. 5. This area can be divided into two distinct regions, namely the rectangular region and the semicircular region.

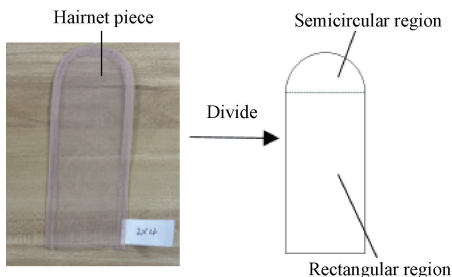


Fig. 5 Region division of hairnet piece

A shorter weaving path can reduce weaving duration and correspondingly increase the weaving efficiency. During the weaving process of a hairnet, the rectangular region and the semicircular region need to be completed in sequence. Therefore, the shortest total weaving duration of a single hairnet can be expressed as

$$\min T_w = \min T_r + \min T_s, \quad (1)$$

where T_w represents the total weaving duration of a single hairnet; T_r denotes the total weaving duration of a rectangular region; T_s indicates the total weaving duration of a semicircular region.

3.1 Weaving path in rectangular region

The distribution of weaving nodes in the rectangular region is shown in Fig. 6. All the odd rows contain the same number of weaving nodes. All the even rows contain the same number of weaving nodes. Due to the alternating grid distribution, even rows have one fewer weaving node than odd rows. Suppose the total number

of rows in the rectangular region is n , where n is even, and the total number of weaving nodes in the first row is m , where m is odd. Then the total number of weaving nodes in the second row will be $m-1$, and the number of weaving nodes in the subsequent rows is cycled in turn.

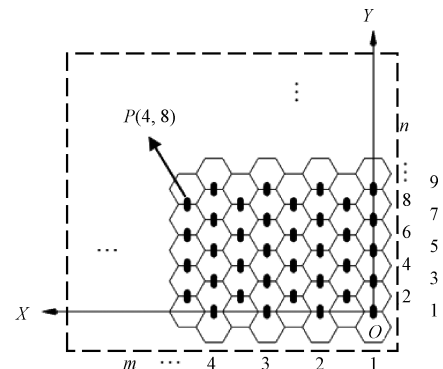


Fig. 6 Distribution of weaving nodes in rectangular region

Take the lower right corner of the rectangular region as the weaving origin, the positive direction of the X axis extends to the left, while the positive direction of the Y axis extends upward. Any weaving node on the hairnet can be represented as $P(m, n)$. For example, the weaving node marked in Fig. 6 is denoted as $P(4, 8)$. Then the shortest total weaving duration in the rectangular region is

$$\min T_r = \min t_1 + \min t_2, \quad (2)$$

where t_1 represents the total knotting duration of all weaving nodes; t_2 represents the total movement duration including the total horizontal movement time and the total longitudinal movement time. The entire weaving of the rectangular region can be regarded as a set from a weaving node P_i to the next weaving node P_j . Let the coordinates of P_i be denoted as $P(m_i, n_i)$, and the coordinates of P_j be denoted as $P(m_j, n_j)$. Then the formula can be obtained

$$t_1 = N_w t_w, \quad (3)$$

where N_w is the number of all weaving nodes in the rectangular region; t_w is the weaving duration of one node. Since P_i and P_j are weaving nodes within the rectangular region, it can be obtained that

$$\forall i \in \{1, 2, \dots, N_w - 1\}, \\ j \in \{2, 3, \dots, N_w\}, j - i = 1, \quad (4)$$

$$t_2 = \sum_{i=1}^{N_w-1} \sum_{j=2}^{N_w} x_{ij} t_H + \sum_{i=1}^{N_w-1} \sum_{j=2}^{N_w} y_{ij} t_L, \quad (5)$$

$$x_{ij} = \begin{cases} 2, & \text{when } |n_i - n_j| = 0, \\ 1, & \text{when } |n_i - n_j| = 1, \\ 0, & \text{others,} \end{cases} \quad (6)$$

$$y_{ij} = |n_i - n_j|, \quad (7)$$

where t_H is the duration required to move half the spacing between two horizontally adjacent nodes; t_L is the duration required to move the full spacing between two longitudinally adjacent nodes; x_{ij} is the coefficient of the horizontal distance from P_i to P_j ; y_{ij} is the coefficient of the longitudinal distance from P_i to P_j .

The entire rectangular region can be viewed as a

loop formed by the first two rows of weaving nodes. Therefore, as long as the fastest weaving path for the first two rows is determined, the optimal weaving path for the entire rectangular region can be established. The first two rows of weaving nodes within the rectangular region are designated as the object, and based on their distribution, two primary weaving paths have been identified as shown in Fig. 7: the S-shaped weaving path and the folding weaving path. In the S-shaped weaving path, the weaving path first begins from $P(1, 1)$ to the left until reaching $P(m, 1)$; then, the weaving path in the second row starts from $P(m-1, 2)$ to the right until reaching $P(1, 2)$. While in the folding weaving path, the nearest node is selected as the next weaving node. The weaving path starts from $P(1, 1)$ to $P(1, 2)$, and then to $P(2, 1)$, and proceeds until reaching the final node $P(m, 1)$; after the two rows of weaving are completed, the path transitions to $P(m, 3)$ to initiate a new round of two-row cyclic weaving.

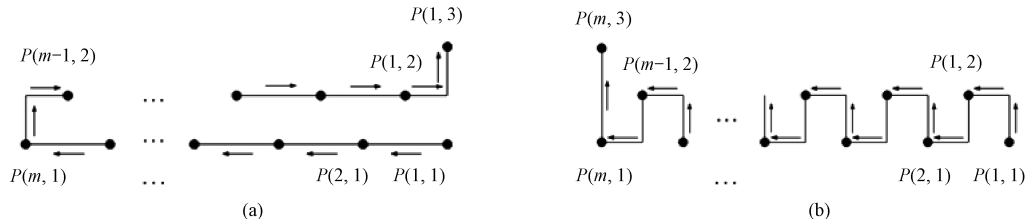


Fig. 7 Two weaving paths in rectangular region: (a) S-shaped weaving path; (b) folding weaving path

The weaving duration comparison of the above two weaving paths is shown in Table 1. The knotting duration is related to the number of all weaving nodes, so it is the same for the two weaving paths. Thus, the movement duration in the moving process is compared. Since the speed of the horizontal and longitudinal movements is the same, the comparison of the movement duration can be

converted into a comparison of the distance as shown in Table 1. As m is a large positive integer, the corresponding distance of the S-shaped weaving path is shorter than that of the folding weaving path. The weaving duration of the S-shaped weaving path is shorter and the efficiency is higher. As a result, the S-shaped weaving path is selected in the rectangular region.

Table 1 Weaving duration comparison of two weaving paths in rectangular region

Weaving path	Knotting duration	Horizontal movement duration	Longitudinal movement duration	Corresponding distance
S-shaped weaving	$(2m - 1)t_w$	$4(m - 1)t_H$	$2t_L$	$2.772m - 0.907$
Folding weaving	$(2m - 1)t_w$	$2(m - 1)t_H$	$2mt_L$	$2.986m - 1.386$

3.2 Weaving path in semicircular region

The distribution of weaving nodes in the semicircular region is illustrated in Fig. 8. The alternating weaving nodes create the shape of the semicircle. As stated in subsection 3.1, row n of the rectangular region contains $m-1$ weaving nodes. Therefore, the first row of the semicircular region contains m weaving nodes. The semicircular region consists of a total of $(m-1)/2$ rows. With the center of the semicircular region as the boundary, the X axis and Y axis are established to ensure that all nodes are symmetrically distributed on both sides of the Y axis.

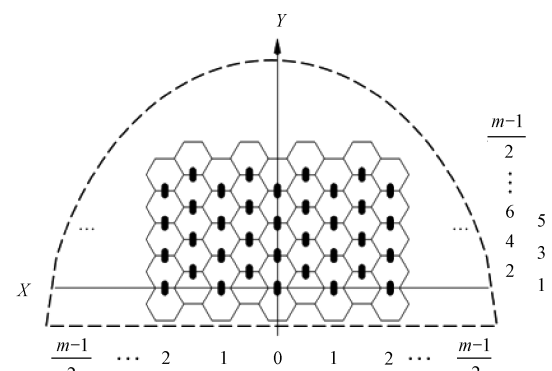
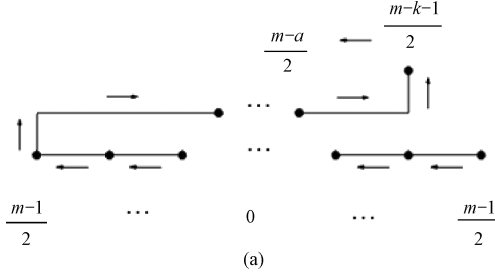


Fig. 8 Distribution of weaving nodes in semicircular region

Starting from the first row and moving upward, the number of weaving nodes in the odd-numbered rows decreases in an arithmetic sequence with a common difference denoted as k . Additionally, the difference in the number of weaving nodes between each odd-numbered row and the even-numbered row above it is a fixed value, denoted as a , where a is an odd number. In the semicircular region, the weaving order remains from

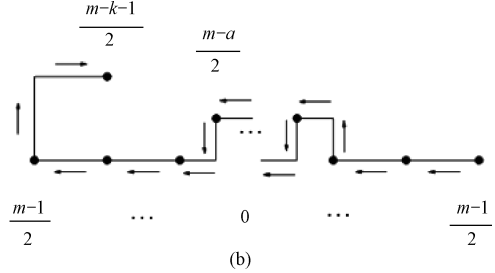


(a)

the bottom up, and the shortest weaving duration of the semicircular weaving path is

$$\min T_s = t_1 + t_2. \quad (8)$$

Based on the distribution of weaving nodes and the weaving requirements, there are two types of weaving paths in the semicircular region as shown in Fig. 9: the S-shaped weaving path and the mixed weaving path.



(b)

Fig. 9 Two weaving paths in semicircular region: (a) S-shaped weaving path; (b) mixed weaving path

In the S-shaped weaving path, the weaving path begins at the rightmost end and proceeds sequentially through the first row of m weaving nodes. The weaving path then moves to the outermost node in the second row and continues from left to right. The mixed weaving path is a combination of S-shaped weaving and folding weaving. The second row contains a fewer weaving nodes than the first row, resulting in no weaving nodes above the outermost nodes of the first row. Consequently, the outer section employs S-shaped weaving, while the middle section utilizes folding weaving. After completing the weaving of the two rows, the weaving path stops at the leftmost node of the first row. In the rectangular region, after completing the first two rows, the S-shaped weaving path must transition from the rightmost node in the second row to the rightmost node in the third row to continue with the next two rows. In contrast, the mixed weaving path requires a movement from the leftmost node in the first row to the leftmost node in the third row. Both weaving paths

necessitate additional movement along a specific route. Consequently, Eq. (5) has been revised to incorporate a compensation distance for this movement.

$$t_2 = \sum_{i=1}^{N_w-1} \sum_{j=2}^{N_w} x_{ij} t_H + \sum_{i=1}^{N_w-1} \sum_{j=2}^{N_w} y_{ij} t_L + \sum_{p=1}^{(m-1)/2} e_p t_H + \sum_{q=1}^{(m-1)/2} e_q t_L, \quad (9)$$

$$e_q = \begin{cases} |n_i - n_j|, & \text{when } |n_i - n_j| \in \{0, 1\}, \\ 0, & \text{others,} \end{cases} \quad (10)$$

$$e_p = \begin{cases} k, & \text{when } |n_i - n_j| = 2, \\ a - k, & \text{others,} \end{cases} \quad (11)$$

where e_q is the compensation factor for the additional longitudinal movement; e_p is the compensation factor for the additional horizontal movement. Since the total number of weaving nodes is the same, the knotting duration is also the same. To compare the movement duration of the two weaving paths, the specific durations are converted into their corresponding distances as shown in Table 2.

Table 2 Weaving duration comparison of two weaving paths in semicircular region

Weaving path	Horizontal movement duration	Longitudinal movement duration	Compensation duration	Corresponding distance
S-shaped weaving	$(4m - 4 - a)t_H$	t_L	$t_L + (a - k)t_H$	$2.772m - 0.693k - 1.172$
Mixed weaving	$2(m - 1)t_H$	$2(m - a)t_L$	$2t_L + kt_H$	$2.986m + 0.693k - 1.6a + 0.214$

Subtract the corresponding distance of the mixed weaving path from that of the S-shaped weaving path to obtain their difference Δf

$$\Delta f = 0.214m + 1.386k - 1.6a + 1.386. \quad (12)$$

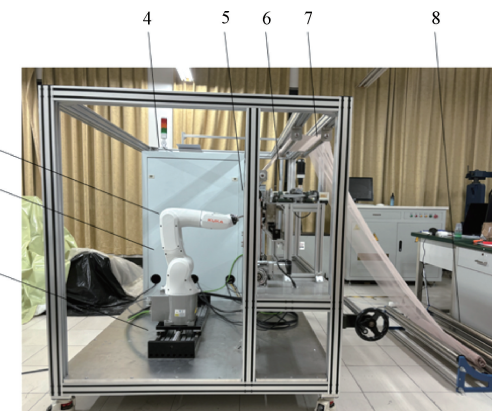
According to the specific dimensions of the hairnet, m is a number larger than 41. This indicates that m is a large positive integer. Additionally, in order to ensure

the number of rows in the hairnet, a and k serving as decreasing factor parameters, should be small positive integers. Compared to the numbers and parameters appearing in Eq. (12), m is obviously much larger than them. Therefore, considering the actual conditions of hairnet weaving, the condition $\Delta f > 0$ always holds. This means that the weaving duration for the mixed weaving path is longer than that for the S-shaped weaving path.

Consequently, in order to maintain the weaving efficiency, the S-shaped weaving path is also selected in the semicircular region.

3.3 Experimental verification of weaving path

To verify the feasibility of the proposed shortest weaving path, experiments are conducted by using the designed automated bionic wig weaving machine, as illustrated in Fig. 10. A standard-sized hairnet ($5.08 \text{ cm} \times 10.16 \text{ cm}$) is selected as the weaving target, and the movement duration across the area of a single hairnet is recorded. According to the designed weaving path, the S-shaped weaving and folding weaving paths are employed in the rectangular region, while the S-shaped weaving and mixed weaving paths are utilized in the semicircular region. Three groups of the movement duration for different weaving paths in both regions are measured in the experiment, as shown in Table 3.



1—ground rail; 2—crochet drive device; 3—corobot; 4—electrical cabinet; 5—hairnet transmission device; 6—hair conveying device; 7—hairnet roll; 8—uncoiler.

Fig. 10 Automated bionic wig weaving machine

Table 3 Movement duration of different weaving paths in each region

Region and weaving path	The first group of movement duration/s	The second group of movement duration/s	The third group of movement duration/s
S-shaped weaving path in rectangular region	6 649. 6	6 651. 8	6 652. 1
Folding weaving path in rectangular region	7 202. 5	7 203. 6	7 204. 5
S-shaped weaving path in semicircular region	704. 6	703. 5	703. 9
Mixed weaving path in semicircular region	774. 3	773. 6	772. 8

In the rectangular region, the movement duration of the S-shaped weaving path saves about 550 s, and the efficiency increases by about 7.7% compared with that of the folding weaving path. In the semicircular region, the movement duration of the S-shaped weaving path saves about 70 s and the efficiency increases by about 9.0% compared with that of the mixed weaving path. The weaving path planning proposed above is accurate, and the S-shaped weaving path is the most efficient.

4 Conclusions

A design for an automated bionic wig weaving process is presented and an automated bionic wig weaving machine is developed along with the conduction of weaving path planning. The main conclusions are as follows.

1) The automated bionic wig weaving process designed in this paper changes the layout of the three elements of manual weaving. The designed automated bionic wig weaving machine can realize horizontal and longitudinal weaving, making the automated continuous weaving of bionic wigs possible.

2) Taking the shortest weaving duration of a single hairnet as the objective function, the theoretical calculations and specific experiments are conducted respectively on the weaving duration of each path in the rectangular region and the semicircular region. In the rectangular region, the efficiency of the S-shaped weaving path increases by 7.7% compared with that of

the folding weaving path; in the semicircular region, the efficiency of the S-shaped weaving path increases by 9.0% compared with that of the mixed weaving path.

References

- [1] ZHANG Y. Rural revitalization industry needs such “unexpected” [N]. *Haidong Daily*, 2022-03-26 (001). (in Chinese)
- [2] LIU G M. Xuchang wig industry export: leverage advantages to produce high-quality products [N]. *China Trade News*, 2022-07-07 (007). (in Chinese)
- [3] MAZEKO ENTERPRISES, INC. Apparatus for implanting hair in manikins, dolls, and the like: US19490124305[P]. 1954-02-02.
- [4] HIROSHI H. Automated hair-transplanting machine for making and method of transplanting hair: JP20000129955 [P]. 2001-10-31. (in Japanese)
- [5] KUANG Z W, LI W G, KONG Z H, et al. Semi-automatic machine models in hair weaving [J]. *Mechanical Engineer*, 2007(9): 129-131. (in Chinese)
- [6] MITSUHIRO M, SHINICHI K, KOUJI M, et al. Hair implant device and method for manufacturing wig using hair implant device: JP2021043944[P]. 2022-06-09. (in Japanese)
- [7] LIN C H. A production process for wigs that uses a three-layer mesh: CN107028263A[P]. 2017-

- 08-11. (in Chinese)
- [8] TAO L, JIN Y C. A weaving technique for wigs: CN105708021B [P]. 2017-09-29. (in Chinese)
- [9] SUN Z H, LYU H Z, ZHANG B M, et al. A method for knotting hair transplant wigs: CN114224004A [P]. 2022-03-25. (in Chinese)
- [10] QIU H, XIE N W, ZHANG W, et al. Preparation of PET/PU elastic nonwoven material [J]. *China Synthetic Fiber Industry*, 2017, 40 (2): 17-20. (in Chinese)
- [11] PEI Y H, YU H. Discussion on the application status and problems of wig materials [J]. *Synthetic Fiber in China*, 2022, 51(12): 28-31. (in Chinese)
- [12] CHENG H M. Process technology design of imitated synthetic hair fiber [D]. Shanghai: Donghua University, 2014. (in Chinese)
- [13] CAI C R. Research on the process of wig production and the key mechanisms of wig production equipment [D]. Shanghai: Donghua University, 2023. (in Chinese)
- [14] LYU H Z, SUN Z H, ZHANG B M, et al. A fully automated wig planting machine: CN202210932166.1 [P]. 2022-11-11. (in Chinese)
- [15] LYU H Z, SUN Z H, ZHANG B M, et al. A crochet drive device used in wig weaving machine: CN202210932174.6 [P]. 2022-11-01. (in Chinese)
- [16] LYU H Z, SUN Z H, ZHANG B M, et al. A control device for hairnet used in wig weaving machine: CN202210931474.2 [P]. 2022-11-11. (in Chinese)
- [17] SUN Z H, LYU H Z, WU J M, et al. A hair strand clamping and feeding device for wig weaving machine: CN202210932172.7 [P]. 2024-07-30. (in Chinese)

仿生假发自动化织造工艺设计与织造路径规划

吕宏展*, 尤佳, 李俊杰, 陆李承, 孙志宏

东华大学 机械工程学院, 上海 201620

摘要: 传统的仿生假发生产由工人手工织造完成, 织造工艺过程复杂, 劳动强度大, 很难实现自动化。针对该问题, 在手工织造原理与工艺分析的基础上, 本文提出了自动化织造工艺和自动假发织造机的设计。根据该织造机的特点和织造结点分布规律, 以单张发网的总织造时长最短为优化目标, 对混合方案的织造工艺进行了连续织造路径规划。分别计算并对比不同织造路径的织造时长, 结果表明 S 型路径的织造时长最短。该自动化织造工艺设计与织造路径规划方法为仿生假发自动化织造的实现提供了理论依据和试验数据。

关键词: 仿生假发; 织造工艺; 假发织造机; 路径规划

Impact of Locally Resonant Phononic Crystal Plates on Noise Reduction in Automotive Mufflers

ZHANG Mengyang¹, ZHU Congyun^{1*}, DING Guofang¹, HUANG Qibai²

1. School of Intelligent Mechatronics Engineering (School of Industrial Design), Zhongyuan University of Technology, Zhengzhou 450007, China

2. School of Mechanical Science and Engineering, Huazhong University of Science and Technology, Wuhan 430074, China

Abstract: This paper presents a locally resonant phononic crystal with excellent noise reduction in the low-frequency range as a soundproofing plate in mufflers. A locally resonant phononic crystal is established, and the bandgap range of the phononic crystal is analyzed by using COMSOL software. Taking the partition plate in the muffler as the object, the acoustic-solid coupling is studied to analyze the sound insulation characteristics of the locally resonant phononic crystal. A phononic crystal plate-like structure is established to analyze its noise reduction performance in the muffler. The results indicate that the locally resonant phononic crystal exhibits favorable low-frequency sound insulation performance within a bandgap range below 200 Hz. At 160 Hz, the noise reduction is 15 dB higher than that of ordinary partition plates. As the number of layers of the phononic crystal plate increases, its noise reduction effect gradually enhances, while the magnitude of the noise reduction increment tends to diminish. At 160 Hz, the single-, double- and triple-layer plates achieve peak reductions of 47, 53 and 57 dB, respectively. Compared with the double-layer phononic crystal plate, the composite of the locally resonant phononic crystal plate and the steel plate has an average noise reduction of 5 dB higher. Through research and analysis of the composite locally resonant phononic crystal plates, more feasible combined structures can be provided for future muffler structural design.

Keywords: acoustic-solid coupling; muffler; low-frequency noise reduction; locally resonant phononic crystal; bandgap characteristic

CLC number: TK421+.6; TB53

Document code: A

Article ID: 1672-5220(2025)05-0558-08

Open Science Identity
(OSID)



0 Introduction

Industrialization and urbanization, particularly the growth of the automobile and transportation sectors, have significantly increased traffic noise, making urban noise

pollution^[1]. In daily life, people are frequently exposed to automotive noise, primarily exhaust noise, making the noise reduction effectiveness of mufflers a crucial factor in evaluating vehicle noise levels. As research on automotive mufflers has progressed, passive mufflers have become the most common noise reduction solution in automobiles. They are generally categorized into reactive, resistive and impedance composite types^[2].

In recent years, researchers have proposed the concept of phononic crystals by drawing an analogy with photonic crystals. Phononic crystals are artificially designed periodic materials or structures with elastic wave bandgaps. By adjusting the material and geometric parameters of phononic crystals, the propagation of elastic waves within specific frequency ranges can be significantly suppressed^[3-5].

Locally resonant phononic crystals, due to the presence of local resonance scatterers, can achieve very low-frequency bandgaps in small-sized topological structures and do not require strict periodicity^[6]. The bandgap and defect state characteristics of phononic crystals are theoretically valuable and practically useful for passive noise reduction, vibration isolation for precision mechanical platforms, and acoustic and vibration filters, offering a new theoretical approach for further vibration and noise reduction in automotive products.

The focus of phononic crystal research lies in the generation mechanisms of bandgaps and their control and regulation. Scholars have conducted extensive research in this area. Wen^[7] and Yu et al.^[8] introduced periodic phononic crystals into common engineering structures like beams and plates, and studied the bandgap and vibration isolation characteristics of typical periodic beam and plate structures. Experimental tests confirmed the existence of bandgap characteristics. Zhang et al.^[9] analyzed the impact of geometric and material parameters on the bandgap characteristics of phononic crystal plates under plane stress assumptions. The bandgap characteristics of

Received date: 2024-08-19

Foundation item: National Natural Science Foundation of China (No. 51705545)

* Correspondence should be addressed to ZHU Congyun, email: zcy711126@163.com

Citation: ZHANG M Y, ZHU C Y, DING G F, et al. Impact of locally resonant phononic crystal plates on noise reduction in automotive mufflers [J]. *Journal of Donghua University (English Edition)*, 2025, 42(5): 558-565.

locally resonant phononic crystals are closely related to the scatterers, and by designing the scatterers appropriately, the bandgap characteristics of phononic crystals can be regulated. Common scatterers include cantilever beams, single cylinders, and composite columns. Fang et al.^[10] analyzed the coupling mechanisms of two types of bandgaps in phononic crystals with beam resonators attached to aluminum plates, achieving coupling of Bragg and local resonance bandgaps in the low to mid-frequency range. Researchers^[11-14] discovered that beam-plate structures with added spring-mass systems and beam resonators exhibited excellent bandgap characteristics, with bandgap frequency ranges exceeding 200 Hz. In terms of sound insulation, Fan et al.^[15] fabricated a three-dimensional phononic crystal with rubber-coated metal spheres embedded in an epoxy resin matrix and measured their sound insulation. Li^[16] measured the sound insulation of two types of one-dimensional phononic crystals through sound insulation box tests, finding that phononic crystals increased sound insulation by about 5 dB in the 100–2 000 Hz frequency range. Assouar et al.^[17] theoretically analyzed the sound insulation mechanisms of aluminum plates with added spring-mass blocks and single rubber columns. He et al.^[18] further studied the impact of lattice constants on the sound insulation characteristics of aluminum plates with added copper-rubber composite columns, indicating that an appropriate lattice constant was needed to achieve a relatively broad sound insulation frequency range. In engineering applications, Shen et al.^[19] provided an overview of domestic and international research on the application of phononic crystals in vibration and noise reduction in ship piping systems, highlighting areas requiring further exploration. Gao et al.^[20] analyzed the sound insulation characteristics of unidirectionally periodic reinforced plate bulkheads in ship cabins at a frequency of 100–10 000 Hz. Ma et al.^[21] applied phononic crystals to the vibration and noise reduction of car roofs, reducing

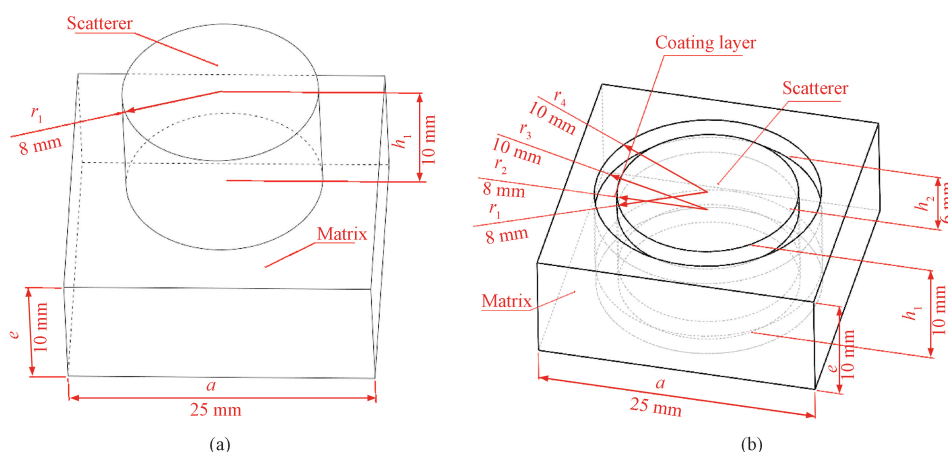
low-frequency vibration noise in car roofs. Zhang^[22] used two-dimensional (2D) phononic crystal plates to block mid-frequency noise caused by vehicle engines, effectively suppressing engine noise transmission in the 600–1200 Hz frequency range. Zhang et al.^[23] applied locally resonant phononic crystals with designed regular octagonal holes to large military aircraft cabins, achieving excellent low-frequency noise insulation with an increase of about 20 dB.

This paper designs a locally resonant phononic crystal plate structure tailored to the noise frequency characteristics of automotive mufflers. A locally resonant phononic crystal unit cell structure is modeled and analyzed by using the finite element software COMSOL to observe the bandgap characteristics and frequency ranges. Based on the bandgap ranges, a corresponding phononic crystal plate structure is applied to the muffler. The transmission loss curve of the muffler is calculated and analyzed in COMSOL to observe the noise reduction effect of the phononic crystal plate, providing a feasible plate structure application for automotive mufflers.

1 Design and Theoretical Analyses

1.1 Phononic crystal unit cell model structure

The phononic crystal unit cell model structure used in this paper is a solid-solid phononic crystal. The formation of the phononic crystal bandgap involves both Bragg scattering and locally resonant mechanisms. According to the different types of bandgaps, the phononic crystal unit cell models can be categorized into conventional phononic crystals (Fig. 1 (a)) and locally resonant phononic crystals (Fig. 1 (b)). Both types of phononic crystals use steel as the scatterer material and aluminum as the matrix material. The locally resonant phononic crystal features an additional coating layer made of silicone rubber. The material parameters of the phononic crystal unit cell are listed in Table 1.



a—lattice constant; r_1 —scattering radius; r_2 —inner radius of coating layer; r_3 —outer radius of coating layer; r_4 —matrix opening radius; e —matrix height; h_1 —scattering body height; h_2 —coating layer axial thickness.

Fig. 1 Phononic crystal unit cell model: (a) ordinary phononic crystal; (b) locally resonant phononic crystal

Table 1 Material parameters of phononic crystal unit cell

Part	Material	Density/(kg/m ³)	Elastic modulus/Pa	Poisson's ratio
Scatterer	Steel	7 850	2.1×10^{11}	0.28
Matrix	Aluminium	2 702	7.2×10^{10}	0.33
Coating layer	Silicone rubber	1 300	1.175×10^5	0.47

1.2 Theoretical calculation of phononic bandgap in phononic crystals

The finite element method is used to compute phononic crystals. Floquet periodic boundary conditions are applied at the unit cell boundaries, and the Bloch wave vector is introduced. This approach allows the band gap characteristics of an infinite phononic crystal to be analyzed by using a representative unit cell structure.

In the solid mechanics module, Floquet periodic boundary conditions are selected and applied to the adjacent boundary surfaces of the unit cell. The periodic boundary condition function is defined as follows:

$$\begin{cases} \mathbf{u}(x+a, y) = \mathbf{u}(x, y) e^{i(\mathbf{k}_x \cdot a)}, \\ \mathbf{u}(x, y+a) = \mathbf{u}(x, y) e^{i(\mathbf{k}_y \cdot a)}, \end{cases} \quad (1)$$

where \mathbf{u} stands for the nodal displacement; a is the lattice constant of the unit cell in the phononic crystal plate structure; \mathbf{k} is the Bloch wave vector confined to the irreducible Brillouin zone, its components in the x and y directions are denoted by \mathbf{k}_x and \mathbf{k}_y , respectively.

After setting the boundary conditions, the unit cell structure of the phononic crystal is meshed by using a standard mesh size. This results in a finite number of connected elements composed of nodes. The characteristic equation within the unit cell is

$$(\mathbf{K} - \omega^2 \mathbf{M}) \mathbf{u} = 0, \quad (2)$$

where \mathbf{K} represents the equivalent stiffness matrix; ω is the fluctuating angular frequency; \mathbf{M} denotes the mass matrix.

The Floquet periodic boundary settings in COMSOL software can constrain the boundary displacement of periodic structures to achieve Bloch boundary conditions, which satisfy the following equation:

$$\mathbf{u}_d = \mathbf{u}_s e^{-i\mathbf{k}_F \cdot (r_d - r_s)}, \quad (3)$$

where \mathbf{k}_F represents the wave vector; \mathbf{u}_s and \mathbf{u}_d represent the target displacement and the initial displacement of the Floquet periodic boundary, respectively. In the phononic crystal structure, r_d and r_s are defined as two characteristic positional parameters. The lattice constant a is given by the difference between them ($a = r_d - r_s$).

In the COMSOL finite element software, characteristic frequencies are added for research, and the step size of the parametric scan is selected. Due to the point group symmetry characteristics of phononic crystals, the Bloch wave vector \mathbf{k} is scanned along the symmetric boundaries of the irreducible Brillouin zone shown in Fig. 2. The scanning path follows the radial direction $M \rightarrow \Gamma \rightarrow X \rightarrow M$. By scanning the Bloch wave

vector \mathbf{k} to obtain its characteristic frequencies and referring to Eqs. (1) and (2), the band structure of the phononic crystal can be determined.

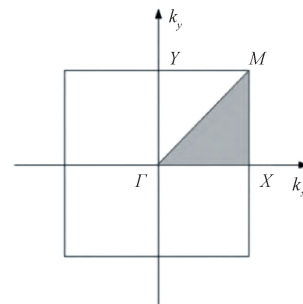


Fig. 2 Brillouin zone of 2D phononic crystal unit cell

1.3 Analysis of bandgap in phononic crystal unit cell structure

By using COMSOL, a simulation analysis was conducted for both regular phononic crystals and locally resonant phononic crystals. Figures 3 and 4 show the Floquet periodic boundary settings for the two types of phononic crystal unit cells, respectively. The unit cell matrix is made of aluminum with a height of 10 mm, while the scatterer is made of steel with a radius of 8 mm and a height of 10 mm. The lattice constant is 25 mm. The Floquet periodic boundary settings for the locally resonant phononic crystal unit cell are the same as those for the regular phononic crystal unit cell. The locally resonant phononic crystal features an embedded structure as shown in Fig. 1 (b), with a silicone rubber coating surrounding the scatterer. The radial thickness of the coating layer is 2 mm, and the axial thickness is 6 mm. The other structural material parameters are the same as those of the regular phononic crystal.

The mesh is defined by using COMSOL's built-in meshing tools, and the mesh refinement meets the requirements for phononic crystal simulation. The bandgap for the regular phononic crystal and the locally resonant phononic crystal unit cells are shown in Fig. 5, in which the horizontal coordinate represents the bandgap period and the vertical coordinate represents the start and end frequencies of the bandgap. It can be observed that the bandgap frequencies of the regular phononic crystal are relatively high, starting at about 40 000 Hz, whereas the bandgap frequencies of the locally resonant phononic crystal start at about 100 Hz. Since typical automotive noise occurs in the low-frequency range, the locally resonant phononic crystal is selected as a muffler baffle for studying its noise reduction performance.

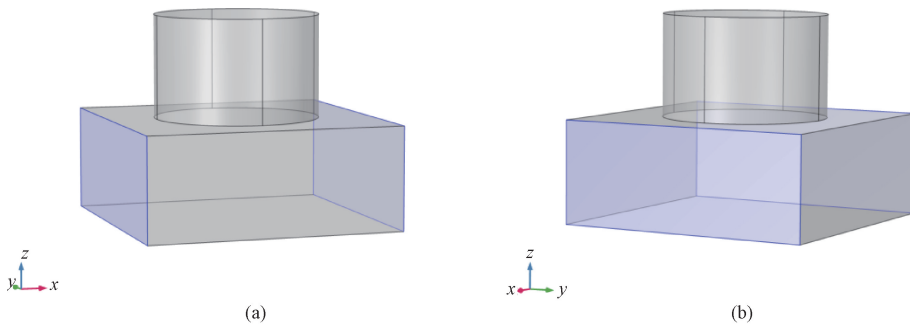


Fig. 3 Floquet periodic boundary settings of regular phononic crystal unit cell; (a) x periodic boundary; (b) y periodic boundary

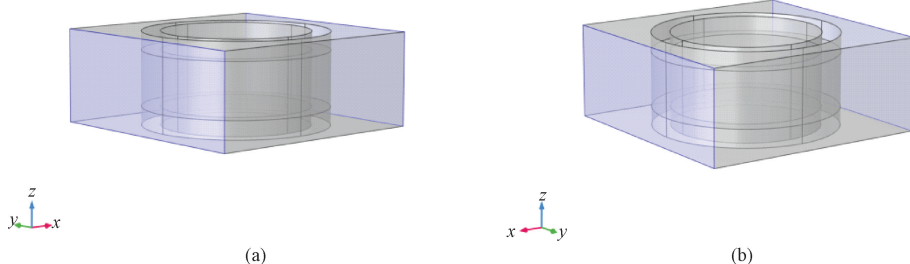


Fig. 4 Floquet periodic boundary settings of locally resonant phononic crystal unit cell; (a) x periodic boundary; (b) y periodic boundary

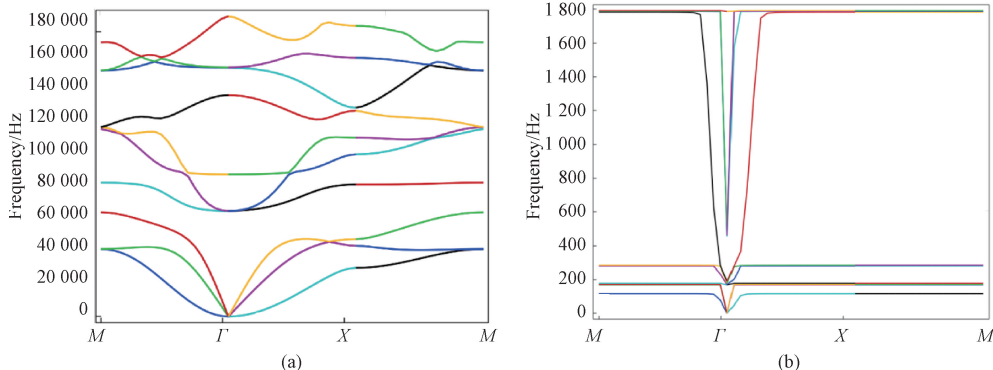


Fig. 5 Bandgap curves of phononic crystal unit cells; (a) regular phononic crystal; (b) locally resonant phononic crystal

1.4 Analysis of noise reduction characteristics of locally resonant phononic crystals

By using the acoustics-structural coupling module in COMSOL, the sound insulation properties of the phononic crystal structure can be calculated. Since both bandgap characteristics and sound insulation properties are based on the ideal phononic crystal (an infinite periodic structure), Floquet periodic boundary conditions can be applied to the surrounding boundaries of the phononic crystal structure. This allows for sound insulation calculations by using the structure of the phononic crystal unit cell and subsequently determines the sound insulation performance of the infinite phononic crystal periodic structure.

A noise reduction finite element model is established in COMSOL, as shown in Fig. 6. On both sides of the phononic crystal unit cell are air domains. The lower air domain is modeled as a background pressure field and is excited by an incident plane wave with a sound pressure amplitude of 1 Pa. Perfectly matched layers (PMLs) are configured at the ends of the air layers. Here, the PMLs

serve to simulate a non-reflective boundary for the sound field. The finite element mesh for the PML must be subdivided into at least 8 layers. The sound insulation properties of the phononic crystal structure and a standard aluminum plate are calculated by using COMSOL with the MUMPS direct solver. The frequency range for the solution is 10–2 000 Hz, with a calculation step size of 50 Hz.

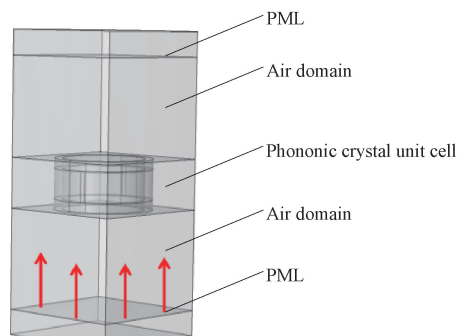


Fig. 6 Noise reduction finite element model

2 Simulation Experiment

2.1 Impact of muffler baffle structure on noise reduction performance

In automotive muffler noise reduction structures, commonly used designs such as high-temperature-resistant and aluminum-foam-based impedance composite mufflers. However, compared to phononic crystals, these

composite mufflers are relatively complex and are not well-suited for creating thinner designs. Therefore, using phononic crystal plates for sound insulation to reduce noise in automotive mufflers is a simpler and more effective noise reduction approach.

To effectively compare the noise reduction performance of phononic crystal mufflers, three muffler models were established as shown in Fig. 7.

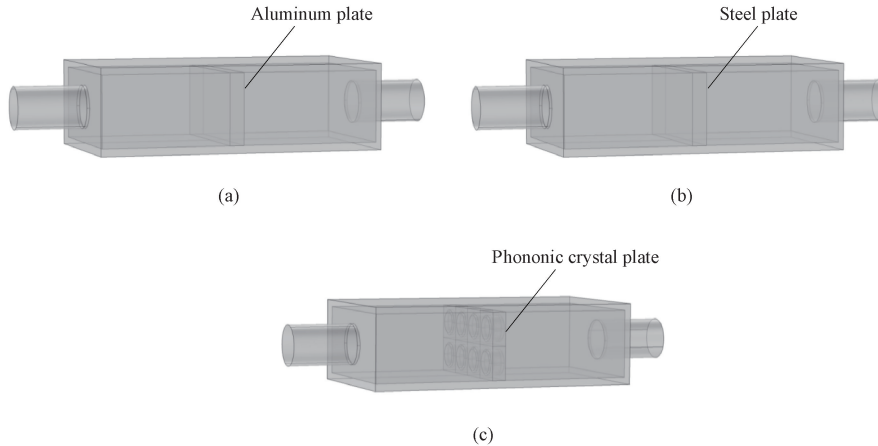


Fig. 7 Muffler models: (a) aluminum plate muffler; (b) steel plate muffler; (c) phononic crystal plate muffler

The transmission loss for these three models was observed at specific frequencies, as illustrated in Fig. 8.

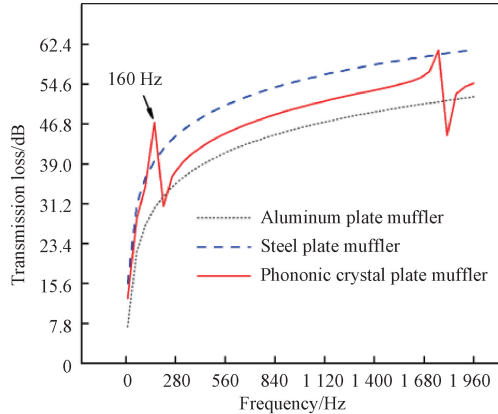


Fig. 8 Muffler transmission loss curve

Figure 8 shows that within the low frequency range of 0–280 Hz, the phononic crystal plate exhibits better noise reduction performance at 160 Hz. However, as the frequency increases, the noise reduction effectiveness of the phononic crystal plate is not as superior as that of the steel plate in the 300–1 700 Hz range. In comparison, the phononic crystal plate outperforms the aluminum plate in terms of the transmission loss below 2 000 Hz. Given that a steel structure would make mufflers heavier, the locally resonant phononic crystal plate is thus a better choice when all factors are considered.

2.2 Effect of the number of phononic crystal plates on noise reduction performance

When studying the noise reduction performance of locally resonant phononic crystal plates in mufflers, it is also important to investigate the effect of the number of phononic crystal plates on noise reduction. By comparing the noise reduction performance of two and three stacked plates to that of a single plate, we can assess the performance enhancement achieved by the multi-layer phononic crystal plate structure. The structural models are shown in Fig. 9. The length, width and height of the plates are 100, 50 and 30 mm, respectively, and the transmission loss results obtained from simulation analysis are depicted in Fig. 10.

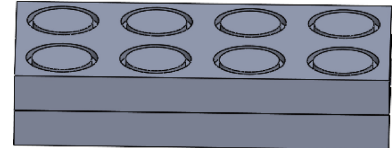


Fig. 9 Structure diagram of a multi-layer phononic crystal plate

Figure 10 shows that transmission loss increases with the number of photonic crystal layers. However, the peak frequencies of the curves remain unchanged, with peaks still occurring at 160 and 1 760 Hz. This indicates that the peak frequencies (or inherent vibrational frequencies) of the multi-layer structure remain unchanged. At the first peak of 160 Hz, the maximum noise reduction values for the single-, double- and triple-layer phononic crystal plates are 47, 53 and 57 dB, respectively. The higher number of layers results in higher transmission loss, but

the incremental benefit of additional layers decreases. Moreover, increasing the number of layers also raises material costs and the overall weight of mufflers. Therefore, selecting an optimal number of layers is crucial for achieving the best noise reduction performance.

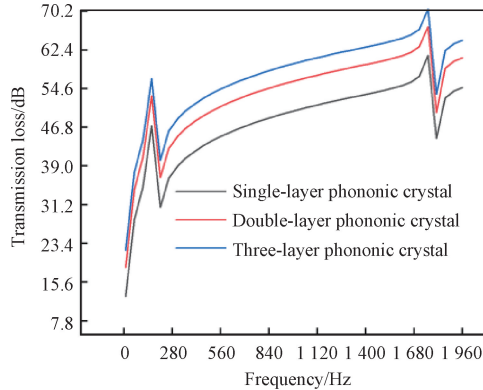


Fig. 10 Transmission loss of phononic crystal plates from simulation analysis

2.3 Analysis of sound insulation characteristics of composite phononic crystal plate

The noise reduction performance of a single phononic crystal plate, as shown in Fig. 8, is inferior to that of a single steel plate at certain frequencies, so we combined standard sound insulation plates with phononic crystal plates to study the noise reduction performance of these composite phononic crystal plates. We used combinations of aluminum plates with phononic crystal plates (aluminum-phononic crystal plate) and steel plates with phononic crystal plates (steel-phononic crystal plate), and compared these plates with a double-layer phononic crystal plate (double-phononic crystal plate). The resulting transmission loss curves are shown in Fig. 11.

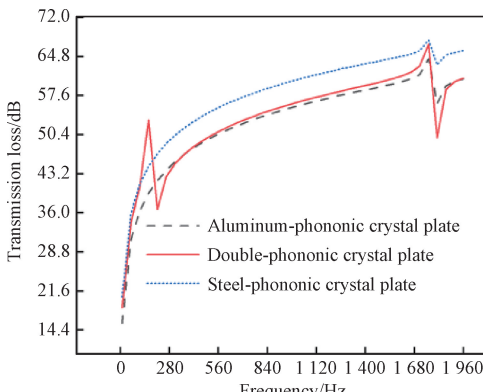


Fig. 11 Transmission loss of composite phononic crystal plates

Figure 11 shows that the double-layer phononic crystal plate exhibits the best noise reduction performance at 160 Hz, reaching 53 dB. However, within a frequency range of 280 – 2 000 Hz, the noise reduction of the

double-layer phononic crystal plate approaches that of the aluminum-phononic crystal plates. The steel-phononic crystal plate shows an average noise reduction improvement of about 5 dB over the double-layer phononic crystal plate. Therefore, when using composite phononic crystal plates, it is advisable to appropriately combine standard sound insulation plates with phononic crystal plates to achieve optimal sound isolation performance.

3 Conclusions

In this study, a locally resonant phononic crystal model was established by using COMSOL and employing acoustic-structural coupling simulation methods. The locally resonant phononic crystals offer superior low-frequency bandgap characteristics compared to conventional phononic crystals, with noticeable noise reduction at specific frequencies and stable performance in the low-frequency range. The locally resonant phononic crystal plate demonstrates certain advantages over aluminum and steel plates in terms of noise reduction. Additionally, when using composite structures, combining a standard plate with good sound insulation properties and phononic crystal plates achieves better noise reduction compared to a double-layer phononic crystal plate. Therefore, phononic crystal plates can be applied in automotive mufflers to achieve effective low-frequency noise reduction.

References

- [1] ZHANG R Q. Research on the noise reduction characteristics of double-layer perforated tube structures [D]. Zhengzhou: Zhongyuan University of Technology, 2023. (in Chinese)
- [2] LIU R J. Theoretical study and analysis of acoustic characteristics of mufflers based on multilayer acoustic materials [D]. Zhengzhou: Zhongyuan University of Technology, 2023. (in Chinese)
- [3] JIANG X, CHAI Y J, GENG Q, et al. Analysis of band gap characteristics of metamaterials in the solid-liquid state of scatterers [J]. *Journal of Vibration Engineering*, 2023, 36(3): 825-836. (in Chinese)
- [4] LI X C, YI X Y, WU X Z. Acoustic band gaps of two-dimensional phononic crystal with rotating square rods [J]. *Journal of Central South University (Science and Technology)*, 2006, 37(2): 269-273. (in Chinese)
- [5] WEN J H, YU D L, ZHAO H G, et al. Elastic wave propagation in artificial periodic structures: vibration and acoustic properties [M]. Beijing: Science Press, China Science Publishing & Media Ltd., 2015. (in Chinese)
- [6] LIU Z Y, ZHANG X X, MAO Y W, et al.

- Locally resonant sonic materials [J]. *Science*, 2000, 289(5485) : 1734-1736.
- [7] WEN J H. Study of the vibrational band gap and damping characteristics of phononic crystals [D]. Changsha: National University of Defense Science and Technology, 2005. (in Chinese)
- [8] YU D L, LIU Y Z, WANG G, et al. Vibration property of two-dimensional phononic crystal thin plate [J]. *Chinese Journal of Mechanical Engineering*, 2006, 42 (2) : 150-154. (in Chinese)
- [9] ZHANG Z, HAN X K, SU K C. Vibration reduction design of thin plate based on band gap features of phononic crystals [J]. *Journal of Synthetic Crystals*, 2016, 45(4) : 872-879. (in Chinese)
- [10] FANG X, WEN J H, BONELLO B, et al. Ultralow and ultra-broad-band nonlinear acoustic metamaterials [J]. *Nature Communications*, 2017, 8(1) : 1288.
- [11] XIAO Y, WEN J H, WEN X S. Flexural wave band gaps in locally resonant thin plates with periodically attached spring-mass resonators [J]. *Journal of Physics D: Applied Physics*, 2012, 45 (19) : 195401.
- [12] XIAO Y, WEN J H, WEN X S. Sound transmission loss of metamaterial-based thin plates with multiple subwavelength arrays of attached resonators [J]. *Journal of Sound and Vibration*, 2012, 331(25) : 5408-5423.
- [13] XIAO Y, WEN J H, HUANG L Z, et al. Analysis and experimental realization of locally resonant phononic plates carrying a periodic array of beam-like resonators [J]. *Journal of Physics D: Applied Physics*, 2014, 47(4) : 045307.
- [14] WU J, BAI X C, XIAO Y, et al. Low frequency band gap and vibration reduction properties of a multi-frequency locally resonant phononic plate [J]. *Acta Physica Sinica*, 2016, 65 (6) : 064602.
- [15] FAN N B, WANG X W. Relationship between structural parameters of sonic crystals and sound transmission loss [J]. *Development and Application of Materials*, 2013, 28 (2) : 51-54. (in Chinese)
- [16] LI S. Fundamental research of phononic crystal and application to vibration and noise reduction [D]. Harbin: Harbin Institute of Technology, 2012. (in Chinese)
- [17] ASSOUAR B, OUDICH M, ZHOU X M. Acoustic metamaterials for sound mitigation [J]. *Comptes Rendus Physique*, 2016, 17(5) : 524-532.
- [18] HE X D, XIAO Y, WEN J H. Influence of lattice constant on sound insulation properties of acoustic metamaterial plates [J]. *Noise and Vibration Control*, 2018, 38 (Sup. 1) : 51-55. (in Chinese)
- [19] SHEN H J, LI Y F, SU Y S, et al. Review of sound and vibration control techniques for ship piping systems and exploration of photonic crystals applied in noise and vibration reduction [J]. *Journal of Vibration and Shock*, 2017, 36 (15) : 163-170. (in Chinese)
- [20] GAO C, SU N, WANG Z C. Numerical analysis of transmission loss performance of periodic stiffened plate in ship cabin [J]. *Ship & Boat*, 2017, 28(2) : 38-42. (in Chinese)
- [21] MA C R, SHAO C, WAN Q M, et al. A locally-resonant phononic crystal for low-frequency vibration control of vehicles [J]. *Journal of Applied Acoustics*, 2018, 37(1) : 152-158. (in Chinese)
- [22] ZHANG J N. Research on sound insulation performance of vehicles based on phononic crystals [D]. Changsha: Hunan University, 2017. (in Chinese)
- [23] ZHANG J L, YAO H, DU J, et al. Low frequency sound insulation characteristics of the locally resonant phononic crystals in the large aircraft cabin [J]. *Journal of the Chinese Ceramic Society*, 2016, 44 (10) : 1440-1445. (in Chinese)

局域共振声子晶体板对汽车消声器降噪的影响

张梦阳¹, 朱从云^{1*}, 丁国芳¹, 黄其柏²

1. 中原工学院 智能机电工程学院(工业设计学院), 河南 郑州 450007

2. 华中科技大学 机械科学与工程学院, 湖北 武汉 430074

摘要: 提出了一种在低频范围具有良好降噪效果的局域共振声子晶体并应用于消声器隔声板。首先, 建立一种局域共振声子晶体, 使用 COMSOL 软件对声子晶体的带隙范围进行分析。其次, 以消声器隔板为研究对象, 通过声固耦合研究, 分析局域共振声子晶体的隔声特性。最后, 建立声子晶体板状结构, 分析其在消声器中的降噪性能。研究结果表明: 局域共振声子晶体的带隙范围在 200 Hz 以下可产生较好的低频隔声效果。在 160 Hz 时比普通隔板降噪高出 15 dB; 随着声子晶体板层数增加, 其降噪效果逐渐增强, 但降噪幅度逐渐减小。在 160 Hz 时, 单层、双层和三层声子晶体板的峰值降噪分别为 47、53 和 57 dB。与双层声子晶体板相比, 钢复合局域共振声子晶体板平均降噪高出 5 dB。研究分析复合局域共振声子晶体板可为未来消声器结构设计提供更可行的组合结构。

关键词: 声固耦合; 消声器; 低频降噪; 局域共振声子晶体; 带隙特性

征稿启事

Journal of Donghua University (English Edition) (JDHUE) 创刊于 1984 年，由中华人民共和国教育部主管、东华大学主办。JDHUE 聚焦纺织、材料、信息及交叉学科前沿，秉承“严谨求实·聚焦前沿·服务行业·创新发展”的办刊宗旨，致力于搭建高水平学术交流平台，为读者呈现前沿科技成果。JDHUE 诚邀广大作者、读者和各界朋友踊跃投稿。

一、征稿方向(包括但不限于)

纺织、材料及其相关领域的研究：纳米材料、功能高分子、功能纤维、高性能纤维、生态染整、功能纺织品、智能制造、环境净化、能量转换与储存、生物医用材料、智能可穿戴系统等。

信息与新一代人工智能研究：智能控制、群智能优化、机器学习、深度学习、计算机视觉、大数据等，及其在智能制造、纺织服装、新材料、智慧医疗等领域中的应用。

跨学科研究：交叉领域的探索与创新。

二、论文质量要求

论文为未公开发表的原创研究论文或综述论文，要求论据充分、数据可靠、行文流畅，具有一定的创新性、学术性、前瞻性。论文语言为英文，附中文摘要。

三、投稿方式

通过官网主页(<https://dhdy.cbpt.cnki.net/portal>)右侧“Author Submission”提交论文。

四、论文格式

论文模板详见官网主页右侧“Download Center”。